# Effects of Vascular Aging on Murine and Human Hemodynamics Revealed by Computational Modeling: Applications to Hypertension Research

by

Federica Cuomo

A dissertation submitted in partial fulfillment
of the requirements for the degree of
Doctor of Philosophy
(Biomedical Engineering)
in the University of Michigan
2019

Doctoral Committee:

Professor C. Alberto Figueroa, Chair
Research Assistant Professor Jose A. Diaz
Professor Krishna Garikipati
Assistant Professor Joan M. Greve

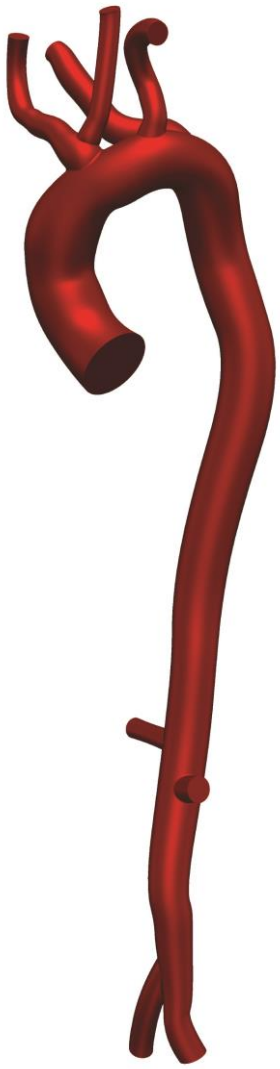

*My Aorta*

Federica Cuomo

cuomofed@umich.edu

ORCID iD:  0000-0002-8874-6557

**Acknowledgments**

I am profoundly grateful to my PhD advisor and mentor Professor C. Alberto Figueroa. Through his guidance as well as his passion for science, he has shaped me into the professional I am today. Through the years, he has always provided insightful feedback and support that has guided my research projects. In addition, I consider him to be a life coach and hope our relationship will continue to grow in the years to come. I thank him for always being available to talk about anything, creating a collaborative and inclusive lab environment, and above all, for giving me this opportunity.

I was immensely fortunate to work on a project born out of a collaboration between my PhD advisor and Professor Jay D Humphrey from Yale University. Prof. Humphrey has been a invaluable mentor and his immeasurable knowledge of the field and passion for science was a source of inspiration throughout my PhD.

I would like to provide a special thank you to my committee members: Professor Jose Diaz for his clinical insight, his contagious happy mood, and invaluable support; Professor Joan Greve for sharing her deep knowledge on small animal research, career advice, enthusiasm and support; and Professor Krishna Garikipati for great discussions and questions that led me to more deeply understand the core of my research.

I am grateful to Dr. Nan Xiao, whose PhD work set the foundation for this project, for imparting invaluable knowledge and for always having time for me, thank you!

I thank Dr. Jacopo Ferruzzi, former PhD student in Professor Jay Humphrey's lab, who collected all the mouse experimental data which made this thesis possible. He became a great friend over the years. Thank you for the long Skype calls, for your patience, and talent at communicating science. I appreciate you always being there to talk through research challenges.

Thank you to Professor Sara Roccabianca whose collaboration made the work on human aging presented in this thesis possible, and who I consider a mentor and a friend.

Thank you to Drs. Nitesh Nama and Miquel Aguirre for their work on ALE, which is briefly overviewed at the end of this thesis, and for being great friends in Ann Arbor. I am grateful to both of them for their consistent advice, support and friendship over the years.

I deeply thank the initial members of the Figueroa Lab: Dr. Kevin Lau, Dr. Des Dillon-Murphy and Dr. Chris Arthurs, who taught me so much, but first of all became lifelong friends. If I was in their company, it was likely I could be seen laughing to tears. Thank you Kev, brother from another mother, we shared so much in this transatlantic move, it is difficult to put into words. Des, it will be near impossible to find a desk neighbor who can keep up with you. And Chris, my morphologically-typical friend, lasagna a la Chris will always be a must to start long and pleasant conversations.

A heartfelt thank you to Sabrina Lynch, my close ally in the Figueroa Lab. She has always been an awesome friend, a travel mate, sweets pusher and made long days in lab much more fun. Thank you for reading this dissertation in its entirety and for always motivating me.

Thank you to the other members of Figueroa's lab: Jonas Shollenberger, Foeke Nauta, Diederik van Bakel, Vasilina Filonoma, Ignas Houben, Kritika Iyer, Christopher Tossas, Pradyumn Agarwal, Ashwin Kannan, Slava Khlebnikov, Marija Marcan, Sabrina Ben Ahmed, Paula Rudenick and Alia Noorani. Thank you for the amazing supportive and collaborative environment you all created, the PhD would have not been the same without every one of you! Thank you for the unique memories and for all those moments that kept me going.

I am grateful for the awesome scientists and friends I met at King's College London when I was introduced to research. I will always bring those awesome years in London with me. A special thank goes to Nika, Devis, Simo and Cata!

Thank you to Humphrey's Lab members who "adopted" me during conferences, among others Matt Bersi, Paolo D Achille, Chiara Bellini, Bart Spronck, Sae-Il Murtada. Their passion for research and scientific curiosity was a great source of inspiration.

I am grateful I met true friends here in Ann Arbor. These years would have not been the same without Rachel, Sydney, Mariana, Dakota, Sebi, Jack and Margot. Amaia and Rosa have been very much missed in the last years. It was awesome to share this journey with all of you!

At the beginning of my graduate school journey I met Dan, I could not have made it without him. I thank him for being the best friend and partner to create memories with, I am excited for all the many great things waiting for us moving forward.

I am so grateful to Dan's family: Sherry, John and Andrew. They always made me feel accepted and became my American family. I thank them for their love and precious advice. After every Atlanta or Dayton visit Dan and I were always rejuvenated like a true Spa.

Grazie ai miei amici storici che hanno fatto il tifo per me dall'Italia: Silvia, Gio, Ale e Bottu; é splendido sapere di poter sempre contare su di loro.

Il grazie più grande di tutti va alla mia famiglia! Grazie mamma e papá per avermi sempre sostenuta, dottorato a 7000 km di distanza incluso. I vostri insegnamenti su come approcciare le difficoltá sono stati fondamentali per finire questo viaggio. Grazie per essere sempre stati pronti a ricordarmi quali sono le cose importanti ogni volta che smarrivo la bussola, per tutti i vostri viaggi transatlantici per venire a trovarmi e per le lunghe chiamate. Grazie a Franci e Dani per il sostegno, per avermi sempre accolto con calore al mio ritorno e fatto sentire come se non fossi mai partita. Grazie a Diego e Cice che mi hanno fatto sentire una super zia, stare lontana da loro é stata dura, ma bastava guardare un loro video per ritrovare il buon umore.

Grazie a tutti i miei zii e cugini, troppi da nominare tutti, per il sostegno e per il caloroso affetto fondamentale per superare i freddi inverni del Michigan.

## Table of Contents

## List of Tables

## List of Figures

**Abstract**

Aging is a primary risk factor for increased central arterial stiffness which is both an initiator and indicator of cardiovascular, neurovascular and renovascular disease. It is hypothesized that an insidious positive feedback loop exists between arterial stiffness and systemic blood pressure. The clinical measurement to assess arterial stiffness non-invasively is carotid to femoral Pulse Wave Velocity (*cf-PWV*), yet controversy still remains. There exists a need to evaluate *cf-PWV* as an early diagnostic of progressive vascular stiffening and to better assess the potential effects of regional variations in central mechanical properties on blood hemodynamics that adversely affect microcirculation in the heart, brain and kidneys.

Computational modeling is a powerful tool to understand the complexity of central arterial function. In this work we used a robust, data-driven computational framework that combines 3D geometric vascular models, Fluid-Structure Interaction (FSI) analyses, Windkessel models to represent the distal vasculature and an external tissue boundary condition to represent perivascular support. FSI methods allowed to account for the deformability of the central vessels and included spatially variable anisotropic tissue properties.

We first introduced a data-driven FSI computational model of the human aorta to simulate effects of aging-related changes in regional wall properties and geometry on several metrics of arterial stiffness. Using the best available biomechanical data, our results for *PWV* compared well to findings reported for large population studies while rendering a higher resolution description of evolving metrics of aortic stiffening. Our results revealed similar spatio-temporal trends between stiffness and its surrogate metrics, except *PWV*, thus indicating a complex dependency of the latter on geometry. Furthermore, our analysis highlighted the importance of the tethering exerted by external tissues.

Due to difficulty in obtaining detailed information on evolving regional mechanical properties in humans, we focused on mouse models of vascular aging, which offer the advantage of easier longitudinal studies and data accessibility. We developed a workflow to combine *in vivo* and *in vitro* biomechanical data to build mouse-specific computational models of the central vasculature. These FSI models are informed by micro-CT imaging, *in vitro* mechanical

characterization of the arterial wall, and *in vivo* ultrasound and pressure measurements. We reproduced central artery biomechanics in adult wild-type, fibulin-5 deficient mice, a model of early vascular aging, and naturally aged wild type mice. Findings were also examined as a function of sex. Computational results compared well with data available in the literature and suggested that *PWV* does not well reflect the presence of regional differences in stiffening and it is affected by vascular wall stiffness heterogeneities. Modeling is also useful for evaluating quantities that are difficult to measure experimentally, including local pulse pressures at the renal arteries and characteristics of the peripheral vascular bed that may be altered by disease.

Notwithstanding the many advantages of animal models, it is important to consider that invasive experimental procedures may alter the quantity of interest. Advanced computational models offer a unique method to evaluate these measurements. Herein we evaluated the effects of commercially available catheters on the very parameters that they are designed to measure, namely murine blood pressure and *PWV*. We investigated two different setups and observed that both alter the measured values of *PWV*.

Lastly, we showed preliminary results involving automatic parameter estimation and expansion of the FSI framework to account for the large motions imposed by the heart on the aorta.

# Chapter 1. Introduction

## 1.1 Hypertension, Aging and Arterial Stiffness

Cardiovascular disease is the number one cause of death in the United States, accounting for 17% of the overall national health care cost. The direct medical cost of cardiovascular disease is predicted to triple from 2010 to 2030[1]. The most prevalent cardiovascular condition is high blood pressure[2], also called hypertension, a leading risk factor of morbidity and mortality[3]. Hypertension is defined by the American Heart Association as a systolic blood pressure value consistently higher than 130 mmHg or a diastolic value higher than 80 mmHg. If left untreated, it can lead to heart disease, stroke, coronary heart disease, neurovascular problems and kidney failure[3]. For this reason, targeting hypertension could prevent large increases in future healthcare costs[1].

Epidemiological studies have shown that aging is a prevailing risk factor for hypertension, due to age related changes in the arterial wall[4]. Age-related changes include luminal dilation of the central elastic arteries, luminal reduction of the small resistance arteries, intimal and medial thickening, reduced compliance of central arteries, endothelial dysfunction, impaired nitric oxide availability, increased reactive oxygen species and inflammation[4,5]. It is now known that arterial changes associated with aging and hypertension are interconnected at the cellular and molecular levels[4]. These structural, functional and molecular changes of the arterial wall lead to an increase in central arterial stiffness, which is known to be both an indicator and initiator of hypertension[6–8]. It is hypothesized that a positive feedback loop exists between arterial stiffness and systemic blood pressure, independent of the starting point[5,9] (Figure 1.1). Increasing blood pressure leads to remodeling and thickening of the arterial wall, with the goal of maintaining constant values of circumferential stress, at the expense of increases in structural stiffness. Increases in structural stiffness cause an earlier reflection of the pressure wave which in return further augments central pulse pressure[9].

The role of the extra cellular matrix is fundamental to understand the mechanical properties of the arterial wall, as well as its remodeling and stiffening[5,10,11]. The principal constituents are proteins like collagen and elastin[12], which are fundamental to explain the alterations in structure and function in hypertension and aging. Collagen provides structure, strength and flexibility of the

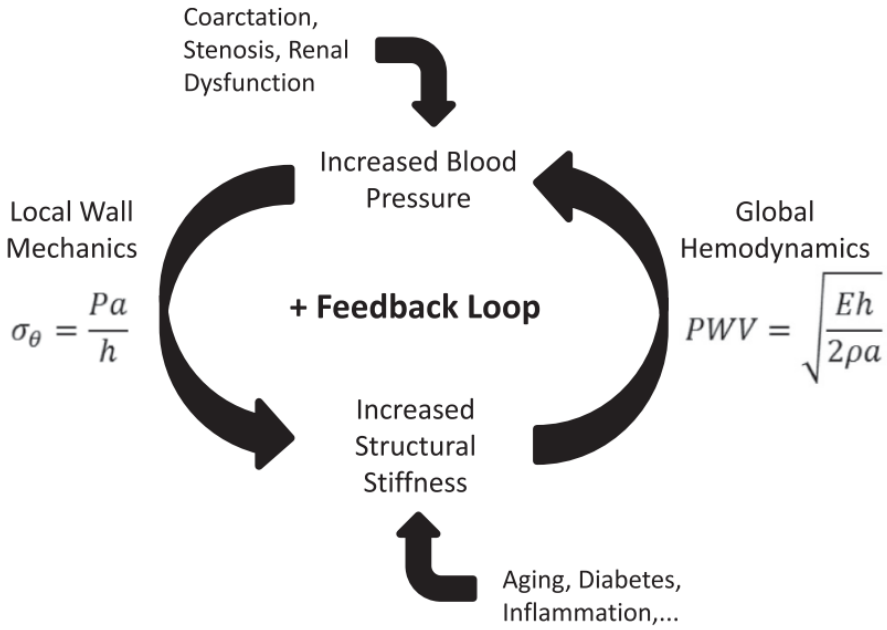


**Figure 1.1.** From Humphrey et al.[9], possible positive feedback loop between local mechanics and global hemodynamics. Increase in structural stiffness of the arterial wall causes an increase in blood presssure and viceversa, indipendently of which event happens first.

vessel wall. Collagen molecules are first organized in collagen microfibrils, which are then organized in fibrils and ultimately in fibers. Fibrils and fibers are organized by interchain cross-links. The directions of cells, microfibril orientations and diameters depend on the stress field of the extracellular matrix. The collagen fibers in the vessel wall are undulated at physiological loads, and are progressively recruited when straightened under the action of applied loads[5,10,12,13]. The half-life of collagen in the cardiovascular system is between 15-90 days. A delicate balance between synthesis and degradation maintains physiological levels of collagen[12]. Contrastingly, elastin is the component of arteries responsible for their large compliance. Elastin is the amorphous component of elastic fibers, whose primary role is to store and return mechanical energy. Expression of elastin begins in mid-gestation and continues through the postnatal period[10]. In the aorta, expression decreases rapidly when the blood pressure stabilizes after birth, and adults have minimal elastin synthesis, which explains why repair of elastic fibers is incomplete in the adult period[10]. Furthermore elastin has a half-life of more than 25 years[14], very different compared to collagen. Arteries exhibit a non-linear mechanical behavior, with stiffness increasing with the degree of loading. At low pressures, tension is borne by elastin while the much stiffer collagen fibers remain folded. As pressure and stretch increase, collagen fibers are gradually distended and

recruited and the vessel becomes progressively stiffer, preventing over-distension at high pressures[15].

Increases in structural stiffness associated with aging and hypertension are mainly due to increases in collagen deposition and cross linking, fragmentation of elastin fiber and buildup of other proteins in the aortic wall[4,16]. Fragmentation of elastin ultimately has two effects on the arterial wall: it leads to both a loss of the most compliant component of the vessel wall and a decrease in the undulation of collagen fibers[13]. Both factors are key contributors to hypertension.

### 1.2 Implications of Arterial Stiffness

The central arteries dampen the pulsation generated by the left ventricle so that blood flow is ultimately continuous at the level of the arterioles and capillaries. The central arteries first distend to accommodate the sudden increase in blood volume and then contract releasing the elastic energy generated during distension. Hence, arteries undergo a regular beating or pulse, which propagates in the form of waves. A forward wave propagates through the wall during systole, and it reflects back due to branching sites, peripheral impedance, and any other variations in arterial geometry and elastic properties. The resulting pressure wave in the central circulation is the sum of the forward and reflected waves[17]. Most reflected waves return to the central circulation during early diastole and thus contribute to augment coronary blood flow. Wave reflections protect the microcirculatory vasculature from excessive energy propagation (see Figure 1.2A).

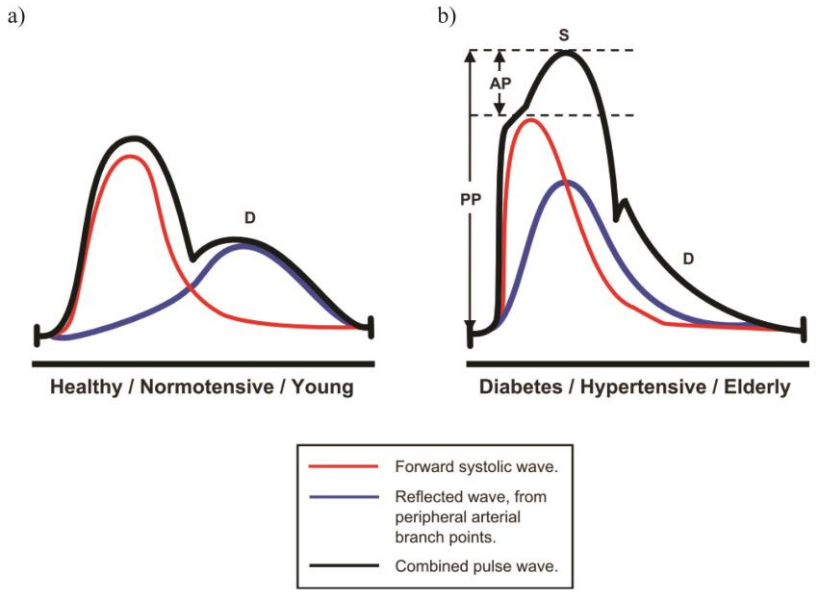


**Figure 1.2.** From Kum and Karalliedde[18], schematic of pressure wave reflection. a) In the young/healthy subject the reflected wave returns in early diastole, augmenting coronary perfusion. b) In the elderly/unhealthy patient increase in stiffness of the arterial wall causes earlier return of the reflected wave, with consequently increase of systolic pressure in the central vessels.

In healthy and young subjects the proximal aorta is more compliant than the rest of the arterial system. The spatial increase in arterial stiffness is associated with increases in pulse pressure as the distance from the heart augments. A pulse pressure amplification of 10 to 15 mmHg is observed between the central aorta and large peripheral arteries such as the radial artery[19]. Pulse pressure amplification is a protective mechanism which allows the heart to pump against a lower systolic blood pressure and hence against a lower afterload[19] (Figure 1.3).

In hypertensive and/or elderly subjects the arterial system is stiffer than in healthy young adults. For this reason the pulse wave travels faster and the reflected wave returns to the central aorta during late systole causing increased systolic blood pressure. The augmented central pulse pressure increases cardiac workload and decreases coronary perfusion. This mechanism is thus a major contributor to the development of left ventricle hypertrophy and heart failure in elderly and hypertensive patients[20] (Figure 2.2B) For this reason pulse pressure amplification is not observed in the elderly (Figure 1.3).

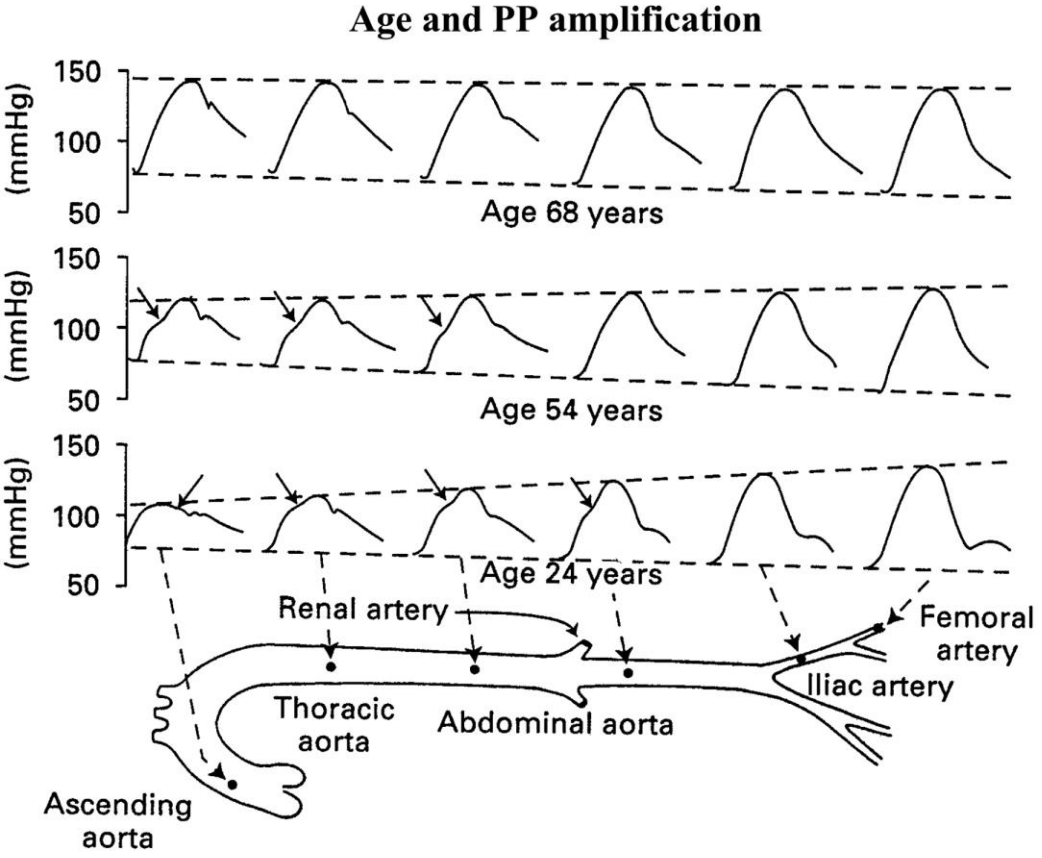


**Figure 1.3.** From Safar and Laurent[21], pressure waves from central to peripheral arteries at different ages. We observe pulse pressure amplification in the young/healthy adult, while in the elderly an increase in central pulse pressure leads to lack of pressure amplification.

Another implication of arterial stiffening has recently become apparent. With stiffened elastic vessels, there is an increase in pulsatile flow and pressure patterns in the microcirculation especially for low resistance organs such as the kidney and the brain[7]. The result is predisposition to dementia and strokes and deterioration of glomerular function in the kidney[7]. Two hypothesis were formulated to explain these observations: i) The pulsations generated by the heart are not cushioned and absorbed by stiffened arteries, hence they are transmitted to the microvasculature, predisposing the subject to vessel rupture, endothelial denudation and thrombotic obstruction of tiny arteries[7]; ii) Central arterial stiffening is observed with aging and disease, while a lack of stiffening for large muscular arteries is demonstrated[22]. Therefore the normal gradient of stiffness decreases from elastic-to-muscular arteries and pressure waves propagate farther distally where they can damage the microcirculation of end-organs[8].

### 1.3 Clinical Metrics of Arterial Stiffness

Epidemiological studies demonstrated the importance of arterial stiffness assessment and its complementary role to measurements of blood pressure to assess arterial health[23]. Measuring arterial stiffness routinely in the clinic requires proficiency in performing and interpreting the measurements, so that patient care[23] can ultimately benefit. Here we review the main indices used as surrogate metrics of arterial stiffness.

**Pulse wave velocity.** Pulse Wave Velocity (*PWV*) is the speed at which pressure waves move down a compliant vessel. The Moens-Korteweg formula: $c = \sqrt{Eh/2\rho r}$, where $c$ is the wave speed, $E$ is the Young's modulus, $\rho$ is the blood density, $h$ is the vessel thickness and $r$ is the vessel radius is an empirical metric to estimate *PWV*. It shows the dependency of *PWV* on both geometry and wall properties and it explains why *PWV* is used as a surrogate for arterial stiffness. However, the Moens-Korteweg equation was derived under assumptions that do not apply to the arterial system: namely inviscid flow, constant vessel area, constant wall thickness and linear material behavior under small strains.

Measuring *PWV* in the clinic requires simultaneous acquisition of pressure or flow waveforms at two locations along the arterial tree, or gating both recordings to a fixed point in the cardiac cycle using electrocardiogram (ECG) traces. *PWV* is then evaluated as the distance between the two measuring locations divided by a metric of the phase lag between the two waveforms. Different methods have been used to acquire these measurements, both invasive techniques such

as pressure catheter measurements and noninvasive techniques such as oscillometry, tonometry, mechanotransducers, ultrasound and magnetic resonance imaging. These techniques vary significantly in cost, and required time to measure and technical expertise[23].

The "Expert consensus document on arterial stiffness"[24] states that carotid to femoral *PWV* (*cf-PWV*) is the only non-invasive comprehensive method which is simple and accurate enough to be considered as a diagnostic procedure[25]. Yet this methods has limitations and pitfalls[25]. The lack of knowledge of the path the waves travel causes uncertainty in *PWV* measurements. There is no wave traveling directly from the carotid to the femoral artery, as such *cf-PWV* is only an estimate of the true values of aortic *PWV*. Two methods are typically used to measure the distance between the locations: directly measured distance between the carotid and femoral measuring location, or subtraction of the suprasternal notch and carotid distance from the suprasternal notch and femoral distance. The second approach attempts to correct for the fact that the wave travels simultaneously towards the carotid and femoral arteries. Both distances are body surface measurements and they do not provide the exact travel path of the wave. These measurements may become unreliable in the elderly or in patients with cardiovascular disease, where the tortuosity of the vessels increases and creates another source of error[25]. Using MRI to measure *PWV* allows clinicians to quantify the exact path length with better accuracy, although the temporal resolution of the waveforms is relatively low compared to the other methods, rising uncertainty in the quantification of the phase lag[25]. Furthermore it is not a method employable routinely in the clinic.

*PWV* is less accurate if the two recording points are close to one another, therefore its use is limited on a large portion of the arterial system. *PWV* is a global, integrated measurement of the properties of the arterial segment under study. Since *cf-PWV* averages the effects of regional differences in wall structure over a large portion of the arterial tree, it may yield a low-sensitivity metric that may reach a diagnostic level only after early regional changes in stiffness have progressed to entrenched changes. Lastly, the values of *PWV* depend on the blood pressure[26–28]: interventions which lower mean arterial pressure also lower *PWV*, but this does not always mean that the arterial stiffness decreased as a result of the intervention[23].

**Augmentation index.** As described in section 1.2, the arterial pressure waveform is a combination of the forward pressure wave created by the heart contraction and the reflected wave. The augmentation index (AIx) aims to quantify this phenomenon, and it's another surrogate of systemic stiffness. It is defined as the ratio between the augmented pressure (AP) and pulse

pressure (PP) expressed as a percentage. The augmented pressure is the difference between the second and first systolic peaks and it's attributed to the reflected wave (see Figure 1.2).

$$AIx = \frac{AP}{PP} * 100$$

Arterial pressure waveforms should be measured and analyzed at the ascending aorta to quantify AIx. The most widely used approach is to perform a radial artery tonometry and then apply a validated transfer function to reconstruct the corresponding central pressure waveform[24]. The common carotid pressure waveform is also analyzed.

AIx depends on both the magnitude of wave reflection and the timing of wave reflection. Many physical and physiological parameters affect the timing, such as the subjects' height, heart rate, aortic stiffnes[29]. Furthermore this metric is very sensitive to the identification of the peaks on the pressure waveform[29]. Lastly, this index loses sensitivity after a certain age[29].

**Distensibility.** Local distensibility is measured to assess local arterial stiffness, defined as

$$Distensibility = \frac{\Delta V}{\Delta P\, V}$$

where $V$ is the volume and $P$ is blood pressure. Both Ultrasound and MRI are used for the measurements. A major advantage is that local arterial stiffness is directly determined from the change in pressure driving the change in volume. To this aim echotracking devices were developed to measure the diameter of the blood vessel of interest at end diastole and stroke change in diameter with a high precision[24]. Blood pressure needs to be recorded simultaneously. This is usually done in the brachial artery or finger, which may not be appropriate if distensibility is being assessed in a more central artery, due to the normal phenomenon of pressure wave amplification towards the periphery[30]. All the superficial arteries are suitable for the geometrical investigation, particularly the common carotid, common femoral, and brachial arteries, where the local pressure can be obtained by applanation tonometry of the vessel in question.

**Systemic compliance.** A method used to estimate systemic arterial stiffness non-invasively is pressure pulse contour analysis. This technique also involves tonometry at the radial artery and the use of a transfer function to reconstruct central pressure waveform. The compliance is then derived, using a modified Windkessel model of the circulation and an assessment of diastolic pressure decay[24,31].

In sum, it is clear that in recent years there has been an increased emphasis on indices of arterial stiffness. We briefly summarized herein the main indices currently available and have

observed that methodological pitfalls need to be overcome. There is a pressing need to improve our ability to interpret current hemodynamic metrics of arterial stiffening and to understand if they can be used as an early indicator of local increases in pulse pressure at the levels of the heart and kidneys. Furthermore we need more rigorous means to investigate how spatial and temporal changes in arterial material properties and geometry impact the global and local hemodynamics.

### 1.4 Image Based Computational Models of Hemodynamics

Computational methods for simulating blood flow have become useful tools to gain insight into the physical behavior of the cardiovascular system in healthy and diseased states. Computational models have advanced to the point that they enable reliable estimates of many hemodynamic quantities, including those important for studying vascular mechanobiology or designing medical devices.

As explained above, consequences of increased central artery stiffness are many, there is a pressing need for a more systematic and objective means to assess effects of local versus global changes in arterial mechanics on the overall hemodynamics. Computational models are a powerful tool to understand the complexity of central artery function which involves many factors such as the branched and tapered vascular tree, regionally varying anisotropic properties of the arterial wall and complex hemodynamics. Among its many advantages, computational modeling provides insight into quantities which are not easily accessible through experiments. They allow high spatial resolution description on metrics such as *PWV*. As explained before, *PWV* measured in the clinic is less reliable when measured using two measurement locations close to each other, but computational models output high temporally resolved waveforms, allowing to asses phase lag accurately between close measurements. Furthermore computational models can help build intuition to interpret clinically available results.

The methods used to model blood flow range from simple lumped parameter models to full 3D formulations of Fluid-Structure Interaction (FSI) techniques. In this work we use a robust, data-driven computational framework that combines a 3D geometric vascular model, a FSI formulation to account for the deformability of the central vessels that includes spatially variable anisotropic tissue properties, Windkessel models to represent the distal vasculature and an external tissue boundary condition to represent perivascular support. We employed this framework to investigate how age-related changes in arterial stiffness are reflected in local and global hemodynamics; how changes in central arterial stiffness with aging and disease affect the peripheral vasculature; and

how we can improve our ability to interpret current clinical hemodynamic metrics of arterial stiffening.

Several studies have reported *in vitro* measurements of biaxial mechanical properties of the aorta as a function of location and age[32–34] and recent advances promise to enable such properties to be inferred *in vivo*[35]. Yet, no current data set includes subject-specific longitudinal medical imaging and associated *in vivo* assessments of arterial wall properties, perivascular support, and regional hemodynamics. In this thesis, we used the best available population data on age-associated changes in aortic wall geometry and mechanics to reproduce hemodynamics in the human aorta at different ages. We then used these models to investigate metrics of arterial stiffening.

Due to difficulty in obtaining detailed information on evolving regional mechanical properties in humans (fundamental to inform FSI computational models), animal models have become increasingly important in studying vascular health and disease. In this thesis we have combined our computational framework with comprehensive sets of data acquired in mice. Most prior analyses of hemodynamics within the central vasculature in mice have been based on rigid wall analyses or simple geometries[36–39]. Here, we developed the first, to the best of our knowledge, FSI models of 3D blood flow in the murine vasculature for adult male and female wild type controls (C57BL/6 x 129/SvEv) and mice models of aging under anesthetized conditions to which results from other models can be compared.

Many of the experimental procedures to assess data necessary to inform accurate FSI models used in this thesis were terminal. Generally speaking, it is challenging to obtain data on biaxial stiffness, aortic anatomy and hemodynamics from the same mouse, making it difficult to perform truly mouse-specific FSI hemodynamic simulations. A key methodological contribution of this work is the development of a workflow to integrate *in vivo* and *in vitro* experimental data on hemodynamics, wall mechanics and anatomy from multiple cohorts into single computational models of vascular biomechanics.

Notwithstanding the many advantages of animal models, it is important to consider possible shortcomings: i) some experimental procedures perturb the quantity of interest; and ii) there are differences between mice and humans that may make it difficult to extrapolate findings. Advanced computational models offer an objective, nonintrusive approach to evaluate these

limitations. In this thesis, we quantified the effects of different commercially available catheter systems to measure *PWV* on the hemodynamics in mice.

Lastly, some features of our computational framework can be further advanced. First of all, our computations rely on a large number of parameters, such as a lumped-parameter heart model, outflow boundary conditions, external tissue support and wall stiffness. For instance, the mouse models considered in this work have approximately 30 outlets, thereby requiring the specification of 90 Windkessel parameters. Estimating these parameters is often the most time consuming and non-systematic task of the modeling process. Data assimilation techniques based on a reduced-order unscented Kalman filter (ROUKF) had been used to estimate parameters such as external tissue support, wall stiffness, and outflow boundary conditions[40,41]. In this work, we showed preliminary work towards incorporating data assimilation technique in our murine models to have a systematic and automatic method for calculating outflow boundary conditions based on the available experimental data. Furthermore, our FSI models employs a linear membrane method for the vessel wall, therefore large motions of the ascending thoracic aorta are not captured. In the Future Computational Enhancement chapter of this thesis, we highlighted the work required for incorporating nonlinear membrane models into our FSI formulation.

### 1.5 Animal Models of Hypertension

Murine models offer numerous advantages for informing FSI computations, particularly given the ability to study diverse mouse models (genetic, pharmacologic and surgical) representing myriad conditions. Furthermore their lifespan is around 2 years and advances in instrumentation allow careful *in vitro* and *in vivo* quantification of arterial wall mechanics and cardiovascular function.

As explained in section 1.1, increases in structural stiffness of the central arteries in humans are mainly due to elastin degradation, increase in collagen and buildup of other proteins in the aortic wall[4]. It has been shown that humans and mice[42] have a similar half-life of vascular elastin although their life-spans are drastically different. Therefore, there are important similarities that allow for mice models to be useful surrogates for research, but the important differences must also be carefully considered.

Old mice exhibit a vascular aging phenotype[43,44], but not as a result of significant changes in elastic fiber integrity. However, genetically modified mouse models can be used to study the effects of graded losses in elastic fiber integrity, with the fibulin-5 deficient mouse displaying the

most dramatic elastopathy in the common carotid artery of multiple viable models of elastic fiber-associated mutations[45]. Fibulin-5 is a glycoprotein that associates with elastin to form elastic fibers, and it is thought to function largely in elastogenesis. Histological evidence reveals disrupted elastic laminae in these mice, primarily in the outer portion of the media. Indeed, it appears that this mouse represents a model of early, stable vascular aging[46].

Multiple mice models of aging are needed to capture the different remodeling mechanisms that contribute to aging and hypertension in humans. In this thesis we investigated two mice models of arterial aging: fibulin 5 deficiency mice and naturally aged wild type mice. Results from these groups are compared to adult wild-type mice used as control.

### 1.6 Structure of Thesis

We first studied hemodynamics of the human aorta for three different age groups and we used these models to investigate metrics of arterial stiffening (**Chapter 2**). Due to the lack of data in human tissue properties, we then combined computational models and mice data. Many of the requisite experimental procedures to acquire data in mice are terminal, therefore typically not all data can be collected from a single mouse. We therefore developed a workflow for combining *in vivo* and *in vitro* data acquired in different animals to build mouse-specific computational models of central vasculature hemodynamics, as described in **Chapter 3.** We then investigated the effects of mechanical and structural changes on hemodynamics in two mouse models of aging: fibulin 5 deficiency (**Chapter 3**) and naturally aged mice (**Chapter 4**) and compared them to wild type mice. In **Chapter 5** we showed how computational models can be used to investigate the effects of commercially available catheters on the specific parameters that they are designed to measure, namely, murine blood pressure and pulse wave velocity. Lastly, we presented preliminary work involving automatic parameter estimation and an expansion of the FSI framework to include the large motions imposed by the heart on the aortic root (**Chapter 6**). The general Discussion of this thesis is presented in **Chapter 7**.

**Chapters 2, 3** and **5** correspond to published peer-reviewed papers. The format of the papers has been adjusted to match the rest of the thesis with minimal changes to the content.

## Bibliography


1. Heidenreich PA, Trogdon JG, Khavjou OA, et al. Forecasting the future of cardiovascular disease in the United States: a policy statement from the American Heart Association. *Circulation*. 2011;123(8):933-944. doi:10.1161/CIR.0b013e31820a55f5.

2. Mensah GA, Brown DW. An overview of cardiovascular disease burden in the United States. *Health Aff*. 2007;26(1):38-48. doi:10.1377/hlthaff.26.1.38.

3. Schmieder RE. End organ damage in hypertension. *Dtsch Arztebl Int*. 2010;107(49):866-73. doi:10.3238/arztebl.2010.0866.

4. Lakatta EG, Wang M, Najjar SS. Arterial aging and subclinical arterial disease are fundamentally intertwined at macroscopic and molecular levels. *Med Clin North Am*. 2009;93(3):583-604. doi:10.1016/j.mcna.2009.02.008.

5. Laurent S, Boutouyrie P. The structural factor of hypertension: large and small artery alterations. *Circ Res*. 2015;116(6):1007-1021. doi:10.1161/CIRCRESAHA.116.303596.

6. Boutouyrie P, Laurent S, Briet M. Importance of arterial stiffness as cardiovascular risk factor for future development of new type of drugs. *Fundam Clin Pharmacol*. 2008;22:241-246. doi:10.1111/j.1472-8206.2008.00584.x.

7. Adji A, O'Rourke MF, Namasivayam M. Arterial stiffness, its assessment, prognostic value, and implications for treatment. *Am J Hypertens*. 2011;24(1):5-17. doi:10.1038/ajh.2010.192.

8. Mitchell GF. Effects of central arterial aging on the structure and function of the peripheral vasculature : implications for end-organ damage. *J Appl Physiol*. 2008;105:1652-1660.

9. Humphrey JD, Harrison DG, Figueroa CA, Lacolley P, Laurent S. Central artery stiffness in hypertension and aging: a problem with cause and consequence. *Circ Res*. 2016;118(3):379-381. doi:10.1161/CIRCRESAHA.115.307722.

10. Wagenseil JE, Mecham RP. Vascular extracellular matrix and arterial mechanics. *Physiol Rev*. 2009;89(3):957-989. doi:10.1152/physrev.00041.2008.

11. Humphrey JD, Dufresne ER, Schwartz MA. Mechanotransduction and extracellular matrix homeostasis. *Nat Rev Mol Cell Biol*. 2014;15(12):802-812. doi:10.1038/nrm3896.

12. Humphrey JD. *Cardiovascular Solid Mechanics: Cells, Tissues, and Organs*.; 2002. doi:10.1017/CBO9781107415324.004.

13. Ferruzzi J, Collins MJ, Yeh AT, Humphrey JD. Mechanical assessment of elastin integrity in fibrillin-1-deficient carotid arteries: implications for Marfan syndrome. *Cardiovasc Res*. 2011;92:287-295. doi:10.1093/cvr/cvr195.

14. Sherratt MJ. Tissue elasticity and the ageing elastic fibre. *Am Aging Assoc*. 2009;31(4):305-325. doi:10.1007/s11357-009-9103-6.

15. Shadwick RE. Mechanical design in arteries. *J Exp Biol*. 1999;202(Pt 23):3305-13.

16. Safar ME. Arterial aging-hemodynamic changes and therapeutic options. *Nat Rev Cardiol*. 2010;7(8):442-449. doi:10.1038/nrcardio.2010.96.

17. Alastruey J, Parker KH, Sherwin SJ. Arterial pulse wave haemodynamics. *11th Int Conf Press Surges*. 2012:401-443.

18. Kum F, Karalliedde J. Critical appraisal of the differential effects of antihypertensive agents on arterial stiffness. *Integr Blood Press Control*. 2010;3:63-71.

19. Barodka VM, Joshi BL, Berkowitz DE, Hogue CW, Nyhan D. Implications of vascular aging. *Anesth Analg*. 2011;112(5):1048-1060. doi:10.1213/ANE.0b013e3182147e3c.

20. Safar ME. Mechanism(s) of systolic blood pressure reduction and drug therapy in hypertension. *Hypertension*. 2007;50:167-171.

21. Safar ME, Laurent P. Pulse pressure and arterial stiffness in rats: comparison with humans. *Am J Physiol Heart Circ Physiol*. 2003;285(4):H1363-9. doi:10.1152/ajpheart.00513.2003.

22. Mitchell GF, Parise H, Benjamin EJ, et al. Changes in arterial stiffness and wave reflection with advancing age in healthy men and women: The Framingham Heart Study. *Hypertension*. 2004;43(6):1239-1245. doi:10.1161/01.HYP.0000128420.01881.aa.

23. Townsend RR. Arterial stiffness: recommendations and standardization. *Pulse*. 2016;4(1):3-7. doi:10.1159/000448454.

24. Laurent S, Cockcroft J, Van Bortel L, et al. Expert consensus document on arterial stiffness: methodological issues and clinical applications. *Eur Heart J*. 2006;27:2588-2605. doi:10.1093/eurheartj/ehl254.

25. Segers P, Kips J, Trachet B, et al. Limitations and pitfalls of non-invasive measurement of arterial pressure wave reflections and pulse wave velocity. *Artery Res*. 2009;3(2):79-88. doi:10.1016/j.artres.2009.02.006.

26. Bramwell JC, Hill A V. The velocity of the pulse wave in man. *Proc R Soc B Biol Sci*. 1922;93:298-306.

27. Kim EJ, Park CG, Park JS, et al. Relationship between blood pressure parameters and pulse wave velocity in normotensive and hypertensive subjects: Invasive study. *J Hum Hypertens*. 2007;21(2):141-148. doi:10.1038/sj.jhh.1002120.

28. Obata Y, Mizogami M, Singh S, et al. The effects of hemodynamic changes on pulse wave velocity in cardiothoracic surgical patients. *Biomed Res Int*. 2016;2016. doi:10.1155/2016/9640457.

29. Swillens A, Segers P. Assessment of arterial pressure wave reflection: Methodological considerations. *Artery Res*. 2008;2(4):122-131. doi:10.1016/j.artres.2008.05.001.

30. Mackenzie IS, Wilkinson IB, Cockcroft JR. Assessment of arterial stiffness in clinical practice. *Q J Med*. 2002;95(2):67-74. doi:10.1093/qjmed/95.2.67.

31. Westerhof N, Lankhaar JW, Westerhof BE. The arterial windkessel. *Med Biol Eng Comput*. 2009;47(2):131-141. doi:10.1007/s11517-008-0359-2.

32. García-Herrera CM, Celentano DJ, Cruchaga M a., et al. Mechanical characterisation of the human thoracic descending aorta: experiments and modelling. *Comput Methods Biomech Biomed Engin*. 2012;15:185-193. doi:10.1080/10255842.2010.520704.

33. Haskett D, Johnson G, Zhou A, Utzinger U, Vande Geest J. Microstructural and biomechanical alterations of the human aorta as a function of age and location. *Biomech Model Mechanobiol*. 2010;9:725-736. doi:10.1007/s10237-010-0209-7.

34. Labrosse MR, Gerson ER, Veinot JP, Beller CJ. Mechanical characterization of human aortas from pressurization testing and a paradigm shift for circumferential residual stress. *J Mech Behav Biomed Mater*. 2013;17:44-55. doi:10.1016/j.jmbbm.2012.08.004.

35. Flamini V, Creane AP, Kerskens CM, Lally C. Imaging and finite element analysis: A methodology for non-invasive characterization of aortic tissue. *Med Eng Phys*. 2015;37(1):48-54. doi:10.1016/j.medengphy.2014.10.006.

36. Feintuch A, Ruengsakulrach P, Lin A, et al. Hemodynamics in the mouse aortic arch as assessed by MRI, ultrasound, and numerical modeling. *Am J Physiol Heart Circ Physiol*. 2007;292(2):H884-H892.

37. Huo Y, Guo X, Kassab GS. The flow field along the entire length of mouse aorta and primary branches. *Ann Biomed Eng*. 2008;36(5):685-699.

38. Trachet B, Renard M, De Santis G, et al. An integrated framework to quantitatively link mouse-specific hemodynamics to aneurysm formation in angiotensin II-infused ApoE -/- mice. *Ann Biomed Eng*. 2011;39(9):2430-2444.

39. Trachet B, Bols J, Degroote J, et al. An animal-specific FSI model of the abdominal aorta in anesthetized mice. *Ann Biomed Eng*. 2015;43(6):1298-1309. doi:10.1007/s10439-015-1310-y.

40. Xiao N. Simulation of 3-D blood flow in the full systemic arterial tree and computational frameworks for efficient parameter estimation. PhD thesis, Stanford University, Stanford, CA, USA. 2014.

41. Moireau P, Bertoglio C, Xiao N, et al. Sequential identification of boundary support parameters in a fluid-structure vascular model using patient image data. *Biomech Model Mechanobiol*. 2013;12(3):475-496. doi:10.1007/s10237-012-0418-3.

42. Davis E. Stability of elastin in the developing mouse aorta: a quantitative radioautographic study. *Histochemistry*. 1993;100(1):17-26.

43. Rammos C, Hendgen-Cotta UB, Deenen R, et al. Age-related vascular gene expression profiling in mice. *Mech Ageing Dev*. 2014;135:15-23. doi:10.1016/j.mad.2014.01.001.

44. Fleenor BS, Marshall KD, Durrant JR, Lesniewski LA, Seals DR. Arterial stiffening with ageing is associated with transforming growth factor-β1-related changes in adventitial collagen: reversal by aerobic exercise. *J Physiol*. 2010;588(20):3971-3982. doi:10.1113/jphysiol.2010.194753.

45. Ferruzzi J, Bersi M, Mecham R, et al. Loss of elastic fiber integrity compromises common carotid artery function: implications for vascular aging. *Artery Res*. 2016;14:41-52. doi:10.1038/mp.2016.136.Loss.

46. Wan W, Gleason RL. Dysfunction in elastic fiber formation in fibulin-5 null mice abrogates the evolution in mechanical response of carotid arteries during maturation. *Am J Physiol Hear Circ Physiol*. 2013;304(5):H674-H686. doi:10.1152/ajpheart.00459.2012.

## Chapter 2. Effects of Age-Associated Regional Changes in Aortic Stiffness on Human Hemodynamics Revealed by Computational Modeling

Federica Cuomo[1]

Sara Roccabianca[2]

Desmond Dillon-Murphy[3]

Nan Xiao[3]

Jay D. Humphrey[4,5],

C. Alberto Figueroa[1,3,6]

[1]Department of Biomedical Engineering, University of Michigan, Ann Arbor, MI, USA

[2]Department of Mechanical Engineering, Michigan State University, East Lansing, MI, USA

[3]Department of Biomedical Engineering, King's College London, London, UK

[4]Department of Biomedical Engineering, Yale University, New Haven, CT, USA

[5]Vascular Biology and Therapeutics Program, Yale School of Medicine, New Haven, CT, USA

[6]Department of Surgery, University of Michigan, Ann Arbor, MI, USA

*Plose One. 2017; 12(3): e0173177*

## 2.1 Introduction

Since publication of the seminal study by Laurent et al.[1], it has become widely accepted that increased central artery stiffness is both an initiator and indicator of cardiovascular, neurovascular, and renovascular risk[2–4]. Among other effects, arterial stiffening increases the speed of propagation of the blood pressure wave along the central arteries (i.e., the pulse wave velocity, *PWV*), which results in an earlier return of reflected waves that augments blood pressure in the proximal aorta during systole (i.e., increases central pulse pressure, *cPP*). Increased *cPP*, in turn, increases the afterload on the heart during systole and decreases coronary perfusion during diastole. Although arterial stiffness is increased in multiple connective tissue disorders (e.g., Marfan syndrome[5,6]), diverse diseases (e.g., diabetes[7] and arthritis[8]), and hypertension[9], an otherwise inevitable cause of stiffening is normal arterial aging[10–12]. Common characteristics of large artery aging include endothelial dysfunction (i.e., reduced nitric oxide bioavailability), decreased smooth muscle cell function (including phenotypic modulation), damage to or degradation of elastic fibers, accumulation of glycosaminoglycans, and remodeling of fibrillar collagens[13–15]. Collectively, such changes in cellular function and extracellular matrix integrity affect local wall stiffness and manifest as altered hemodynamics.

The current gold standard clinical measure of arterial stiffening is the carotid-to-femoral pulse wave velocity (*cf-PWV*[16,17]), but other metrics (e.g., the augmentation index related to *cPP*) have found utility as well[18,19]. Most assessments of such metrics have been based on large clinical studies that seek to correlate disease presentation with changes in the metric of interest, which has yielded considerable insight. Nevertheless, the causes and consequences of increased central artery stiffness are many, and there is a pressing need for a more systematic and objective means to assess effects of local versus global changes in arterial mechanics on the overall hemodynamics. Fortunately, a number of studies report in vitro measurements of the biaxial mechanical properties of the aorta as a function of location and age[20–22] and recent advances promise to enable characteristic properties to be inferred in vivo[23]. In this work, we use such data on aortic properties to inform a novel computational model of hemodynamic changes as a function of age. We submit that computational modeling is a powerful tool for investigating potential effects of regional differences in arterial geometry and wall properties on pulse wave propagation and other clinical

metrics of arterial stiffening. Specifically, we establish a baseline model of a young, healthy human aortic tree and then examine in silico the effects of age-associated changes in aortic wall geometry and wall properties on the overall hemodynamics. Based on a consistent comparison of data from many papers on aortic properties[24], we consider effects of regional changes in vessel caliber, length, and tortuosity (conduit characteristics) as well as wall thickness and biaxial material stiffness (wall characteristics) on the local and global hemodynamics. Using a subject-specific anatomical model to perform the fluid-solid interaction (FSI) simulations within the aorta allows us to prescribe realistic values of distal resistances to capture appropriate flow splits to the branches. We show that there are strong regional differences in all computed hemodynamics and that the distribution of *PWV* along the aorta, unlike other metrics of stiffening, does not always mirror the prescribed distribution of circumferential tissue stiffness. Furthermore, our analysis highlights the importance of external tissue support on the biomechanics of the aorta and its main branches. It is only through iterative adjustment of this external tissue support that we identified regionally-varying levels of transmural pressure that enabled a matching of all hemodynamic and biomechanical data on stiffness, pulse pressure, and pulse wave velocity for the three different age groups ranging from 30 to 75 years of age.

### 2.2 Methods

Medical imaging now provides exquisite information on overall luminal geometries and it is thereby easy to capture subject-specific geometries at many ages of interest. There are also growing databases on changes in molecular and cellular mechanisms within the aorta with aging[14,15] which manifest as the observed changes in aortic properties[24], aortic length[25], and hemodynamics[11]. Yet, no current data set includes subject-specific longitudinal medical imaging and associated in vivo assessments of arterial wall properties, perivascular support, and regional hemodynamics. Hence, our strategy was, first, to define a subject-specific model for a young, healthy subject and, second, to age this model numerically by prescribing population-averaged geometries and material properties. In this way, we could study parametrically the effects of local and global changes in mechanics without adding inherent complexity due to biological variability in the aorta from subject to subject. Illustrative results are thus provided for three numerically aged vasculatures, one each for 40, 60, and 75-year-old (yo) subjects.

### 2.2.1 Subject-Specific Baseline Geometric Model, Pressures, and Flow

Geometric data were extracted from magnetic resonance images collected previously for a healthy 30 yo male volunteer, with written consent from the individual and according to guidelines from the Institutional Review Board at King's College London, UK. Briefly, the open-source modeling package CRIMSON[26] was used to construct the baseline geometric model, with centerline paths identified from the medical images along each vessel of interest and 2D contours drawn, with discrete spacing, perpendicular to each path to define the vessel lumen at those locations. Groups of contours were then lofted to create a 3D volume for each vessel (i.e., aorta and primary branches) and a union operation was used to merge the individual vessels into a single analytical geometric model[27]. See Figure 2.1 (left).

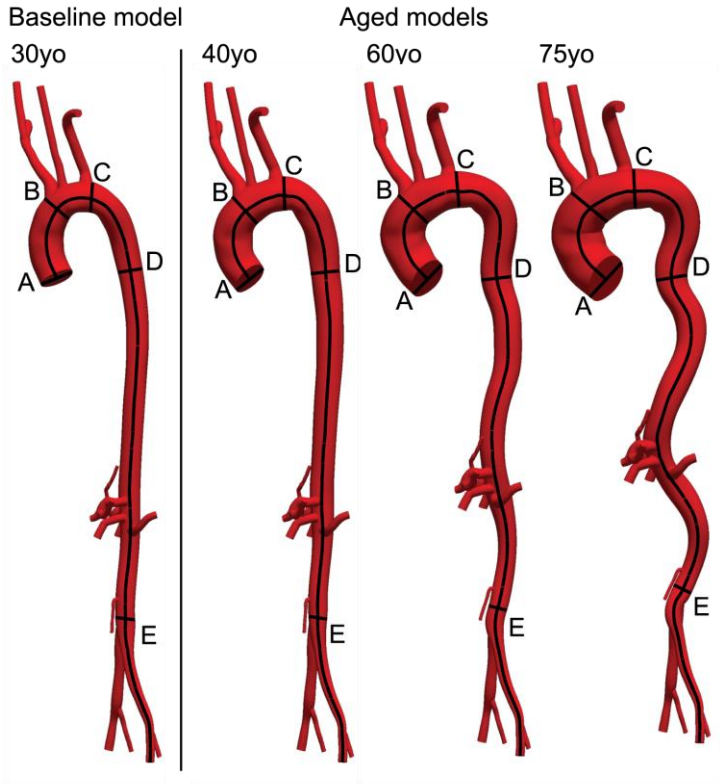


| | Diameter ($10^{-3}$ m) | | | |
|---|---|---|---|---|
| | 30 yo | 40 yo | 60 yo | 75 yo |
| A | 26.5 | 28.4 | 32.9 | 33.1 |
| B | 26.4 | 27.9 | 31.6 | 31.9 |
| C | 23.1 | 26.2 | 29.5 | 30.0 |
| D | 19.2 | 23.3 | 24.2 | 25.7 |
| E | 14.8 | 15.0 | 14.8 | 14.8 |

| | Length ($10^{-3}$ m) | | | |
|---|---|---|---|---|
| | 30 yo | 40 yo | 60 yo | 75 yo |
| AB | 61.8 | 64.2 | 68.2 | 72.4 |
| BC | 26.5 | 28.7 | 32.9 | 37.8 |
| CD | 69.4 | 72.6 | 81.0 | 90.1 |

**Figure 2.1.** Schematics of the baseline 30 yo subject-specific model and the three numerically aged models corresponding to the 40, 60, and 75 yo groups. The tables summarize the prescribed values of regional inner diameters and aortic centerline lengths. All dimensions are given in mm.

The mean arterial pressure (*MAP*) for this baseline subject was acquired noninvasively using applanation tonometry at the right carotid and right femoral arteries, also having obtained written consent from the individual and according to guidelines from the Institutional Review Board at King's College London, UK. Central *MAP* was estimated from the right carotid pressure

data whereas abdominal aortic *MAP* was estimated from the femoral artery data. Values for the baseline geometry at three select sites are listed in Table 2.1 along with values of blood pressure. Lastly, a flow waveform (mean 5.79 L/min, heart rate 60 bpm) was also collected non-invasively with phase contrast MRI under rest in the supine position for the same subject. We emphasize that, due to the lack of subject-specific regional material properties, we did not perform FSI simulations for this young subject; we merely, used these data to generate a baseline model that could be numerically aged. Clearly, there is a pressing need for reliable regional biaxial data for the aorta from young healthy subjects as well[24].

**Table 2.1.** Geometric parameters (inner radius) and wall properties (material stiffness and wall thickness) calculated at a transmural pressure given by the difference between mean arterial pressure (*MAP*) and external pressure (*EP*). Also listed are the in vivo axial and circumferential stretches as a function of three ages and locations, namely, the ascending thoracic aorta (ATA), proximal descending thoracic aorta (DTA), and infrarenal abdominal aorta (IAA). Material stiffness *K* is given in circumferential (θ) and axial (Z) directions.

| Age (yo) | Location | Inner Radius ($10^{-3}$ m) | Wall Thickness ($10^{-3}$ m) | *MAP* (mmHg) | *EP* (mmHg) | In vivo Axial Stretch | In vivo Circ. Stretch | $K_{\theta\theta\theta\theta}$ ($10^6$ Pa) | $K_{zzzz}$ ($10^6$ Pa) |
|---|---|---|---|---|---|---|---|---|---|
| 30 | ATA | 13.2 | 1.80 | 89 | - | - | - | - | - |
| | DTA | 9.60 | 1.76 | 89 | - | - | - | - | - |
| | IAA | 7.81 | 1.14 | 91 | - | - | - | - | - |
| 40 | ATA | 14.07 | 2.00 | 93 | 7 | 1.15 | 1.34 | 0.40 | 0.28 |
| | DTA | 11.63 | 1.70 | 93 | 2 | 1.17 | 1.24 | 0.50 | 0.46 |
| | IAA | 8.24 | 1.05 | 95 | 0 | 1.23 | 1.24 | 1.46 | 1.30 |
| 60 | ATA | 16.13 | 2.45 | 95 | 17 | 1.08 | 1.22 | 0.75 | 0.27 |
| | DTA | 12.08 | 1.90 | 95 | 12 | 1.09 | 1.21 | 0.71 | 0.64 |
| | IAA | 8.27 | 1.50 | 97 | 0 | 1.09 | 1.12 | 1.66 | 1.51 |
| 75 | ATA | 16.25 | 2.90 | 102 | 15 | 1.03 | 1.14 | 0.91 | 0.41 |
| | DTA | 12.71 | 2.15 | 102 | 10 | 1.03 | 1.22 | 1.02 | 0.58 |
| | IAA | 8.98 | 1.92 | 105 | 0 | 1.04 | 1.01 | 2.14 | 1.97 |

### 2.2.2 Age Related Changes in Geometry, Hemodynamics, and Wall Properties

There is considerable population-averaged information available on aging-associated changes in aortic geometry (namely, luminal diameter, segment length, and local curvature), blood pressures and flows, and wall properties (material stiffness and thickness of the wall). Whereas we merely extracted and used geometric and hemodynamic information directly from key papers[16,24,28,29], information on changes in regional mechanical properties required further analysis. Note, therefore, that we had previously recreated biaxial data from 6 published studies and performed a consistent nonlinear parameter estimation for a "four-fiber family" strain energy function that captures the biaxial stress-stretch behaviors[24]. Specifically, this phenomenological constitutive

relation adopts a mass-averaged constrained mixture approach and defines strain-energy functions for individual structurally significant constituents: a neo-Hookean relation for the elastin-dominated amorphous matrix and a Fung-Type exponential for the collagen fiber-dominated anisotropy. For purposes of FSI simulations, a vessel of interest can then be modeled as a single-layered, thin-walled cylindrical tube, elongated to in vivo values of axial stretch and pressurized to transmural pressure (*TP*). That is, although the thin-walled assumption is not appropriate for studies of arterial wall mechanobiology[30], it yet provides the correct values of the mean wall stress (which reflect actual stress distributions since residual stresses homogenize the transmural distribution) and, importantly, the correct values of structural stiffness that are essential in FSI simulations. Toward that end, we used the theory of small deformations superimposed on large to compute in vivo relevant values of biaxial material stiffness[31], which when combined with wall thickness yields the structural stiffness in a computationally efficient manner[32]. By using this approach, we were able to refer the nonlinear constitutive behavior to an in vivo configuration, near the mean arterial pressure ($MAP = P_{dias} + (P_{sys} - P_{dias})/3$), rather than needing to prescribe a stress-free configuration (often characterized by an opening angle that differs regionally and evolves with disease and aging).

Because best-fit values of the material parameters in this four-fiber family model were previously presented for three broad age groups (< 30, 31 to 60, and > 61), we re-evaluated the data to identify values for narrower age groups (30-49, 50-69, and 70-80 yo) and three primary regions of interest: ascending thoracic aorta (ATA), proximal descending thoracic aorta (DTA), and infrarenal abdominal aorta (IAA). The three aged models considered in this study (40, 60, and 75 yo) thus correspond to the mean ages of these three groups. Regional values of biaxial material stiffness over the physiologic range of age-specific diastolic-to-systolic pressures were then computed using the theory of small on large at the mean transmural pressure (*TP*) (i.e., the difference between *MAP* and external pressure (*EP*) due to perivascular tissue support) at age-specific values of in vivo axial stretch. Values of the computed biaxial material stiffness are listed in Table 2.1 for the three primary sites available. Table 2.2 further shows the published studies used herein to fit the model at each aortic location and age group. These studies are the same as those used previously[24], with the exception that data from Haskett et al.[21] were not used to inform the model at DTA or IAA locations for the younger age groups since the resulting values of stiffness were much higher than those inferred from other studies.

A multistep approach was then used to numerically age the subject-specific 30 yo model in a controlled manner: First, we increased the length of the aorta to reflect changes observed with aging. Craiem et al.[28] noted that this lengthening is not uniform and that, per each 10 years of aging, the ascending aorta (from the branching point of the left coronary artery to that of the brachiocephalic artery) exhibits a 3% increase in length, the aortic arch (from the brachiocephalic artery to the left subclavian) a 7% increase in length, and the descending aorta (from the left subclavian artery to the intersection of the thoracic aorta with a horizontal plane through the coronary sinus) a 5% increase in length (Figure 2.1). Using a custom algorithm in MATLAB (Mathworks, Natick, MA), the centroid for each aortic contour was calculated throughout the thoracic region and a 3D cubic spline was used to interpolate the centroids. This spline was then modified to reflect the changes in length with aging from 30 to 40, 60, and then 75 yo. Moreover, each aortic contour was shifted and rotated to lie at the same relative position to the new spline. Finally, for the branching vessels, the centroid of the contour nearest to the aorta was rotated and shifted to maintain the same position and orientation relative to the modified spline.

Second, we incorporated the expected slight decrease in subject height due to aging[29]. Using a method similar to that used to modify aortic length, we reduced the overall distance between the aortic root and the iliac bifurcation without altering the arc length of the aorta. This resulted in an increase in aortic tortuosity. Third, we incorporated directly reported regional changes in aortic diameter with aging[24]. The diameters of the subject-specific 30 yo model were increased with aging, scaling each contour relative to its position along the length of the aorta. Branching vessel diameters were uniformly scaled based on the scaling factor at the closest point on the aortic arc length (Figure 2.1). Fourth, starting from values of wall thickness for a 30 yo patient reported in Roccabianca et al.[24], values of wall thickness in aging were chosen such that the same trend of inner radius to wall thickness ratio previously defined was maintained. Fifth, results for *MAP* for the 30 yo baseline subject (Table 2.1) were extrapolated for the older age groups following the previously found trend of pressure as a function of age (Figure 5 in Roccabianca et al.[24]). Because there are no reported values of regional variations in the external pressure *EP* exerted on the vessel wall by the perivascular tissue, these values were estimated separately for each age group via an iterative approach detailed below in the "external tissue support" section.

**Table 2.2.** List of published studies in the literature used herein to define the model at each specific location and age group.

| Age (yo) | Location | Haskett et al.[21] | Labrosse et al.[22] | Vorp et al.[33] | Geest Vande et al.[34] | Garcia-Herrera et al.[20] | Martin et al.[35] |
|---|---|---|---|---|---|---|---|
| 40 | ATA | x | | x | | | |
| | DTA | | | | | x | |
| | IAA | | | | x | | |
| 60 | ATA | x | x | x | | | |
| | DTA | | x | | | x | |
| | IAA | | x | | x | | |
| 75 | ATA | x | x | | | | x |
| | DTA | | x | | | | |
| | IAA | x | | | x | | |

### 2.2.3 Computational Framework

**Numerical Methods.** Using an approach similar to that described previously[36,37], we employed a coupled-momentum method to model interactions between the arterial wall and blood flow[38]. This method is fundamental to model and capture arterial wave propagation and pulse pressure, but adds minimal computational cost to that of rigid wall formulations. Each arterial segment was thus modeled as an incompressible elastic membrane endowed with a thickness (to provide appropriate structural stiffness) and characterized by the appropriately linearized (over a cardiac cycle) biaxial tissue properties listed in Table 2.1. This linearization is justified by experimental evidence showing a near linear response over physiological ranges of pressure, particularly with age-associated stiffening, and is sufficient to compute values of PWV, one of the key goals of this paper[36,39–41]

**Specification of vessel wall properties.** The centerline path of the aorta was defined in terms of normalized arc-length $s \in [0,1]$ from the aortic root to the aorto-iliac bifurcation. Local values of biaxial stiffness and thickness were assigned at $s = 0.12$ for the ATA, $s = 0.4$ for the DTA and $s = 0.88$ for the IAA and interpolated linearly along the aorta (Figure 2.2). The values of biaxial stiffness and thickness were also extrapolated constantly from $s = 0.12$ to the aortic root and from $s = 0.88$ to the left and right iliac arteries. Stiffness values for the carotid artery were prescribed as a function of aging based on limited data in the literature[42], namely values of an "elastic modulus". Given the lack of data, the subclavian arteries were assigned the same value of stiffness as the carotid arteries since they have comparable radii. Thus, the carotid and subclavian arteries are the only vessels in the model where the assigned tissue properties are isotropic. Note, therefore, that fully biaxial and anisotropic regionally-specific values were prescribed within the region of primary interest for the hemodynamics (i.e., the aorta) and that prescribing reduced-order 0D models (e.g., Windkessels that account for peripheral compliance) for all supra-aortic vessels

minimizes the need to prescribe the 3D elastic properties of these vessels precisely. In vivo measures of distensibility and *PWV* suggest that elastic arteries stiffen with aging whereas muscular arteries do not[43]. For this reason, we kept the stiffness of mesenteric, celiac, and renal arteries unchanged for the three age groups. Given the lack of any data to the contrary, we assumed that muscular aortic branches are stiffer than the aorta at a young age, but become comparable in stiffness when the aorta stiffens with aging[43]. Thus, these vessels were assigned a stiffness similar to that of the 75 yo abdominal aorta at the renal level for all age groups.

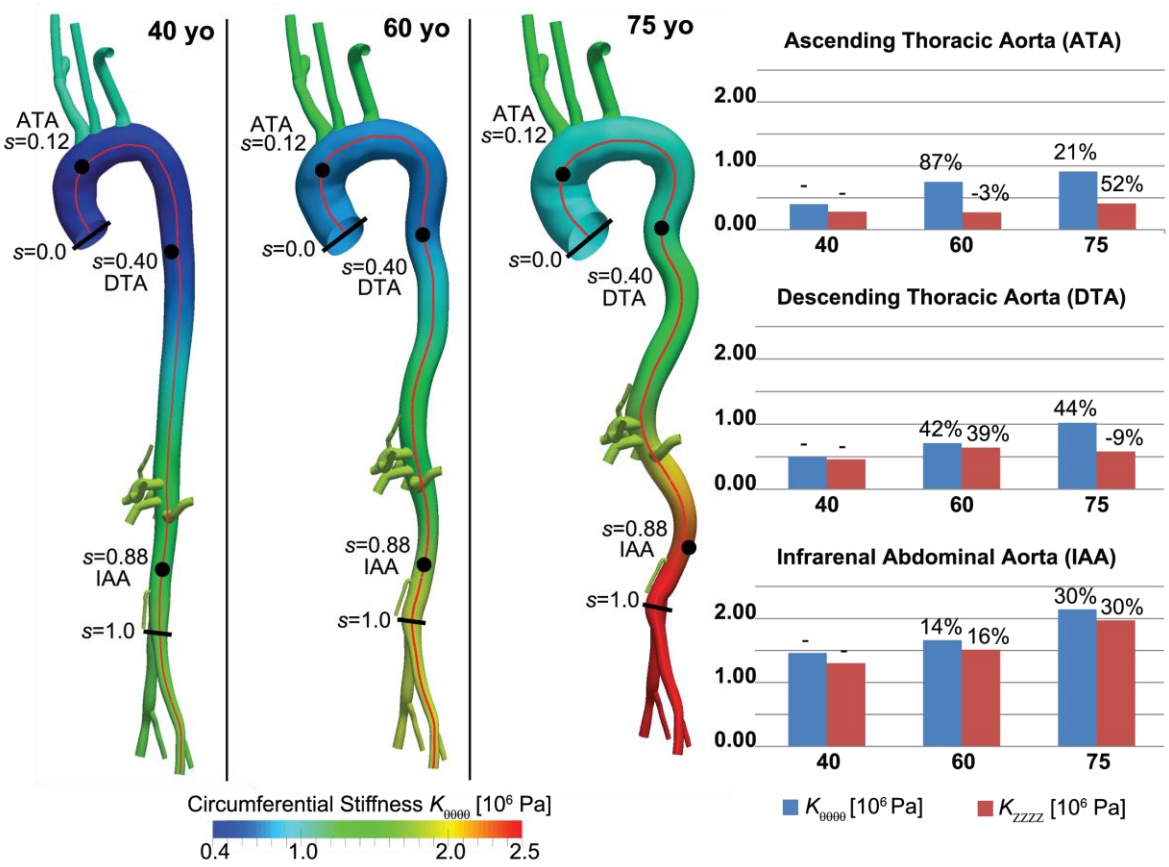


**Figure 2.2.** 3D geometrical models for 40, 60, and 75 yo human subjects (*left*) and associated values of segmental biaxial material stiffness (MPa) in three regions (*right*): ascending thoracic aorta (ATA), proximal descending thoracic aorta (DTA), and infrarenal abdominal aorta (IAA). Lengths along the aortic centerline are parameterized by $s \in [0,1]$, where $s = 0$ corresponds to the aortic root at the beginning of the ATA and $s = 1$ to the aorto-iliac bifurcation (left). Listed values of aortic material stiffness (right) were assigned at locations indicated by the black dots within the ATA, DTA and IAA and linearly interpolated to obtain a continuous distribution of stiffness, as illustrated colorimetrically on the aortic geometries for the circumferential values. Stiffness was assigned separately in circumferential (blue) and axial (red) directions at each location and for each age group. The % numbers refer to the percent difference in value relative to the prior age group.

**External tissue support.** Arteries are supported by external tissues or organs, which constrain the motion of the vessels via an effective external pressure (*EP*). A simple traction boundary condition was applied on the outer side of the vessel wall to mimic the effects of a

distributed viscoelastic force imparted by the perivascular tissue[44]. This traction boundary condition consists of a viscoelastic term with two distributed parameters: a stiffness coefficient ($k_s$) and a damping coefficient ($c_s$). From a computational perspective, this boundary condition helps to prevent high frequency oscillations (in contrast to pulsatile motions) of the wall, which arise in slender vessels under pulsatile flow and no external support[36]. The functional form of this traction is:

$$\boldsymbol{\sigma} \cdot \boldsymbol{n} = -k_s \boldsymbol{u} - c_s \boldsymbol{v}$$

where $\boldsymbol{u}$ and $\boldsymbol{v}$ are the displacement and velocity field, respectively. The weak form of the FSI problem including this boundary condition is given in Cuomo et al.[37]. Here, we adopted spatially variable values of external tissue support parameters and allowed the parameter values to change with aging. Due to the lack of experimental data on these parameters, an iterative approach was used to choose the values $k_s$ and therefore the *EP* acting on vessel wall (Figure 2.3). The value of $c_s$ was set to the minimum value that eliminates spurious oscillations in the arterial tree and was kept constant through the iterative process (see Figure 2.4).

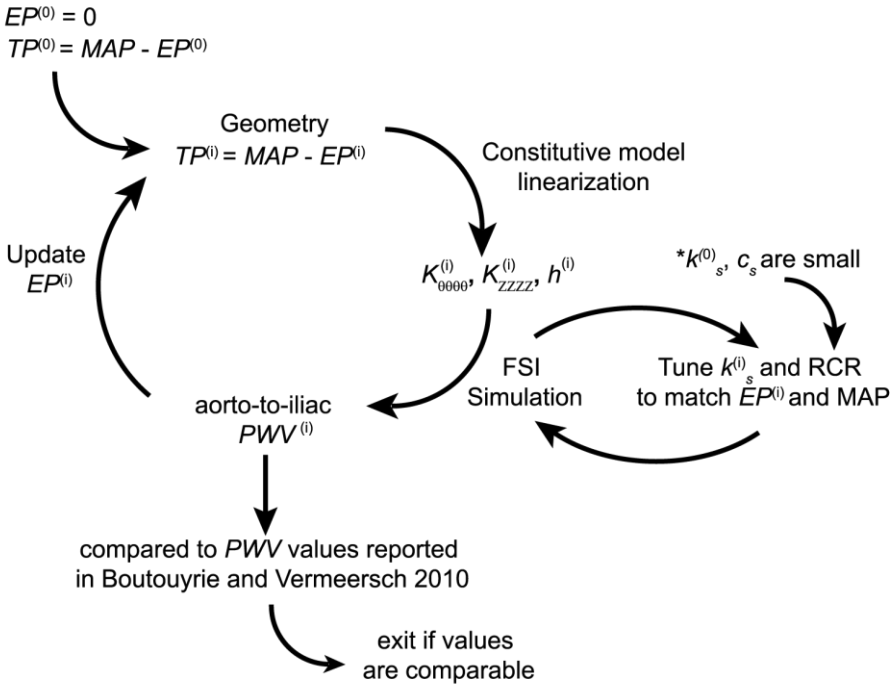


**Figure 2.3.** Iterative approach for tuning external tissue support parameters: stiffness coefficient $k_s$ and damping coefficient $c_s$.

Given the geometry and an initial guess of the $TP^{(0)}$, the constitutive model was computed as described above. Initially, *EP* is set to 0 mmHg, therefore $TP^{(0)} = MAP$. An initial FSI simulation was then run with small values of $k_s$ and $c_s$ that produce an *EP* of approximately 0 mmHg. The

computed aorto-iliac *PWV* was then compared to the values reported in Boutouyrie and Vermeersch[16]. If the computed aorto-iliac *PWV* values were too high, a higher value of *EP* was considered. This effectively reduced the *TP* and resulted in a lower local wall stiffness, especially in the circumferential direction. Given a new set of values for biaxial stiffness and thickness, the external tissue parameter $k_s$ was iteratively estimated via subsequent FSI simulations until the new value of *EP* was matched. This iterative process was continued until the computed values of aorto-iliac *PVW* matched the values in Boutouyrie and Vermeersch[16] for each age group. During this iterative process we aimed to preserve our previous findings of increasing stiffness along the aorta for each age group[24]. To satisfy this stiffening pattern along the aortic length, while reproducing the reported values of *PWV* for each age group, a heterogeneous distribution of external tissue was needed, with the largest values in the thoracic region and smallest (zero) in the abdominal region for each age group. The final spatially-varying values of *EP* and external tissue support $k_s$ are reported in Table 2.1 and Figure 2.4, respectively. For the purposes of external tissue support, the aorta was divided into three segments: ATA from $s = 0$ to $s = 0.25$, DTA from $s = 0.25$ to $s = 0.66$, and IAA for $s > 0.66$. The upper branches and lower branches received the same external tissue support as the ATA and IAA, respectively.

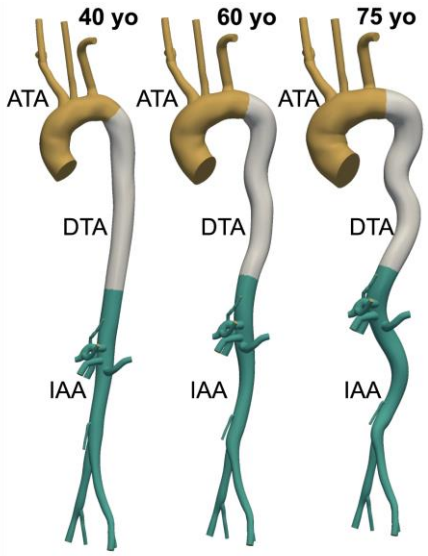


| | 40 yo | | 60 yo | | 75 yo | |
|---|---|---|---|---|---|---|
| | $k_s$ ($10^4$ Pa m$^{-1}$) | $c_s$ ($10^4$ Pa s m$^{-1}$) | $k_s$ ($10^4$ Pa m$^{-1}$) | $c_s$ ($10^4$ Pa s m$^{-1}$) | $k_s$ ($10^4$ Pa m$^{-1}$) | $c_s$ ($10^4$ Pa s m$^{-1}$) |
| ATA | 30 | 1 | 135 | 1 | 145 | 1 |
| DTA | 15 | 1 | 125 | 1 | 135 | 1 |
| IAA | 1 | 1 | 1 | 1 | 1 | 1 |

**Figure 2.4.** Spatial and temporal distribution of external tissue support parameters: stiffness coefficient $k_s$ and damping coefficient $c_s$.

**Table 2.3.** Outflow boundary conditions. Numerical values for the three-element Windkessel models prescribed at each branch. Values were adjusted following the procedure described in Xiao et al.[36], and consist of proximal resistance ($R_{prox}$), distal resistance ($R_{dist}$) and compliance ($C$). $R_{dist}$ was the only parameter that increased with aging. This increment was required to reproduce the reported increased values of *MAP* with aging.

| | $R_{prox}$ $10^9$ Kg/(m⁴·s) | | | $R_{dist}$ $10^9$ Kg/(m⁴·s) | | | $C$ $10^{-9}$ (m⁴·s)/Kg | | |
|---|---|---|---|---|---|---|---|---|---|
| Vessel | 40 yo | 60 yo | 75 yo | 40 yo | 60 yo | 75 yo | 40 yo | 60 yo | 75 yo |
| Right Subclavian | 0.2 | | | 1.60 | 1.66 | 1.75 | 1.68 | | |
| Left Subclavian | 0.18 | | | 1.53 | 1.58 | 1.68 | 1.75 | | |
| Right Carotid | 0.23 | | | 1.91 | 1.98 | 2.09 | 1.40 | | |
| Left Carotid | 0.22 | | | 1.80 | 1.86 | 1.97 | 1.49 | | |
| Right Renal | 0.24 | | | 1.12 | 1.16 | 1.24 | 2.43 | | |
| Left Renal | 0.25 | | | 1.15 | 1.20 | 1.27 | 2.36 | | |
| Celiac Artery | 0.35 | | | 1.53 | 1.59 | 1.70 | 1.78 | | |
| Gastric Artery | 1.20 | | | 5.59 | 5.81 | 6.18 | 0.49 | | |
| Splenic Artery | 0.55 | | | 2.50 | 2.60 | 2.76 | 1.09 | | |
| Superior Mesenteric | 0.23 | | | 0.60 | 0.63 | 0.67 | 4.65 | | |
| Inferior Mesenteric | 1.40 | | | 3.82 | 3.99 | 4.28 | 0.73 | | |
| Right Ext. Iliac | 0.08 | | | 1.49 | | | 2.15 | | |
| Right Int. Iliac | 0.29 | | | 5.50 | | | 0.56 | | |
| Left Ext. Iliac | 0.08 | | | 1.49 | | | 2.15 | | |
| Left Int. iliac | 0.30 | | | 5.45 | | | 0.56 | | |

**Inlet and outlet boundary conditions.** The flow waveform (mean 5.79 L/min, heart rate 60 bpm) measured with phase contrast MRI in the 30 yo volunteer under supine, rest conditions was used as an inlet boundary condition. Since cardiac output remains nearly constant at resting conditions with aging[45,46], the same inlet flow was prescribed for all three aged models. Finally, outlet boundary conditions were prescribed using a coupled multi-domain method that represents the distal vasculature to the level of capillaries via individual three element (Resistance-Capacitance-Resistance) Windkessel models coupled to each outlet of the 3D models[47]. The parameters associated with these outlet conditions were tuned individually for each age group (Table 2.3) to ensure appropriate flow splits and to match the *MAP* used to calculate the linearized stiffness listed in Table 2.1[36].

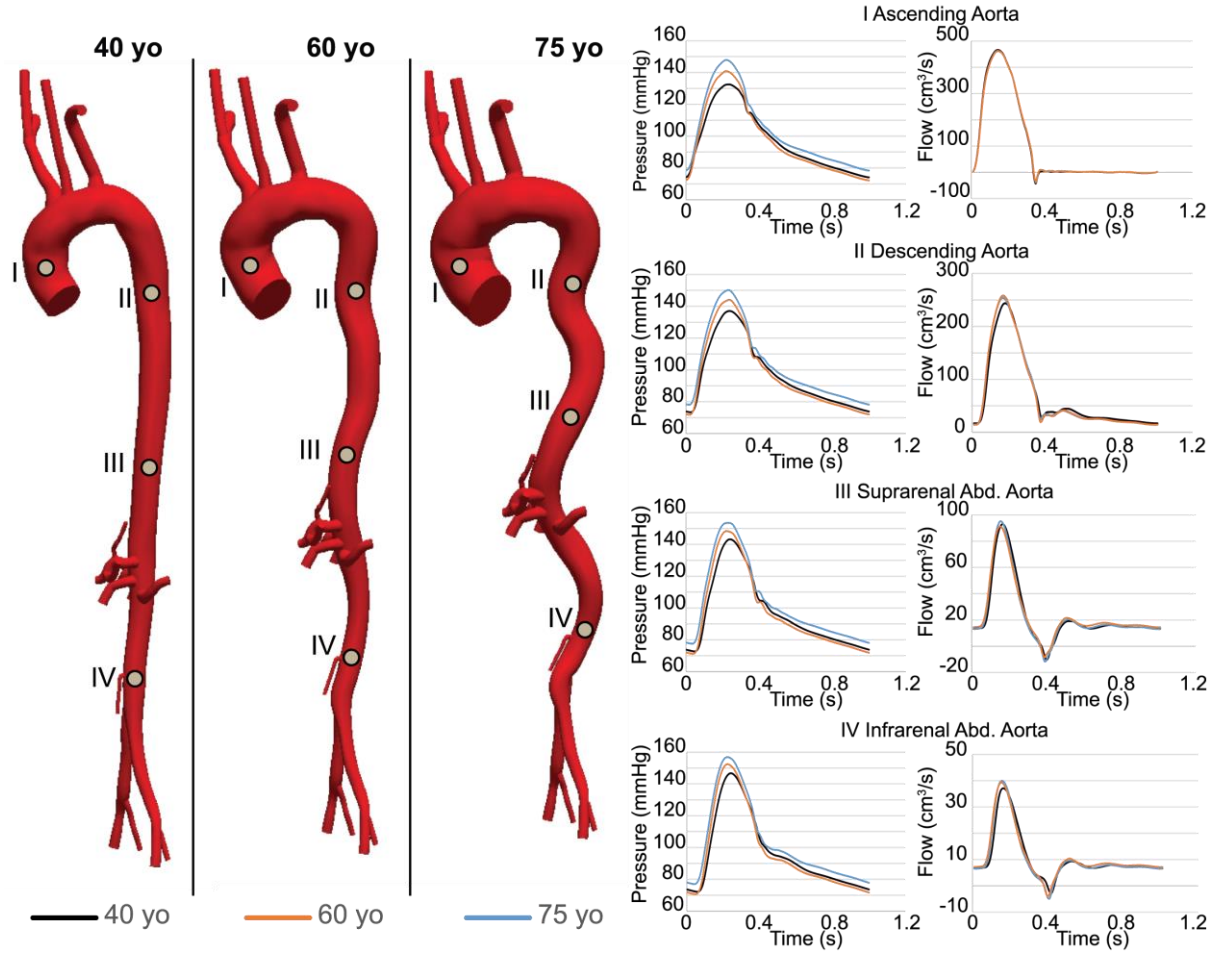


**Figure 2.5**. Pressure and flow waveforms for 40 (black), 60 (orange) and 75 (blue) yo subjects at four different locations along the aorta; namely ATA (I), DTA (II), SAA (III) and IAA (IV).

## 2.3 Results

Figure 2.5 depicts pressure and flow waveforms at four different locations down the aorta for the different ages. Pressure waveforms show larger central pulse pressure and smaller pressure amplification for the 60 and 75 yo cases. Changes in flow waveforms are subtle. A good matching was obtained between the computed *MAP* and *EP* acting on the vessel wall and the *MAP* and *EP* used to calculate the linearized stiffness of the wall. The computed values of pressure are listed in Table 2.4. The computed *MAP* resulted mainly from tuning the distal resistance of the Windkessel parameters for each age group; this parameters increased the total resistance of the distal vasculature by 2.55% for the transition from 40 to 60 yo, and of 4.06% for the transition from 60 to 75 yo.

**Table 2.4.** Computed mean arterial pressure (*MAP*) and external pressure (*EP*) for the three age groups at three locations: ascending thoracic aorta (ATA), descending thoracic aorta (DTA) and infrarenal abdominal aorta (IAA). The computed values match well the corresponding values in Table 2.1 used to calculate the linearized stiffness.

| Age (yo) | Location | *MAP* (mmHg) | *EP* (mmHg) |
|---|---|---|---|
| 40 | ATA | 93.6 | 7.16 |
| | DTA | 94.6 | 1.76 |
| | IAA | 96.3 | 0.04 |
| 60 | ATA | 95.1 | 16.6 |
| | DTA | 95.9 | 10.4 |
| | IAA | 97.0 | 0.02 |
| 75 | ATA | 101.6 | 16.1 |
| | DTA | 102.2 | 8.9 |
| | IAA | 102.9 | 0.02 |

Figure 2.6 compares the spatial distribution of four different metrics or consequence of arterial stiffening – local pulse pressure (*PP*), distensibility, pulse wave velocity (*PWV*), and changes in strain energy stored during the cardiac cycle ($\Delta W$) – to the distribution of prescribed values of circumferential material stiffness. The first three of these four metrics are routinely measured clinically; the fourth of these metrics, stored energy, is motivated by recent findings in a mouse model of pre-mature aging in which changes in stiffness are due to a genetically defined connective tissue disorder[48]. Results are also shown for six different anatomical segments along the aorta: ATA from $s = 0$ to 0.12 (segment 1), aortic arch from $s = 0.12$ to 0.38 (segment 2), DTA from $s = 0.38$ to 0.55 (segment 3), suprarenal abdominal aorta from $s = 0.55$ to 0.71 (segment 4), IAA from $s = 0.71$ to 1 (segment 5), and iliac artery from $s = 1$ to 1.27 (segment 6). This visualization enables a spatially detailed description of the different metrics.

Distensibility was calculated using cross-section area, $D = (d^2_{sys} - d^2_{dia})/(d^2_{dia} \cdot PP)$, rather than diameter, as is common in magnetic resonance imaging studies. The pulse wave velocity *PWV* was calculated as the ratio of the distance between two locations of interest and the transient time of the pressure pulse between these locations. In contrast to most clinical assessments, this distance was computed herein from the actual centerline of the vessel, not the straight line distance. The transient time between two waveforms was measured using an intersecting tangent algorithm that defines the foot of a pressure waveform as the intersection between the horizontal tangent intersecting its diastolic minimum and the tangent to the maximum systolic gradient; we used the algorithm developed in MATLAB by Gaddum et al.[49]. Finally, the change in strain energy throughout the cardiac cycle was calculated via the work done on the aorta given the assumption of no dissipation and no change in length: $\Delta W = 0.5(P_{sys}\text{-}P_{dia}) \cdot (A_{sys}\text{-}A_{dia})/A_{dia}$. The latter is an

excellent assumption for all regions except the ATA, which experiences lengthening and shortening over the cardiac cycle, though data are lacking to quantify this as a function of aging.

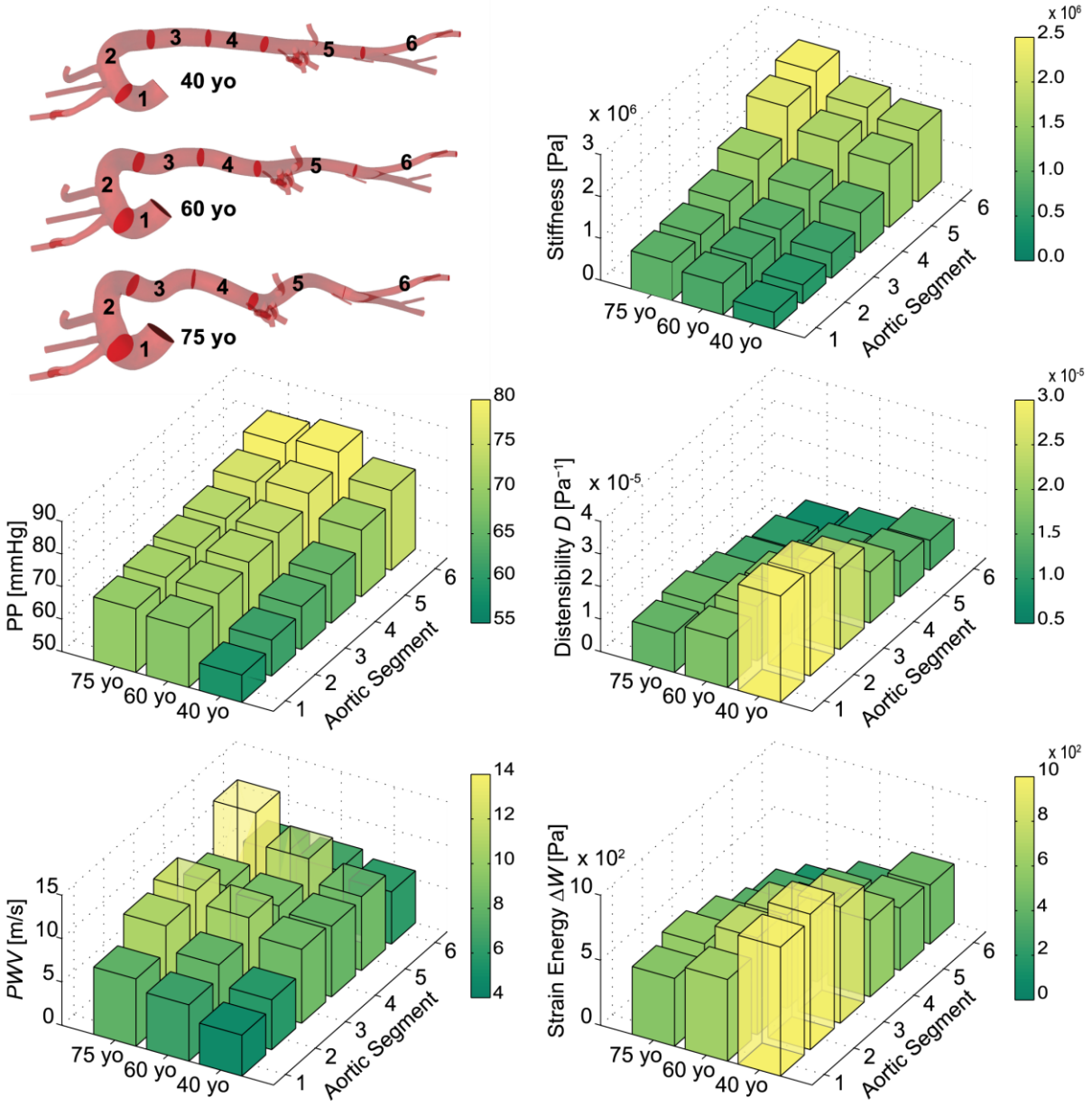


**Figure 2.6.** Computed values of circumferential material stiffness (Pa), local pulse pressure (*PP*, in mmHg), distensibility ($Pa^{-1}$), pulse wave velocity (*PWV*, in m/s), and change in strain energy storage ($\Delta W$, in Pa x 100) as a function of region (aortic segments 1 to 6) for three different ages: 40, 60, and 75 yo. The 18 different computed values for each of the 5 metrics consistently show strong regional variations at each age.

Overall, the spatial distributions of our simulated values compared well with reported data on pulse pressure[50] and distensibility[24,51]. Local pulse pressure *PP* increased along the aorta: from 58 at the ascending aorta to 75 mmHg at iliac bifurcation in the 40 yo model; from 68 to 81 mmHg in the 60 yo model; and from 69 to 80 mmHg in the 75 yo model. These results reveal important

features. As reported previously[50], there is an amplification of pulse pressure along the aorta, particularly at younger ages: a 17 mmHg pulse amplification at age 40 reduces to 11 mmHg at age 75. The pressure waveforms along the aorta thus become more alike in amplitude and contour with aging, which is to say that distal amplification attenuates with aging. Finally, we also reproduced the reported increase in *MAP* in the ATA with aging. This change resulted largely from the increased resistance in the 3D geometrical model arising from the increased tortuosity (cf. Figure 2.1) and the increased total peripheral resistance represented by the Windkessel models (cf. Table 2.3). Consistent with the literature, the largest predicted change in *PP* is between 40 yo and 60 yo, while 60 yo and 75 yo have more similar values. Indeed, it is at 50-55 yo that there tends to be, on average, dramatic changes in central pulse pressure and *cf-PWV*[10]. Overall, the computed regional patterns of *PP* follow the prescribed distribution of circumferential stiffness down the aorta for the three different ages. As expected, distensibility *D* decreases distally along the aorta at a given age, particularly in the younger healthy model. It similarly decreases with aging at each individual location, especially in the most proximal segments.

Unlike for the other three metrics of interest, the distribution of *PWV* along the aorta does not follow the prescribed distribution of circumferential stiffness everywhere (Figure 2.6). This difference arose, in part, because *PWV* results from both arterial geometry and stiffness. That is, *PWV* is influenced strongly by arterial tapering (which is not normalized as in the calculation of distensibility) and branching, and thus is difficult to intuit even with the aid of simplified equations such as Moens-Korteweg (which assumes uniform geometry and properties). Lastly, the distribution of changes in stored strain energy $\Delta W$ is comparable to the distensibility patterns.

Notwithstanding the utility of visual comparisons of spatio-temporal differences in the four clinical metrics of interest (Figure 2.6), we computed the correlation coefficient of each of these metrics with the prescribed circumferential material stiffness; this was done both spatially at a given age (Table 2.5) and temporally at a given location (Table 2.6). Briefly, using the software R (www.r-project.org/), Pearson correlation coefficients were computed as the ratio of the covariance to the product of the standard deviations of the two variables; hence a value of 1.0 reveals a perfect correlation, with positive and negative values indicating proportional and inverse correlations, respectively. At any given age, the spatial correlation with circumferential material stiffness is greater than 0.9 for *PP*, *D*, and $\Delta W$, but not *PWV*, which has correlation values smaller than 0.3. At any given location, the correlation with circumferential stiffness is greater than 0.9 for

all metrics with the exception for *PP*, where the correlation decreases to 0.7 for segments 3 and 4 and to 0.5 for segments 5 and 6. This finding reflects the relatively constant values of *PP* in the distal segments of the aorta with aging, despite the increase in tissue stiffness. A visual examination of the rows and columns of each bar plot in Figure 2.6 confirms the correlation coefficients reported in Tables 2.5 and 2.6.

**Table 2.5.** Correlation between four key calculated metrics (pulse pressure *PP*, distensibility, pulse wave velocity *PWV*, and the change in stored elastic energy $\Delta W$, each at the center of each of six key aortic segments; cf. Figure 2.6) and the associated prescribed circumferential material stiffness for a given age group.

| | 40 yo | 60 yo | 75 yo |
|---|---|---|---|
| ***PP*** | 0.979 | 0.960 | 0.966 |
| **Distensibility** | -0.960 | -0.981 | -0.988 |
| ***PWV*** | 0.312 | 0.099 | 0.067 |
| $\Delta W$ | -0.953 | -0.958 | -0.963 |

**Table 2.6.** Correlation between four key calculated metrics (pulse pressure *PP*, distensibility, pulse wave velocity *PWV* and the change in stored elastic energy $\Delta W$) and the prescribed circumferential material stiffness at the center of each of six key aortic segments (cf. Figure 2.6).

| | Segment 1 | Segment 2 | Segment 3 | Segment 4 | Segment 5 | Segment 6 |
|---|---|---|---|---|---|---|
| ***PP*** | 0.970 | 0.907 | 0.772 | 0.740 | 0.592 | 0.504 |
| **Distensibility** | -0.983 | -0.964 | -0.946 | -0.952 | -0.944 | -0.893 |
| ***PWV*** | 0.993 | 0.994 | 0.970 | 0.997 | 0.982 | 0.840 |
| $\Delta W$ | -0.996 | -0.993 | -0.996 | -0.999 | -0.998 | -0.939 |

Computed values of aortic root-to-iliac and carotid-to-iliac *PWV* are reported in Table 2.7. These values are contrasted with measured values for *cf-PWV* for different age groups in a population with no risk factors[16,51]. Because methods for acquiring *PWV* in patients can vary in terms of calculation of transient time and path length, Boutouyrie and Vermeersch[16] standardized the transient time on the intersecting tangent algorithm and the path length on the direct distance. Because of the latter, they also used a scaling factor of 0.8 to convert the *PWV* obtained using direct distance to 'real' aorto-to-iliac *PWV*, since direct distance overestimates *PWV*. This scaling factor was reported by Weber et al.[52] based on comparisons of results inferred from both *cf-PWV* calculated with direct distance path length and aorto-to-iliac *PWV* calculated with an invasively measured real path length. In contrast, no scaling factor was used for the reported *cf-PWV* values measured by others[51]. These values, although measured between carotid-to-femoral, are compared directly to our carotid-to-iliac results since our geometrical models do not extend to the levels of

the femoral arteries. Similar trends are observed over time between our results and the population data. Our results agree better, however, with population data in which aortic length was corrected.

**Table 2.7.** Values of pulse wave velocity (*PWV*, in m/s) calculated over two segments, from the aortic root to the iliac bifurcation (left) and from the carotid artery to the iliac artery (right). Computations are compared with reported values by Boutouyrie and Vermeersch[16] and Redheuil et al.[51]. Values in Boutouyrie and Vermeersch[16] were originally measured as carotid-to-femoral, then scaled by 0.8 to represent aorto-iliac values, following Weber et al.[52]. Conversely, values in Redheuil et al.[51] correspond to carotid-to-femoral *PWV* with uncorrected path lengths. Our results show a better agreement with population data in which aortic length was corrected, as would be expected given our use of actual path lengths.

| | Aortic Root-Iliac bifurcation *PWV* | | Carotid-to-Iliac artery *PWV* | |
|---|---|---|---|---|
| Age | Computed | Reported [16] | Computed | Reported [51] |
| 40 yo | 6.9 | 6.9 | 9.7 | 7.75 |
| 60 yo | 9.0 | 9.3 | 11.8 | 11.15 |
| 75 yo | 11.0 | 10.9 | 14.4 | 13.8 |

## 2.4 Discussion

Although *cf-PWV* is considered by many as the gold standard clinical measure of arterial stiffness (e.g., [12,16]), it represents an average over a large portion of the arterial tree. Significant regional differences in aortic mechanics (geometry or properties) that could manifest with aging or disease and have detrimental effects on cardiac function can initially have limited impact on the numerical values of *cf-PWV*. The key question, therefore, is whether *cf-PWV* can detect early regional changes in aortic properties that could increase disease risk. Although this issue could be addressed via a lengthy clinical study, computational models enable time- and cost-efficient initial assessments. It was for such reasons that we developed a FSI model based on the best available, population-averaged data of arterial stiffness, *MAP*, *PWV*, and aortic radii and length found in literature.

Whereas the present 3D FSI study appears to be unique, Vardoulis et al.[53] used a 1D computational fluid dynamics model to assess potential effects of the location of a synthetic aortic graft on overall systemic hemodynamics. In particular, they contrasted effects of placing a graft in either the ascending or the descending thoracic aorta. Noting that such grafts introduce a highly localized change in aortic stiffness (modeled to be 3 to 5 times stiffer than the native aorta), it was found that an ascending graft augments the forward wave whereas a descending graft augments reverse flow (i.e., wave reflections). The former results in greater increases in central pulse pressure, thus they concluded that "patients who receive ascending aorta grafts are more prone to systolic hypertension." Xiao et al.[36] performed a 3D computational study in which three different distributions of aortic stiffness and the corresponding hemodynamics were investigated on a fixed

arterial model. Results demonstrated well-known trends of increased *PWV* and *cPP*, but reduced PP amplification, with increased levels of stiffness.

It should be noted that we focused on but three ages, ~40, 60, and 75 yo. The subject-specific 30 yo model was not analyzed due to the lack of data for wall properties of the ascending aorta at this age, where extensibility and distensibility are very important. There is clearly a need for more data focusing on this particular age range. The lack of simulations for ages ~ 50 to 55 was also intentional, for it is during this period that there tends to be dramatic changes in *cPP*[10], ascending aortic distensibility[51], and even brachial artery flow mediated dilation[14]. Hence, results could vary considerably depending on the specific values used for geometry and properties. Notwithstanding the need for a detailed analysis of the hemodynamics during this critical period of aging, using current values that are averaged over 50 to 55 years of age (cf. [21]) could be misleading and thus was avoided.

We examined spatial and temporal distributions of four different metrics of aortic stiffening: *PP*, *D*, *PWV* and $\Delta W$ relative to the distribution of circumferential material stiffness. As well known, there is a *PP* amplification along the aorta at the younger ages that diminishes over time due to an increase in *cPP*[50]. Higher changes in c*PP* between groups are expected if a younger age was considered, but as noted above this was not possible due to the lack of reliable data on ATA stiffness for a population younger than 40 yo.

Predicted values of *D* compared well with literature data. Redheuil et al.[51] reported values of distensibility for ATA of $3.1\text{x}10^{-5}$ $Pa^{-1}$, $1.8\text{x}10^{-5}$ $Pa^{-1}$, $1.2\text{x}10^{-5}$ $Pa^{-1}$ and $1.0\text{x}10^{-5}$ $Pa^{-1}$, for age groups 40-49, 50-59, 60-69, and >70 years old, respectively. Garcia-Herrera et al.[54] reported values of distensibility for the ATA of $2.0\text{x}0^{-5}$ $Pa^{-1}$ and $0.98\text{x}10^{-5}$ $Pa^{-1}$ for age groups 16-36 yo and 65-90, respectively. Koullias et al.[55] reported values of distensibility for the ATA of $1.87\text{x}10^{-5}$ $Pa^{-1}$ in 64 years old patients. These values are in close agreement with our computations as shown in Figure 2.6, the exact numbers being: $3.27\text{x}10^{-5}$ $Pa^{-1}$, $1.49\text{x}10^{-5}$ $Pa^{-1}$ and $1.21\text{x}10^{-5}$ $Pa^{-1}$ for 40, 60 and 75 years old age groups, respectively.

The distribution of *PWV* in Figure 2.6 reveals notable differences with age at segment 5 (renal arteries) and less remarkable variations at segments 4 (suprarenal abdominal aorta) and 6 (iliac artery) for the three ages. Given a certain age group, *PWV* is the only metric with low correlation coefficients relative to circumferential stiffness (Table 2.5), due to its dependency on non-normalized arterial geometry, which contrasted with the other metrics which are strictly

related to the stiffness. Furthermore, *PWV* is often obtained clinically without measuring the actual path length between the two recorded waveforms. Boutouyrie and Vermeersch[16] used a 0.8 correction factor to relate the *cf-PWV* measured using direct distance to the 'real' aortic root-iliac bifurcation *PWV*. Indeed our aortic root-iliac bifurcation *PWV* compared well to their results (noting that the *TP* was tuned to match their *PWV* data). On the other hand, our results on carotid-to-iliac *PWV* show larger discrepancies with the values of *cf-PWV* reported by Redheuil et al.[51], who did not use correction factors for the aortic length. Use of the correct path-length is thus critical in computing *PWV*. Sugawara et al.[56] also investigated the importance of the 0.8 correction factor in the assessment of *PWV*.

The change in strain energy storage during the cardiac cycle was calculated using $\Delta W = 0.5(P_{sys}-P_{dia})\cdot(A_{sys}-A_{dia})/A_{dia}$, which is an accurate estimate in all regions other than ATA. Unlike other aortic segments, the ATA experiences large deformations in the axial direction during the cardiac cycle, hence extensibility contributes to strain energy storage in the ATA. To properly account for this contribution to the ATA strain energy, our FSI computational model must be extended to include the large motion imposed by the heart on the aortic root and clinical data are needed to quantify actual changes in length over the cardiac cycle. We do not expect that this limitation has a significant impact on the computed values of *PWV*, *PP*, and distensibility in other parts of the aorta since these metrics are mainly determined by the arterial stiffness and the geometry of the vessel.

This work confirmed the importance of tethering exerted by perivascular tissue on the aorta[57]. Since reported values of external pressure exerted on the aortic wall are wanting (cf. [58]) we estimated them iteratively until our results satisfied typical values of tissue properties, *PP*, and *cf-PWV* for each age group. The pressure exerted by the perivascular tissue, fundamental to investigate *PWV*, was modeled via a simple traction boundary condition acting on the arterial wall. Modeling explicitly the interactions between aorta and surrounding organs would allow a thorough study of the contact stresses among the different tissues, but this was beyond the scope of this work. Dynamic data on wall motion would also allow one to identify regions with distinct levels of external support. Since all the models were aged virtually, we lack such data. Rather, we considered three (arbitrary and simple) regions of external tissue support with distinct values of external stiffness and damping.

It should be noted that as we adjusted the external tissue parameter $k_s$, computed *PWV* and *PP* changed. Larger values of $k_s$ result in larger *PWV* and *PP*. The sensitivity of these changes is small, however; it takes a 5-fold increase in $k_s$ to increase *PP* by 50% and *PWV* by 250%. In the limit of very large external tissue support, the *PP* would approach that of a rigid vessel, and the *PWV* would become infinite. Tissue tethering affects motion in potentially all directions: radial, circumferential and axial directions. We focused on the role of tethering in the radial direction, which has a direct impact on *PWV*, distensibility, and other reported metrics. Time-resolved data would enable investigating the impact of tethering in the axial and circumferential directions.

Although the present model represents multiple important advances, there is yet a need for additional data to better inform it and a need for some computational improvements. Aging likely affects the peripheral vasculature and hence the associated outlet boundary conditions. Changes in *MAP* resulting from the increase in tortuosity with aging were not enough to reproduce the increase in *MAP*. Hence, we tuned the distal resistance $R_{dist}$ of the Windkessel model at each age to match the *MAP*. This increase in peripheral resistance suggests that the distal vasculature becomes constricted with aging, which would be consistent with a myogenic-driven inward remodeling[59,60]. Having measurements of flow and pressure at the branches for each age group would allow us to estimate the values of the Windkessel parameters with more certainty. Given the evidence that the primary muscular arteries - such as brachial and radial and presumably mesenteric, renal, and celiac arteries - do not stiffen with aging[61], we assigned unchanged stiffness to these vessels for all age groups. Given the lack of data regarding the material properties of muscular arteries, we assigned stiffness values comparable to those in the aorta at the renal level at 75 yo. More information on these vessels is needed. Finally, from a computational perspective, our model must be expanded to account for the large displacements imposed by the heart on the aortic root.

In conclusion, advances in medical imaging and computational biomechanics now enable subject-specific models of large portions of the vasculature to be used to explore important interactions between the evolving wall mechanics and the hemodynamics. Such models reveal the need for more precise and complete regionally-specific longitudinal data, however, which promise to enable us to glean increased insight into the complex interactions between local mechanics / pathobiology and global hemodynamics / pathophysiology that relate central arterial stiffening to diverse diseases[62].

## Bibliography


1. Laurent S, Boutouyrie P, Asmar R, et al. Aortic stiffness is an independent predictor of all-cause and cardiovascular mortality in hypertensive patients. *Hypertension*. 2001;37:1236-1241. doi:10.1161/01.HYP.37.5.1236.

2. Boutouyrie P, Laurent S, Briet M. Importance of arterial stiffness as cardiovascular risk factor for future development of new type of drugs. *Fundam Clin Pharmacol*. 2008;22:241-246. doi:10.1111/j.1472-8206.2008.00584.x.

3. Adji A, O'Rourke MF, Namasivayam M. Arterial stiffness, its assessment, prognostic value, and implications for treatment. *Am J Hypertens*. 2011;24(1):5-17. doi:10.1038/ajh.2010.192.

4. Mitchell GF. Effects of central arterial aging on the structure and function of the peripheral vasculature : implications for end-organ damage. *J Appl Physiol*. 2008;105:1652-1660.

5. Jondeau G, Boutouyrie P, Lacolley P, et al. Central pulse pressure is a major determinant of ascending aorta dilation in Marfan syndrome. *Circulation*. 1999;99:2677-2681. doi:10.1161/01.CIR.99.20.2677.

6. Lacolley P, Challande P, Osborne-Pellegrin M, Regnault V. Genetics and pathophysiology of arterial stiffness. *Cardiovasc Res*. 2009;81:637-648. doi:10.1093/cvr/cvn353.

7. Zieman SJ, Melenovsky V, Kass DA. Mechanisms, pathophysiology, and therapy of arterial stiffness. *Arterioscler Thromb Vasc Biol*. 2005;25:932-943.

8. Cioffi G, Viapiana O, Ognibeni F, et al. Clinical profile and outcome of patients with rheumatoid arthritis and abnormally high aortic stiffness. *Eur J Prev Cardiol*. 2016. doi:10.1177/2047487316649762.

9. Lemarié C a., Tharaux PL, Lehoux S. Extracellular matrix alterations in hypertensive vascular remodeling. *J Mol Cell Cardiol*. 2010;48:433-439.

10. O'Rourke MF, Hashimoto J. Mechanical factors in arterial aging. A clinical perspective. *J Am Coll Cardiol*. 2007;50(1):1-13. doi:10.1016/j.jacc.2006.12.050.

11. Safar ME. Arterial aging-hemodynamic changes and therapeutic options. *Nat Rev Cardiol*. 2010;7(8):442-449. doi:10.1038/nrcardio.2010.96.

12. Barodka VM, Joshi BL, Berkowitz DE, Hogue CW, Nyhan D. Implications of vascular aging. *Anesth Analg*. 2011;112:1048-1060. doi:10.1213/ANE.0b013e3182147e3c.

13. Arribas SM, Hinek A, González MC. Elastic fibres and vascular structure in hypertension. *Pharmacol Ther*. 2006;111:771-791. doi:10.1016/j.pharmthera.2005.12.003.

14. Lakatta EG, Wang M, Najjar SS. Arterial aging and subclinical arterial disease are fundamentally intertwined at macroscopic and molecular levels. *Med Clin North Am*. 2009;93(3):583-604. doi:10.1016/j.mcna.2009.02.008.

15. Sawabe M. Vascular aging: From molecular mechanism to clinical significance. *Geriatr Gerontol Int*. 2010;10:213-220. doi:10.1111/j.1447-0594.2010.00603.x.

16. Boutouyrie P, Vermeersch SJ. Determinants of pulse wave velocity in healthy people and in the presence of cardiovascular risk factors: Establishing normal and reference values. *Eur Heart J*. 2010;31:2338-2350. doi:10.1093/eurheartj/ehq165.

17. Najjar SS, Scuteri A, Shetty V, et al. Pulse wave velocity is an independent predictor of the longitudinal increase in systolic blood pressure and of incident hypertension in the Baltimore longitudinal study of aging. *J Am Coll Cardiol*. 2008;51(14):1377-1383. doi:10.1055/s-0029-1237430.

18. Agabiti-Rosei E, Mancia G, O'Rourke MF, et al. Central blood pressure measurements and antihypertensive therapy: A consensus document. *Hypertension*. 2007;50:154-160. doi:10.1161/HYPERTENSIONAHA.107.090068.

19. Wang KL, Cheng HM, Sung SH, et al. Wave reflection and arterial stiffness in the prediction of 15-year all-cause and cardiovascular mortalities: A community-based study. *Hypertension*. 2010;55(201):799-805. doi:10.1161/HYPERTENSIONAHA.109.139964.

20. García-Herrera CM, Celentano DJ, Cruchaga M a., et al. Mechanical characterisation of the human thoracic descending aorta: experiments and modelling. *Comput Methods Biomech Biomed Engin*. 2012;15:185-193. doi:10.1080/10255842.2010.520704.

21. Haskett D, Johnson G, Zhou A, Utzinger U, Vande Geest J. Microstructural and biomechanical alterations of the human aorta as a function of age and location. *Biomech Model Mechanobiol*. 2010;9:725-736. doi:10.1007/s10237-010-0209-7.

22. Labrosse MR, Gerson ER, Veinot JP, Beller CJ. Mechanical characterization of human aortas from pressurization testing and a paradigm shift for circumferential residual stress. *J Mech Behav Biomed Mater*. 2013;17:44-55. doi:10.1016/j.jmbbm.2012.08.004.

23. Flamini V, Creane AP, Kerskens CM, Lally C. Imaging and finite element analysis: A methodology for non-invasive characterization of aortic tissue. *Med Eng Phys*. 2015;37(1):48-54. doi:10.1016/j.medengphy.2014.10.006.

24. Roccabianca S, Figueroa CA, Tellides G, Humphrey JD. Quantification of regional differences in aortic stiffness in the aging human. *J Mech Behav Biomed Mater*. 2014;29:618-634. doi:10.1016/j.jmbbm.2013.01.026.

25. Sugawara J, Hayashi K, Yokoi T, Tanaka H. Age-associated elongation of the ascending

aorta in adults. *JACC Cardiovasc Imaging*. 2008;1(6):739-748.

26. CRIMSON CardiovasculaR Integrated Modelling and SimulatiON. (2017) Available from: http://www.crimson.software.

27. Dillon-Murphy D, Noorani A, Nordsletten D, Figueroa CA. Multi-modality image-based computational analysis of haemodynamics in aortic dissection. *Biomech Model Mechanobiol*. 2015;15:857-876. doi:10.1007/s10237-015-0729-2.

28. Craiem D, Chironi G, Redheuil A, et al. Aging impact on thoracic aorta 3D morphometry in intermediate-risk subjects: looking beyond coronary arteries with non-contrast cardiac CT. *Ann Biomed Eng*. 2012;40(5):1028-38. doi:10.1007/s10439-011-0487-y.

29. Sorkin JD, Muller DC, Andres R. Longitudinal change in height of men and women : Implications for interpretation of the body mass index. 1999;150(9):969-977.

30. Bellini C, Ferruzzi J, Roccabianca S, Di Martino ES, Humphrey JD. A microstructurally motivated model of arterial wall mechanics with mechanobiological implications. *Ann Biomed Eng*. 2014;42(3):488-502. doi:10.1007/s10439-013-0928-x.

31. Baek S, Gleason RL, Rajagopal KR, Humphrey JD. Theory of small on large: Potential utility in computations of fluid–solid interactions in arteries. *Comput Methods Appl Mech Eng*. 2007;196:3070-3078.

32. Figueroa CA, Baek S, Taylor CA, Humphrey JD. A computational framework for fluid–solid-growth modeling in cardiovascular simulations. *Comput Methods Appl Mech Eng*. 2009;198:3583-3602.

33. Vorp D a., Schiro BJ, Ehrlich MP, Juvonen TS, Ergin MA, Griffith BP. Effect of aneurysm on the tensile strength and biomechanical behavior of the ascending thoracic aorta. *Ann Thorac Surg*. 2003;75:1210-1214. doi:10.1016/S0003-4975(02)04711-2.

34. Geest JP Vande, Sacks MS, Vorp DA. Age dependency of the biaxial biomechanical behavior of human abdominal aorta. *J Biomech Eng*. 2004;126:815-822. doi:10.1115/1.1824121.

35. Martin C, Pham T, Sun W. Significant differences in the material properties between aged human and porcine aortic tissues. *Eur J Cardio-thoracic Surg*. 2011;40(1):28-34. doi:10.1016/j.ejcts.2010.08.056.

36. Xiao N, Humphrey J, Figueroa C. Multi-scale computational model of three-dimensional hemodynamics within a deformable full-body arterial network. *J Comput Phys*. 2014;244:22-40.

37. Cuomo F, Ferruzzi J, Humphrey JD, Figueroa CA. An experimental–computational study of catheter induced alterations in pulse wave velocity in anesthetized mice. *Ann Biomed Eng*. 2015;43(7):1555-1570. doi:10.1007/s10439-015-1272-0.

38. Figueroa CA, Vignon-Clementel IE, Jansen KE, Hughes TJR, Taylor CA. A coupled momentum method for modeling blood flow in three-dimensional deformable arteries. *Comput Methods Appl Mech Eng*. 2006;195:5685-5706.

39. Zhou J, Fung YC. The degree of nonlinearity and anisotropy of blood vessel elasticity. *Proc Natl Acad Sci*. 1997;94(26):14255-14260. doi:10.1073/pnas.94.26.14255.

40. Xiao N, Alastruey J, Figueroa CA. A systematic comparison between 1-D and 3-D hemodynamics in compliant arterial models. *Int J Numer Method Biomed Eng*. 2014;30(2):204-231. doi:10.1002/cnm.2598.

41. Alastruey J, Xiao N, Fok H, et al. On the impact of modelling assumptions in multi-scale, subject-specific models of aortic haemodynamics. *J R Soc Interface*. 2016;13(119):20160073. doi:10.1098/rsif.2016.0073.

42. Riley W a., Barnes RW, Evans GW, Burke GL. Ultrasonic measurement of the elastic modulus of the common carotid artery. The Atherosclerosis Risk in Communities (ARIC) Study. *Stroke*. 1992;23:952-956. doi:10.1161/01.STR.23.7.952.

43. Mitchell GF, Parise H, Benjamin EJ, et al. Changes in arterial stiffness and wave reflection with advancing age in healthy men and women: The Framingham Heart Study. *Hypertension*. 2004;43(6):1239-1245. doi:10.1161/01.HYP.0000128420.01881.aa.

44. Moireau P, Xiao N, Astorino M, et al. External tissue support and fluid-structure simulation in blood flows. *Biomech Model Mechanobiol*. 2012;11(1-2):1-18.

45. Ferrari AU, Radaelli A, Centola M. Invited review: aging and the cardiovascular system. *J Appl Physiol*. 2003;95:2591-2597. doi:10.1152/japplphysiol.00601.2003.

46. Strait JB, Lakatta EG. Aging-associated cardiovascular changes and their relationship to heart failure. *Heart Fail Clin*. 2012;8(1):143-164. doi:10.1016/j.hfc.2011.08.011.

47. Vignon-Clementel IE, Figueroa CA, Jansen KE, Taylor CA. Outflow boundary conditions for 3D simulations of non-periodic blood flow and pressure fields in deformable arteries. *Comput Methods Biomech Biomed Engin*. 2010;13:1-16.

48. Ferruzzi J, Bersi MR, Uman S, Yanagisawa H, Humphrey JD. Decreased elastic energy storage, not increased material stiffness, characterizes central artery dysfunction in fibulin-5 deficiency independent of sex. *J Biomech Eng*. 2015;137(3):031007.

49. Gaddum NR, Alastruey J, Beerbaum P, Chowienczyk P, Schaeffter T. A technical assessment of pulse wave velocity algorithms applied to non-invasive arterial waveforms. *Ann Biomed Eng*. 2013;41(12):2617-2629.

50. Nichols WW, O'Rourke MF. *McDonald's Blood Flow in Arteries Theoretical, Experimental and Clinical Principles*. Fourth Edi.; 1998.

51. Redheuil A, Yu WC, Wu CO, et al. Reduced ascending aortic strain and distensibility:

Earliest manifestations of vascular aging in humans. *Hypertension*. 2010;55:319-326. doi:10.1161/HYPERTENSIONAHA.109.141275.

52. Weber T, Ammer M, Rammer M, et al. Noninvasive determination of carotid-femoral pulse wave velocity depends critically on assessment of travel distance: a comparison with invasive measurement. *J Hypertens*. 2009;27(8):1624-1630.

53. Vardoulis O, Coppens E, Martin B, Reymond P, Tozzi P, Stergiopulos N. Impact of aortic grafts on arterial pressure: A computational fluid dynamics study. *Eur J Vasc Endovasc Surg*. 2011;42(5):704-710. doi:10.1016/j.ejvs.2011.08.006.

54. Garcia-Herrera CM, Celentano DJ. Modelling and numerical simulation of the human aortic arch under in vivo conditions. *Biomech Model Mechanobiol*. 2013;12(6):1143-1154. doi:10.1007/s10237-013-0471-6.

55. Koullias G, Modak R, Tranquilli M, Korkolis DP, Barash P, Elefteriades JA. Mechanical deterioration underlies malignant behavior of aneurysmal human ascending aorta. *J Thorac Cardiovasc Surg*. 2005;130(3). doi:10.1016/j.jtcvs.2005.02.052.

56. Sugawara J, Hayashi K, Tanaka H. Arterial path length for arterial stiffness: Methodological consideration. *Am J Hypertens*. 2016;29(11):1237-1244. doi:10.1093/ajh/hpw075.

57. Hodis S, Zamir M. Arterial wall tethering as a distant boundary condition. *Phys Rev E*. 2009;80(5). doi:10.1103/PhysRevE.80.051913.

58. Humphrey JD, Na S. Elastodynamics and arterial wall stress. *Ann Biomed Eng*. 2002;30(4):509-523. doi:10.1114/1.1467676.

59. Mulvany MJ. Small artery remodelling in hypertension. *Basic Clin Pharmacol Toxicol*. 2012;110(1):49-55. doi:10.1111/j.1742-7843.2011.00758.x.

60. Jacobsen JCB, Mulvany MJ, Holstein-Rathlou N-H. A mechanism for arteriolar remodeling based on maintenance of smooth muscle cell activation. *Am J Physiol Regul Integr Comp Physiol*. 2008;294:R1379-R1389. doi:10.1152/ajpregu.00407.2007.

61. Laurent S, Boutouyrie P. The structural factor of hypertension: large and small artery alterations. *Circ Res*. 2015;116(6):1007-1021. doi:10.1161/CIRCRESAHA.116.303596.

62. Humphrey JD, Harrison DG, Figueroa CA, Lacolley P, Laurent S. Central artery stiffness in hypertension and aging: a problem with cause and consequence. *Circ Res*. 2016;118(3):379-381. doi:10.1161/CIRCRESAHA.115.307722.

## Chapter 3. Sex-Dependent Differences in Central Artery Hemodynamics in Normal and Fibulin-5 Deficient Mice: Implications for Aging

Federica Cuomo[1*]

Jacopo Ferruzzi[2*]

Pradyumn Agarwal[1]

Chen Li[1]

Zhen W. Zhuang[3]

Jay D. Humphrey[2,4],

C. Alberto Figueroa[1,5]

[*]These authors contributed equally

[1]Department of Biomedical Engineering, University of Michigan, Ann Arbor, MI, USA

[2]Department of Biomedical Engineering, Yale University, New Haven, CT, USA

[3]Translational Research Imaging Center, Yale University, New Haven, CT, USA

[4]Vascular Biology and Therapeutics Program, Yale University, New Haven, CT, USA

[5]Department of Surgery, University of Michigan, Ann Arbor, MI, USA

*Proceedings of the Royal Society A. 2019;* 475(2221): 20180076

***Contributions.*** *All the experimental work showed in this chapter was performed by Dr. Jacopo Ferruzzi at Yale University. Zhen W. Zhuang contributed to collect the micro-CT image data.*

## 3.1 Introduction

Aging is a primary risk factor for increased central artery stiffness[1], which in turn is a strong indicator and initiator of cardiovascular, neurovascular, and renovascular disease[2]. Arterial aging in humans associates with many changes in cellular activity and extracellular matrix architecture, including a progressive loss of elastic fiber integrity[3]. That is, the aging phenotype results in part from mechanical damage to and proteolytic degradation of elastic fibers, which we have shown can decrease collagen fiber undulation and thereby exacerbate the arterial stiffening[4]. Notwithstanding the availability of considerable histopathological, biomechanical, and clinical data on the effects of aging of the central vasculature in humans, it is difficult to obtain detailed information on evolving regional mechanical properties[5,6] and associated effects on the hemodynamics[7]. For this reason, mouse models have become increasingly important in studying vascular health and disease.

Old mice exhibit a vascular aging phenotype[8,9], but not due to significant changes in elastic fiber integrity because of the combination of a short lifespan and the long normal half-life of vascular elastin[10]. We have shown, however, that genetically modified mouse models can be used to study effects of graded losses in elastic fiber integrity, with the fibulin-5 deficient mouse displaying the most dramatic elastopathy in the common carotid artery of multiple viable models of elastic fiber associated mutations that we studied[11]. Indeed, it appears that this mouse represents a model of early, stable vascular aging[12]. Fibulin-5 is a glycoprotein that associates with elastin to form elastic fibers and it is thought to function largely in elastogenesis. Histological evidence reveals disrupted elastic laminae in these mice, primarily in the outer portion of the media.

The current clinical gold standard measure of central artery stiffness is the pulse wave velocity (*PWV*), often measured from the carotid to the femoral artery[2]. The Moens-Korteweg relation reveals that *PWV* depends on the intrinsic material stiffness of the wall as well as wall thickness and luminal radius. This relation assumes that each of these quantities is spatially uniform, however, which is clearly not the case over substantial lengths of the central vasculature. There is pressing need, therefore, to assess better the potential effects of regional variations in central arterial geometry and mechanical properties on the hemodynamics that can adversely affect the microcirculation in the heart, brain, and kidneys. Towards this end, one can combine *in vitro* (mechanical properties) and *in vivo* (geometric and hemodynamic) data with sophisticated computational models to account directly for regional variations along the central vasculature.

Such computations can provide information not otherwise measured easily and can help build intuition that is helpful in interpreting clinically available results.

In this paper, we meld *in vitro* information from regional biaxial mechanical testing of five different central arteries with *in vivo* information from non-invasive micro-CT and ultrasound as well as invasive catheterization to build computational hemodynamic models of the central vasculature in four different animal groups: male and female wild-type and fibulin-5 deficient mice. Specifically, we perform fluid-solid-interaction (FSI) simulations over the central vasculature and compare associated regional flows and pressure waves as well as computed pulse wave velocities. Notwithstanding significant advantages of studies in mice, there are also challenges. Small perturbations in anesthesia and temperature can introduce variability in measurements within and across animals. Furthermore, because many of the requisite experimental procedures are terminal, it is difficult to obtain data on biaxial stiffness, aortic anatomy, and hemodynamics from the same mouse, making it challenging to perform truly mouse-specific FSI hemodynamic simulations informed by the aforementioned data. In this paper, we propose a strategy to assign hemodynamic and structural stiffness data for four different groups of mice to individual micro-CT aortic models to produce calibrated computational results that provide general insights into quantities not easily obtained through experiments, such as pressure indices in the renal arteries or values of peripheral resistance and compliance, which can then be compared across diverse groups.

### 3.2 Methods

The animals were divided into four groups to investigate effects of sex and genotype: WT males (WT_M), WT females (WT_F), KO males (KO_M), and KO females (KO_F). All animals were 20 to 22 weeks of age, except for one 36-week old male KO mouse. Due to the impracticality of collecting complete *in vivo* and *in vitro* data sets from any single animal, these four basic experimental groups were divided in three cohorts (Figure 3.1):

- An anatomy cohort, for which we collected noninvasive *in vivo* micro-CT data on the temporal mean vascular geometry.
- A wall mechanics cohort, for which we collected regional *in vitro* biaxial data on five central vessels: the common carotid artery (CCA) as well as the ascending thoracic aorta (ATA),

descending thoracic aorta (DTA), suprarenal abdominal aorta (SAA), and infrarenal abdominal aorta (IAA).

- A hemodynamics cohort, for which we collected noninvasive *in vivo* ultrasound data on cyclic changes in geometry and flow as well as invasive *in vivo* data on cyclic pressures.

External factors that can influence such measurements, such as age and body mass, and similarly the type and level of anesthesia, heart rate, and body temperature were kept as consistent as possible across all four groups. Our overall strategy to build mouse-specific computational models was as follows: regional wall mechanics data were assigned to each micro-CT anatomical model using values of local radii and previously obtained material properties and wall thicknesses for each of the four groups[13] while hemodynamics data were mapped to each model using body mass based allometric scaling of quantities such as cardiac output, total arterial resistance, and total arterial compliance. Therefore, this workflow relied on "group-specific" data to prescribe the parameters needed to perform FSI analyses for each specific member of the anatomy cohort. For the sake of simplicity, we refer to the output of this workflow as 'mouse-specific' given the individual micro-CT scans, even though it relies on a mass and radius scaling laws for each of the four animal groups considered.

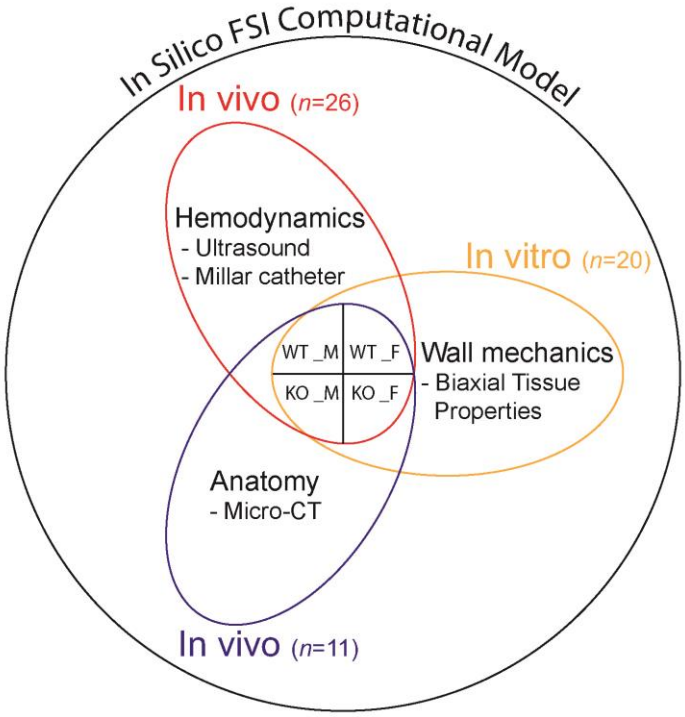


**Figure 3.1.** Three experimental cohorts of mice were used to acquire data on hemodynamics, wall properties, and aortic anatomy for four groups of mice: adult male and female homozygous *Fbln5*$^{+/+}$ (WT) and *Fbln5*$^{-/-}$ (KO) mice. The experimental data were synthesized to create an *in silico* FSI computational model of the unsteady hemodynamics and regional wall mechanics.

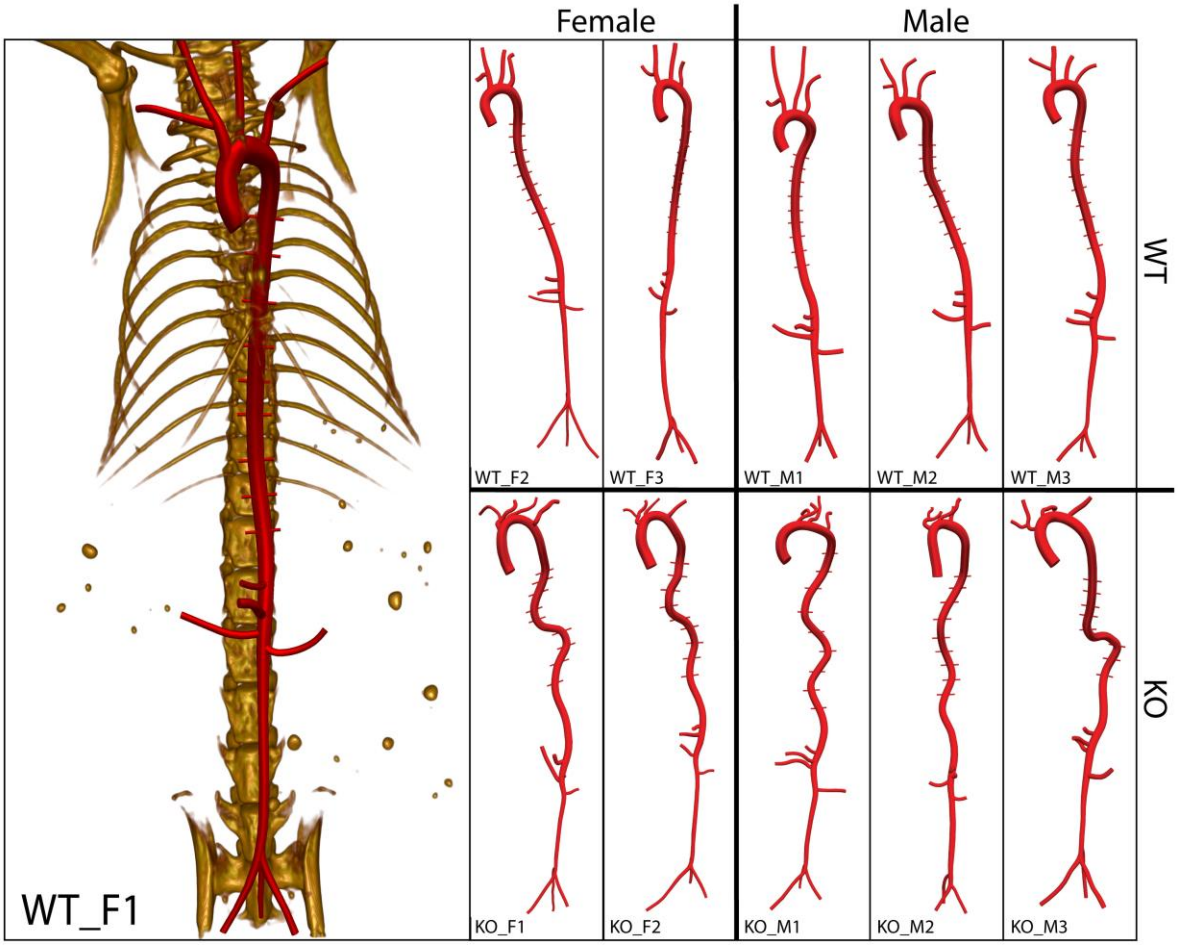


**Figure 3.2.** Anatomical models created for each of the four groups: female and male WT and KO. The KO mice had a marked increase in aortic tortuosity, particularly in the DTA. All animals were 20 to 22 weeks of age, except for one 36-week old male KO mouse (KO_M3). The image for WT_F1 shows the associated skeleton, which although not shown for the other 10 cases was nevertheless used to locate the pairs of intercostal branches that were not visible on the micro-CT scans.

### 3.2.1 Experimental

**Anatomy.** Briefly, mice were anesthetized using 1-2% isoflurane, then given a bolus intravenous (jugular vein) injection of a nanoemulsion formulation (Fenestra VC, MediLumine Inc., Montreal, CA), at a dose of 0.2 ml/20 g, as a blood-pool contrast agent designed for prolonged vascular imaging. Immediately thereafter, the animal was placed prone inside a micro-CT scanner (eXplore CT120, GE healthcare) for non-gated whole body scanning. The images were reconstructed as isotropic 49x49x49 $\mu m^3$ voxels. All reconstructions were done with a Feldkamp algorithm and all images were calibrated with standard Hounsfield units (HU) using microView. A relatively constant heart rate (±10%) was achieved by careful maintenance of the level of isoflurane anesthesia and body temperature during each scan. Image data were collected for $n = 3$

mice per group, except for the KO_F group for which $n = 2$. Hence, $n = 11$ mice were imaged. These specimens were used to define the anatomical models (Figure 3.2).

**Wall mechanics**. As reported previously[13], biaxial material properties were estimated at four different locations along the aorta (ATA, DTA, SAA, and IAA) and within one CCA using data collected via a custom computer-controlled biaxial testing device[14]. Briefly, following standard preconditioning, seven cyclic loading protocols were performed: cyclic pressure diameter tests from 10 to 140 mmHg at three different fixed values of axial stretch (95, 100, 105% of the *in vivo* value) and cyclic axial extension tests at four fixed values of transmural pressure (10, 60, 100, 140 mmHg). Best-fit values of the eight model parameters within a "four-fiber family" constitutive model were determined for $n = 5$ animals per group (for a total of $n = 20$ mice) using a nonlinear regression algorithm to minimize the difference between predicted and measured pressure-diameter and axial force-stretch data from the last unloading cycle of all seven testing protocols.

**Hemodynamics.** Following inhalation anesthesia, the mouse was gently laid on its back and secured on a surgical platform having a recirculating heating pad (TP-500 Heat Therapy Pump, Gaymar Industries Inc., Orchard Park, NY) to maintain body temperature. Next, the midline thorax and abdomen were shaved and an ultrasound gel applied. Mean blood velocity and luminal diameters were then acquired via ultrasound (Vevo 2100 system, FUJIFILM VisualSonics) within the ATA, IAA, and CCA. Cardiac output (CO) was measured similarly with transthoracic echocardiography, then central aortic pressure was measured using a SPR-1000 Millar pressure catheter. A total of $n = 26$ mice were studied across the four groups.

### 3.2.2 Computational

We employed the custom computational hemodynamics framework CRIMSON[15] to perform the FSI studies. These simulations included 3D anatomical models of the aorta and main branches, spatially-variable mechanical properties of the central vasculature, 3-element Windkessel models used as outflow boundary conditions for each branch of the anatomical models, and an external tissue support formulation to simulate effects of perivascular tissue on aortic hemodynamics. We also used a posteriori gradient-based mesh adaptation methods for iterative mesh refinement[16]. Blood viscosity was 0.004 kg/(m s) and blood density was 1060 kg/m$^3$. Below we describe the workflow used to meld into single computational models the experimental data acquired in the 3 cohorts of mice (Figure 3.1).

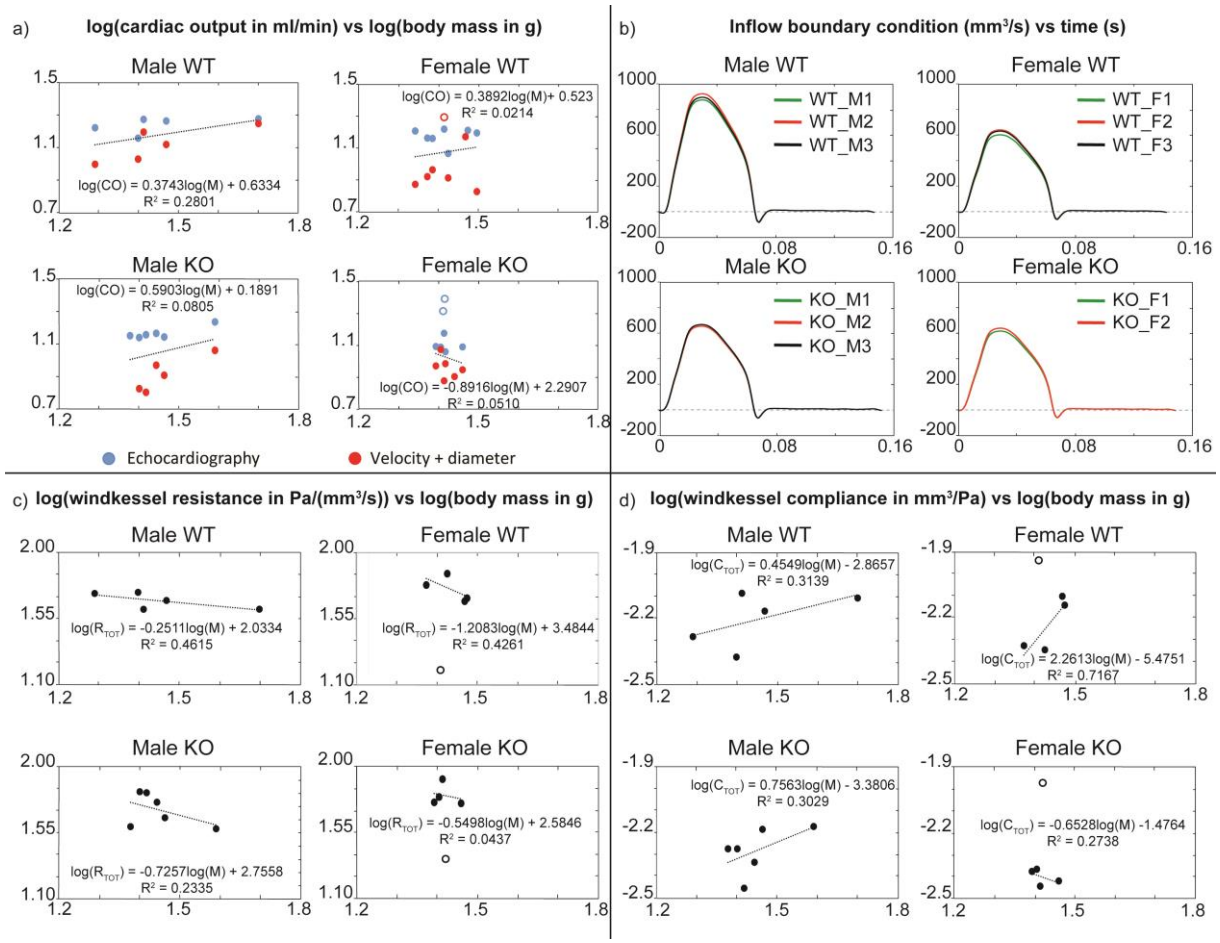


**Figure 3.3**. a) Allometric scaling of cardiac output (CO) for each of the four groups based on echocardiographic and ultrasound-derived velocity and diameter data. b) Mouse-specific flow waveforms mapped to each specimen in the anatomy cohort. c) Allometric scaling of total arterial resistance ($R_{TOT}$) for each of the four groups. d) Allometric scaling of total arterial compliance ($C_{TOT}$) for each of the four groups.

**Anatomical Models**. 3D anatomical models of the central vasculature were reconstructed from the micro-CT image data using the CRIMSON GUI. A 2D semi-automatic segmentation procedure followed by 3D lofting generated a non-uniform rational basis splines (NURBS) description of each vasculature. Briefly, centerline paths were identified from the micro-CT images and 2D contours were drawn, with discrete spacing, perpendicular to each path to define the vessel lumen at the 2D contour locations. Contours were then lofted to create 3D volumes for each vessel (i.e., aorta and primary branches) and a union operation was used to merge individual vessels into a single analytical geometric model. The aortic root was not always discernible in the images, thus the length of the ATA was adjusted for each model according to the mean *in vivo* axial length measured with ultrasound for that group. Lastly, nine pairs of intercostal arteries (not

visible in the image data) were added to each model using the location of the ribs as a reference, resulting in $n$ = 11 anatomical models (Figure 3.2).

Field-driven mesh adaptation techniques were employed to refine the finite element meshes in areas of expected large velocity gradients[16]. The final unstructured field-adapted meshes ranged between $1.4 \cdot 10^6$ tetrahedral elements, with $2.5 \cdot 10^4$ nodes, to $2.2 \cdot 10^6$ tetrahedral elements, with $4.0 \cdot 10^5$ nodes.

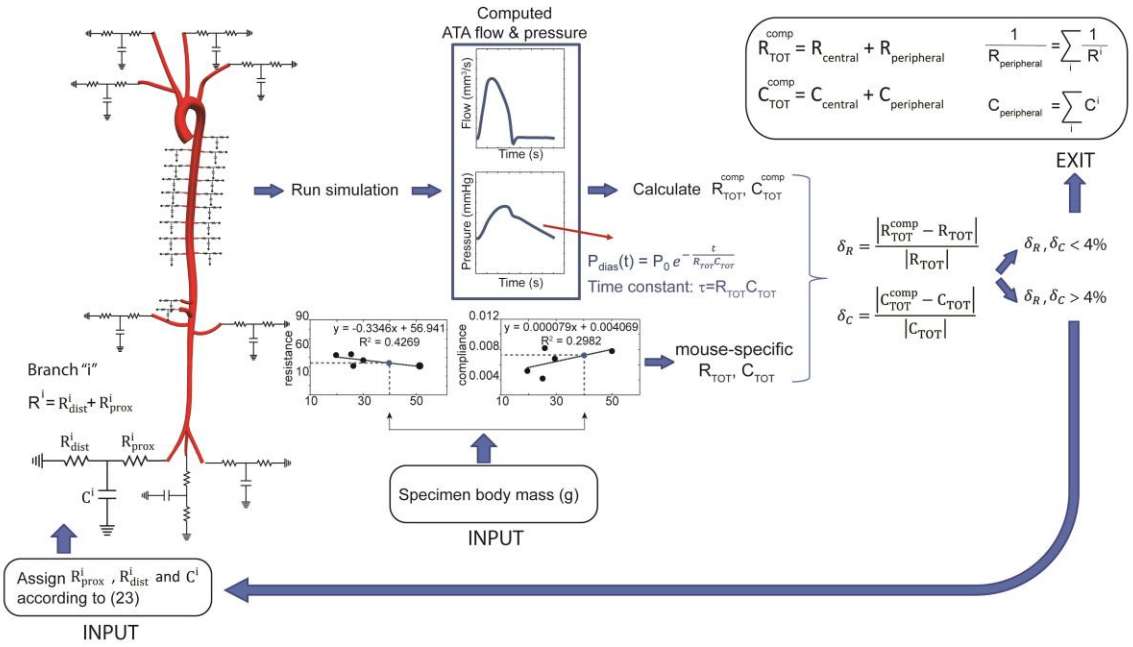


**Figure 3.4.** Workflow for mouse-specific peripheral boundary conditions. For each of the 26 mice in the hemodynamics cohort, $R_{TOT}$ and $C_{TOT}$ were estimated from the measured ATA pressure and flow waveforms by $R_{TOT} = P_{MEAN} / CO$ with $C_{TOT}$ then determined by fitting the diastolic portion of the pressure waveform with an exponential decay function ($P_{dias}(t) = \exp(-t/R_{TOT}C_{TOT})$)[21,22]. Using allometric scaling, specific values of $R_{TOT}$ and $C_{TOT}$ were then prescribed for each of the 11 mice in the anatomy cohort. Values of $R^i_{prox}$, $R^i_{dist}$, and $C^i$ were estimated iteratively following a prior method[23] for each vessel "i" until the computed total central resistance and compliance $R^{comp}{}_{TOT}$ and $C^{comp}{}_{TOT}$ matched the experimental values $R_{TOT}$ and $C_{TOT}$.

**Wall mechanics and biaxial tissue properties.** One needs a FSI method to capture pulse wave propagation within a distensible vasculature. Toward this end, we employed a coupled momentum formulation[17] and modeled each vascular segment as an incompressible elastic membrane of thickness $h$ characterized by a 5x5 stiffness matrix that was linearized about the mean arterial pressure[18], with all quantities varying from region to region. Specifically, the regionally dependent values of material stiffness were determined from a nonlinear, anisotropic stored energy function using the theory of small deformations superimposed on large[19], which naturally accounts for regionally dependent values of the *in vivo* axial extension and circumferential distension at mean arterial pressure. The axial stretch was estimated via the cross-

over point in the *in vitro* force-length tests performed at four different pressures[20] whereas the circumferential stretch was calculated from the *in vivo* diameter assessed by micro-CT and the unloaded diameter measured ex vivo. It should be noted, however, that the ATA also experiences a cyclic axial extension throughout the cardiac cycle of the same order of magnitude as the cyclic circumferential distension. The mean axial stretch of the ATA was estimated from micro-CT measured lengths *in vivo* and unloaded lengths measured *in vitro*. The regionally dependent mean values of wall stiffness and thickness are listed in Table 3.1. They were mapped directly onto segments of each anatomical model at the following five regions: ATA, DTA, SAA, IAA, and CCA. Values within the DTA were further subdivided into proximally and distally segments (pDTA and dDTA) using individual stretches. Values elsewhere were populated by linearly interpolating values at the aforementioned six sites.

Most arteries are supported externally by perivascular tissues, which constrain vascular motions via an effective external pressure ($P_{EXT}$). A traction boundary condition was applied on the outer vascular wall to mimic effects of a distributed viscoelastic stress imparted by perivascular tissue or organs. Specifying this viscoelastic stress requires two spatially distributed parameters: a stiffness coefficient ($k_s$) and a damping coefficient ($c_s$). The parameter $k_s$ was estimated using an iterative approach for each aortic location. For each aortic location an experimental $P_{EXT}$ was estimated using the in vitro transluminal pressure and the in vivo catheter-based luminal pressure. The computed $P_{EXT}$ was calculated as $P_{EXT} = -k_s u - c_s v$, where u and v are the radial components of the displacement and velocity vectors, respectively. Values of $k_s$ where iterated until the discrepancy between experimental and computed $P_{EXT}$ was less than 5%. The value of $c_s$ was simply set to the minimum value that eliminated spurious oscillations in the computed wall motion. Final values for $k_s$ and $P_{EXT}$ are listed in Table 3.2.

**Table 3.1**. Values of circumferential ($\mathfrak{C}_{\theta\theta}$) and axial ($\mathfrak{C}_{zz}$) material stiffness, in MPa, and wall thickness (h), in μm, at six vascular locations – ascending thoracic aorta (ATA), proximal descending thoracic aorta (pDTA), distal descending thoracic aorta (dDTA), suprarenal abdominal aorta (SAA), infrarenal abdominal aorta (IAA), and common carotid artery (CAA) – for specimens from all four groups: male – M and female – F, wild-type (WT) and fibulin-5 null (KO).

| | | **Wild Type_Male (WT_M)** | | | | | **Wild Type_Female (WT_F)** | | | | |
|---|---|---|---|---|---|---|---|---|---|---|---|
| | | **WT_M1** | **WT_M2** | **WT_M3** | **mean** | **std** | **WT_F1** | **WT_F2** | **WT_F3** | **mean** | **std** |
| **ATA** | $\mathfrak{C}_{\theta\theta}$ | 0.41 | 0.38 | 0.28 | 0.35 | 0.07 | 0.38 | 0.22 | 0.25 | 0.28 | 0.09 |
| | $\mathfrak{C}_{zz}$ | 0.32 | 0.31 | 0.31 | 0.31 | 0.01 | 0.56 | 0.54 | 0.52 | 0.54 | 0.02 |
| | **h** | 55.21 | 56.37 | 59.54 | 57.04 | 2.24 | 50.00 | 55.92 | 54.46 | 53.46 | 3.08 |
| **pDTA** | $\mathfrak{C}_{\theta\theta}$ | 1.19 | 1.79 | 0.48 | 1.15 | 0.66 | 0.56 | 0.56 | 0.40 | 0.51 | 0.10 |
| | $\mathfrak{C}_{zz}$ | 3.10 | 4.17 | 1.91 | 3.06 | 1.13 | 2.00 | 1.99 | 1.72 | 1.91 | 0.16 |
| | **h** | 40.41 | 38.79 | 45.44 | 41.55 | 3.47 | 43.47 | 43.55 | 45.94 | 44.32 | 1.40 |
| **dDTA** | $\mathfrak{C}_{\theta\theta}$ | 0.71 | 0.84 | 0.48 | 0.68 | 0.18 | 0.41 | 0.36 | 0.28 | 0.35 | 0.06 |
| | $\mathfrak{C}_{zz}$ | 2.28 | 2.49 | 1.91 | 2.23 | 0.29 | 1.74 | 1.66 | 1.54 | 1.65 | 0.10 |
| | **h** | 45.44 | 42.10 | 45.44 | 44.32 | 1.93 | 45.69 | 46.71 | 48.62 | 47.00 | 1.49 |
| **SAA** | $\mathfrak{C}_{\theta\theta}$ | 0.49 | 0.44 | 0.28 | 0.40 | 0.11 | 0.30 | 0.36 | 0.26 | 0.31 | 0.05 |
| | $\mathfrak{C}_{zz}$ | 1.43 | 1.85 | 1.20 | 1.50 | 0.33 | 1.16 | 1.66 | 1.11 | 1.31 | 0.30 |
| | **h** | 38.84 | 46.05 | 42.89 | 42.60 | 3.61 | 41.75 | 44.46 | 42.95 | 43.05 | 1.36 |
| **IAA** | $\mathfrak{C}_{\theta\theta}$ | 0.59 | 0.25 | 0.19 | 0.34 | 0.21 | 0.17 | 0.14 | 0.28 | 0.20 | 0.07 |
| | $\mathfrak{C}_{zz}$ | 2.14 | 1.59 | 1.48 | 1.74 | 0.36 | 2.08 | 2.04 | 2.27 | 2.13 | 0.13 |
| | **h** | 34.28 | 38.63 | 40.67 | 37.86 | 3.27 | 35.98 | 37.07 | 32.91 | 35.32 | 2.15 |
| **CCA** | $\mathfrak{C}_{\theta\theta}$ | 0.28 | 0.33 | 0.36 | 0.33 | 0.04 | 0.21 | 0.43 | 0.74 | 0.46 | 0.27 |
| | $\mathfrak{C}_{zz}$ | 1.04 | 1.08 | 1.10 | 1.07 | 0.03 | 1.03 | 1.27 | 1.77 | 1.35 | 0.38 |
| | **h** | 30.56 | 29.79 | 29.43 | 29.93 | 0.58 | 31.02 | 27.92 | 26.37 | 28.44 | 2.37 |

**Table 3.1 continued**

| | | Knockout_Male (KO_M) | | | | | Knockout_Female (KO_F) | | | | |
|---|---|---|---|---|---|---|---|---|---|---|---|
| | | **KO_M1** | **KO_M2** | **KO_M3** | **mean** | **std** | **KO_F1** | **KO_F2** | **-** | **mean** | **std** |
| **ATA** | $\tau_{00}$ | 0.47 | 0.25 | 0.47 | 0.40 | 0.13 | 0.65 | 0.83 | - | 0.74[ab] | 0.13 |
| | $\tau_{ZZ}$ | 0.21 | 0.18 | 0.06 | 0.15[b] | 0.08 | 0.99 | 0.80 | - | 0.90[ab] | 0.13 |
| | **h** | 64.31 | 69.31 | 81.35 | 71.66[b] | 8.76 | 63.65 | 63.29 | - | 63.47 | 0.25 |
| **pDTA** | $\tau_{00}$ | 0.93 | 0.60 | 1.14 | 0.89 | 0.27 | 1.25 | 1.15 | - | 1.20 | 0.07 |
| | $\tau_{ZZ}$ | 2.61 | 2.14 | 2.89 | 2.55 | 0.38 | 2.72 | 2.61 | - | 2.66 | 0.08 |
| | **h** | 55.84 | 57.95 | 54.98 | 56.26[b] | 1.53 | 56.83 | 57.22 | - | 57.02[b] | 0.27 |
| **dDTA** | $\tau_{00}$ | 0.41 | 0.31 | 0.81 | 0.51 | 0.26 | 0.91 | 0.79 | - | 0.85 | 0.08 |
| | $\tau_{ZZ}$ | 1.86 | 1.70 | 2.44 | 2.00 | 0.39 | 2.34 | 2.21 | - | 2.28 | 0.09 |
| | **h** | 60.08 | 61.90 | 56.48 | 59.49[b] | 2.76 | 58.30 | 58.98 | - | 58.64[b] | 0.48 |
| **SAA** | $\tau_{00}$ | 0.30 | 0.30 | 0.78 | 0.46 | 0.28 | 0.39 | 0.21 | - | 0.30 | 0.13 |
| | $\tau_{ZZ}$ | 1.34 | 1.34 | 1.89 | 1.52 | 0.32 | 1.62 | 1.32 | - | 1.47 | 0.21 |
| | **h** | 52.82 | 52.75 | 48.05 | 51.20[b] | 2.73 | 49.24 | 53.27 | - | 51.25[b] | 2.85 |
| **IAA** | $\tau_{00}$ | 0.10 | 0.32 | 0.12 | 0.18 | 0.12 | 0.07 | 0.09 | - | 0.08 | 0.01 |
| | $\tau_{ZZ}$ | 1.65 | 2.26 | 1.70 | 1.87 | 0.34 | 1.58 | 1.64 | - | 1.61 | 0.04 |
| | **h** | 60.20 | 50.08 | 57.96 | 56.08[b] | 5.31 | 60.80 | 57.72 | - | 59.26[b] | 2.18 |
| **CCA** | $\tau_{00}$ | 0.15 | 0.23 | 0.18 | 0.19 | 0.04 | 0.25 | 0.05 | - | 0.15 | 0.14 |
| | $\tau_{ZZ}$ | 1.63 | 1.85 | 1.73 | 1.73[b] | 0.11 | 1.96 | 1.46 | - | 1.71 | 0.35 |
| | **h** | 40.47 | 38.35 | 39.34 | 39.38[b] | 1.06 | 37.30 | 48.17 | - | 42.73 | 7.69 |

[a] $p < 0.05$ between M and F of the same genotype; [b] $p < 0.05$ between WT and KO of the same sex

**Table 3.2.** External tissue support stiffness coefficient ($k_s$) (Pa $mm^{-1}$) and computed external pressure ($P_{EXT}$), in mmHg, at six locations (ATA, pDTA and dDTA, SAA, IAA and CAA) for all four groups (male - M and female - F, WT and KO).

| | | **Wild-Type_Male (WT_M)** | | | | | **Wild-Type_Female (WT_F)** | | | | |
|---|---|---|---|---|---|---|---|---|---|---|---|
| | | WT_M1 | WT_M2 | WT_M3 | mean | std | WT_F1 | WT_F2 | WT_F3 | mean | std |
| ATA | $k_s$ | 14000 | 16000 | 21000 | 17000 | 3606 | 13500 | 22000 | 3600 | 13033 | 9209 |
| | $P_{EXT}$ | 22 | 25 | 31 | 26 | 5 | 25 | 38 | 34 | 32 | 6 |
| pDTA | $k_s$ | -28500 | -75000 | 16500 | -29000 | 45752 | 9000 | 10000 | 15000 | 11333 | 3215 |
| | $P_{EXT}$ | -17 | -36 | 15 | -13 | 25 | 8 | 9 | 19 | 12 | 6 |
| dDTA | $k_s$ | 40500 | -4800 | 15000 | 16900 | 22710 | 16500 | 20500 | 22000 | 19667 | 2843 |
| | $P_{EXT}$ | 33 | -4 | 13 | 14 | 18 | 17 | 20 | 25 | 21 | 4 |
| SAA | $k_s$ | 13000 | 3800 | 21000 | 12600 | 8607 | 20000 | 32000 | 4500 | 18833 | 1378 |
| | $P_{EXT}$ | 15 | 5 | 25 | 15 | 10 | 24 | 30 | 26 | 27 | 3 |
| IAA | $k_s$ | 12000 | 32000 | 37500 | 27167 | 13420 | 47000 | 39000 | 33000 | 39667 | 7024 |
| | $P_{EXT}$ | 6 | 28 | 32 | 22 | 14 | 35 | 39 | 25 | 33 | 7 |
| CCA | $k_s$ | 38000 | 37500 | 37500 | 37667 | 289 | 50000 | 29500 | -17500 | 20667 | 3460 |
| | $P_{EXT}$ | 22 | 20 | 17 | 20 | 2 | 29 | 13 | -5 | 12 | 17 |
| | | **Knockout_Male (KO_M)** | | | | | **Knockout_Female (KO_F)** | | | | |
| | | KO_M1 | KO_M2 | KO_M3 | Mean | std | KO_F1 | KO_F2 | - | mean | std |
| ATA | $k_s$ | 11200 | 25000 | -185 | 12005 | 12612 | 23500 | 13000 | - | 18250 | 7425 |
| | $P_{EXT}$ | 11 | 23 | 0 | 12 | 12 | 16 | 8 | - | 12 | 6 |
| pDTA | $k_s$ | -95000 | -23500 | -185000 | - | 80926 | -128000 | -100000 | - | -114000 | 1979 |
| | $P_{EXT}$ | -28 | -9 | -37 | -25 | 14 | -34 | -29 | - | -31 | 3 |
| dDTA | $k_s$ | -9000 | 12000 | -76000 | -24333 | 45960 | -52000 | -21200 | - | -36600 | 2177 |
| | $Pe_{XT}$ | -5 | 7 | -24 | -7 | 15 | -16 | -8 | - | -12 | 5 |
| SAA | $k_s$ | -6500 | -1400 | -58000 | -21967 | 31310 | 24000 | 33000 | - | 28500 | 6364 |
| | EXT | -5 | -1 | -24 | -10[b] | 12 | 19 | 32 | - | 25[a] | 9 |
| IAA | $k_s$ | 12000 | -18000 | 20000 | 4667 | 20033 | 55000 | 34000 | - | 44500 | 1484 |
| | $P_{EXT}$ | 8 | -8 | 12 | 4 | 11 | 39 | 34 | - | 37[a] | 4 |
| CCA | $k_s$ | 24000 | 10000 | 19000 | 17667 | 7095 | 68000 | 81500 | - | 74750 | 9546 |
| | $P_{EXT}$ | 9 | 3 | 7 | 6 | 3 | 17 | 50 | - | 34 | 23 |

[a] $p < 0.05$ between M and F of the same genotype; [b] $p < 0.05$ between WT and KO of the same sex

**Hemodynamics.** Mouse-specific hemodynamic data were assigned to micro-CT based anatomical models separately for each of the four groups using allometric scaling of quantities such as cardiac output, total arterial resistance, and total arterial compliance. Allometric scaling laws are of the form: $Y = Y_0 M^b$, where $Y$ is the quantity of interest, $Y_0$ is a normalization constant, $M$ is the body mass, and $b$ is a scaling exponent. Allometric scaling can be used within a species or across species, with coefficients determined by plotting the quantities of interest against body mass in log-log plots and performing linear regressions of the form $\log(Y) = \log(Y_0) + b * \log(M)$[24]. This scaling was used to inform the inlet and peripheral boundary conditions for each specimen.

*Inlet boundary condition:* Velocity and diameter data measured with ultrasound at the ATA were used to calculate a time-averaged flow waveform for each mouse ($n$ = 26) within the hemodynamics cohort. Each flow waveform was then Fourier-interpolated using 36 modes. Waveforms showing artifacts such as spurious systolic oscillations or lack of diastolic backflow were disregarded. The remaining waveforms were aligned at the peak diastolic backflow and averaged. This procedure produced a single flow waveform template using data across the four groups (WT_M, WT_F, KO_M, and KO_F) that was then scaled for each micro-CT anatomy as follows. Allometric scaling of CO was performed separately for the four groups (Figure 3.3a) with CO measured using two different techniques: echocardiographic changes in left ventricular volume (blue dots in the figure) and ultrasonic-derived velocity and diameter measurements in the ATA (red dots), each over multiple cardiac cycles. Three measurements were considered outliers and excluded from the regression (empty circles in Figure 3.3a): two echocardiographic measurements in KO females and one velocity+diameter measurement in a WT female. Allometric scaling for each group makes it possible to assign mouse-specific values of cardiac output to each of the specimens in the four different groups.

*Additional considerations for CO scaling*: Hemodynamic data for flow and pressure were acquired under different experimental conditions, representing different degrees of invasiveness. Mean blood velocity and diameter were measured non-invasively with ultrasound while central aortic pressure was measured invasively with a catheter, both under similar levels of anesthesia. As we will see in Chapter 5, we investigated the hemodynamic impact of catheters placed within the murine aorta and observed a reduction in CO[18] relative to conditions without a catheter. Therefore, we further scaled down the estimated CO for each animal by 7% across the four groups.

The mouse-specific values of CO were then mapped to the common flow waveform template, resulting in flow waveforms for each of the four groups (Figure 3.3b).

*Peripheral boundary conditions*: We used a multiscale approach to prescribe outflow boundary conditions. Lumped parameter models of the distal circulation were coupled to each outlet surface for each mouse-specific model: total arterial resistance ($R_{TOT}$) and total arterial compliance ($C_{TOT}$) were estimated from measured ATA pressure and flow waveforms for each mouse in the hemodynamics cohort[21]. Namely, $R_{TOT} = P_{MEAN} / CO$ whereas $C_{TOT}$ was determined by fitting the diastolic part of the pressure waveform with an exponential decay ($P_{dias}(t) = \exp(-t/R_{TOT}C_{TOT})$)[22]. Allometric scaling of $R_{TOT}$ and $C_{TOT}$ was then performed for each mouse in the anatomic cohort (Figure 3.3c and 3.3d). Figure 3.4 illustrates the overall workflow for specifying mouse-specific outflow boundary conditions. Two key inputs are:

1. Specific values of $R_{TOT}$ and $C_{TOT}$ (Table 3.3) were prescribed for each of the 11 mice in the anatomy cohort based on their body mass. $R_{TOT}$ and $C_{TOT}$ were then decomposed into the sum of components representing central ($R_{central}$, $C_{central}$) and peripheral ($R_{peripheral}$, $C_{peripheral}$) contributions:

$$R_{TOT} = R_{central} + R_{peripheral}$$
$$C_{TOT} = C_{central} + C_{peripheral}$$

   where $R_{central}$ and $C_{central}$ are set by the anatomy and tissue properties of the specimen.
2. Three-element Windkessel (RCR) models were coupled to each outlet branch "i", each characterized by a resistance $R^i$ (divided between proximal $R^i_{prox}$ and distal $R^i_{dist}$ resistances) and a compliance $C^i$. Initial estimates for these parameters were obtained as detailed in Xiao et al.[23]. The following method was used to evaluate $R_{peripheral}$ and $C_{peripheral}$ for each of the 11 mice. A simulation was run and the computed ATA flow and pressure waveforms were used to calculate values of $R^{comp}_{TOT}$ and $C^{comp}_{TOT}$. If the discrepancy between these computed values and experimentally-determined $R_{TOT}$ and $C_{TOT}$ was larger than 4%, further iterations were made for $R^i_{prox}$, $R^i_{dist}$ and $C^i$ for all branches. The relation between the parameters of all Windkessel models with the values of resistance and compliance of the entire peripheral vasculature ($R_{peripheral}$, $C_{peripheral}$) is:

$$\frac{1}{R_{peripheral}} = \sum_i \frac{1}{R^i}, \qquad C_{peripheral} = \sum_i C^i \ .$$

Knowledge of $R_{TOT}$, $C_{TOT}$, $R_{peripheral}$, and $C_{peripheral}$ allows one to compute $R_{central}$, $C_{central}$ for each specimen. Lastly, the following regional flow distributions were targeted: 17% of CO to the innominate artery, 10% to the left carotid, and 17% to the IAA[25,26].

**Table 3.3.** Body mass and corresponding adjusted values of cardiac output (CO), total resistance ($R_{TOT}$), and total compliance ($C_{TOT}$) assigned to each computational model via allometric scaling. Body mass (g); CO (ml/min); $R_{TOT}$ (Pa/(mm$^3$/s); $C_{TOT}$ (mm$^3$/Pa).

| **Wild-Type_Male (WT_M)** | | | | | **Wild-Type_Female (WT_F)** | | | | |
|---|---|---|---|---|---|---|---|---|---|
| **Mouse** | **Body** | **CO** | **$R_{TOT}$** | **$C_{TOT}$** | **Mouse** | **Body** | **CO** | **$R_{TOT}$** | **$C_{TOT}$** |
| **WT_M1** | 33 | 14.8 | 44.8 | 0.0067 | **WT_F1** | 23 | 10.5 | 69.0 | 0.0040 |
| **WT_M2** | 38 | 15.6 | 43.2 | 0.0071 | **WT_F2** | 27 | 11.2 | 56.9 | 0.0058 |
| **WT_M3** | 35 | 15.2 | 44.1 | 0.0069 | **WT_F3** | 26 | 11.0 | 59.5 | 0.0053 |
| **mean** | 36 | 15.2 | 44.1 | 0.0069 | **mean** | 25[a] | 10.9[a] | 61.8[a] | 0.0050[a] |
| **std** | 3 | 0.4 | 0.8 | 0.0002 | **Std** | 2 | 0.4 | 6.4 | 0.0009 |
| **Knockout_Male (KO_M)** | | | | | **Knockout_Female (KO_F)** | | | | |
| **Mouse** | **Body** | **CO** | **$R_{TOT}$** | **$C_{TOT}$** | **Mouse** | **Body** | **CO** | **$R_{TOT}$** | **$C_{TOT}$** |
| **KO_M1** | 31 | 10.9 | 47.2 | 0.0056 | **KO_F1** | 25 | 10.3 | 65.5 | 0.0041 |
| **KO_M2** | 30 | 10.9 | 48.3 | 0.0055 | **KO_F2** | 24 | 10.7 | 67.0 | 0.0042 |
| **KO_M3** | 31 | 10.7 | 47.2 | 0.0056 | - | - | - | - | - |
| **mean** | 31[b] | 10.9[b] | 47.5 | 0.0056[b] | **mean** | 24[a] | 10.5 | 66.2[a] | 0.0041[a] |
| **std** | 1 | 0.1 | 0.7 | 0.0001 | **Std** | 1 | 0.3 | 1.1 | 0.0001 |

[a] $p < 0.05$ between M and F of the same genotype; [b] $p < 0.05$ between WT and KO of the same sex.

### 3.2.3 Statistical Analysis

Computed results are presented as mean ± SEM. One-way ANOVA was used to assess differences among the four groups. Post-hoc pairwise comparisons were performed using the Benjamini-Hochberg correction method, with $p < 0.05$ considered significant. All analyses were performed using the open source statistical software R.

### 3.2.4 Pulse Wave Velocity Analysis

*PWV* was calculated as the ratio of the centerline distance between two locations of interest and the corresponding pressure pulse transit time. The transit time was measured using an "intersecting tangent algorithm" that defines the foot of a pressure waveform as the intersection between the horizontal tangent intersecting its diastolic minimum and the tangent to the maximum

systolic gradient[27]. Three commonly used *PWV* metrics were compared: left carotid to iliac artery (CCA-iliac), ascending thoracic aorta to infrarenal abdominal aorta (ATA-IAA), and ascending thoracic aorta to iliac artery (ATA-iliac).

### 3.3 Results

For purposes of illustration, Figure 3.5 summarizes results of computed local (cyclic pressure and flow) and global (*PWV*) hemodynamics based on anatomical models endowed with mouse-specific regional biaxial tissue properties for four representative mice: one male and one female WT (left, grey waveforms and bar plots) and one male and one female KO (right, black waveforms and bar plots). Mouse- and region-specific values of circumferential and axial material stiffness and wall thickness are shown in the center of the figure. The actual computational domains are shown only for WT_F1 and KO_F1, but recall that Figure 3.2 shows all 11 anatomical models. In general, the KO mice exhibited marked increases in aortic length and tortuosity, especially in the ATA and DTA. Figure 3.5 reveals further that, while there are not marked differences in circumferential material stiffness $\mathfrak{C}_{\theta\theta}$ between these WT and KO mice, there is an overall increase in thickness $h$ in KO compared to WT for both sexes and thus increased structural stiffness. Nonetheless, circumferential material stiffness is largest at the pDTA (location C) and smallest at the infrarenal aorta (location F) for all four mice used in this comparison; the axial material stiffness $\mathfrak{C}_{zz}$ is largest at the pDTA (location C) but smallest at the ATA (location B). Computed flow and pressure waveforms are shown in the left and right sides of the figure. While the WT male has a larger CO than its female counterpart, CO is similar between these male and female KOs. The KO mice also show increased central pulse pressures (cPP) for both sexes: 35 vs 48 mmHg for WT and KO males and 32 vs 53 mmHg for WT and KO females. The differences in pulse pressure (PP) between WT and KO mice diminish in the distal part of the aorta where values are comparable across genotypes for both male (30 vs 25 mmHg) and female (28 vs 31 mmHg). As examples, the figure also shows the pressure pulse transit time between the ATA and IAA for the males. ATA-IAA *PWV* is larger for these KO mice, with a more substantial increase for females (4.47 vs 3.16 m/s) compared to the males (4.03 m/s vs 3.85 m/s). In the following, we summarize results for global hemodynamics, regional geometry, wall mechanics and hemodynamics, and pulse wave velocity for all mice constituting all four groups.

**Table 3.4.** Separation of $R_{TOT}$ into central ($R_{central}$) and peripheral ($R_{peripheral}$) vasculature components for all four groups. All values are reported in ($Pa/(mm^3/s)$).

| Wild-Type_Male (WT_M) | | | | | | Wild-Type_Female (WT_F) | | | | | |
|---|---|---|---|---|---|---|---|---|---|---|---|
| **Mouse** | **$R_{TOT}$** | **$R_{central}$** | **% tot** | **$R_{peripheral}$** | **% tot** | **Mouse** | **$R_{TOT}$** | **$R_{central}$** | **% tot** | **$R_{peripheral}$** | **% tot** |
| **WT_M1** | 45.93 | 2.42 | 5 | 43.51 | 95 | **WT_F** | 68.44 | 3.83 | 6 | 65.01 | 94 |
| **WT_M2** | 44.09 | 2.64 | 6 | 41.45 | 94 | **WT_F** | 58.09 | 3.96 | 7 | 54.13 | 93 |
| **WT_M3** | 45.05 | 3.24 | 7 | 41.81 | 93 | **WT_F** | 61.02 | 3.88 | 6 | 58.76 | 94 |
| **mean** | 45.02 | 2.77 | - | 42.25 | - | **mean** | 62.65[a] | 3.89 | - | 58.76[a] | - |
| **std** | 0.92 | 0.43 | - | 1.10 | - | **std** | 5.56 | 0.07 | - | 5.62 | - |
| **Knockout_Male (KO_M)** | | | | | | **Knockout_Female (KO_F)** | | | | | |
| **Mouse** | **$R_{TOT}$** | **$R_{central}$** | **% tot** | **$R_{peripheral}$** | **% tot** | **Mouse** | **$R_{TOT}$** | **$R_{central}$** | **% tot** | **$R_{peripheral}$** | **% tot** |
| **KO_M1** | 48.46 | 6.03 | 12 | 42.42 | 88 | **KO_F1** | 66.54 | 6.52 | 10 | 60.01 | 90 |
| **KO_M2** | 49.42 | 4.68 | 9 | 44.74 | 91 | **KO_F2** | 67.89 | 8.16 | 12 | 59.74 | 88 |
| **KO_M3** | 47.96 | 4.30 | 9 | 43.66 | 91 | **-** | - | - | - | - | - |
| **mean** | 48.61 | 5.01[b] | - | 43.61 | - | **mean** | 67.21[a] | 7.34[ab] | - | 59.88[a] | - |
| **std** | 0.74 | 0.91 | - | 1.16 | - | **std** | 0.96 | 1.16 | - | 0.20 | - |

[a] $p < 0.05$ between M and F of the same genotype; [b] $p < 0.05$ between WT and KO of the same sex.

**Table 3.5.** Separation of $C_{TOT}$ into central ($C_{central}$) and peripheral ($C_{peripheral}$) vasculature components for each specimen. All values are reported in ($mm^3/Pa$).

| Wild-Type_Male (WT_M) | | | | | | Wild-Type_Female (WT_F) | | | | | |
|---|---|---|---|---|---|---|---|---|---|---|---|
| **Mouse** | **$C_{TOT}$** | **$C_{central}$** | **% tot** | **$C_{peripheral}$** | **% tot** | **Mouse** | **$C_{TOT}$** | **$C_{central}$** | **% tot** | **$C_{peripheral}$** | **%** |
| **WT_M1** | 0.0066 | 0.0018 | 27 | 0.0049 | 73 | **WT_F1** | 0.0040 | 0.0020 | 51 | 0.0020 | 49 |
| **WT_M2** | 0.0070 | 0.0011 | 16 | 0.0059 | 84 | **WT_F2** | 0.0059 | 0.0009 | 15 | 0.0051 | 85 |
| **WT_M3** | 0.0069 | 0.0010 | 15 | 0.0059 | 85 | **WT_F3** | 0.0054 | 0.0043 | 80 | 0.0011 | 20 |
| **mean** | 0.0068 | 0.0013 | - | 0.0055 | - | **mean** | 0.0051[a] | 0.0024 | - | 0.0027 | - |
| **std** | 0.0002 | 0.0004 | - | 0.0006 | - | **std** | 0.0010 | 0.0018 | - | 0.0021 | - |
| **Knockout_Male (KO_M)** | | | | | | **Knockout_Female (KO_F)** | | | | | |
| **Mouse** | **$C_{TOT}$** | **$C_{central}$** | **% tot** | **$C_{peripheral}$** | **% tot** | **Mouse** | **$C_{TOT}$** | **$C_{central}$** | **% tot** | **$C_{peripheral}$** | **%** |
| **KO_M1** | 0.0055 | 0.0003 | 6 | 0.0052 | 94 | **KO_F1** | 0.0040 | 0.0005 | 11 | 0.0035 | 89 |
| **KO_M2** | 0.0053 | 0.0007 | 13 | 0.0046 | 87 | **KO_F2** | 0.0040 | 0.0004 | 11 | 0.0036 | 89 |
| **KO_M3** | 0.0055 | 0.0009 | 17 | 0.0046 | 83 | **-** | - | - | - | - | - |
| **mean** | 0.0054 | 0.0006 | - | 0.0048 | - | **mean** | 0.0040[a] | 0.0004 | - | 0.0036 | - |
| **std** | 0.0001 | 0.0003 | - | 0.0004 | - | **std** | 0.0001 | 0.0000 | - | 0.0001 | - |

[a] $p < 0.05$ between M and F of the same genotype; [b] $p < 0.05$ between WT and KO of the same sex.

### 3.3.1 Global Hemodynamics

Table 3.3 lists mouse-specific values of adjusted CO, $R_{TOT}$, $C_{TOT}$ that were assigned to each specimen of the anatomy cohort via allometric scaling. WT males have a statistically higher CO compared to the other groups. Females have a statistically significantly higher $R_{TOT}$ and lower $C_{TOT}$ compared to males. Figure 3.3a seems to suggest that KO_F exhibit a negative trend between CO and body mass, but subjects in this group display little variability in body mass. The WT_F group shows a steep increase in both $R_{TOT}$ and $C_{TOT}$ with body mass.

Figure 3.6a separates $R_{TOT}$ into central ($R_{central}$, in red) and peripheral ($R_{peripheral}$, in blue) components. $R_{peripheral}$ accounts for more than 80% of the total vasculature resistance for all four groups. $R_{TOT}$ and $R_{peripheral}$ are statistically higher in females compared to males of the same genotype. $R_{central}$ is higher in the KO compared to WT of the same sex, which is consistent with the smaller radii and increased tortuosity in the KO. Figure 3.6b separates $C_{TOT}$ into central ($C_{central}$, in red) and peripheral ($C_{peripheral}$, in blue) components. $C_{TOT}$ is smaller in the KO males and females (statistically only for the males), due in part to the increase in structural stiffness and decrease in radii, which result in smaller cyclic strains. $C_{TOT}$ is statistically smaller in the female compared to male of the same genotype. Surprisingly, $C_{peripheral}$ accounts for more than 70% of the total compliance for all groups except WT female. Numerical values are reported in Table 3.4 and 3.5.

We also compared experimental and computed pressures within the ATA for each group (Figure 3.7). The computed pressure decay and PP match well the experimental data. We observe a larger variability in the experimental data compared to the computed results, due in part to a wider range of body mass in the hemodynamics cohort than in the anatomy cohort. For WT_M, body mass ranged between 20-50 g for the hemodynamics cohort vs. 33-38 g for the anatomy cohort. For the remaining groups, the ranges in body mass for the hemodynamics and anatomy cohorts were: 24-39 vs. 30-31 g for KO_M; 22-31 vs. 23-27 g for WT_F; and 25-29 vs. 24-25 g for KO_F. The WT_F group showed the largest variability in the computed pressure due to the stronger dependence of $R_{TOT}$ and $C_{TOT}$ with respect to body mass, as noted above. Specific values of computed systolic ($P_{SYS}$), mean ($P_{MEAN}$), diastolic ($P_{DIAS}$), and central pulse (cPP) pressures are listed in the table embedded in Figure 3.7. There is an increase in cPP in KO groups compared to WT in males and females, though with a fundamental difference: diastolic pressure decreases in the males but systolic pressure increases in the females. Our computational simulations captured the same behavior. Male WT have higher cPP compared to females; conversely, female KO have

higher cPP and $P_{MEAN}$ than males. Finally, note that the Reynolds number in our simulations ranged from Re = 611 in the ATA at peak systole to Re = 0.6 in the intercostal arteries at diastole.

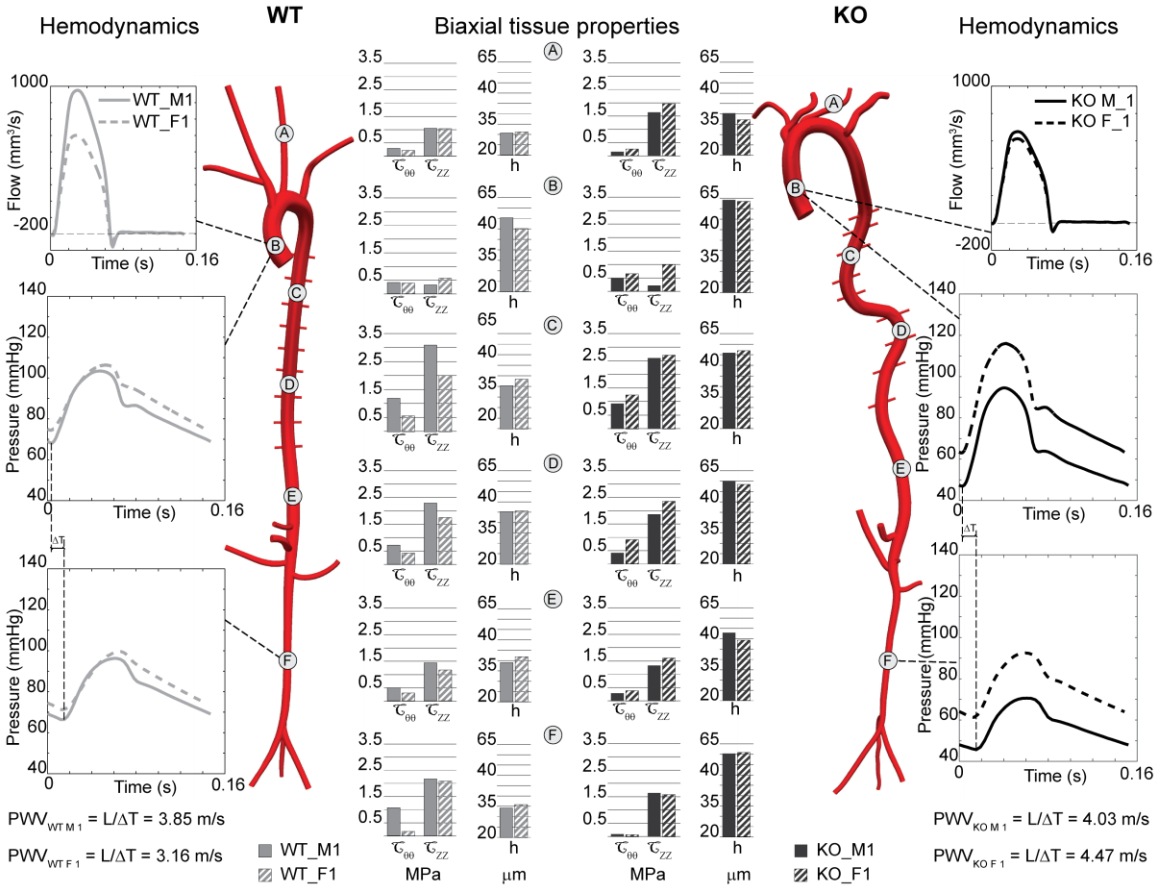


**Figure 3.5.** Computed global and local hemodynamics based on mouse-specific geometric models (two micro-CT models shown for illustrative purposes, WT_F1 and KO_F1) and mouse-specific biaxial tissue properties (biaxial material stiffness and wall thickness) for four representative subjects: WT_M1 and WT_F1 on the left and KO_M1 and KO_F1 on the right. Additional mouse-specific values are in Table 3.1.

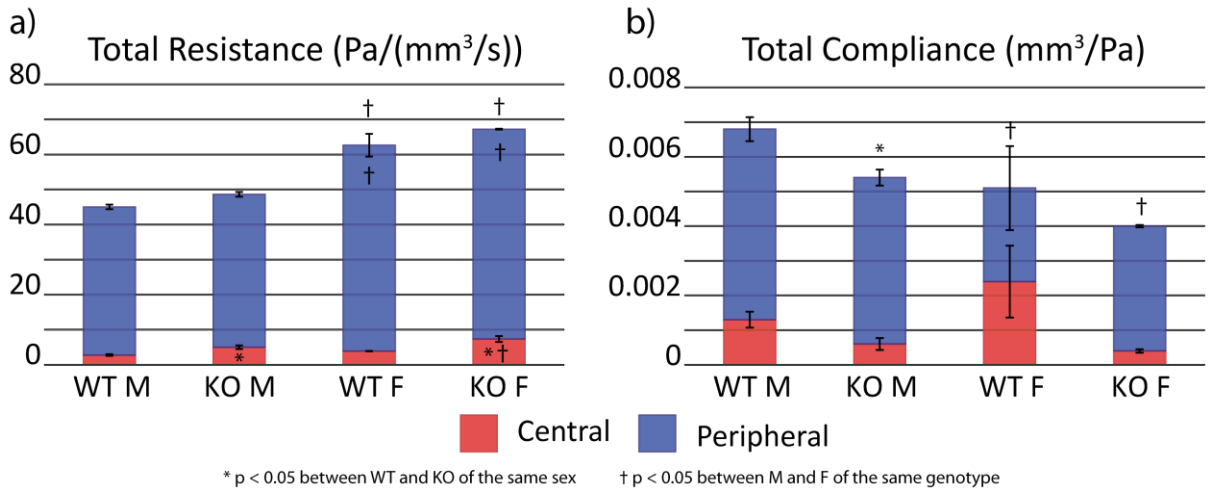


**Figure 3.6**. Separation of $R_{TOT}$ (a) and $C_{TOT}$ (b) into central (red) and peripheral (blue) components for all four groups.

### 3.3.2 Regional Wall Mechanics, Hemodynamics and Inner Diameter Data

Figure 3.8 illustrates $P_{MEAN}$, PP, structural stiffness ($C_{\theta\theta}$**h*), material stiffness ($C_{\theta\theta}$), wall thickness (*h*), and internal diameter (*id*) along the aorta and CCA for the WT (gray bar) and KO (black bar) groups. Numerical values are reported in Figure 3.7 and Tables 3.1, 3.6 and 3.7. $P_{MEAN}$ is the time average of the computed pressure at the locations of interest and it drops along the aorta as expected: male WT and KO have a comparable drop in $P_{MEAN}$ from the ATA to the iliac artery (9 and 10 mmHg, respectively) while female WT have a smaller drop in $P_{MEAN}$ compared to the KO (10 and 16 mmHg, respectively). KO males have statistically smaller $P_{MEAN}$ than WT males and KO females at all locations. Bar plots of the distribution of computed PP reveal an attenuation of the pulse along the aorta in all four groups. As noted earlier, male and especially female KOs have higher PP compared to their WT counterparts in the proximal part of the aorta: WT and KO have ATA PP of 39 vs 44 mmHg, respectively, for the male and 30 vs 54 mmHg, respectively, for the female. Differences in PP between WT and KO mice diminish in the distal part of the aorta. Iliac artery PP is slightly larger in the WT than the KO in males (23 vs 19 mmHg) but identical for the females (19 vs 19 mmHg). KO females have statistically higher PP than KO males and WT females at all locations except the iliac artery. Mouse-specific values of $C_{\theta\theta}$ and *h* were determined from experimental data on wall mechanics and assigned to the different locations along the arterial tree, as explained in Section 3.2.2. All four groups have a similar distribution of $C_{\theta\theta}$**h* along the aorta: a peak value at the pDTA and a gradual decrease in the distal part of the aorta with the smallest values at the IAA and iliac artery. KO groups exhibit higher $C_{\theta\theta}$**h* than WT in the proximal aorta but an opposite trend at the IAA, iliac, and carotid artery for both males and females. Furthermore, males have overall higher $C_{\theta\theta}$**h* than females for the WT groups; conversely, females have higher $C_{\theta\theta}$**h* than males in the KO. $C_{\theta\theta}$ have a similar distribution as $C_{\theta\theta}$**h* along the aorta for all four groups. For the males, WT and KO alternate higher values between the two groups at different locations. KO females exhibit higher values in the proximal part of the aorta and lower values in the distal part compared to WT. KO females have statistically higher $C_{\theta\theta}$**h* and $C_{\theta\theta}$ at the ATA compared to WT female and KO male. Wall thickness *h* shows a marked increase for the KO groups compared to WT along the entire aorta for both males and females. The higher values of *h* in KO groups are statistically significant at all locations except at the ATA and CCA for the females. Inner diameter (*id*) values were extracted from the anatomy reconstructed from the micro-

CT data as explained in Section 3.2.2. *Id* is overall smaller in KO compared to WT mice. Figure 3.9 further compares experimental and computed values of diameter distension ($d_{systole}$-$d_{diastole}$)/$d_{diastole}$ at the ATA, SAA, IAA and CCA for each group.

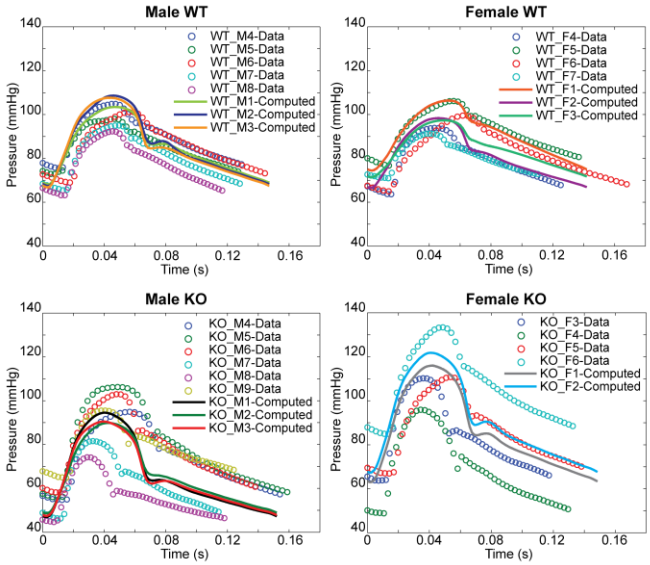


| WT_M | | | | | WT_F | | | | |
|---|---|---|---|---|---|---|---|---|---|
| Mouse | $P_{MEAN}$ | $P_{SYS}$ | $P_{DIAS}$ | cPP | Mouse | $P_{MEAN}$ | $P_{SYS}$ | $P_{DIAS}$ | cPP |
| WT M1 | 80 | 103 | 68 | 35 | WT F1 | 85 | 106 | 74 | 32 |
| WT M2 | 81 | 109 | 67 | 41 | WT F2 | 77 | 98 | 67 | 32 |
| WT M3 | 80 | 108 | 67 | 41 | WT F3 | 80 | 97 | 71 | 26 |
| mean | 80 | 107 | 67 | 39 | mean | 81 | 101 | 71 | 30[a] |
| std | 1 | 3 | 1 | 3 | std | 4 | 5 | 4 | 3 |
| KO_M | | | | | KO_F | | | | |
| Mouse | $P_{MEAN}$ | $P_{SYS}$ | $P_{DIAS}$ | cPP | Mouse | $P_{MEAN}$ | $P_{SYS}$ | $P_{DIAS}$ | cPP |
| KO M1 | 63 | 95 | 47 | 48 | KO F1 | 81 | 116 | 63 | 53 |
| KO M2 | 62 | 90 | 49 | 41 | KO F2 | 85 | 122 | 67 | 54 |
| KO M3 | 62 | 90 | 47 | 43 | - | - | - | - | - |
| mean | 62[b] | 92[b] | 48[b] | 44 | mean | 83[a] | 119 | 65[ab] | 51[ab] |
| std | 1 | 3 | 1 | 3 | std | 3 | 4 | 3 | 1 |

[a] $p < 0.05$ between M and F of the same genotype

[b] $p < 0.05$ between WT and KO of the same sex

**Figure 3.7.** Comparison of experimental (circles) and computed (solid lines) pressure waveforms within the ATA (section B in Figure 3.5) for all four groups ($n$ = 4-5 mice per hemodynamics cohort, n = 2-3 per anatomy cohort). The embedded table lists values of computed mean ($P_{MEAN}$), systolic ($P_{SYS}$), diastolic ($P_{DIAS}$), and central pulse (cPP) pressure within the ATA. All values are reported in mmHg. We aimed to reproduce murine hemodynamics under anesthesia. Notice the greater specimen-to-specimen variation in KO compared to WT mice, independent of sex.

**Table 3.6**. Computed mean ($P_{MEAN}$), pulse (PP), systolic ($P_{SYS}$), and diastolic ($P_{DIAS}$) pressures – all in mmHg – for all four groups (male and female, WT and KO) at six locations: pDTA, dDTA, SAA, IAA, iliac artery, and CCA.

| | | Wild Type_Male (WT_M) | | | | | Wild Type_Female (WT_F) | | | | |
|---|---|---|---|---|---|---|---|---|---|---|---|
| | | **WT_M** | **WT_M** | **WT_M** | **mean** | **std** | **WT_F1** | **WT_F2** | **WT_F3** | **mean** | **std** |
| **pDTA** | **$P_{MEAN}$** | 79 | 80 | 78 | 79 | 1.2 | 84 | 76 | 78 | 80 | 4.2 |
| | **PP** | 34 | 39 | 35 | 36 | 2.8 | 31 | 29 | 23 | 28[a] | 4.0 |
| | **$P_{SYS}$** | 101 | 106 | 102 | 103 | 2.9 | 105 | 96 | 94 | 98 | 5.8 |
| | **$P_{DIAS}$** | 68 | 67 | 66 | 67 | 0.6 | 74 | 66 | 71 | 70 | 3.8 |
| **dDTA** | **$P_{MEAN}$** | 78 | 79 | 77 | 78 | 1.1 | 83 | 75 | 77 | 79 | 4.3 |
| | **PP** | 32 | 37 | 33 | 34 | 18 | 30 | 28 | 22 | 27[a] | 4.4 |
| | **$P_{SYS}$** | 99 | 104 | 99 | 101 | 2.6 | 104 | 94 | 92 | 96 | 6.3 |
| | **$P_{DIAS}$** | 67 | 67 | 66 | 67 | 0.6 | 73 | 66 | 70 | 70 | 3.7 |
| **SAA** | **$P_{MEAN}$** | 77 | 79 | 76 | 77 | 1.3 | 83 | 74 | 76 | 78 | 4.3 |
| | **PP** | 31 | 36 | 31 | 32 | 2.8 | 30 | 27 | 21 | 26 | 4.4 |
| | **$P_{SYS}$** | 98 | 102 | 97 | 99 | 3.0 | 103 | 92 | 91 | 95 | 6.5 |
| | **$P_{DIAS}$** | 67 | 67 | 66 | 67 | 0.6 | 72 | 65 | 69 | 69 | 3.6 |
| **IAA** | **$P_{MEAN}$** | 76 | 77 | 74 | 76 | 1.4 | 81 | 72 | 74 | 76 | 4.5 |
| | **PP** | 30 | 33 | 29 | 31 | 2.3 | 28 | 23 | 21 | 24[a] | 3.8 |
| | **$P_{SYS}$** | 96 | 99 | 93 | 96 | 2.8 | 100 | 88 | 88 | 92 | 6.7 |
| | **$P_{DIAS}$** | 66 | 66 | 65 | 66 | 0.8 | 71 | 64 | 67 | 68 | 3.5 |
| **Iliac** | **$P_{MEAN}$** | 75 | 72 | 69 | 72 | 3.0 | 77 | 65 | 71 | 71 | 6.1 |
| | **PP** | 27 | 25 | 18 | 23 | 4.6 | 26 | 13 | 20 | 19 | 6.6 |
| | **$P_{SYS}$** | 93 | 89 | 81 | 87 | 6.0 | 94 | 73 | 85 | 84 | 10.4 |
| | **$P_{DIAS}$** | 66 | 64 | 63 | 64 | 1.6 | 68 | 61 | 65 | 65 | 3.9 |
| **CCA** | **$P_{MEAN}$** | 77 | 80 | 79 | 79 | 1.5 | 83 | 76 | 79 | 79 | 3.3 |
| | **PP** | 32 | 40 | 38 | 37 | 3.7 | 31 | 30 | 25 | 29[a] | 2.7 |
| | **$P_{SYS}$** | 99 | 107 | 104 | 103 | 3.9 | 103 | 96 | 96 | 98 | 4.2 |
| | **$P_{DIAS}$** | 66 | 67 | 67 | 67 | 0.2 | 72 | 66 | 70 | 70 | 3.3 |

**Table 3.6 continued**

| | | Knockout_Male (KO_M) | | | | | Knockout_Female (KO_F) | | | | |
|---|---|---|---|---|---|---|---|---|---|---|---|
| | | KO_M | KO_M | KO_M | mean | std | KO_F1 | KO_F2 | - | mean | std |
| pDTA | $P_{MEAN}$ | 61 | 60 | 60 | $60^{b}$ | 0.4 | 78 | 83 | - | $81^{a}$ | 3.5 |
| | PP | 41 | 36 | 38 | 38 | 2.9 | 46 | 48 | - | $47^{ab}$ | 1.1 |
| | $P_{SYS}$ | 88 | 84 | 85 | $86^{b}$ | 2.2 | 109 | 115 | - | $112^{ab}$ | 4.2 |
| | $P_{DIAS}$ | 47 | 48 | 47 | $47^{b}$ | 0.8 | 63 | 67 | - | $65^{a}$ | 3.1 |
| dDTA | $P_{MEAN}$ | 58 | 58 | 58 | $58^{b}$ | 0.4 | 77 | 82 | - | $79^{a}$ | 3.6 |
| | PP | 33 | 31 | 31 | 32 | 1.1 | 43 | 44 | - | $43^{ab}$ | 0.8 |
| | $P_{SYS}$ | 80 | 79 | 78 | $79^{b}$ | 0.6 | 105 | 111 | - | $108^{ab}$ | 4.1 |
| | $P_{DIAS}$ | 46 | 48 | 47 | $47^{b}$ | 0.7 | 62 | 67 | - | $65^{a}$ | 3.3 |
| SAA | $P_{MEAN}$ | 56 | 56 | 56 | $56^{b}$ | 0.1 | 75 | 80 | - | $78^{a}$ | 3.9 |
| | PP | 30 | 27 | 28 | 28 | 1.4 | 38 | 40 | - | $39^{ab}$ | 1.1 |
| | $P_{SYS}$ | 76 | 75 | 75 | $75^{b}$ | 1.0 | 100 | 107 | - | $104^{a}$ | 4.6 |
| | $P_{DIAS}$ | 46 | 47 | 47 | $47^{b}$ | 0.5 | 62 | 67 | - | $65^{a}$ | 3.5 |
| IAA | $P_{MEAN}$ | 54 | 55 | 55 | $55^{b}$ | 0.6 | 72 | 76 | - | $74^{a}$ | 2.8 |
| | PP | 25 | 25 | 24 | $25^{b}$ | 0.5 | 31 | 29 | - | $30^{b}$ | 1.8 |
| | $P_{SYS}$ | 71 | 72 | 71 | $71^{b}$ | 0.6 | 92 | 95 | - | $94^{a}$ | 1.6 |
| | $P_{DIAS}$ | 46 | 47 | 47 | $46^{b}$ | 0.6 | 61 | 66 | - | $64^{a}$ | 3.4 |
| Iliac | $P_{MEAN}$ | 50 | 53 | 53 | $52^{b}$ | 1.8 | 65 | 70 | - | $67^{a}$ | 3.2 |
| | PP | 16 | 21 | 19 | 19 | 2.6 | 19 | 18 | - | 19 | 0.5 |
| | $P_{SYS}$ | 60 | 67 | 66 | 64 | $3.5^{b}$ | 78 | 82 | - | $80^{a}$ | 2.9 |
| | $P_{DIAS}$ | 44 | 46 | 46 | 46 | $1.0^{b}$ | 59 | 64 | - | $61^{a}$ | 3.4 |
| CCA | $P_{MEAN}$ | 58 | 61 | 60 | $59^{b}$ | 1.6 | 77 | 81 | - | $79^{a}$ | 2.4 |
| | PP | 39 | 38 | 40 | 39 | 0.7 | 49 | 42 | - | $45^{b}$ | 4.6 |
| | $P_{SYS}$ | 84 | 86 | 86 | $86^{b}$ | 1.4 | 110 | 109 | - | $109^{ab}$ | 0.7 |
| | $P_{DIAS}$ | 45 | 48 | 46 | $46^{b}$ | 1.7 | 61 | 67 | - | $64^{a}$ | 4.0 |

[a] $p < 0.05$ between M and F of the same genotype; [b] $p < 0.05$ between WT and KO of the same sex

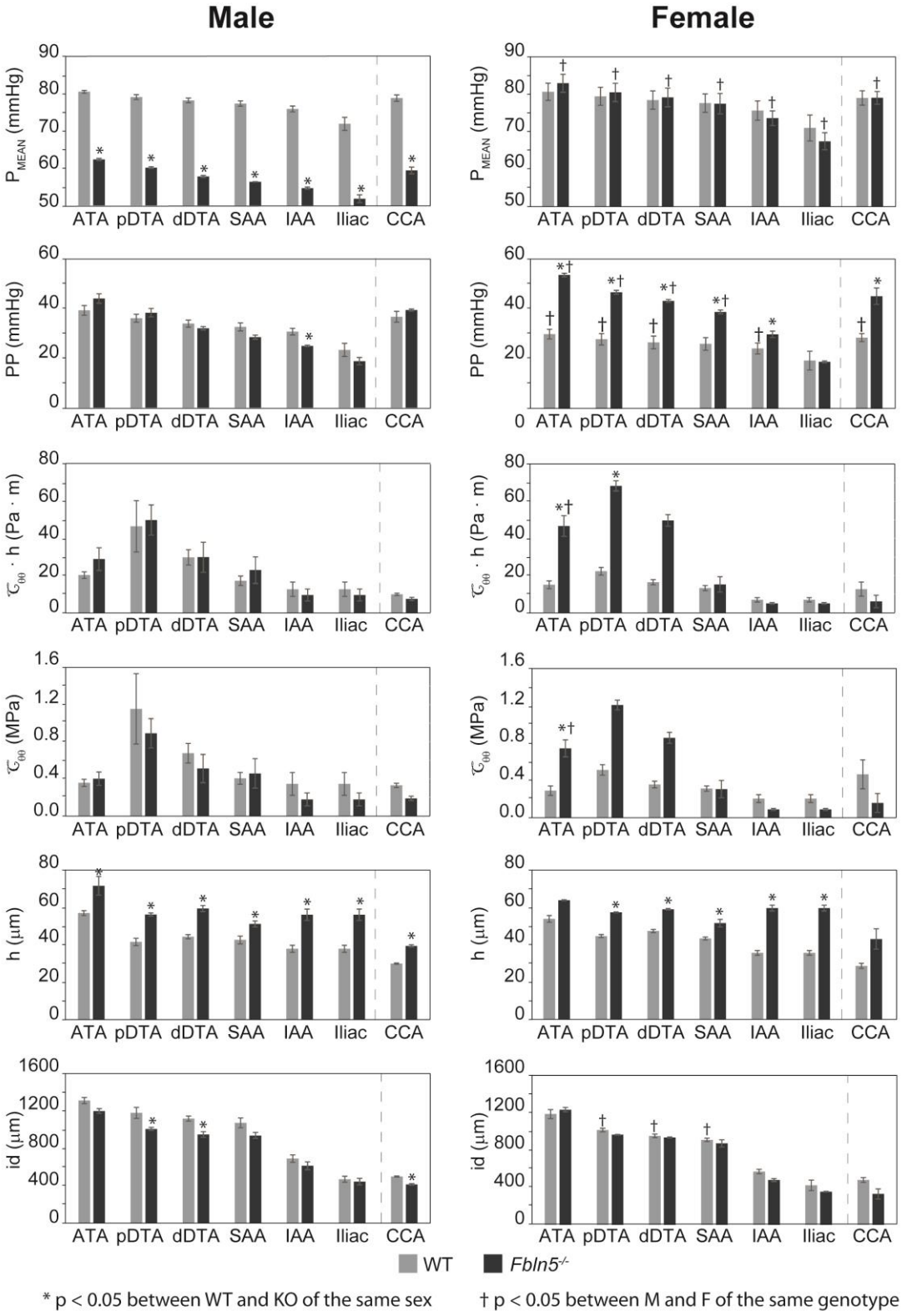


**Figure 3.8.** Regional values (mean ± SEM) of mean blood pressure ($P_{MEAN}$), pulse pressure (PP), structural stiffness ($\mathcal{T}_{\theta\theta}$**h*), circumferential material stiffness ($\mathcal{T}_{\theta\theta}$), wall thickness (*h*), and internal diameter (*id*) for male and female WT (gray bars) and KO (black bars) mice.

**Table 3.7.** Values of internal diameter (id), in μm, measured from 3D anatomical models at ATA, pDTA and dDTA, SAA, IAA, iliac artery and CCA.

| | Wild Type_Male (WT_M) | | | | | Wild Type_Female (WT_F) | | | | |
|---|---|---|---|---|---|---|---|---|---|---|
| | **WT_M** | **WT_M** | **WT_M** | **mean** | **std** | **WT_F1** | **WT_F2** | **WT_F3** | **mean** | **std** |
| **ATA** | 1355 | 1331 | 1245 | 1310 | 58 | 1275 | 1129 | 1134 | 1179 | 83 |
| **pDTA** | 1207 | 1261 | 1064 | 1177 | 102 | 1030 | 1028 | 970 | 1009[a] | 34 |
| **dDTA** | 1130 | 1155 | 1064 | 1117 | 47 | 976 | 952 | 912 | 947[a] | 32 |
| **SAA** | 1084 | 1155 | 974 | 1071 | 91 | 934 | 872 | 906 | 904[a] | 31 |
| **IAA** | 762 | 668 | 631 | 687 | 68 | 553 | 535 | 612 | 567 | 40 |
| **Iliac** | 519 | 407 | 471 | 466 | 56 | 381 | 348 | 530 | 419 | 97 |
| **CCA** | 483 | 497 | 503 | 494 | 10 | 431 | 485 | 517 | 478 | 43 |
| | **Knockout_Male (KO_M)** | | | | | **Knockout_Male (KO_M)** | | | | |
| | **KO_M** | **KO_M** | **KO_M** | **mean** | **std** | **KO_F1** | **KO_F2** | **KO_F3** | **mean** | **std** |
| **ATA** | 1228 | 1145 | 1217 | 1197 | 45 | 1202 | 1249 | - | 1226 | 33 |
| **pDTA** | 1013 | 972 | 1031 | 1005[b] | 30 | 963 | 956 | - | 960 | 5 |
| **dDTA** | 934 | 903 | 1001 | 946[b] | 50 | 936 | 924 | - | 930 | 8 |
| **SAA** | 901 | 903 | 1001 | 935 | 57 | 905 | 828 | - | 867 | 54 |
| **IAA** | 556 | 691 | 583 | 610 | 71 | 461 | 492 | - | 477 | 22 |
| **Iliac** | 419 | 394 | 509 | 441 | 60 | 347 | 357 | - | 352 | 7 |
| **CCA** | 397 | 424 | 411 | 411[b] | 14 | 381 | 275 | - | 328 | 75 |

[a] $p < 0.05$ between M and F of the same genotype; [b] $p < 0.05$ between WT and KO of the same sex

Figure 3.10 shows computed pressure (left) and flow (right) waveforms for WT (dashed line) and KO (solid line) males (left column) and females (right column) at 6 different locations: ATA, SAA, IAA, left CCA, left renal artery, and right iliac artery. Visualization of the pressure waveforms shows qualitatively similar details as discussed above, but we observe further the different specimens instead of just mean values analyzed in Figure 3.8. Results from Figure 3.8 are again evident: KO males exhibit lower $P_{MEAN}$ compared to WT, while the WT and KO females have comparable $P_{MEAN}$. KO models have an augmented cPP (both for male and especially female) compared to WT. The PP decreases down the length of the murine aorta and there are no differences in PP between WT and KO at the IAA. In the renal artery, WT and KO males have a

PP of 31 and 24 mmHg, respectively, while WT and KO females have a PP of 24 and 32 mmHg, respectively. There are not substantial differences in flow waveforms between WT and KO even though male WT have higher CO. There is a good qualitative agreement between our computed flow waveform and the velocity reported by Hartley et al. [28]. We can observe backflow in the ATA and SAA, but not in the IAA, CCA, and renal arteries.

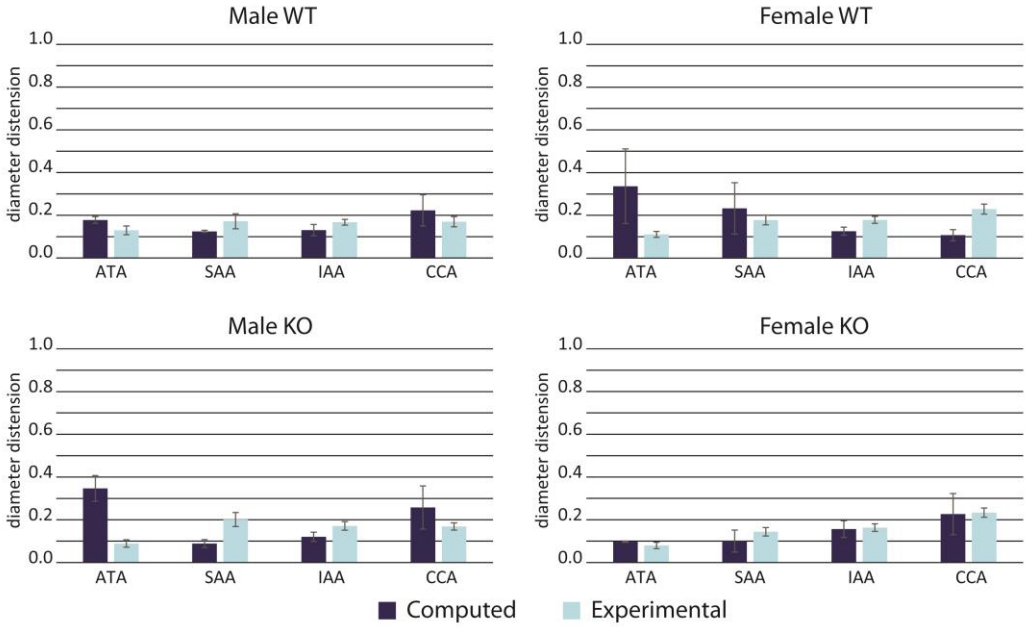


**Figure 3.9.** Comparison of computed (dark blue) and experimental (light blue) values of diameter distension. Diameter distension is calculated as $(d_{systole}-d_{diastole})/d_{diastole}$ and reported at the ascending thoracic aorta (ATA), suprarenal abdominal aorta (SAA), infrarenal abdominal aorta (IAA), and common carotid artery (CCA) for each group.

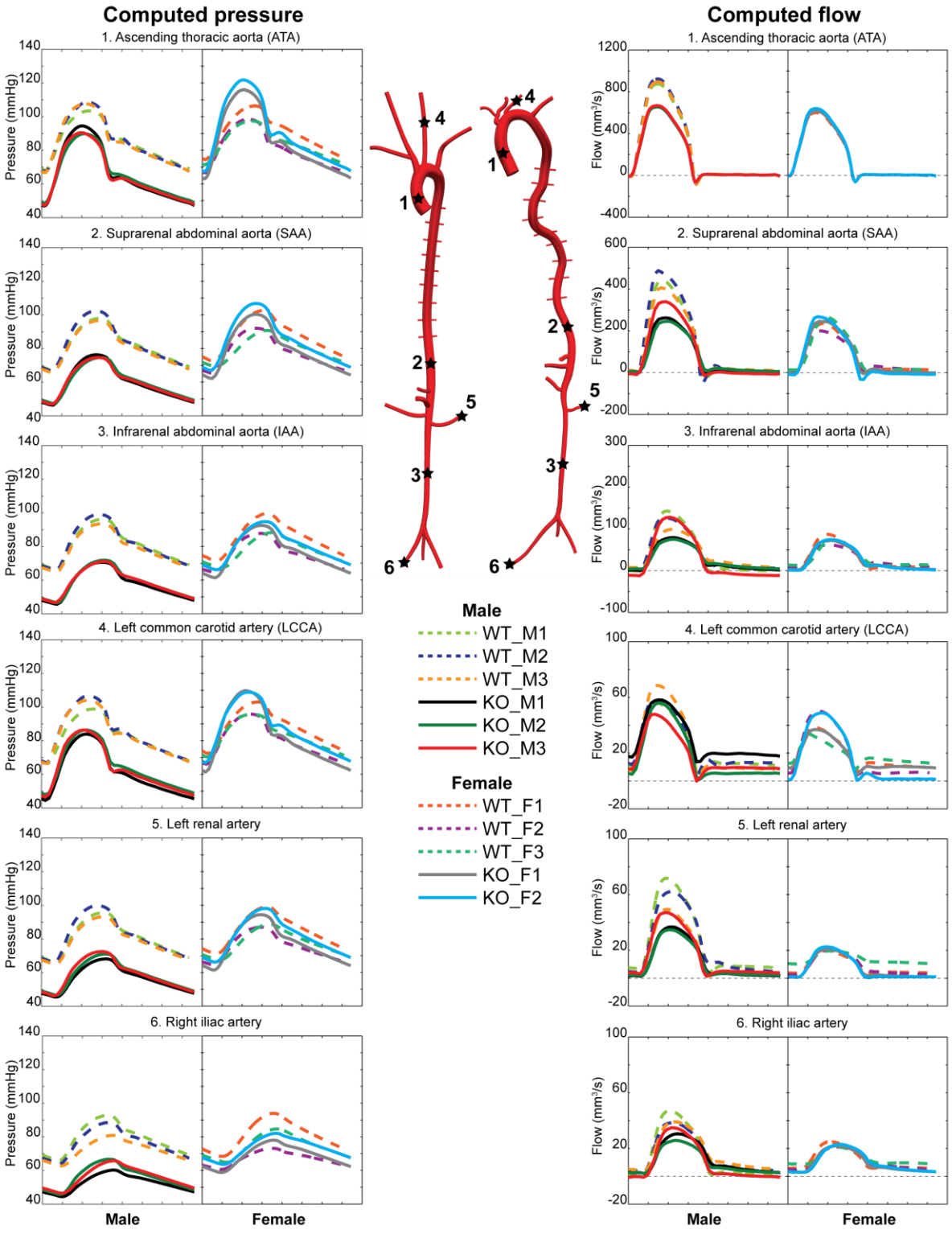


**Figure 3.10.** Computed pressure (left) and flow (right) waveforms for WT (dashed lines; for, example, left anatomical model) vs KO (solid lines; for example, right anatomical model) for both males (first column) and females (second column) at 6 different locations: 1. ascending thoracic aorta (ATA), 2. suprarenal abdominal aorta (SAA), 3. infrarenal abdominal aorta (IAA), 4. left common carotid artery (LCCA), 5. left renal artery, and 6. right iliac artery.

**Table 3.8.** Values of aortic length (L) in mm, aortic pulse transit time (PTT) in ms, and pulse wave velocity (PWV) in m/s, from left carotid to iliac artery (CCA-iliac), from aortic root to infrarenal abdominal aorta (ATA-IAA), and from aortic root to iliac bifurcation (ATA-iliac) for all four groups.

| | | Wild-Type_Male (WT_M) | | | | | Wild-Type_Female (WT_F) | | | | |
|---|---|---|---|---|---|---|---|---|---|---|---|
| | | WT_M1 | WT_M2 | WT_M3 | mean | std | WT_F1 | WT_F2 | WT_F3 | mean | std |
| L | CCA-iliac | 56.2 | 55.9 | 51.6 | 54.6 | 2.5 | 50.8 | 51.9 | 37.0 | 46.6 | 8.3 |
| | ATA-IAA | 42.7 | 44.5 | 43.2 | 43.5 | 0.9 | 38.5 | 40.0 | 42.6 | 40.3[a] | 2.0 |
| | ATA-iliac | 52.2 | 55.2 | 53.5 | 53.6 | 1.5 | 48.4 | 52.3 | 55.0 | 51.9 | 3.3 |
| PTT | CCA-iliac | 9.7 | 12.2 | 14.9 | 12.3 | 2.6 | 14.7 | 15.7 | 20.9 | 17.1 | 3.3 |
| | ATA-IAA | 11.1 | 10.9 | 12.0 | 11.3 | 0.6 | 12.2 | 11.9 | 17.8 | 14.0 | 3.3 |
| | ATA-iliac | 13.6 | 14.3 | 16.9 | 14.9 | 1.7 | 19.6 | 18.3 | 23.8 | 20.6 | 2.9 |
| PWV | CCA-iliac | 5.8 | 4.6 | 3.5 | 4.6 | 1.2 | 3.5 | 3.3 | 1.8 | 2.8 | 0.9 |
| | ATA-IAA | 3.9 | 4.1 | 3.6 | 3.8 | 0.2 | 3.2 | 3.4 | 2.4 | 3.0 | 0.5 |
| | ATA-iliac | 3.8 | 3.9 | 3.2 | 3.6 | 0.04 | 2.5 | 2.9 | 2.3 | 2.5[a] | 0.3 |
| | | Knockout_Male (KO_M) | | | | | Knockout_Female (KO_F) | | | | |
| | | KO_M1 | KO_M2 | KO_M3 | mean | std | KO_F1 | KO_F2 | - | mean | std |
| L | CCA-iliac | 59.0 | 51.6 | 62.8 | 57.8 | 5.7 | 62.9 | 60.3 | - | 61.6 | 1.8 |
| | ATA-IAA | 49.2 | 49.4 | 51.8 | 50.1[b] | 1.4 | 50.1 | 49.5 | - | 49.8[b] | 0.5 |
| | ATA-iliac | 60.4 | 58.6 | 64.3 | 61.1[b] | 2.9 | 61.0 | 61.2 | - | 61.1[b] | 0.1 |
| PTT | CCA-iliac | 14.9 | 12.6 | 16.2 | 14.6 | 1.8 | 15.9 | 15.4 | - | 15.7 | 0.4 |
| | ATA-IAA | 12.2 | 13.0 | 10.5 | 11.9 | 1.3 | 11.2 | 13.7 | - | 12.5 | 1.8 |
| | ATA-iliac | 17.2 | 15.0 | 17.8 | 16.7 | 1.5 | 18.2 | 20.5 | - | 19.4 | 1.6 |
| PWV | CCA-iliac | 4.0 | 4.1 | 3.9 | 4.0 | 0.1 | 4.0 | 3.9 | - | 3.9 | 0.0 |
| | ATA-IAA | 4.0 | 3.8 | 4.9 | 4.3 | 0.6 | 4.5 | 3.6 | - | 4.0 | 0.6 |
| | ATA-iliac | 3.5 | 3.9 | 3.6 | 3.7 | 0.2 | 3.4 | 3.0 | - | 3.2 | 0.3 |

[a] $p < 0.05$ between M and F of the same genotype, [b] $p < 0.05$ between WT and KO of the same sex.

### 3.3.3 Computed Pulse Wave Velocity

We calculated three different commonly used values of *PWV*: CCA-iliac, ATA-IAA and ATA-iliac; specific values are in Table 3.8 along with path length and computed transit time. In Figure 3.10 we compare values of computed *PWV* with corresponding values of spatially averaged structural stiffness (i.e., a weighted mean within the segments of interests, considering the length of each segment as a weight). KO groups tend to have higher structural stiffness than WT groups

of the same sex. WT males have higher structural stiffness than WT females; conversely, KO males have lower structural stiffness than KO females. Computed *PWV* does not follow the same trends as structural stiffness. CCA-iliac stiffness increases by 14% from WT to KO in males but the associated *PWV* decreases by 14%. A 14% increase for ATA-iliac stiffness results in only a 2% increase in *PWV*. Furthermore, the higher values of structural stiffness of KO females compared to KO males is not captured by any of the *PWV* metrics. *PWV* depends on many factors, including arterial properties, geometries, and flow as well as perivascular support. Furthermore, we found that heterogeneity of the structural stiffness of the arterial wall contributes to changes in the measured *PWV* [29–33].

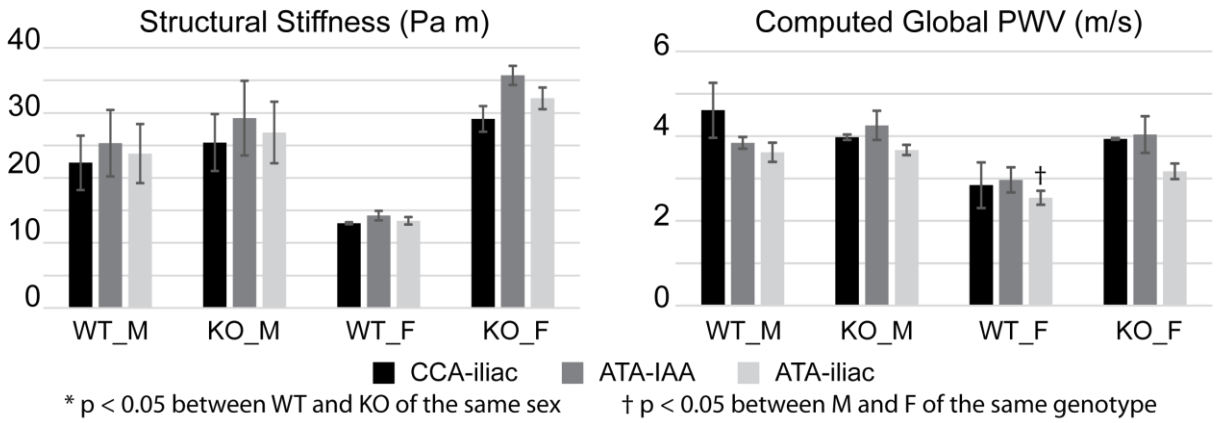


**Figure 3.11.** Values (mean ± SEM) of measured structural stiffness (left) and computed *PWV* (right) for all four groups. Both quantities are calculated for three different portions of the arterial tree: left common carotid artery to iliac artery (CCA-iliac), ascending thoracic aorta to infrarenal abdominal aorta (ATA-IAA), and ascending thoracic aorta to iliac artery (ATA-iliac).

### 3.3.4 Effects of Structural Stiffness Heterogeneity on *PWV*

We want to quantify the effects of spatial heterogeneity in wall structural stiffness on the measured *PWV*. We used Womersley's deformable wall analytical solution[29,34] and vascular impedance[32] theories to compute *PWV* in an elastic tube consisting of two segments of different homogenous wall properties of the same length: segment 1 and segment 2 (see 3.12a). A flow waveform $Q_0(t)$ was prescribed at the inlet face. The characteristic impedance for each segment was computed. Pressure and flow were assumed to have forward and backward components due to wave reflections[33]. Assuming no outlet wave reflections (i.e. terminal reflection coefficient $\Gamma^{(2)}=0$), we computed the input impedance of the second segment. Then, at the interface between segments we assumed continuity of pressure and flow, thus the terminal impedance of segment 1 was equal to the input impedance of segment 2. The reflection coefficient at the interface ($\Gamma^{(1)}$) and the input impedance at the inlet were then computed. Lastly, pressure and flow fields were

expressed in terms of the reflection coefficients and characteristic impedance, and ultimately transformed into the domain.

Table 3.9 reports the parameters used for this study. We considered two cases, where the stiffness of segments 1 and 2 were defined as:

- **Case 1** (E1 < E2 ): E1 = (1 - *a*)*E, E2 = (1 + *a*)*E
- **Case 2** (E1 > E2 ): E1 = (1 + *a*)*E, E2 = (1 - *a*)*E

The heterogeneity index *a* varied between 0 and 0.6 resulting in a maximum difference between $E_1$ and $E_2$ of 120%. Note that in all cases the average stiffness of the entire vessel E is constant.

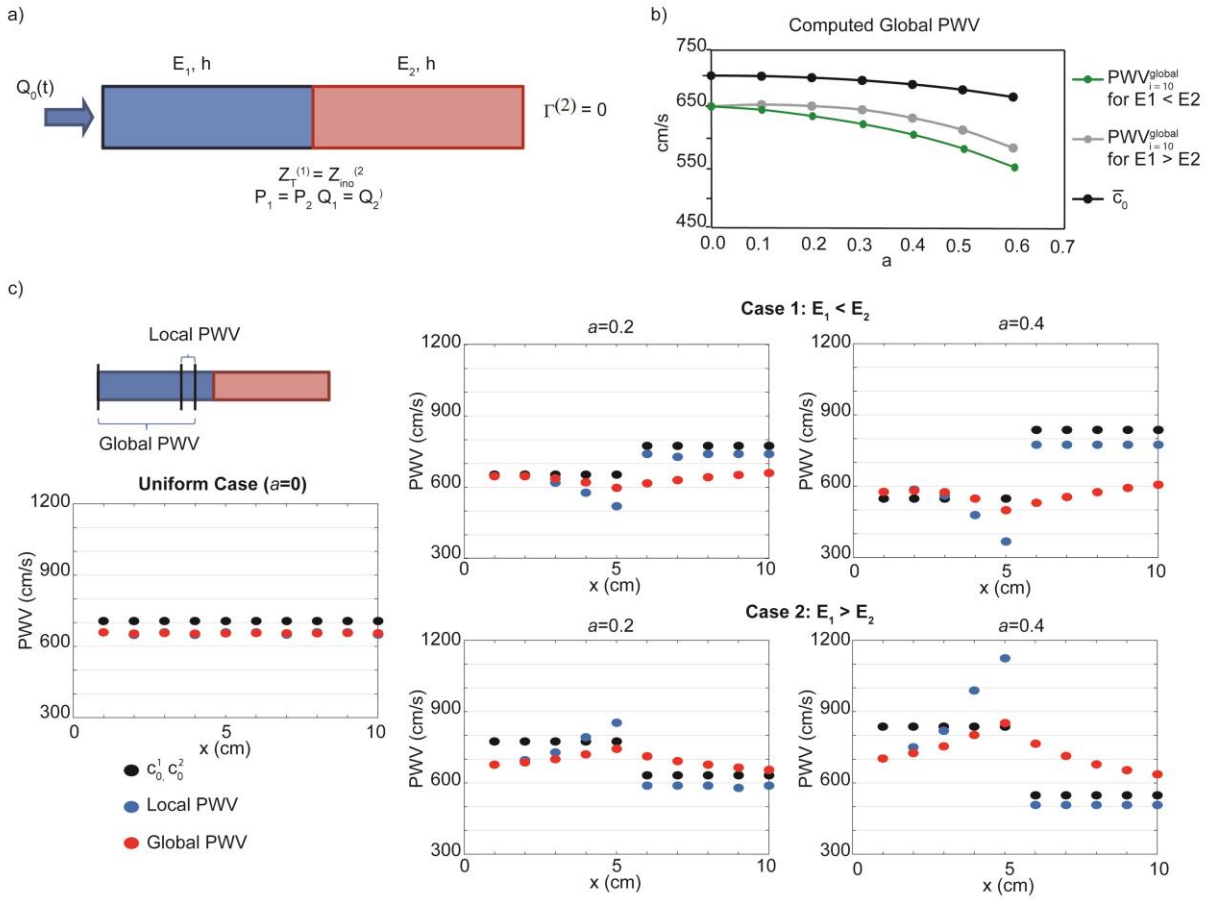


**Figure 3.12.** a) Schematic of the test performed: a longitudinally constrained vessel divided into two segments of the same length; b) Computed values of $PWV_{i=10}^{global}$ at different values of index heterogeneity *a* for case 1 (green), case 2 (gray) and Moens-Korteweg *PWV* $\bar{c_0}$ (black) estimates; c) Spatial distribution of local and global *PWV* and $c_0^1, c_0^2$ for segments 1 and 2, respectively for *a*=0, *a*=0.2, *a*=0.4 for both case 1 and 2.

The Moens-Korteweg estimate of *PWV* ($c_0$) for a homogenous vessel is $c_0 = \sqrt{Eh/2Rp}$. Similarly, the Moens-Korteweg *PWV* values ($c_0^1, c_0^2$) were obtained for each vessel segment. *PWV* was defined as the average value of the Moens-Korteweg approximation ($\bar{c_0}$) for the entire vessel:

$$c_0^1 = \sqrt{\frac{(1-a)Eh}{2Rp}},\ \ c_0^2 = \sqrt{\frac{(1+a)Eh}{2Rp}},$$

$$\bar{c_0} = 0.5(c_0^1 + c_0^2) = 0.5c_0\left(\sqrt{(1-a)} + \sqrt{(1+a)}\right);$$

It is easy to see that $\bar{c_0}$ predicts a reduction in *PWV* with increased values of heterogeneity.

Spatial distributions of *PWV* down the vessel were computed by dividing the vessel into 10 sections of 1 cm each. *PWV* was obtained as the ratio between distance and transit time between the flow waveforms at two locations. We defined *PWV* with respect to the inlet as "global *PWV*", or with respect to previous discrete location as "local *PWV*", according to the following:

$$PWV_i^{local} = \frac{\Delta l_i}{\Delta t^{q_i - q_{i-1}}}, \qquad PWV_i^{global} = \frac{l_i}{\Delta t^{q_i - q_1}}, \qquad \Delta l_i = l_i - l_{i-1}$$

where $\Delta t^{q_i - q_{i-1}}$ is the transit time between the flow waveforms extracted at location $i$ and $i-1$, for $i = 1,..10$.

Figure 3.12b shows the values of global $PWV_{i=10}^{global}$ for different values of *a*. For case 1 (green line), *PWV* decreased with increased level of heterogeneity. When *a*=0.6, *PWV* decreased by 16% compared to the uniform case (*a*=0). For case 2 (gray line) *PWV* was virtually constant for values of $a \leq 0.2$ and decreased by 10% for *a*=0.6. The dependence of $\bar{c_0}$ on *a* is also shown in the plot. These results show that, despite the spatial average of the stiffness of the entire vessel (E) being constant, values of computed and theoretical *PWV* decreased with increased heterogeneity of structural stiffness. The computed values of *PWV* show a higher decrease compared to the uniform case (a=0) than the Moens-Korteweg estimate of *PWV*.

Figure 3.12c shows the spatial distribution of Moens-Korteweg *PWV* ($c_0^1, c_0^2$), local ($PWV_i^{local}$) and global ($PWV_i^{global}$) pulse wave velocities along the vessel for cases 1 and 2. For the uniform case (*a*=0), local and global *PWV* are equal and constant along the vessel; we also observed that in this case $c_0^1 = c_0^2 = c_0 = \bar{c_0}$ overestimates the computed local and global *PWV*. For case 1 when *a*=0.2 local *PWV* decreased in the first segment and was constant in the second segment. Local *PWV* slowed down in the first segment which is due to wave reflections at the interface between segments. Another contributor to this *PWV* slowdown is the dispersion of the wall deformation wave caused by the stiffness difference at the interface. The same pattern was observed when *a*=0.4, with a lower value of local *PWV* at the end of segment 1 and higher values of local *PWV* in segment 2. For case 2, we observed opposite trends: local *PWV* increased down

the length of segment 1, whereas in segment 2 displayed a constant value. The local increase of *PWV* can be explained by the stiffness change at the interface, which shows lower flow resistance than the inlet, thus accelerating the pulse wave. We observed a larger increase in local *PWV* in segment 1 for case 2 than the degree of decrease for case 1. This explains why in Figure 3.12b the global *PWV* in case 2 is above the global *PWV* in case 1.

In Figure 3.11 we saw that, despite higher values of structural stiffness in KO_F compared to KO_M, the computed global *PWV* is lower in the female group. We observed higher heterogeneity of structural stiffness in the KO_F compared to KO_M (see Figure 3.8) which can explain these *PWV* results in Figure 3.11 (right). Indeed, from Figure 3.12b we may conclude that high values of heterogeneity of material properties of the arterial wall cause a decrease in measured *PWV*. Note that the *PWV* reported in section 3.3 corresponds to ($PWV_{i=outlet}^{global}$).

**Table 3.9.** Parameters used to compute *PWV* in an elastic tube with two distinct homogenous structural stiffness using Womersley's deformable wall analytical solution and vascular impedance theories.

| | |
|---|---|
| Vessel length (cm) | 10 |
| Vessel radius (cm) | 0.07 |
| Wall thickness *h* (cm) | 0.007 |
| Wall stiffness E (dyn/cm$^2$) | 10e+06 |
| Poisson's ratio | 0.5 |
| Wall density (g/cm$^3$) | 1 |
| Blood viscosity (dyn s/cm$^2$) | 0.04 |
| Heterogeneity index *a* | $0 \leq a \leq 0.6$ |

## 3.4 Discussion

Central artery stiffening plays critical roles in dictating both the local wall mechanics / mechanobiology and the global hemodynamics / pathophysiology [35], which is particularly important since local and global effects appear to relate within a potentially insidious positive feedback loop [36]. Computational FSI studies can thus contribute significantly to our understanding of these complex, clinically important feedback loops. We previously presented FSI simulations for the human central vasculature[7] using the best data available in the literature on age-dependent (30, 40, 60, and 75 years old) regional variations in aortic properties[6]. Results were generally consistent with clinical findings, including age-associated increases in pulse wave velocity and central pulse pressure. Importantly, we also quantified progressive age-related reductions in elastic energy stored during a cardiac cycle, which relates to local biomechanical functionality. Limitations, however, included a lack of complete data on young healthy subjects as well as a lack of detailed anatomic changes with aging – we increased luminal diameters and axial lengths numerically based on reported trends.

As noted earlier, murine data offer some advantages over human data for informing FSI computations, particularly given the ability to study diverse mouse models (genetic, pharmacologic, and surgical) representing myriad conditions. One of the key contributions of this study, therefore, is development of FSI models for adult male and female wild type (WT) controls (C57BL/6 x 129/SvEv) under anesthetized conditions to which results from other models can be compared. Importantly, Bellini et al.[37] recently showed for the ATA that biomechanical properties are similar across multiple mouse models used as controls (including C57BL/6 and C57BL/6 x 129/SvEv), hence the present results are likely broadly representative of wild-type controls.

In addition to the WT group, we also developed FSI models of the adult fibulin-5 null (*Fbln5*$^{-/-}$ or KO) mouse model, which represents a stable model of early vascular aging given its loss of elastic fiber integrity[12]. Despite prior studies of mechanical properties[13] and basic cardiovascular function[38] in fibulin-5 null mice, we present the first detailed FSI simulations for this important mouse model. Both WT and KO groups were further divided by sex. Although chronological age was consistent across the four groups, the variability within the KO groups may have resulted from different degrees of elastopathy, which is to say that responses to a genetic mutation need not progress the same as different mice age. It will also be interesting to compare results from WT and *Fbln5*$^{-/-}$ mice to similar calculations for naturally aged mice, but this was beyond the current scope. In particular, although the structural integrity of the elastic fibers and laminae appear to be largely preserved in aged murine vessels, the age-related increase in collagen and glycosaminoglycans necessarily reduces the percent elastin within the wall[39,40]. Hence, energy storage and distensibility are reduced in aging and cases of elastopathy, but for different reasons.

Although longitudinal data can be collected noninvasively in mice (e.g., micro-CT and ultrasound), associated information on biaxial wall properties, thickness, and histological composition require terminal procedures. Hence, typically not all data can be collected from a single mouse. A key methodological contribution of this paper is development of a workflow to integrate *in vivo* and *in vitro* experimental data on hemodynamics, wall mechanics, and anatomy from multiple cohorts into single "mouse-specific" computational models of vascular biomechanics. Indeed, because hemodynamic conditions can even be influenced strongly by differences in anesthetic depth from imaging session-to-session, the ability to normalize results by body mass can decrease inherent variability in measurements within and across subjects. We thus developed a methodology to assign mouse-specific hemodynamic data to micro-CT based models

of the central vasculature using body mass based allometric scaling of quantities such as CO, $R_{TOT}$, and $C_{TOT}$. Local values of biaxial material stiffness and wall thickness can also be assigned in a mouse-specific manner, with associated linear interpolations as needed.

### 3.4.1 Biomechanical Characteristics

Information obtained from calibrated computational groups yields the following advantages relative to the experimental data from which it is derived: i) insights can be gleaned for quantities not easily accessible through experiments, such as pressure indices at the level of the renal arteries or values of peripheral resistance and compliance for different genotypes and sexes; ii) a high resolution description of quantities such as *PWV*, which further enables interpretation of complex interdependencies among these quantities and spatial variations in stiffness and anatomy. In the following paragraphs, we summarize statistically significant differences in hemodynamics and biomechanics for the different groups:

**Sex differences**

- Wild-type mice: Males have larger body mass and higher CO than females, but $P_{MEAN}$ is comparable between males and females (which suggests that $R_{TOT}$ is smaller in males). Males also show smaller $R_{peripheral}$, larger $C_{TOT}$ and higher PP within the ATA, pDTA, dDTA, IAA and CCA. Females have smaller *id* at pDTA, dDTA and SAA. ATA-IAA length and ATA-iliac PWV is larger in the males.
- Fibulin-5 null mice: Females have smaller body mass and larger $R_{TOT}$, $R_{peripheral}$, $R_{central}$ and $P_{MEAN}$ than males though CO is comparable between the two groups. Conversely, $C_{TOT}$ is larger in the males. Females have larger pressure indices ($P_{MEAN,}$ $P_{SYS,}$ $P_{DIAS}$, and cPP) in the ATA compared to the males. Lastly, females have larger material and structural stiffness in the ATA.

**Genotype differences**

- Male: KO_M mice have lower body mass, CO, and $C_{TOT}$ than WT. KO mice have higher $R_{central}$ than WT. Within the ATA, the KO mice have lower values of $P_{MEAN}$, $P_{SYS}$ and $P_{DIAS}$. The KO mice also have lower $P_{MEAN}$ at all other locations along the aorta as well as in the CCA and lower PP at IAA. The KOs also have an overall larger thickness *h* and smaller *id* within the pDTA, dDTA and CCA, which explains higher $R_{central.}$ KOs have greater ATA-IAA and ATA-iliac centerline lengths.
- Female: The KO_F mice have larger $R_{central}$ compared to WT, due to increased tortuosity. The KO mice also have higher $P_{SYS}$, $P_{DIAS}$ and cPP within the ATA and higher PP at all other

locations except the IAA. The KOs have higher material and structural stiffness at the ATA and higher structural stiffness at pDTA. Thickness *h* is larger in the KO at all locations except for ATA and CCA. KOs have greater ATA-IAA and ATA-iliac centerline lengths.

The following indices, although not reflecting statistically significant differences due to the small number of samples, are also worth noting: i) Both male and female KO groups have higher structural stiffness in the proximal part of the aorta compared to WT of the same sex. Conversely, KO groups have lower structural stiffness in the distal part of the aorta (namely, IAA and iliac artery). These differences result in higher PP in in the proximal part of the aorta in the KO groups compared to WT and lower (for males) or comparable (for females) PP distally. These findings suggest a greater loss of functionality in the proximal aorta with loss of elastic fiber integrity compared to the distal part, consistent with the expected differential elastin:collagen ratios in normalcy. ii) The increase in cPP in the KO groups seems to follow two different mechanisms in the male and female mice. cPP increases in the males mainly due to a decrease in diastolic pressure associated with a larger stiffness and lower CO. Conversely, cPP increases in the females mainly due to an increase in systolic pressure associated with a larger stiffness and maintained CO. These computational trends reflect the experimental data. iii) The distribution of total compliance between central and peripheral components revealed that WT_F are the only group in which $C_{central}$ accounts for more than 50% of the total compliance. This finding suggests that healthy females have larger aortic compliance than healthy males and thus could exhibit different responses during the progression of certain cardiovascular diseases.

Differently from what we observe in humans[41], $C_{peripheral}$ accounted for more than 70% of the total compliance in all the other groups. From physiological and biomechanical perspectives, there are clearly fundamental differences between the human and murine cardiovascular systems. For example, mice have a much faster heart rate, much smaller dimensions, lower Reynolds and Womersley numbers, and, most critically for our purposes, a different distribution of aortic stiffness and pulse amplification along the aorta compared to humans. Moreover, species with faster heart rates exhibit higher arterial elastin:collagen ratios and higher in vivo axial stretches[42]. The mouse aorta also has significant contractile capability, which is less expected in the human, though contractility was not modeled directly due to expected lower extent under anesthesia but also a general lack of information on in vivo values. These differences might help explain our reported distribution of compliance, noting that the anesthesia could contribute further to an over-

estimation of the total compliance, which in turn could explain the large estimates of peripheral compliance. Figure 3.4 illustrates this point: whereas the time constant $\tau$ is set directly by fitting an exponential decay to the diastolic portion of the aortic waveform, and contributes to $C_{TOT,}$ an under-estimation of the total resistance $R_{TOT}$ from the cardiac output and mean pressure, which is lower under anesthesia, would necessarily lead to an over-estimation of the total compliance $C_{TOT}$. This issue must certainly be investigated further, but it is beyond the current scope to perform a detailed comparison across species.

### 3.4.2 Pulse Wave Velocity

We compared three computed metrics of *PWV* (CCA-iliac, ATA-IAA, and ATA-iliac) with the corresponding spatial averages of structural stiffness. We observed that *PWV* does not always capture regional differences or changes in stiffness, which is often a key manifestation of vascular disease. Specific examples of these discrepancies are:

*Sex Differences*

- Fibulin-5 null mice: Although the females have a greater average aortic structural stiffness, all three *PWV* metrics were lower in females compared to males. This difference is due to the complex interdependence of *PWV* on geometry, stiffness, and flow. We also found that regional differences in structural stiffness impacts the measured *PWV*, specifically greater heterogeneity results in lower *PWV*.

*Genotype Differences*

- Male mice: CCA-iliac stiffness was larger in the KOs compared to WTs while the *PWV* was less. In addition to the previously discussed impact of spatial stiffness heterogeneity on *PWV*, it is worth noting that no physical pulse travels between the CCA and the iliac, adding complexity to the interpretation of this index.

To validate our computational findings on *PWV*, we estimated the experimental *PWV* from the available data. Using the Doppler velocity measured in the ATA and IAA, we estimated the pulse transit time in each mouse of the hemodynamics cohort using a foot-to-foot algorithm. Centerline aortic length was then measured from the micro-CT cohort to estimate the experimental *PWV*. Mean values of experimental ATA-IAA *PWV* are (in m/s): 3.5 ± 0.2 for WT_M, 3.9 ± 1.2 for WT_F, 5.9 ± 0.6 for KO_M and 4.7 ± 0.4 for KO_F. Our computated values (Table 3.8) are thus similar to those from the experimental data. Specifically, larger values of ATA-IAA PWV are observed in both KO groups. Our *PWV* values also agree with those reported in the literature by

Hartley et al.[43], who reported aortic *PWV* of 3.79 ± 0.1 m/s in ten WT C57BL/6J mice 13 months-old.

### 3.4.3 Comparison to Prior Work

Notwithstanding prior computational fluid dynamics studies (i.e., hemodynamics in the presence of rigid walls) in mice (e.g., [25,26,44,45]), to the best of our knowledge there have been few mouse-specific 3D FSI models of central hemodynamics besides our prior study of the effects of catheter size on murine hemodynamics[18]. Trachet and colleagues[46] studied abdominal aortic flows in angiotensin II infused mice to gain insight into the preferential occurrence of dissection in the suprarenal aorta while De Wilde and colleagues[47] studied the effects of anesthesia, rest, and exercise on hemodynamics in the carotid artery. Because both of these excellent studies focused on local regions, the arterial wall properties (modeled using an isotropic Arruda-Boyce model) were assumed to be spatially uniform, with wall thickness assumed to be 10% of the local radius. These models also relied on *in vivo* measurements of velocity and geometry assessed in a representative animal. Due to the impracticality of collecting multiple types of biomechanical data from the same animal, these studies did not include pressure waveforms from the same subject. Our 11 models, in contrast, were built on regional *in vitro* biaxial mechanical testing as well as *in vivo* ultrasound and pressure measurements for groups of ~5 mice for each of the four groups: WT_M, WT_F, KO_M, and KO_F. There are, therefore, no results to which we can compare directly. Note, however, that Aslanidou et al.[48] developed a 1D model of the anesthetized murine cardiovascular system based on micro-CT images of male wild type C57BL/6J and *ApoE*$^{-/-}$ mice (12-15 weeks old) and literature data. This model included 85 arterial segments and was validated against catheter-based pressure and ultrasound-based diameter and velocity waveforms. Our WT_M results compare well with their findings, as, for example, 15 vs 14 ml/min for cardiac output and 3.8 vs 4.4 m/s for ATA-IAA *PWV*, respectively. Our ATA $P_{MEAN}$ was lower (80 vs 98 mmHg, which could reflect different levels of anesthesia), but we observed a similar 4 mmHg drop in $P_{MEAN}$ from the ATA to the IAA. Our computed value of PP in the ATA was similar (39 vs 41.7 mmHg), but there was a substantial difference in drop in PP from the ATA to the IAA (8 mmHg in our study vs. 1.5 mmHg in Aslanidou and colleagues). Finally, our values for $R_{TOT}$ and $C_{TOT}$ for the WT_M are similar to those reported by Segers et al.[49], who fitted a four-element Windkessel model to experimental data ($R_{TOT}$ = 54.66 ± 17.33 vs. our $R_{TOT}$ = 45.0 ± 0.5 Pa/(mm$^3$ s), and $C_{TOT}$ = 0.00375 ± 0.00113 mm$^3$/Pa vs our $C_{TOT}$ = 0.0068 ± 0.0001 mm$^3$/Pa). Our value of $C_{central}$ (0.0013

± 0.0002) in the WT_M group compared well with that reported by Guo and Kassab[50] (0.002 $mm^3/Pa$), who studied the relationship of $C=\Delta V/\Delta P$ for the aorta and its main branches including the iliac bifurcation.

### 3.4.4 Limitations

Nevertheless, our model, like all others, remains to be improved. Biaxial material properties were measured in only five central arteries; additional measurements in vessels such as the subclavians, iliacs, and mesenterics should be considered in the future. Albeit measured *in vitro*, the extreme axial extensibility of the ATA was not captured by our FSI model, thus changes in ATA volume during systole are likely underestimated. This limitation could lead to an underestimation of the axial compliance of the ATA, a key contributor to $C_{central}$, which in turn could lead to a larger cPP. Because of biaxial coupling of wall mechanics, this issue could also help explain discrepancies between experimental and computed values of diameter distension at the ATA as shown in Figure 3.9.

Our model also does not account for the Fåhræus-Lindqvist effect, which describes a significant decrease in the apparent blood viscosity in vessels of diameters less than 300 μm[51]. The intercostal arteries of our models have a diameter of 170 μm and the renal and tail arteries of two WT female models have a diameter slightly smaller than 300 μm. In these locations the higher viscosity considered likely resulted in slightly higher values of both mean flow and mean pressure [cf. [48]], with no significant effects on the outlet boundary conditions and thus overall results.

### 3.4.5 Conclusions

We presented a new workflow for studying mouse-specific hemodynamics in the central vasculature including fluid-solid interactions and regionally varying biaxial arterial wall properties. Results for adult wild-type mice should serve as important controls for many future studies involving diverse genetic, pharmacological, and surgical mouse models. In addition, we studied an important mouse model (*Fbln5*$^{-/-}$) of early vascular aging due to a marked elastopathy and as a function of sex. Increased structural stiffness of the proximal central arteries in *Fbln5*$^{-/-}$, due largely to increased wall thickness and collagen:elastin ratios, led to increases in cPP and *PWV* in both male and female mice. This increased *PWV* did not reflect well the underlying regional differences in stiffness, however, thus suggesting that this spatially averaged measure is not sensitive to local changes per se, particularly when comparing results between males and females.

## Bibliography


1. Mitchell GF, Parise H, Benjamin EJ, et al. Changes in arterial stiffness and wave reflection with advancing age in healthy men and women: The Framingham Heart Study. *Hypertension*. 2004;43(6):1239-1245. doi:10.1161/01.HYP.0000128420.01881.aa.

2. Laurent S, Cockcroft J, Van Bortel L, et al. Expert consensus document on arterial stiffness: methodological issues and clinical applications. *Eur Heart J*. 2006;27:2588-2605. doi:10.1093/eurheartj/ehl254.

3. Lakatta EG, Wang M, Najjar SS. Arterial aging and subclinical arterial disease are fundamentally intertwined at macroscopic and molecular levels. *Med Clin North Am*. 2009;93(3):583-604. doi:10.1016/j.mcna.2009.02.008.

4. Ferruzzi J, Collins MJ, Yeh AT, Humphrey JD. Mechanical assessment of elastin integrity in fibrillin-1-deficient carotid arteries: implications for Marfan syndrome. *Cardiovasc Res*. 2011;92:287-295. doi:10.1093/cvr/cvr195.

5. Ferruzzi J, Vorp D a, Humphrey JD. On constitutive descriptors of the biaxial mechanical behaviour of human abdominal aorta and aneurysms. *J R Soc Interface*. 2011;8(56):435-450. doi:10.1098/rsif.2010.0299.

6. Roccabianca S, Figueroa CA, Tellides G, Humphrey JD. Quantification of regional differences in aortic stiffness in the aging human. *J Mech Behav Biomed Mater*. 2014;29:618-634. doi:10.1016/j.jmbbm.2013.01.026.

7. Cuomo F, Roccabianca S, Dillon-Murphy D, Xiao N, Humphrey JD, Figueroa CA. Effects of age-associated regional changes in human central artery mechanics on systemic hemodynamics revealed by computational modeling. *PLoS One*. 2017;12(3):1-21. doi:10.7302/Z24B2Z7Z.

8. Rammos C, Hendgen-Cotta UB, Deenen R, et al. Age-related vascular gene expression profiling in mice. *Mech Ageing Dev*. 2014;135:15-23. doi:10.1016/j.mad.2014.01.001.

9. Fleenor BS, Marshall KD, Durrant JR, Lesniewski LA, Seals DR. Arterial stiffening with ageing is associated with transforming growth factor-β1-related changes in adventitial collagen: reversal by aerobic exercise. *J Physiol*. 2010;588(20):3971-3982. doi:10.1113/jphysiol.2010.194753.

10. Davis E. Stability of elastin in the developing mouse aorta: a quantitative radioautographic study. *Histochemistry*. 1993;100(1):17-26.

11. Ferruzzi J, Bersi M, Mecham R, et al. Loss of elastic fiber integrity compromises common

carotid artery function: implications for vascular aging. *Artery Res*. 2016;14:41-52. doi:10.1038/mp.2016.136.Loss.

12. Wan W, Gleason RL. Dysfunction in elastic fiber formation in fibulin-5 null mice abrogates the evolution in mechanical response of carotid arteries during maturation. *Am J Physiol Hear Circ Physiol*. 2013;304(5):H674-H686. doi:10.1152/ajpheart.00459.2012.

13. Ferruzzi J, Bersi MR, Uman S, Yanagisawa H, Humphrey JD. Decreased elastic energy storage, not increased material stiffness, characterizes central artery dysfunction in fibulin-5 deficiency independent of sex. *J Biomech Eng*. 2015;137(3):031007.

14. Gleason RL, Gray SP, Wilson E, Humphrey JD. A multiaxial computer-controlled organ culture and biomechanical device for mouse carotid arteries. *J Biomech Eng*. 2004;126(6):787-795. doi:10.1115/1.1824130.

15. CRIMSON CardiovasculaR Integrated Modelling and SimulatiON. (2017) Available from: http://www.crimson.software.

16. Sahni O, Müller J, Jansen KE, Shephard MS, Taylor CA. Efficient anisotropic adaptive discretization of the cardiovascular system. *Comput Methods Appl Mech Eng*. 2006;195:5634-5655.

17. Figueroa CA, Vignon-Clementel IE, Jansen KE, Hughes TJR, Taylor CA. A coupled momentum method for modeling blood flow in three-dimensional deformable arteries. *Comput Methods Appl Mech Eng*. 2006;195:5685-5706.

18. Cuomo F, Ferruzzi J, Humphrey JD, Figueroa CA. An experimental–computational study of catheter induced alterations in pulse wave velocity in anesthetized mice. *Ann Biomed Eng*. 2015;43(7):1555-1570. doi:10.1007/s10439-015-1272-0.

19. Baek S, Gleason RL, Rajagopal KR, Humphrey JD. Theory of small on large: Potential utility in computations of fluid–solid interactions in arteries. *Comput Methods Appl Mech Eng*. 2007;196:3070-3078.

20. Ferruzzi J, Bersi MR, Humphrey JD. Biomechanical phenotyping of central arteries in health and disease: advantages of and methods for murine models. *Ann Biomed Eng*. 2013;41(7):1311-1330. doi:10.1007/s10439-013-0799-1.

21. Stergiopulos N, Westerhof N. Role of total arterial compliance and peripheral resistance in the determination of systolic and diastolic aortic pressure. *Pathol Biol (Paris)*. 1999;47(6):641-7.

22. Simon AC, Safar ME, Levenson JA, London GM, Levy BI, Chau NP. An evaluation of large arteries compliance in man. *Am Jouornal Physiol*. 1979;237(5):H550-4.

23. Xiao N, Alastruey J, Figueroa CA. A systematic comparison between 1-D and 3-D hemodynamics in compliant arterial models. *Int J Numer Method Biomed Eng*. 2014;30(2):204-231. doi:10.1002/cnm.2598.

24. Les AS, Yeung JJ, Schultz GM, Herfkens RJ, Dalman RL, Taylor CA. Supraceliac and infrarenal aortic flow in patients with abdominal aortic aneurysms: mean fows, waveforms, and allometric scaling relationships. *Cardiovasc Eng Technol*. 2010;1(1):39-51. doi:10.1007/s13239-010-0004-8.

25. Feintuch A, Ruengsakulrach P, Lin A, et al. Hemodynamics in the mouse aortic arch as assessed by MRI, ultrasound, and numerical modeling. *Am J Physiol Heart Circ Physiol*. 2007;292(2):H884-H892.

26. Greve JM, Les AS, Tang BT, et al. Allometric scaling of wall shear stress from mice to humans: quantification using cine phase-contrast MRI and computational fluid dynamics. *Am J Physiol Heart Circ Physiol*. 2006;291(4):H1700-H1708.

27. Gaddum NR, Alastruey J, Beerbaum P, Chowienczyk P, Schaeffter T. A technical assessment of pulse wave velocity algorithms applied to non-invasive arterial waveforms. *Ann Biomed Eng*. 2013;41(12):2617-2629.

28. Hartley CJ, Reddy AK, Madala S, Entman ML, Michael LH, Taffet GE. Doppler velocity measurements from large and small arteries of mice. *Am J Physiol Hear Circ Physiol*. 2011;301(2):H269-H278. doi:10.1152/ajpheart.00320.2011.

29. Womersley JR. XXIV . Oscillatory motion of a viscous liquid in a thin-walled elastic tube — I : The linear approximation for long waves. *London, Edinburgh, Dublin Philos Mag J Sci*. 1955;46(373):199-221. doi:10.1080/14786440208520564.

30. Womersley JR. Method for the calculation of velocity, rate of flow and viscous drag in arteries when the pressure gradient is known. *J Physiol*. 1955;(127):553-563. doi:10.1259/bjr/96847348.

31. Figueroa CA. A coupled-momentum method to model blood flow and vessel deformation in human arteries: applications in disease research and simulation-based medical planning, Chapter 2: Mathematics and physics of pulsatile flow in deformable vessels. 2006.

32. Nichols W, O'Rourke M, Vlachopoulos C. *McDonald's Blood Flow in Arteries: Theoretical, Experimental and Clinical Principles.* 5th ed. New York: Oxford University Press.; 1998.

33. van de Vosse FN, Stergiopulos N. Pulse wave propagation in the arterial tree. *Annu Rev Fluid Mech*. 2011;43(1):467-499. doi:10.1146/annurev-fluid-122109-160730.

34. Womersley JR. Method for the calculation of velocity, rate of flow and viscous drag in arteries when the pressure gradient is known. *J ournal Physiol*. 1955;(127):553-563. doi:10.1259/bjr/96847348.

35. Laurent S, Boutouyrie P. The structural factor of hypertension: large and small artery alterations. *Circ Res*. 2015;116(6):1007-1021. doi:10.1161/CIRCRESAHA.116.303596.

36. Humphrey JD, Harrison DG, Figueroa CA, Lacolley P, Laurent S. Central artery stiffness

in hypertension and aging: a problem with cause and consequence. *Circ Res*. 2016;118(3):379-381. doi:10.1161/CIRCRESAHA.115.307722.

37. Bellini C, Caulk AW, Li G, Tellides G, Humphrey JD. Biomechanical phenotyping of the murine aorta: what is the best control? *J Biomech Eng*. 2017;139(4). doi:10.1115/1.4035551.

38. Le VP, Stoka K V, Yanagisawa H, Wagenseil JE. Fibulin-5 null mice with decreased arterial compliance maintain normal systolic left ventricular function, but not diastolic function during maturation. *Physiol Rep*. 2014;2(3):1-16. doi:10.1002/phy2.257.

39. Donato AJ, Walker AE, Magerko K, et al. Life-long caloric restriction reduces oxidative stress and preserves nitric oxide bioavailability and function in arteries of old mice. *Aging Cell*. 2013;12(5):772-783. doi:10.1111/acel.12103.Life-Long.

40. Ferruzzi J, Madziva D, Caulk AW, Tellides G, Humphrey JD. Compromised mechanical homeostasis in arterial aging and associated cardiovascular consequences. *Biomech Model Mechanobiol*. 2018;17(5):1281-1295. doi:10.1007/s10237-018-1026-7.

41. Saouti N, Marcus JT, Vonk Noordegraaf A, Westerhof N. Aortic function quantified: the heart's essential cushion. *J Appl Physiol*. 2012;113(8):1285-1291.

42. Humphrey JD, Eberth JF, Dye WW, Gleason RL. Fundamental role of axial stress in compensatory adaptations by arteries. *J Biomech*. 2009;42(1):1-8.

43. Hartley C, Reddy A, Madala S, et al. Hemodynamic changes in apolipoprotein E-knockout mice. *Am J Physiol Heart Circ Physiol*. 2000;279(5):H2326-H2334.

44. Huo Y, Guo X, Kassab GS. The flow field along the entire length of mouse aorta and primary branches. *Ann Biomed Eng*. 2008;36(5):685-699.

45. Trachet B, Renard M, De Santis G, et al. An integrated framework to quantitatively link mouse-specific hemodynamics to aneurysm formation in angiotensin II-infused ApoE -/- mice. *Ann Biomed Eng*. 2011;39(9):2430-2444.

46. Trachet B, Bols J, Degroote J, et al. An animal-specific FSI model of the abdominal aorta in anesthetized mice. *Ann Biomed Eng*. 2015;43(6):1298-1309. doi:10.1007/s10439-015-1310-y.

47. Wilde D De, Trachet B, Debusschere N, et al. Assessment of shear stress related parameters in the carotid bifurcation using mouse-specific FSI simulations. *J Biomech*. 2016;49(11):2135-2142. doi:10.1016/j.jbiomech.2015.11.048.

48. Aslanidou L, Trachet B, Reymond P, Fraga-Silva RA, Segers P, Stergiopulos N. A 1D model of the arterial circulation in mice. *ALTEX*. 2015;33(1):13-28. doi:10.14573/altex.1507071.

49. Segers P, Georgakopoulos D, Afanasyeva M, et al. Conductance catheter-based assessment

of arterial input impedance, arterial function, and ventricular-vascular interaction in mice. *Am J Physiol Heart Circ Physiol*. 2005;288(3):H1157-64.

50. Guo X, Kassab GS. Variation of mechanical properties along the length of the aorta in C57bl/6 mice. *Am J Physiol Heart Circ Physiol*. 2003;285(6):H2614-22. doi:10.1152/ajpheart.00567.2003.

51. Robin Fahraeus, Torsten Lindqvist. The viscosity of blood in narrow capillary tubes. *Am J Physiol*. 1931;96(3):562-568.

## Chapter 4. Central Artery Hemodynamics in Naturally Aged Mice

***Contributions.*** *All the experimental work showed in this chapter was performed by Dr. Jacopo Ferruzzi. Zhen W. Zhuang contributed to collect the micro-CT image data.*

### 4.1 Introduction

Aging is a major risk factor for cardiovascular disease, due to age-related changes in the arterial wall that lead to increased arterial wall stiffness[1]. Increase in central arterial stiffness is recognized as both initiator and indicator of cardiovascular, neurovascular and renovascular problems[2,3]. In humans, an increase in arterial stiffness is mainly due to degradation of elastic fibers and increased deposition of collagen and other proteins[1,4]. Naturally aged mice exhibit a vascular aging phenotype due to distributed increase of collagen and GAGs, but not due to degradation of elastin[5]. Vascular elastin is similar in mice and humans, with a half-life of more than 25 years[6,7], suggesting that elastin fibers remains intact during the normal life-span (~2 years) of a healthy mouse.

Given the importance of arterial aging on hemodynamics[4,8] and couplings between large and small vessels[2], it is essential to investigate the effects of regional variations in wall properties on local and global hemodynamics. Towards this aim, we combined *in vivo* and *in vitro* data on 100 week-old aged mice with computational modeling. In this work we built computational hemodynamic models of the central vasculature of three female aged mice employing the methods presented in Chapter 3. Specifically, we assigned hemodynamic and structural stiffness data acquired in different animals to individual micro-CT aortic models to produce calibrated computational results that provide general insights into quantities not easily obtained through experiments. The results are presented by comparing data from 20 week-old female wild type (WT_F) and Fbln5$^{-/-}$ (KO_F) mice groups (presented in Chapter 3). Fibulin-5 deficiency mouse is a model of accelerated aging, due to impair elastic fiber fibrillogenesis[9].

## 4.2 Methods

All animal procedures were approved by the Institutional Animal Care and Use Committee (IACUC) of Yale University. Normal female wild-type mice were allowed to age naturally to ~100 weeks (Aging_F). The Aging_F mice were obtained as Fbln5+/+ by breeding Fbln5+/− heterozygous pairs on a mixed C57BL/6 x 129/SvEv background. Due to the impracticality of collecting complete *in vivo* and *in vitro* data sets from any single animal at the prescribed endpoint the mice were divided in two cohorts:

- An anatomy cohort, for which we collected noninvasive *in vivo* micro-CT data on the temporal mean vascular geometry.
- A wall mechanics and hemodynamics cohort, for which we collected regional *in vitro* biaxial data on five central vessels and noninvasive *in vivo* ultrasound data on cyclic changes in geometry and flow as well as invasive *in vivo* data on cyclic pressures[5].

We followed the strategy proposed in Chapter 3[10] to build mouse-specific computational models using population data. Specifically, regional wall mechanics data were assigned to each micro-CT anatomical model using values of local radii while hemodynamics data were mapped to each model using body mass based allometric scaling of quantities such as cardiac output, total arterial resistance, and total arterial compliance.

### 4.2.1 Experimental

**Anatomy.** As described in section 3.2.1, mice were anesthetized using 1-2% isoflurane, then given a bolus intravenous (jugular vein) injection of a nanoemulsion formulation (Fenestra VC, MediLumine Inc., Montreal, CA), at a dose of 0.2 ml/20 g, as a blood-pool contrast agent designed for prolonged vascular imaging. Immediately thereafter, the animal was placed prone inside a micro-CT scanner (eXplore CT120, GE healthcare) for non-gated whole body scanning. The images were reconstructed as isotropic 49x49x49 $\mu m^3$ voxels. A relatively constant heart rate (±10%) was achieved by careful maintenance of the level of isoflurane anesthesia and body temperature during each scan. Image data were collected for $n = 3$ female naturally aged mice.

**Hemodynamics and wall mechanics**. As previously reported[5], following isoflurane inhalation anesthesia (2–3% for induction, 1.5% for maintenance), the mouse was gently laid on its back and secured on a surgical platform having a recirculating heating pad (TP-500 Heat Therapy Pump, Gaymar Industries Inc., Orchard Park, NY) to maintain body temperature at 37°C.

Mean blood velocity and luminal diameters were then acquired via ultrasound (Vevo 2100 system, FUJIFILM VisualSonics) within the ATA, IAA, and CCA. Cardiac output (CO) was measured similarly with transthoracic echocardiography, then central aortic pressure was measured using a SPR-1000 Millar pressure catheter with a diameter of 1F. A total of $n$ = 10 female naturally aged mice were studied.

While still under anesthesia the mice were euthanized and biaxial material properties were estimated for $n$ = 5 mice. Biaxial tissue properties were assessed at four different locations along the aorta (ATA, DTA, SAA, and IAA) and within one CCA. A custom computer-controlled biaxial testing device[11] was used to perform cyclic testing, and a four-fiber family model was used to fit the data as explained in section 3.2.1.

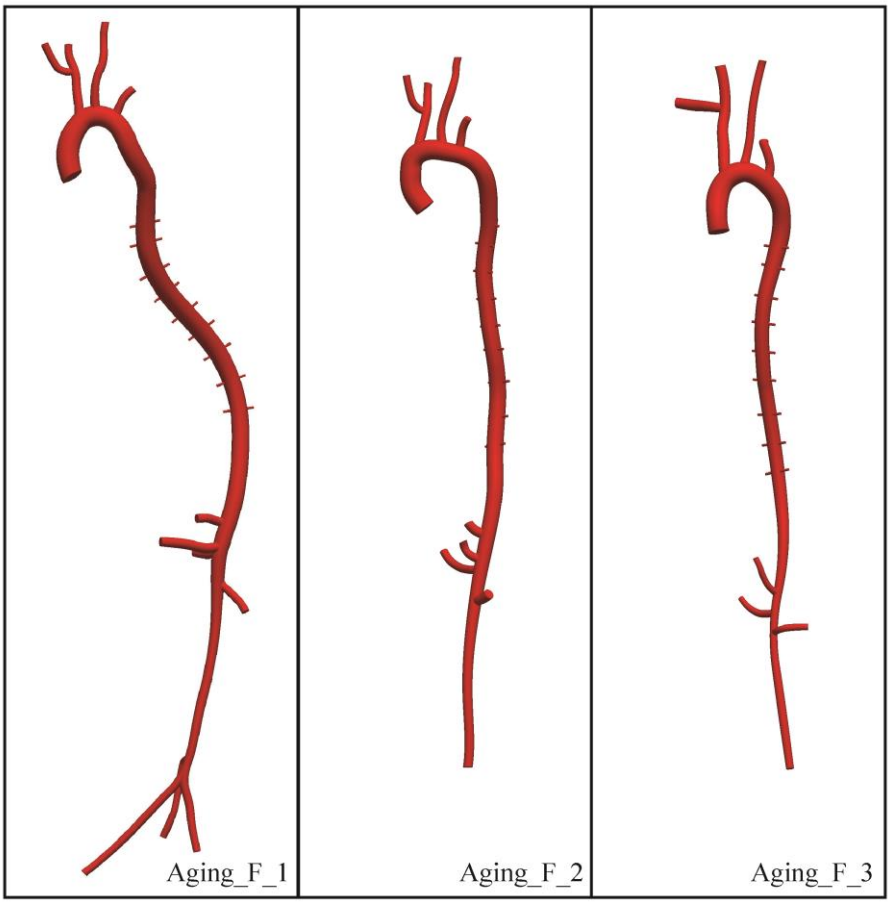


**Figure 4.1.** 3D anatomical models reconstructed for 3 female wild type mice naturally aged to 100 weeks.

### 4.2.2 Computational

We employed the custom computational hemodynamics framework CRIMSON[12] to perform Fluid-Structure-Interaction (FSI) studies. These simulations included 3D anatomical

models of the aorta and its main branches, spatially-variable mechanical properties of the central vasculature, 3-element Windkessel models used as outflow boundary conditions for each outflow branch of the anatomical models, and an external tissue support formulation to simulate effects of perivascular tissue on aortic hemodynamics. We also used *a posteriori* gradient-based mesh adaptation methods for iterative mesh refinement[13]. The workflow used to combine the computational models and experimental data acquired in the 2 cohorts of mice into a single model is described in Chapter 3 and summarized below:

**Anatomical Models**. 3D anatomical models of the central vasculature were reconstructed from the micro-CT image data using the CRIMSON GUI. Nine pairs of intercostal arteries (not visible in the image data) were added to each model using the location of the ribs as reference. The image data for the Aging_F_1 model did not include the upper vessels which carry a large portion of the cardiac output and are vital to obtain a realistic representation of hemodynamics in the central arteries. Thus we added the upper vessels of model Aging_F_2 to Aging_F_1. The three final anatomical models for the Aging_F group are shown in Figure 4.1. Velocity field-driven mesh adaptation techniques were employed to refine the finite element meshes in areas of expected large velocity gradients[13]. The final unstructured adapted meshes ranged between $1.8 \cdot 10^6$ tetrahedral elements, with $3.2 \cdot 10^4$ nodes, to $2.4 \cdot 10^6$ tetrahedral elements, with $4.4 \cdot 10^5$ nodes.

**Wall mechanics.** We employed an FSI method to capture pulse wave propagation, using a coupled momentum formulation[14]. Each vascular segment was modeled as an incompressible elastic membrane of thickness *h* characterized by a 5x5 stiffness matrix with all quantities varying from region to region. Specifically, the regionally dependent values of material stiffness were determined from a nonlinear, anisotropic stored energy function using the theory of small deformations superimposed on large[15]. This theory naturally accounts for regionally dependent values of *in vivo* axial extension and circumferential distension at mean arterial pressures. The axial stretch was estimated via the cross-over point in the force-length tests performed at four different pressures[16], whereas the circumferential stretch was calculated from the *in vivo* diameter assessed by micro-CT and the unloaded diameter measured *ex vivo*. It should be noted, however, the ATA also experiences a cyclic axial extension throughout the cardiac cycle of the same order of magnitude as the cyclic circumferential distension. The mean axial stretch of the ATA was estimated from micro-CT measured lengths *in vivo* and unloaded lengths measured *in vitro*. The regionally dependent mean values of wall stiffness and thickness are listed in Table 4.1. They were

mapped directly onto segments of each anatomical model at the following five regions: ATA, DTA, SAA, IAA, and CCA. Values within the DTA were further subdivided into proximal and distal segments (pDTA and dDTA) using individual stretches. Values elsewhere were populated by linearly interpolating values at the aforementioned six sites.

**Table 4.1**. Values of circumferential ($C_{\theta\theta}$) and axial ($C_{zz}$) material stiffness, in MPa, and wall thickness (h), in μm, at six vascular locations – ascending thoracic aorta (ATA), proximal descending thoracic aorta (pDTA), distal descending thoracic aorta (dDTA), suprarenal abdominal aorta (SAA), infrarenal abdominal aorta (IAA), and common carotid artery (CAA) – for the three Aging_F models.

| | | Aging_Female (Aging_F) | | | | |
|---|---|---|---|---|---|---|
| | | **Aging_F1** | **Aging_F2** | **Aging_F3** | **mean** | **std** |
| **ATA** | $C_{\theta\theta}$ | 0.87 | Times | 0.67 | 0.77 | 0.10 |
| | $C_{zz}$ | 0.51 | 0.48 | 0.38 | 0.46 | 0.06 |
| | **h** | 48.29 | 49.34 | 52.10 | 49.91 | 1.97 |
| **pDTA** | $C_{\theta\theta}$ | 3.64 | 0.84 | 1.23 | 1.90 | 1.52 |
| | $C_{zz}$ | 5.51 | 2.87 | 3.34 | 3.90 | 1.41 |
| | **h** | 44.02 | 49.27 | 47.63 | 46.97 | 2.69 |
| **dDTA** | $C_{\theta\theta}$ | 2.47 | 0.52 | 0.20 | 1.06 | 1.22 |
| | $C_{zz}$ | 4.56 | 2.41 | 1.85 | 2.94 | 1.43 |
| | **h** | 45.17 | 51.77 | 59.34 | 52.09 | 7.09 |
| **SAA** | $C_{\theta\theta}$ | 1.49 | 0.65 | 0.12 | 0.75 | 0.69 |
| | $C_{zz}$ | 2.57 | 1.72 | 0.96 | 1.75 | 0.80 |
| | **h** | 41.60 | 45.16 | 59.38 | 48.71 | 9.41 |
| **IAA** | $C_{\theta\theta}$ | 0.22 | 0.32 | 0.12 | 0.22 | 0.10 |
| | $C_{zz}$ | 1.89 | 2.14 | 1.59 | 1.87 | 0.27 |
| | **h** | 50.97 | 48.80 | 56.12 | 51.96 | 3.76 |
| **CCA** | $C_{\theta\theta}$ | 0.83 | 0.83 | 0.88 | 0.85 | 0.03 |
| | $C_{zz}$ | 1.98 | 1.98 | 2.06 | 2.00 | 0.05 |
| | **h** | 28.01 | 28.01 | 27.87 | 27.96 | 0.08 |

**Hemodynamics.** Mouse-specific hemodynamic data were used to inform inlet and peripheral boundary conditions for each anatomical model as explained in section 3.2.2.

Allometric scaling of cardiac output, total arterial resistance, and total arterial compliance for the Aging_F group are shown in Figure 4.2.

### 4.2.3 Pulse Wave Velocity Analysis

Aortic *PWV* was calculated as the ratio of the centerline distance between ATA and IAA and the corresponding pressure pulse transit time. The transit time was measured using an "intersecting tangent algorithm" that defines the foot of a pressure waveform as the intersection between the horizontal tangent intersecting its diastolic minimum and the tangent to the maximum systolic gradient[17].

### 4.2.4 Statistical Analysis

Computed results are presented as mean ± SEM. One-way ANOVA was used to assess differences among the three groups. Post-hoc pairwise comparisons were performed using the Benjamini-Hochberg correction method, with $p < 0.05$ considered significant. All analyses were performed using the open source statistical software R.

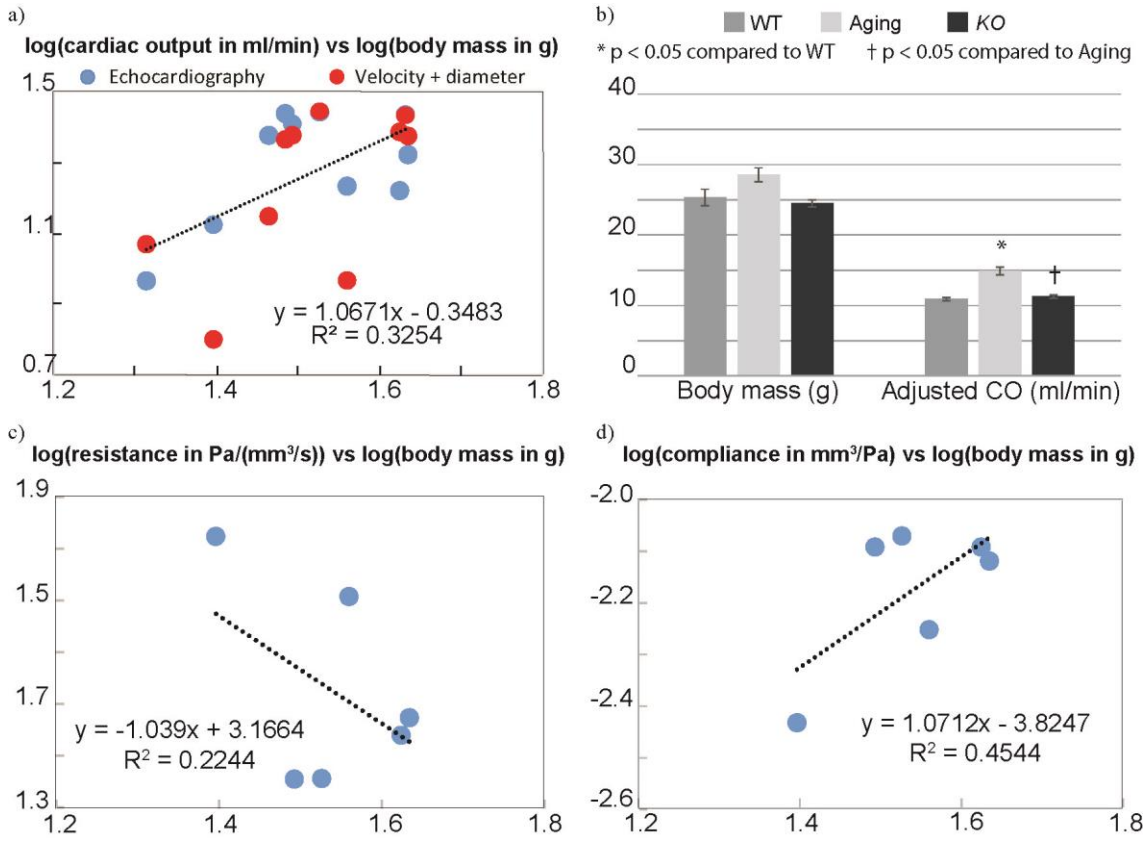


**Figure 4.2**. a) Allometric scaling of cardiac output (CO) based on echocardiographic (blue dots) and ultrasound-derived velocity and diameter data (red dots). b) Comparison of average body mass and Adjusted CO between WT, Aging and KO female groups). c) Allometric scaling of total arterial resistance ($R_{TOT}$). d) Allometric scaling of total arterial compliance ($C_{TOT}$).

## 4.3 Results

Figure 4.3 summarizes the computed results for Aging_F1, the subject among the three models for which vascular aging has progressed the most. Figure 4.3 shows computed local (cyclic pressure and flow) and global (*PWV*) hemodynamics based on the anatomical model endowed with mouse-specific regional biaxial tissue properties. Mouse- and region-specific values of circumferential and axial material stiffness and wall thickness are shown on the right, while the actual computational domain is shown in the center of the figure. Circumferential material stiffness is largest at the pDTA (location C) and smallest at the infrarenal aorta (location F); the axial material stiffness $\mathfrak{C}_{ZZ}$ is also largest at the pDTA (location C) but smallest at the ATA (location B). Computed flow and pressure waveforms are shown in the left side of the figure. As examples, the figure also shows the pressure pulse transit time between the ATA and IAA pressure waveforms, quantified to calculate *PWV*.

Next, we summarize the results for global hemodynamics, regional hemodynamics, geometry and wall mechanics, and pulse wave velocity of naturally aged mice. Furthermore, we compare our computed results for 100 week-old female mice to 20 week-old female wild type (WT_F) and Fbln5$^{-/-}$ (KO_F) mice presented in Chapter 3.

### 4.3.1 Global Hemodynamics

Table 4.2 lists mouse-specific values of body mass of each specimen of the anatomy cohort together with adjusted CO, $R_{TOT}$, $C_{TOT}$ that were assigned to each specimen via allometric scaling. Aging_F body mass and adjusted CO are compared to WT_F and KO_F groups in Figure 4.2b. Although not statistically significant, Aging_F has a higher body mass and statistically higher CO compared to the other groups.

Figure 4.4a compares $R_{TOT}$ and its central ($R_{central}$, in red) and peripheral ($R_{peripheral}$, in blue) components between the three groups of mice. As expected, $R_{peripheral}$ accounts for more than 80% of the total vasculature resistance. $R_{TOT}$, $R_{central}$ and $R_{peripheral}$ are statistically lower for Aging_F compared to both other groups, which is consistent with a higher body mass. $R_{central}$ is statistically higher in the KO_F than WT_F, due to smaller radii and increased tortuosity. Figure 4.4b separates $C_{TOT}$ into central ($C_{central}$, in red) and peripheral ($C_{peripheral}$, in blue) components. There are not statistically significant differences in compliance. Numerical values are reported in Table 3.4, 3.5, 4.2 and 4.3.

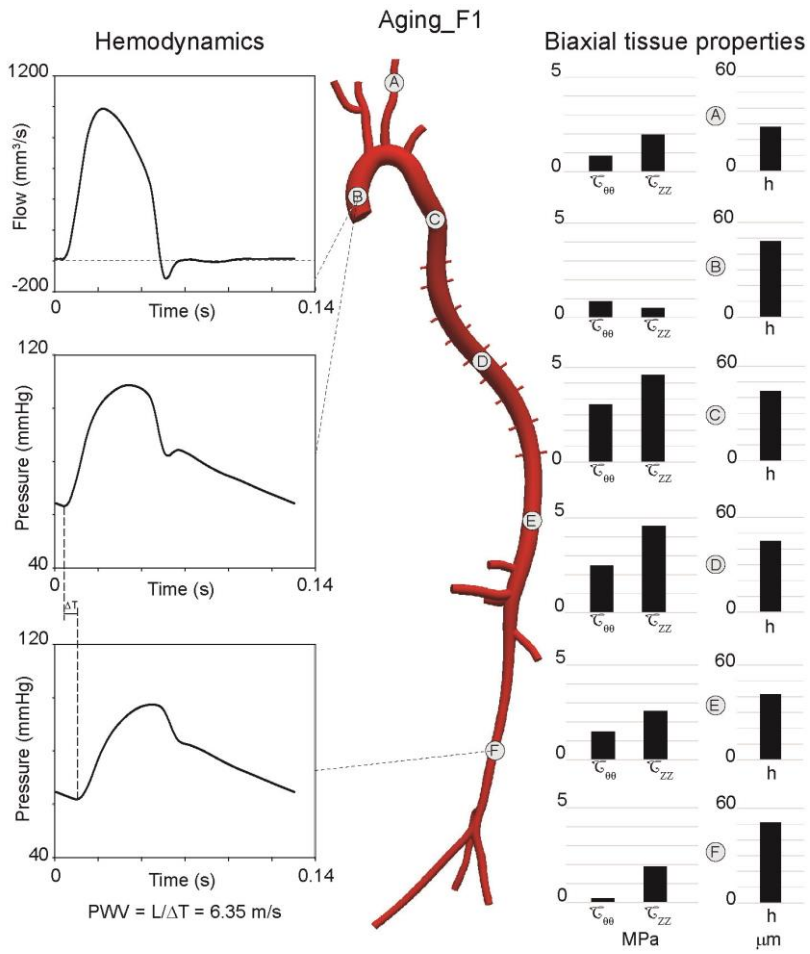


**Figure 4.3.** Computed global and local hemodynamics based on a mouse-specific geometric model and mouse-specific biaxial tissue properties (biaxial material stiffness and wall thickness) for subject Aging_F1. Additional mouse-specific values are in Table 4.1.

**Table 4.2.** Body mass and corresponding adjusted values of cardiac output (CO), total resistance ($R_{TOT}$), and total compliance ($C_{TOT}$) assigned to each computational model via allometric scaling. Body mass (g); CO (ml/min); $R_{TOT}$ (Pa/(mm$^3$/s); $C_{TOT}$ (mm$^3$/Pa).

| **Aging_Female (Aging_F)** | | | | |
|---|---|---|---|---|
| **Mouse** | **Body Mass** | **CO** | **$R_{TOT}$** | **$C_{TOT}$** |
| **Aging_F1** | 30.5 | 16.0 | 42.1 | 0.0058 |
| **Aging_F2** | 27.3 | 14.2 | 47.2 | 0.0052 |
| **Aging_F3** | 27.9 | 14.5 | 46.2 | 0.0053 |
| **mean** | 28.6 | 14.9 | 45.2 | 0.0054 |
| **std** | 1.7 | 0.9 | 2.7 | 0.0003 |

**Table 4.3.** Separation of $R_{TOT}$ into central ($R_{central}$) and peripheral ($R_{peripheral}$) vasculature components for each specimen. All values are reported in (Pa/(mm$^3$/s)).

| Aging_Female (Aging_F) | | | | |
|---|---|---|---|---|
| **Mouse** | **Body Mass** | **CO** | **$R_{TOT}$** | **$C_{TOT}$** |
| **Aging_F1** | 30.5 | 16.0 | 42.1 | 0.0058 |
| **Aging_F2** | 27.3 | 14.2 | 47.2 | 0.0052 |
| **Aging_F3** | 27.9 | 14.5 | 46.2 | 0.0053 |
| **mean** | 28.6 | 14.9 | 45.2 | 0.0054 |
| **std** | 1.7 | 0.9 | 2.7 | 0.0003 |

**Table 4.4.** Separation of $C_{TOT}$ into central ($C_{central}$) and peripheral ($C_{peripheral}$) vasculature components for each specimen. All values are reported in (mm$^3$/Pa).

| Aging_Female (Aging_F) | | | | | |
|---|---|---|---|---|---|
| **Mouse** | **$C_{TOT}$** | **$C_{central}$** | **% tot** | **$C_{peripheral}$** | **% tot** |
| **Aging_F1** | 0.0058 | 0.0009 | 16% | 0.004904 | 85% |
| **Aging_F2** | 0.0052 | 0.0016 | 31% | 0.003589 | 69% |
| **Aging_F3** | 0.0053 | 0.0020 | 38% | 0.003271 | 62% |
| **mean** | 0.0054 | 0.0015 | - | 0.0039 | - |
| **std** | 0.0003 | 0.0006 | - | 0.0009 | - |

Figure 4.5a compares experimental and computationally computed pressures within the ATA for the Aging_F group. The computed pressure decay and pulse pressure (PP) match well with the experimental data. We observe a larger variability in the experimental data compared to the computed results, due in part to a wider range of body masses in the hemodynamics cohort than in the anatomy cohort. Body mass ranged between 21-43 g for the hemodynamics cohort vs. 27-30 g for the anatomy cohort. Figure 4.5b compares computed pressures within the ATA between WT_F, Aging_F and KO_F groups. We can notice an increase in cPP in the Aging_F compared to WT_F due to an increase in systolic pressure ($P_{SYS}$). cPP is further augmented in the KO_F group due to a further increase in $P_{SYS}$. We do not observe visible differences in pressure decay slopes. Specific values of computed systolic ($P_{SYS}$), mean ($P_{MEAN}$), diastolic ($P_{DIAS}$), and central pulse (cPP) pressures for Aging_F group are listed in Table 4.5.

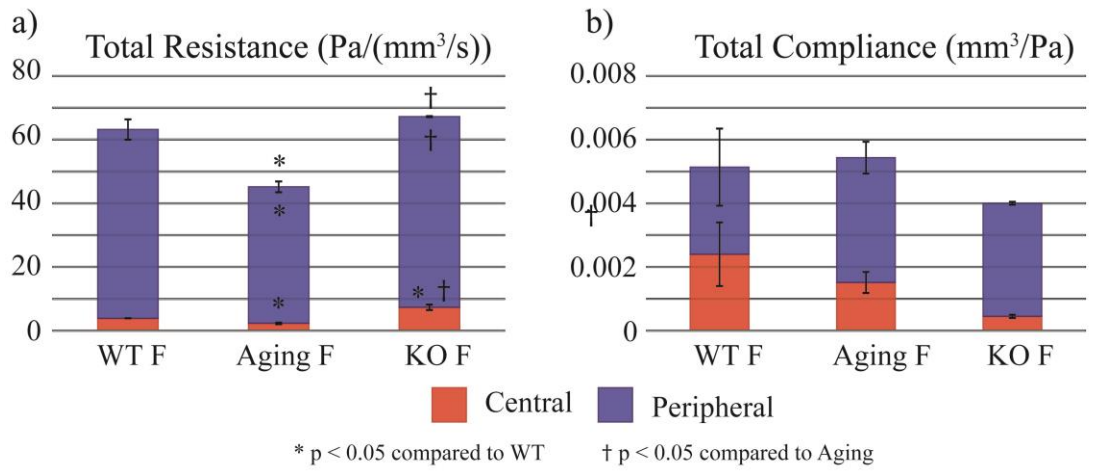


**Figure 4.4**. Separation of $R_{TOT}$ (a) and $C_{TOT}$ (b) into central (red) and peripheral (blue) components for WT_F, Aging_F and KO_F groups.

### 4.3.2 Regional Wall Mechanics, Hemodynamics and Inner Diameter Data

Figure 4.6 shows $P_{MEAN}$, PP, material stiffness ($C_{\theta\theta}$), wall thickness (*h*), structural stiffness ($C_{\theta\theta}$**h*) and internal diameter (*id*) along the aorta and CCA for WT_F (gray bar), Aging_F (light gray bars) and KO_F (black bar) groups. Numerical values are reported in Figure 3.7 and Tables 3.1, 3.6, 3.7, 4.1, 4.5 and 4.6. $P_{MEAN}$ is the time average of the computed pressures at the locations of interest and it drops along the aorta as expected. Although not significant, $P_{MEAN}$ is higher in the KO_F group compared to the other groups in the proximal part of the aorta. Bar plots of computed PP show that KO_F mice have statistically higher values of central PP compared to both WT and Aging groups, but not distally at the IAA. Aging_F mice have increased values of central PP compared to WT, but not as high as KO_F. At IAA only Aging_F have statistically higher PP compared to WT. Both $P_{MEAN}$ and PP bar plots reveal that the severity of the vascular aging phenotype is higher in the KO group compared to the naturally aged mice. Furthermore we can observe an attenuation of the pulse along the aorta in all groups.

Mouse-specific values of $C_{\theta\theta}$ and *h* were determined from experimental data on wall mechanics and assigned to the different locations along the arterial tree, as explained in Section 4.2.2. All three groups have a similar distribution of $C_{\theta\theta}$ and $C_{\theta\theta}$**h* along the aorta: a peak value at the pDTA and a gradual decrease in the distal part of the aorta with the smallest values at the IAA. Both Aging and KO females exhibit higher values in the proximal part of the aorta and comparable values in the distal part compared to WT. Aging females have statistically higher $C_{\theta\theta}$**h* and $C_{\theta\theta}$ at the ATA compared to WT female. We observe large variability in tissue

properties in the Aging group at pDTA, dDTA and SAA locations. Wall thickness *h* shows a marked increase for the KO groups compared to both WT and Aging along the entire aorta.

Inner diameter values were extracted from the anatomy reconstructed from the micro-CT data as explained in Section 4.2.2. *Id* is overall larger in Aging compared to WT and KO mice, as expected due to the higher body mass and CO.

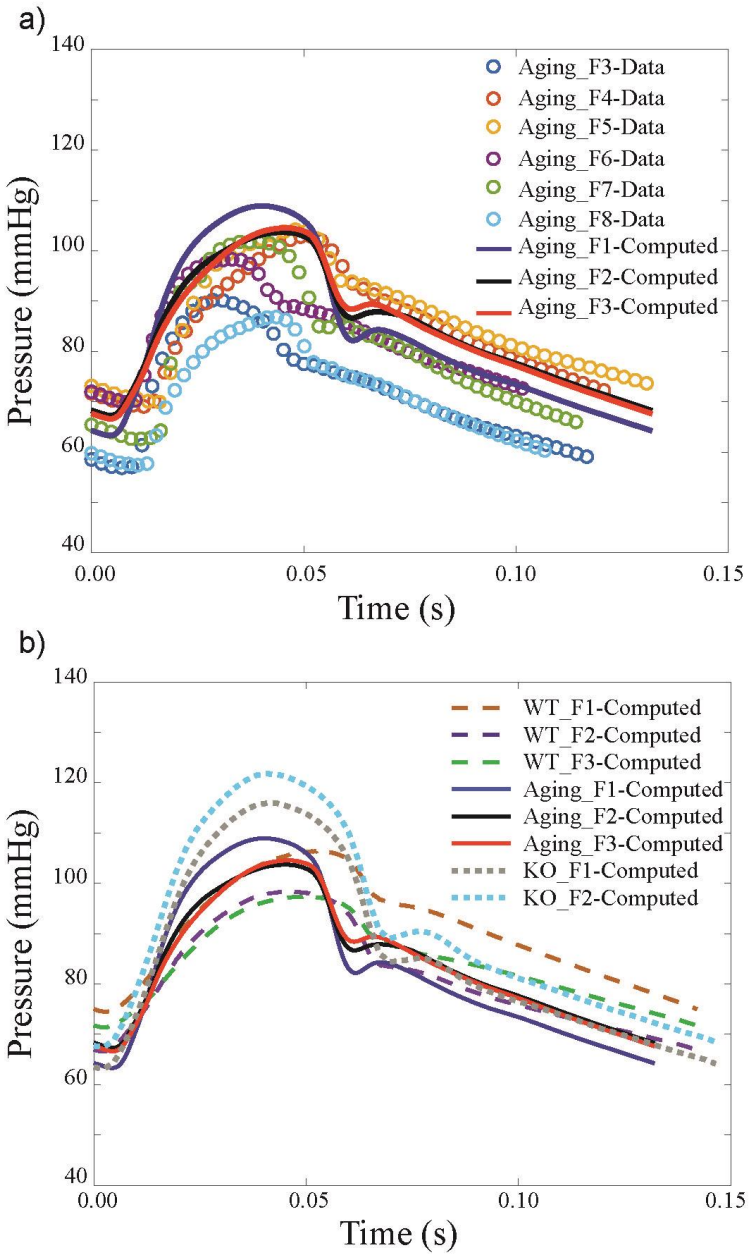


**Figure 4.5.** a) Comparison of experimental (circles) and computed (solid lines) pressure waveforms within the ATA for Aging_F group. b) Comparison of pressure waveforms computed within the ATA for WT_F (dashed line), Aging_F (solid line) and KO_F (dotted line) groups.

**Table 4.5**. Computed mean ($P_{MEAN}$), pulse (PP), systolic ($P_{SYS}$), and diastolic ($P_{DIAS}$) pressures – all in mmHg – for Aging_F group at five locations: pDTA, dDTA, SAA, IAA and CCA.

| | | Aging_Female (Aging_F) | | | | |
|---|---|---|---|---|---|---|
| | | **Aging_F1** | **Aging_F2** | **Aging_F3** | **mean** | **std** |
| **ATA** | $P_{MEAN}$ | 79 | 79 | 79 | 79 | 79 |
| | **PP** | 46 | 36 | 38 | 40 | 46 |
| | $P_{SYS}$ | 109 | 104 | 105 | 106 | 109 |
| | $P_{DIAS}$ | 63 | 67 | 67 | 66 | 63 |
| **pDTA** | $P_{MEAN}$ | 78 | 78 | 79 | 78 | 78 |
| | **PP** | 43 | 35 | 37 | 38 | 43 |
| | $P_{SYS}$ | 107 | 102 | 104 | 104 | 107 |
| | $P_{DIAS}$ | 63 | 67 | 67 | 65 | 63 |
| **dDTA** | $P_{MEAN}$ | 77 | 78 | 78 | 77 | 77 |
| | **PP** | 42 | 34 | 36 | 37 | 42 |
| | $P_{SYS}$ | 105 | 100 | 101 | 102 | 105 |
| | $P_{DIAS}$ | 63 | 66 | 66 | 65 | 63 |
| **SAA** | $P_{MEAN}$ | 76 | 77 | 76 | 77 | 76 |
| | **PP** | 40 | 34 | 35 | 36 | 40 |
| | $P_{SYS}$ | 103 | 100 | 99 | 101 | 103 |
| | $P_{DIAS}$ | 62 | 66 | 65 | 64 | 62 |
| **IAA** | $P_{MEAN}$ | 74 | 75 | 71 | 73 | 74 |
| | **PP** | 36 | 33 | 29 | 33 | 36 |
| | $P_{SYS}$ | 97 | 98 | 91 | 95 | 97 |
| | $P_{DIAS}$ | 62 | 64 | 61 | 63 | 62 |
| **CCA** | $P_{MEAN}$ | 77 | 78 | 78 | 78 | 0 |
| | **PP** | 44 | 35 | 36 | 38 | 5 |
| | $P_{SYS}$ | 107 | 101 | 102 | 103 | 3 |
| | $P_{DIAS}$ | 63 | 67 | 66 | 65 | 2 |

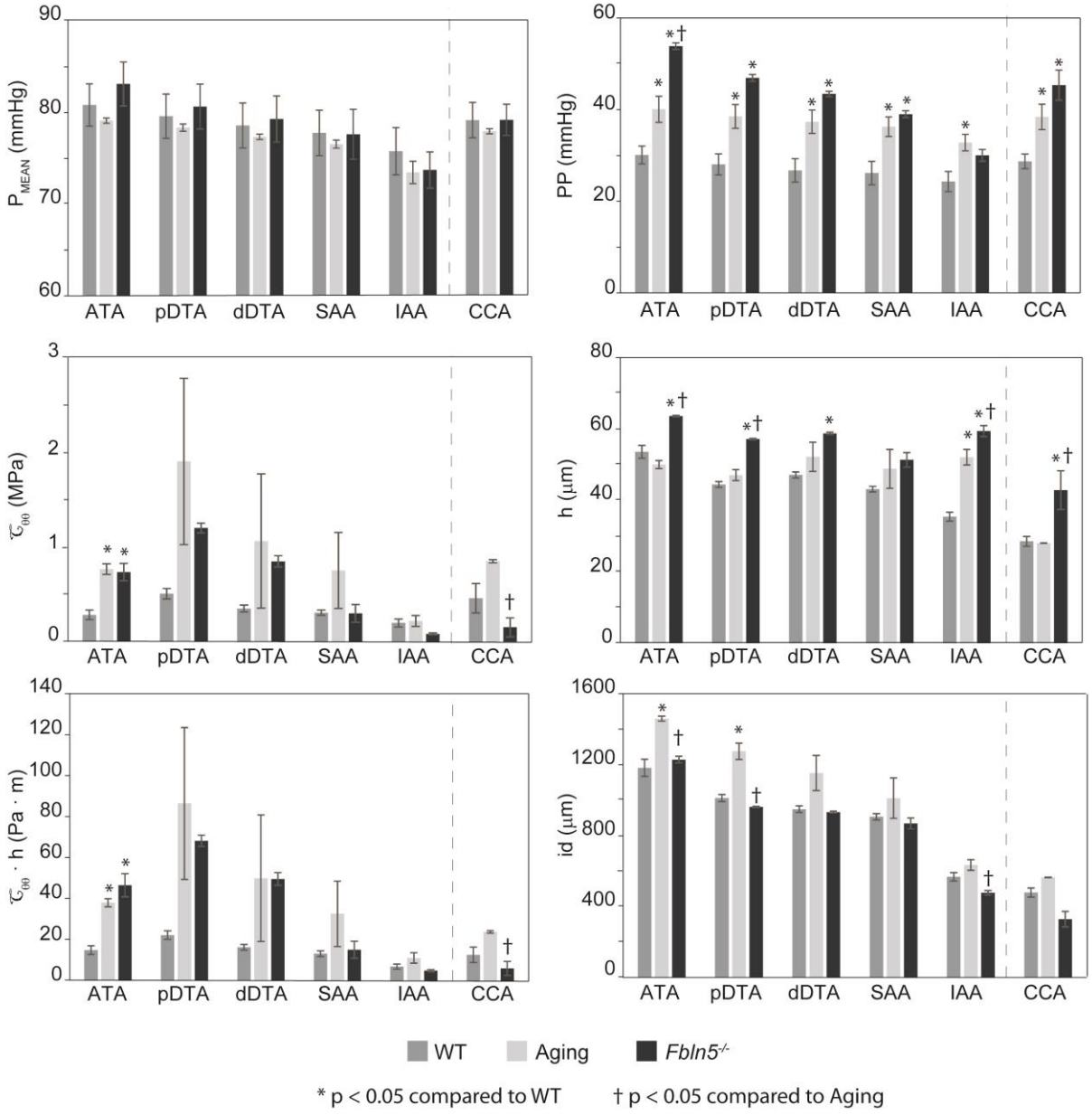


**Figure 4.6.** Regional values (mean ± SEM) of mean blood pressure ($P_{MEAN}$), pulse pressure (PP), circumferential material stiffness ($\mathcal{T}_{\theta\theta}$), wall thickness (*h*), structural stiffness ($\mathcal{T}_{\theta\theta}$**h*) and internal diameter (*id*) for WT_F (gray bars), Aging_F (light gray bars) and KO_F (black bars) mice.

**Table 4.6.** Values of internal diameter (*id*), in μm, measured from 3D anatomical models at ATA, pDTA and dDTA, SAA, IAA, and CCA.

| | Aging_Female (Aging_F) | | | | |
|---|---|---|---|---|---|
| | **Aging_F1** | **Aging_F2** | **Aging_F3** | **mean** | **std** |
| **ATA** | 1481 | 1454 | 1433 | 1456 | 24 |
| **pDTA** | 1361 | 1206 | 1251 | 1273 | 80 |
| **dDTA** | 1324 | 1143 | 983 | 1150 | 171 |
| **SAA** | 1168 | 1069 | 788 | 1009 | 197 |
| **IAA** | 644 | 677 | 575 | 632 | 52 |
| **CCA** | - | 561 | 564 | 563 | 2 |

### 4.3.3 Computed Pulse Wave Velocity

We calculated computed values of ATA-IAA *PWV*; specific values are in Table 3.8 along with path length and computed transit time. Figure 4.7 compares values of computed ATA-IAA *PWV* with corresponding values of spatially averaged structural stiffness (i.e., a weighted mean within the segments of interest, considering the length of each segment as a weight). Between Aging_F and KO_F groups we observe a difference in PWV of 4% corresponding to a difference in stiffness of 22%, this is due to the higher structural stiffness heterogeneity observed in the Aging group.

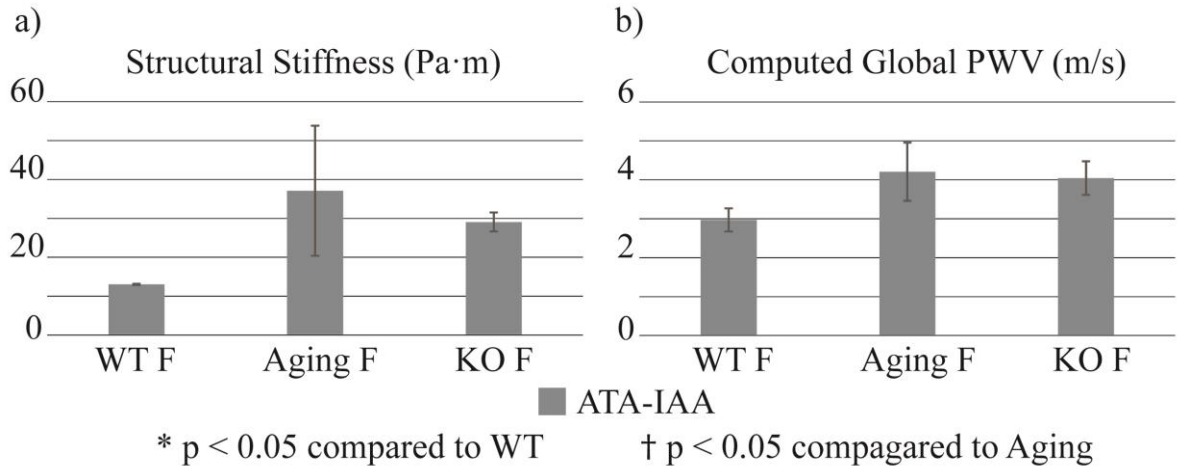


**Figure 4.7.** Values (mean ± SEM) of measured structural stiffness (left) and computed *PWV* (right) for WT, Aging and KO female groups. Both quantities are calculated from ascending thoracic aorta to infrarenal abdominal aorta (ATA-IAA).

**Table 4.7.** Values of aortic length (L) in mm, aortic pulse transit time (PTT) in ms, and pulse wave velocity (PWV) in m/s, from aortic root to infrarenal abdominal aorta (ATA-IAA) for Aging_F group.

| Aging_Female (Aging_F) | | | |
|---|---|---|---|
| **Mouse** | **PTT** | **L** | **PWV** |
| **Aging_F1** | 0.013 | 66.29 | 5.26 |
| **Aging_F2** | 0.0123 | 51.82 | 4.21 |
| **Aging_F3** | 0.0163 | 51.30 | 3.15 |
| **mean** | 0.014 | 56.47 | 4.21 |
| **std** | 0.002 | 8.51 | 1.06 |

## 4.4 Discussion

In the past decades central arterial stiffness has increasingly been recognized as fundamental to predict and prevent cardiovascular events[2,4,18,19]. The use of advanced computational models can help us investigate the effects of regional changes in wall properties on global and local hemodynamics. We previously developed FSI models of hemodynamics in the central arteries of Wild Type and Fbn5$^{-/-}$ mice under anesthetized conditions[10] (Chapter 3). The Fbn5$^{-/-}$ mouse is a model of advance vascular aging, due to a compromised genesis of elastin fibers[9]. In this chapter we investigated hemodynamics in naturally aged mice, which present a vascular aging phenotype mainly due to increased deposition of collagen and GAGs.

One key contribution of this study is the development of the first FSI model of anesthetized female 100 week-old mice, to which other results can be compared to. Furthermore, we previously developed and presented (Chapter 3) a methodology to assign mouse-specific hemodynamics and wall mechanics data to micro-CT based models of the central vasculature using body mass based allometric scaling of quantities such as CO, $R_{TOT}$, and $C_{TOT}$. Local values of biaxial material stiffness and wall thickness can also be assigned in a mouse-specific manner, with associated linear interpolations as needed. In this chapter we demonstrated that the methods proposed in Chapter 3 can be applied to a different group of mice.

Herein, we compared the computed hemodynamics of female 100 week-old mice to both 20 week-old female wild type and Fbn5$^{-/-}$ mice. We found that both Aging_F and KO_F groups exhibit an increase in cPP due to an increase in $P_{SYS}$; the increase in KO_F is larger

compared to Aging_F. In the distal part of the aorta (IAA) we observed a statistically significant higher PP in the Aging_F compared to WT, but not in the KO. Furthermore we observed a marked increase in wall thickness *h* for the KO groups compared to both WT and Aging along the entire aorta. The Aging_F group has statistically higher *h* values compared to WT only in the IAA. Aging females have statistically higher $C_{\theta\theta}$*$h$ and $C_{\theta\theta}$ at the ATA compared to WT female. These findings suggest that:

i) KO_F present greater loss of functionality in the proximal part compared to the distal part of the aorta, consistent with the expected differential elastin:collagen ratios in normalcy and loss of fibulin-5 affecting elastogenesis. Conversely, naturally aged mice do not show different degrees of loss of functionality in the aorta. Computed results of hemodynamics show an equal vascular aging phenotype in both the thoracic and abdominal aorta.

ii) Both Aging_F and KO_F exhibit a vascular aging phenotype, although to somewhat of a greater extent in fibulin-5 deficiency mice.

We observed a higher degree of variability in the Aging_F group, especially in the tissue properties (Figure 4.6), while KO_F mice are more consistently different than WT_F. Vascular aging does not progress at the same pace in all subjects and time is not the only factor that impacts aging. For this reason we summarized the computed results for the Aging_F subject who exhibited the highest degree of vascular aging phenotype in Figure 4.3.

The approach employed in this work allowed us to investigate the distribution of total resistance and compliance ($R_{TOT}$ and $C_{TOT}$) among central ($R_{central}$ and $C_{central}$) and peripheral ($R_{peripheral}$ and $C_{peripheral}$) vasculature. Figure 4.4b shows the comparison of compliance distribution between WT_F, Aging_F and KO_F groups of mice. Although not significant, we observe a progressive decrease in $C_{central}$ from WT_F to KO_F. The decrease in $C_{central}$ in the Aging_F compared to WT_F can be explained by an increase in structural stiffness, besides the larger diameters. The KO_F exhibit the smallest $C_{central}$ due to both the increase in structural stiffness and smaller diameters. Hence, the higher degree of severity of the vascular aging phenotype presented by KO_F compared to Aging_F is also reflected by the lower compliance of the central vessels.

## Bibliography


1. Lakatta EG, Wang M, Najjar SS. Arterial aging and subclinical arterial disease are fundamentally intertwined at macroscopic and molecular levels. *Med Clin North Am*. 2009;93(3):583-604. doi:10.1016/j.mcna.2009.02.008.

2. Laurent S, Boutouyrie P. The structural factor of hypertension: large and small artery alterations. *Circ Res*. 2015;116(6):1007-1021. doi:10.1161/CIRCRESAHA.116.303596.

3. Mitchell GF. Effects of central arterial aging on the structure and function of the peripheral vasculature : implications for end-organ damage. *J Appl Physiol*. 2008;105:1652-1660.

4. Safar ME. Arterial aging-hemodynamic changes and therapeutic options. *Nat Rev Cardiol*. 2010;7(8):442-449. doi:10.1038/nrcardio.2010.96.

5. Ferruzzi J, Madziva D, Caulk AW, Tellides G, Humphrey JD. Compromised mechanical homeostasis in arterial aging and associated cardiovascular consequences. *Biomech Model Mechanobiol*. 2018;17(5):1281-1295. doi:10.1007/s10237-018-1026-7.

6. Sherratt MJ. Tissue elasticity and the ageing elastic fibre. *Am Aging Assoc*. 2009;31(4):305-325. doi:10.1007/s11357-009-9103-6.

7. Davis E. Stability of elastin in the developing mouse aorta: a quantitative radioautographic study. *Histochemistry*. 1993;100(1):17-26.

8. O'Rourke MF, Hashimoto J. Mechanical factors in arterial aging. A clinical perspective. *J Am Coll Cardiol*. 2007;50(1):1-13. doi:10.1016/j.jacc.2006.12.050.

9. Wan W, Gleason RL. Dysfunction in elastic fiber formation in fibulin-5 null mice abrogates the evolution in mechanical response of carotid arteries during maturation. *AJP Hear Circ Physiol*. 2013;304(5):H674-H686. doi:10.1152/ajpheart.00459.2012.

10. Cuomo F, Ferruzzi J, Agarwal P, et al. Sex-dependent differences in central artery haemodynamics in normal and fibulin-5-deficient mice: implications for ageing. *Proc R Soc A*. 2019;475:20180076. doi:10.1098/rspa.2018.0076.

11. Gleason RL, Gray SP, Wilson E, Humphrey JD. A multiaxial computer-controlled organ culture and biomechanical device for mouse carotid arteries. *J Biomech Eng*. 2004;126(6):787-795. doi:10.1115/1.1824130.

12. CRIMSON CardiovasculaR Integrated Modelling and SimulatiON. (2017) Available from: http://www.crimson.software.

13. Sahni O, Müller J, Jansen KE, Shephard MS, Taylor CA. Efficient anisotropic adaptive discretization of the cardiovascular system. *Comput Methods Appl Mech Eng*. 2006;195:5634-5655.

14. Figueroa CA, Vignon-Clementel IE, Jansen KE, Hughes TJR, Taylor CA. A coupled momentum method for modeling blood flow in three-dimensional deformable arteries. *Comput Methods Appl Mech Eng*. 2006;195:5685-5706.

15. Baek S, Gleason RL, Rajagopal KR, Humphrey JD. Theory of small on large: Potential utility in computations of fluid–solid interactions in arteries. *Comput Methods Appl Mech Eng*. 2007;196:3070-3078.

16. Ferruzzi J, Bersi MR, Humphrey JD. Biomechanical phenotyping of central arteries in health and disease: advantages of and methods for murine models. *Ann Biomed Eng*. 2013;41(7):1311-1330. doi:10.1007/s10439-013-0799-1.

17. Gaddum NR, Alastruey J, Beerbaum P, Chowienczyk P, Schaeffter T. A technical assessment of pulse wave velocity algorithms applied to non-invasive arterial waveforms. *Ann Biomed Eng*. 2013;41(12):2617-2629.

18. Laurent S, Boutouyrie P, Asmar R, et al. Aortic stiffness is an independent predictor of all-cause and cardiovascular mortality in hypertensive patients. *Hypertension*. 2001;37:1236-1241. doi:10.1161/01.HYP.37.5.1236.

19. Humphrey JD, Harrison DG, Figueroa CA, Lacolley P, Laurent S. Central artery stiffness in hypertension and aging: a problem with cause and consequence. *Circ Res*. 2016;118(3):379-381. doi:10.1161/CIRCRESAHA.115.307722.

## Chapter 5. An Experimental-Computational Study of Catheter Induced Alterations in Pulse Wave Velocity in Anesthetized Mice

Federica Cuomo[1,3,*]

Jacopo Ferruzzi[2,*]

Jay D. Humphrey[2]

C. Alberto Figueroa[1,3,4]

[*]These authors contributed equally

[1]Department of Biomedical Engineering, King's College London, London, UK

[2]Department of Biomedical Engineering, Yale University, New Haven, CT, USA

[3]Departments of Biomedical Engineering, University of Michigan, Ann Arbor, MI, USA

[4]Departments of Surgery, University of Michigan, Ann Arbor, MI, USA

*Annals of Biomedical Engineering. 2015; 43(7): 1555-1570*

***Contributions.*** *All the experimental work explained in this chapter was performed by Dr. Jacopo Ferruzzi at Yale University.*

## 5.1 Introduction

Since the mid-1990s, genetically modified mice have been used widely to study cardiovascular diseases and their treatment. With this increased use of mice came a need for new methods and devices for data acquisition. Many of the requisite measurements are complicated, however, by the smallness of the cardiovascular system and high heart rate in mice; non-invasive and invasive methods of measurement thus remain in continual development. Furthermore, given the difficulty of performing studies on conscious mice, anesthesia is often required for both non-invasive and invasive measurements. Since anesthesia alters heart rate, cardiac output, and blood pressure, these changes must be considered when interpreting data on cardiovascular function. Among the many available anesthetic agents, 1-2% isoflurane delivered by inhalation has been proven to preserve cardiovascular function better than others, with physiologic and hemodynamic parameters closer to those measured under conscious conditions[1].

Like anesthesia, many invasive methods of measuring cardiovascular parameters also alter the very quantity that is of interest. Prime examples include measurement of central (blood) pulse pressure (cPP) and the (pressure) pulse wave velocity (PWV), each of which is typically achieved by introducing a catheter within the vasculature or cardiac chamber either acutely or chronically (as needed for telemetry systems). The potential impact of a pressure catheter on the hemodynamics of the mouse remains unclear from a theoretical perspective and necessarily cannot be evaluated experimentally without invoking many assumptions. There is a pressing need, therefore, to understand better the effects of measurement technique on the data collected and, accordingly, to identify the best methods to assess cPP or PWV. Toward this end, computational modeling offers an objective, nonintrusive approach for evaluating current methods of measurement as well as for identifying possible improvements in experimental design or even new technological approaches to measure hemodynamics in mice.

In this paper, we use a customized version of the well validated fluid-solid-interaction (FSI) code *SimVascular* to compare computational results for a baseline model of anesthetized mouse hemodynamics with experimental data. Following tuning and validation of the baseline model, we evaluate potential effects on the hemodynamics due to the use of two commercially available catheters for measuring cPP and aortic PWV. The latter metric necessarily requires simultaneous acquisition of two pressure or two flow waveforms at two locations along the vascular tree as well as knowledge of the distance between these locations. That is, PWV is typically evaluated as the

distance between two measuring locations divided by a metric of the phase lag for the two recorded waveforms. The computational models considered in this paper reproduce two different approaches to simultaneously acquire pressure waveforms at two different locations. The overall computational model includes a heart model to capture ventricular-vascular coupling, which allows an evaluation of how cardiac output varies with different afterload conditions resulting from either anesthesia or insertion of a catheter.

## 5.2 Methods

### 5.2.1 Biomechanical Experiments

All animal procedures were approved by the Institutional Animal Care and Use Committee of Yale University. Male wild-type mice on a mixed C57BL/6 × 129/SvEv background were used between 20 and 27 weeks of age. Specific experimental and theoretical methods for quantifying physiological variables and biomechanical properties are described in detail elsewhere[2]. Herein, we only review basic procedures and present those data fundamental for informing the present computational model. All *in vivo* data were acquired under isoflurane anesthesia since we sought to capture the hemodynamics under typical experimental conditions. By altering heart rate and cardiac output, anesthesia reduces blood pressure and thus both the vascular geometry (inner radius and wall thickness) and wall stiffness that are important determinants of cPP and PWV.

**Geometry**. The basic computational domain was obtained via vascular corrosion casting. Briefly, a single mouse was euthanized at 27 weeks of age via an overdose of Beuthanasia, the thoracic cavity was opened surgically, and the left ventricle was cannulated at its apex using a 21G needle. The aorta was then flushed with heparinized saline (110 U/kg) and perfusion fixed at 100 mmHg for one hour with 10% formalin. The superior vena cava was used as an exit site during flushing, but was subsequently closed using 6-O sutures to enable pressurization. A Batson's no. 17 Plastic Replica Kit (Polysciences, Warrington, PA) was used to fill the aorta and major branches with plastic while maintaining a perfusion pressure of ~100 mmHg within the ventricle. The mouse was subsequently immersed overnight in an ice bath to allow heat to dissipate while the polymer cured and the body was macerated in 25% KOH. The resulting plastic cast (Figure 5.1a) was digitized using micro-CT (eXplore CT120, GE Healthcare). The image stack had a spatial resolution of 49.217 × 49.217 × 98.434 microns with dimensions of 480 × 328 × 858 voxels. Arterial cross-sections were segmented semi-automatically using a 2D level set method within a

customized version of the open source software package *SimVascular* (SimBios National Center for Biomedical Computing, Stanford, CA), thus yielding a 3D geometric model of the mouse aorta and its major branches (Figure 5.1b).

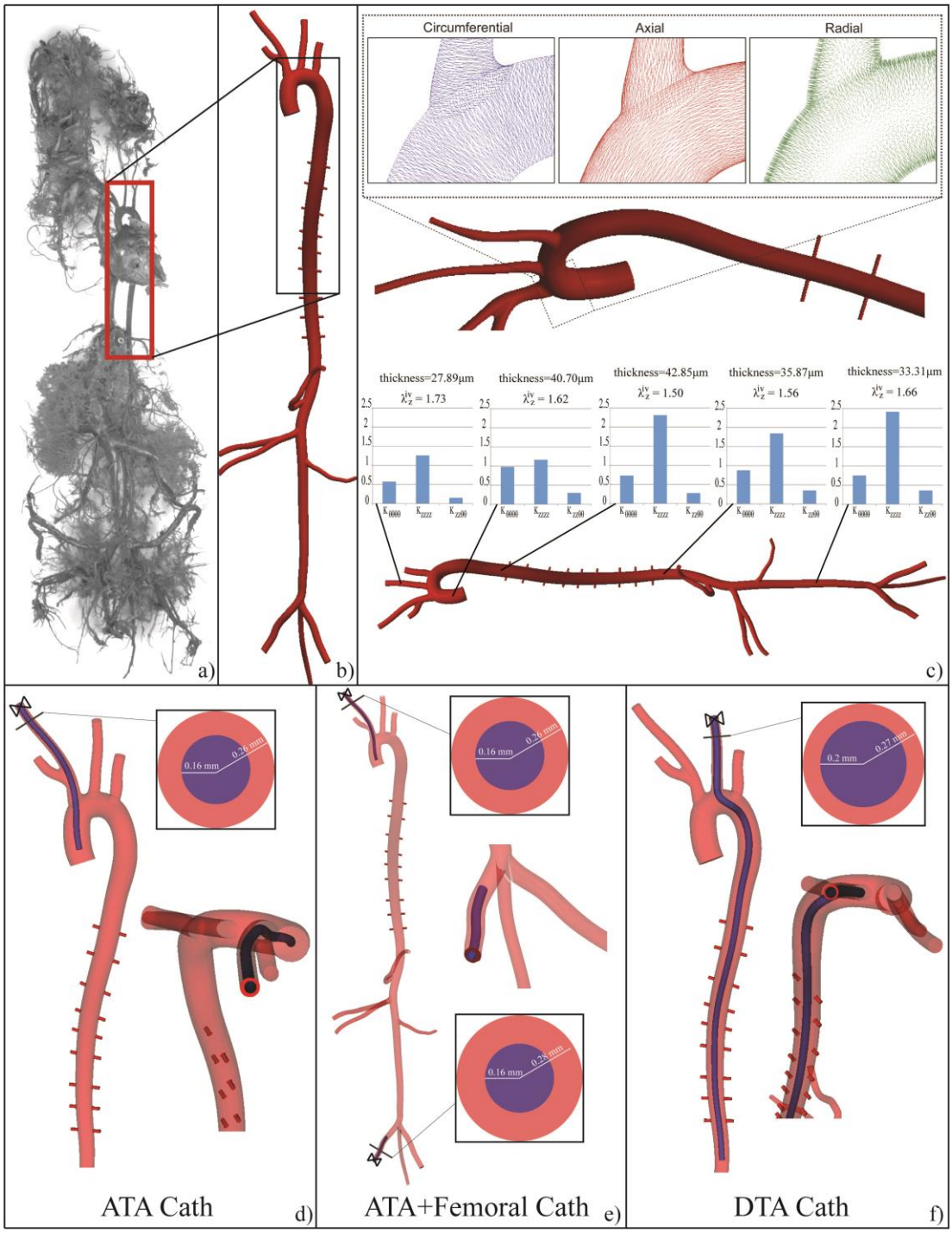


**Figure 5.1.** a) Corrosion cast of the vasculature in an illustrative example of adult mouse; b) Computational model of the aorta and main branches built from the cast; c) Regional biaxial tissue properties in the ATA, DTA, SAA, IAA, and CCA locations, mapped to the mouse-specific geometry; d) ATA catheter model; e) ATA+Femoral catheter model; f) DTA catheter model.

**Physiological measurements.** We used illustrative non-invasive and invasive data collected from another mouse (20 weeks of age) to inform our baseline computational model since the vascular corrosion casting is a destructive technique. Briefly, the mouse was anesthetized using 1.5% isoflurane and secured on a heated surgical platform (Indus Instruments, Houston, TX) to monitor cardiac and respiratory rates. Ultrasound data were collected using a Vevo 2100 system (Visualsonic, Toronto, Canada). B-mode imaging was used to locate the ascending thoracic aorta (ATA), proximal descending thoracic aorta (DTA), suprarenal abdominal aorta (SAA), infrarenal abdominal aorta (IAA), and one common carotid artery (CCA). For each of these sections, M-mode sequences were recorded for a short axis view and used to measure inner diameters at systole and diastole from nine cardiac cycles. Average diameters for the different sections are shown in Table 5.1. Color Doppler imaging was used to find the long axis view that would allow the most accurate measurements of mean blood velocity in both the ATA and IAA. Pulsed Doppler data were thus collected just after the aortic valve in the ATA and just before the iliac bifurcation in the IAA; all measurements were angle corrected. Similar to Trachet et al.[3], we employed the auto-trace function within the Vevo 2100 data analysis software to extract blood velocity waveforms over multiple cardiac cycles. Raw data were analyzed using MATLAB (Mathworks, Natick, MA), including outlier elimination and ensemble averaging to obtain an average waveform representing a mean cardiac cycle. Similar to Gaddum et al.[4], we defined the foot of the blood velocity waveform as the intersection between two tangents: the horizontal tangent intersecting its diastolic minimum and the tangent to the maximum systolic gradient, which was evaluated using a $4^{th}$-order accurate central differences scheme (given the constant sampling rate). Hence, the aortic pulse transit time was calculated as the time lag between the average feet of the ATA and IAA blood velocities. Finally, a SPR-1000 pressure catheter (Millar, Houston, TX) having a 1F outer diameter tip was inserted via the right common carotid artery and positioned halfway between the aortic root and the base of the brachiocephalic artery. Correct positioning of the pressure transducer was assessed via B-Mode ultrasound imaging and continuous pressure data were recorded over multiple cardiac cycles. Central blood pressures measured under isoflurane anesthesia revealed systolic and diastolic values of 96 and 65 mmHg, respectively. Aortic pressure waveforms were ensemble averaged using the R-peak of the EKG signal to separate adjacent cardiac cycles. The resulting mean ATA pressure waveform was used to inform and to validate our computational model (see Figure 5.2).

**Table 5.1** *In vivo* internal diameters at peak systole and diastole for the five primary arterial segments in the vascular model (ascending thoracic aorta (ATA), descending thoracic aorta (DTA), suprarenal abdominal aorta (SAA), infra-renal abdominal aorta (IAA), common carotid artery (CCA),) as measured by M-mode ultrasound.

| ATA | | DTA | | SAA | | IAA | | CCA | |
|---|---|---|---|---|---|---|---|---|---|
| systole (mm) | diastole (mm) | systole (mm) | diastole (mm) | systole (mm) | diastole (mm) | systole (mm) | diastole (mm) | systole (mm) | diastole (mm) |
| 1.563 | 1.193 | 1.361 | 1.153 | 1.129 | 0.868 | 0.782 | 0.678 | 0.606 | 0.502 |

**Biaxial arterial properties.** Mean biaxial data sets ($n$ = 5 mice, 21.3 ± 0.4 weeks of age) for each of the aforementioned five primary measurement sites (ATA, DTA, SAA, IAA, and CCA) consisted of pressure-diameter (*P-d*) protocols performed separately at three fixed axial stretches (*in vivo* and 5% above and below *in vivo*) and axial force-length (*f-l*) protocols performed separately at four fixed pressures (10, 60, 100, and 140 mmHg). These protocols are designed to characterize the behavior of arterial tissue exposed not only to the luminal pressure, but also to a considerable degree of axial stretching. Experimental pressure, diameter, axial force, and axial stretch data from these seven protocols were reduced using a two-dimensional four-fiber family constitutive model[5] to fit the observed behaviors. Using the theory of small deformations superimposed on large[6], the nonlinear material behavior was linearized to obtain *in vivo* relevant values of anisotropic wall stiffness using the individual *in vivo* value of axial stretch for each region and the mean blood pressure measured invasively under anesthesia (i.e., 75 mmHg). Our FSI formulation (see Section 2.2) employs an enhanced linearized membrane model of the wall, whereby non-zero values of the stiffness tensors are organized within a 5 × 5 matrix for each site[7]. This stiffness matrix is first defined in the cylindrical coordinates of the mechanical testing, but then transformed according to the local *in vivo* coordinate system given by unit normal vectors in circumferential, axial, and radial directions (see Figure 5.1c).

### 5.2.2 Simulation Framework

We employed a multi-scale, multi-domain modeling approach that combines a heart model, a 3D geometrical vascular model, a FSI model to account for the deformability of the central vessels, and Windkessel models to represent the distal vascular beds. Our strategy was, first, to define a baseline computational model for a mouse that reproduced the measured anesthetized conditions and, second, to investigate how PWV is altered by invasive measurements, namely, when assessed using two different commercially available catheter systems.

**Geometry**. Micro-CT measurements of the vascular cast were reconstructed using a customized version of *SimVascular* to obtain a basic geometric model. The primary segments

constituting the model were the aorta (including the ATA, DTA, SAA, and IAA) as well as the subclavian, carotid, renal, mesenteric, celiac, and tail arteries. Despite multiple attempts, the corrosion casting process (euthanized conditions) did not maintain the precise dimensions measured non-invasively (anesthetized conditions), hence diameters reconstructed from the micro-CT data were scaled using *in vivo* data measured with M-mode ultrasound (Table 5.1). Specifically, the centroid and radius were first determined along each vascular segment, then the inner radii were scaled up (or down) such that the mean radius of each segment matched the expected dimension. Different scaling factors were used for each segment; for those vessels for which a known diameter was not available, the scale factor of the closest segment was used. Our casting method did not provide confident visualization of the intercostal arteries, which account for a significant percentage of the cardiac output due to the large size of the mouse rib cage relative to the rest of the body. To render both the pressure gradient along the thoracic aorta and the relevant flow distributions more realistic, intercostal arteries were added using reported reference diameters and branch distances[8]. For each of the nine pairs of intercostals, branch locations were defined as relative lengths along the aorta, namely the path spline (Table 5.2). Branch origins were defined using the mean of the centers of the two nearest aortic segments, weighted by the relative distance to each segment. The intercostal paths were defined as straight lines parallel to the branching angle of the corresponding renal artery and perpendicular to the aorta path.

After building the baseline model (Figure 5.1b), two additional 3D models were created to represent illustrative scenarios whereby commercial catheters are used to assess PWV[9,10]. In the first scenario, two 1F diameter catheters (SPR-1000; Millar, Houston, TX) are inserted and secured in the ATA (via the right CCA) and in the right iliac artery (via the right femoral artery). Herein, we refer to this model as the "ATA+Femoral catheter" (Figure 5.1e). In the second scenario, a 1.2F diameter dual-sensor pressure catheter (Scisense, Inc., London, Ontario, Canada) is inserted through the left CCA down into the descending aorta, covering a much longer length in part due to the need to host two pressure sensors. We refer to this model as the "DTA catheter" (Figure 5.1f). For the sake of completeness, we considered a third scenario in which a single Millar catheter is inserted in the right CCA and into the ATA or left ventricle. This scenario, used experimentally to quantify pressure in the ascending aorta or left ventricle, does not enable the assessment of PWV as it does not provide simultaneous recordings of pressure at two different locations. We refer to this model as "ATA catheter" (Figure 5.1d) and we considered it in order to reproduce the

hemodynamic conditions during our experimental measurements. We assumed that the catheters were stiff and fixed in position throughout the cardiac cycle without contacting any of the vessel boundaries. Furthermore, given that the blood vessel around the catheter is usually occluded with a ligature to prevent bleeding, we enforced complete occlusion in the vessels where the catheters are inserted and secured.

**Table 5.2.** Fractional longitudinal position of the intercostal pairs along the aorta from Guo et al.[8]

| **Location down the aorta** | **Fractional longitudinal position** |
|---|---|
| Aortic Semilunar valve | 0 |
| First pair of intercostal arteries | 0.20±0.013 |
| Second pair of intercostal arteries | 0.24±0.014 |
| Third pair of intercostal arteries | 0.29±0.0066 |
| Fourth pair of intercostal arteries | 0.34±0.0087 |
| Fifth pair of intercostal arteries | 0.38±0.0080 |
| Sixth pair of intercostal arteries | 0.42±0.0064 |
| Seventh pair of intercostal arteries | 0.47±0.0087 |
| Eight pair of intercostal arteries | 0.51±0.0096 |
| Ninth pair of intercostal arteries | 0.55±0.012 |
| Common iliac artery | 1 |

**Mesh adaptation**. Initial meshes of linear tetrahedral elements were generated using meshing libraries in *SimVascular*. A global value for an element size of 0.08 mm was used together with a local refinement in the intercostal arteries. Within these parameters, a mesh of 1.2 million elements and 250 thousand nodes was obtained for the baseline model; 1.9 million elements and 400 thousand nodes for the ATA catheter; 2.1 million elements and 433 thousand nodes for the ATA+Femoral catheter; and 3.1 million elements and 623 thousand nodes for the DTA catheter. These initial meshes were used to run simulations for 7 cardiac cycles using 2700 time steps per cycle ($T_{cycle}$ = 0.135s). The results of these simulations were then used to adapt the meshes based on the distributions of velocity gradients (Hessians) throughout the arterial network. The mesh adaptation algorithm reduced or increased the mesh density in regions of low or high velocity gradients, respectively[11]. Finally, mesh independence studies were performed to obtain converged values of PWV in the final meshes; for this purpose we adopted a two-step mesh adaptation strategy. The final adapted meshes had 1.4 million elements and 273 thousand nodes for the baseline, 1.3 million and 259 thousand nodes for the ATA catheter, 3.0 million and 557 thousand

nodes for the ATA+Femoral catheter, and 1.6 million elements and 315 thousand nodes for the DTA catheter models.

**Computational methods**. Similar to our prior large-scale study of the human arterial tree[12], we used a multi-domain framework to study the hemodynamics in the four different models. Namely, we modeled pressure and velocity fields in all vessels from the heart to the capillaries using a Dirichlet-to-Neuman variational FSI multi-scale method. In particular, we coupled a novel lumped parameter heart model with the inlet surface of the 3D model and we coupled traditional lumped parameter Windkessel models with the outlet surfaces throughout the arterial tree.

The heart model consisted of a series of 0D components representing chambers and valves; the pumping action of the heart, modeled using a time-varying elastance, generated flow and pressure within the coupled 3D model. Details on the heart model can be found elsewhere[13–15]. Parameters for the heart model (Table 5.3) were tuned to obtain a cardiac output of 12 ml/min consistent with reports by others[16] as well as experimentally measured pressures for the baseline model (96 mmHg systolic, 65 mmHg diastolic; see Figure 5.2). Thereafter, the parameters were kept fixed for the three different catheters geometries, with the assumption that the heart has a decreased ability to adapt to different afterload conditions under anesthesia[17,18]. The Windkessel models coupled to each outlet of the 3D domain represent effects from small arteries and arterioles down to the capillary level; for details, see Vignon-Clementel et al.[19]. Specific values of the parameters of the Windkessel models were computed using a 1D theory[20], then tuned to reach reported values flow splits[16,21,22] (Table 5.6) and pressures measured *in vivo* (see Figure 5.2). The tuned parameters (Table 5.4) were used for all four simulations, hypothesizing that effects on vasodilatation or vasoconstriction due to anesthesia did not change with the placement of different catheters.

**Table 5.3.** Heart model parameters tuned to match desired levels of cardiac output given in the literature, and the experimentally measured pressure for the baseline model.

| | | |
|---|---|---|
| Maximum Elastance [Pa $(mm^3)^{-1}$] | | 430 |
| Time to maximum Elastance [s] | | 0.07 |
| Time to Relax [s] | | 0.0125 |
| End Diastolic Volume [$mm^3$] | | 44 |
| Atrial preload [Pa] | | 667 |
| Aortic valve | Resistance [Pa s $(mm^3)^{-1}$] | 0.0001 |
| | Inductance [Pa s $(mm^3)^{-1}$] | 0.0001 |
| Mitral valve | Resistance [ Pa s $(mm^3)^{-1}$] | 0.0001 |
| | Inductance [ Pa s $(mm^3)^{-1}$] | 0.0001 |
| Left ventricular resistance [ Pa s $(mm^3)^{-1}$] | | 0.00015 |

**Table 5.4.** Tuned Windkessel parameters: $R_p$, C, $R_d$ represent, respectively, the proximal resistance, the compliance and the distal resistance for each outlet.

| **Vascular Segment** | **$R_p$** [ Pa s $(mm^3)^{-1}$] | **C** [Pa $(mm^3)^{-1}$] | **$R_d$** [ Pa s $(mm^3)^{-1}$] |
|---|---|---|---|
| Right common carotid | 38.10 | $2.81 \cdot 10^{-4}$ | 560.31 |
| Left common carotid | 44.71 | $3.23 \cdot 10^{-4}$ | 488.08 |
| Right subclavian | 40.29 | $2.69 \cdot 10^{-4}$ | 585.44 |
| Left subclavian | 23.52 | $3.54 \cdot 10^{-4}$ | 443.21 |
| Intercostal | 189.74 | $4.48 \cdot 10^{-5}$ | 3512.80 |
| Celiac | 61.38 | $1.76 \cdot 10^{-4}$ | 892.23 |
| Mesenteric | 68.24 | $1.62 \cdot 10^{-4}$ | 969.62 |
| Right renal | 52.23 | $2.00 \cdot 10^{-4}$ | 785.85 |
| Left renal | 134.53 | $9.55 \cdot 10^{-5}$ | 1651.87 |
| Right iliac | 31.26 | $2.31 \cdot 10^{-4}$ | 680.06 |
| Left iliac | 2.19 | $2.25 \cdot 10^{-4}$ | 696.05 |
| Tail | 11.17 | $8.55 \cdot 10^{-5}$ | 851.70 |

Blood flow – vessel wall interactions are fundamental to wave propagation within an arterial network; they were modeled herein using a coupled-momentum method[23]. The wall properties were prescribed in three steps. First, the regionally dependent values of linearized anisotropic tissue stiffness that were measured *in vitro* (ATA, DTA, SAA, IAA, and CCA) were mapped directly onto segments corresponding to the excised vessels (Figure 5.1c). Second, values of stiffness within regions bounded proximally and distally by measured values were populated by linearly interpolating the local values. Third, by assuming little variation in properties under anesthesia, distal values of stiffness were prescribed based on data taken from the closest location: the stiffness of the iliac and the tail arteries ware prescribed from the IAA, that for middle branches (right and left renal, celiac, mesenteric arteries) were set with values from the nearest point in the abdominal aorta, and that for upper branches (right and left carotids and subclavians) were set to have the stiffness of the common carotid.

To capture the nonlinear behavior, whereby higher stiffness is observed for higher stresses, an iterative approach adjusted the values of stiffness in response to any changes in pressure that resulted from introducing a catheter. Specifically, the linearized stiffness computed from the four-family constitutive model was initially calculated using a mean pressure of 75 mmHg along the entire model, corresponding to the mean aortic pressure measured in the ascending aorta *in vivo*. After running a simulation, the distribution of mean pressures along the model was used to recalculate regional values of linearized stiffness and the simulation was run again with the updated values. This process was adopted for each of the four cases. The iterative procedure was terminated

when the current mean pressures differed from the mean pressures from the previous iteration by less than 2% (Table 5.5).

**Table 5.5.** Tuned linearized circumferential ($C_{\theta\theta}$) and axial ($C_{ZZ}$) material stiffness and thickness (h) for each case at five different locations: ascending thoracic aorta (ATA), descending thoracic aorta (DTA), suprarenal abdominal aorta (SAA), infrarenal abdominal aorta (IAA) and common carotid artery (CAA).

| | | ATA | DTA | SAA | IAA | CAA |
|---|---|---|---|---|---|---|
| Baseline | $C_{\theta\theta}$ (MPa) | 0.98 | 0.72 | 0.88 | 0.75 | 0.57 |
| | $C_{ZZ}$ (MPa) | 1.16 | 2.29 | 1.80 | 2.32 | 1.23 |
| | h (μm) | 40.69 | 42.93 | 36.07 | 33.61 | 27.98 |
| ATA Cath | $C_{\theta\theta}$ (MPa) | 1.05 | 0.76 | 0.90 | 0.73 | 0.60 |
| | $C_{ZZ}$ (MPa) | 1.19 | 2.37 | 1.86 | 2.39 | 1.29 |
| | h (μm) | 40.31 | 42.59 | 35.77 | 33.40 | 27.77 |
| ATA+Femoral Cath | $C_{\theta\theta}$ (MPa) | 1.09 | 0.80 | 0.96 | 0.78 | 0.64 |
| | $C_{ZZ}$ (MPa) | 1.20 | 2.43 | 1.92 | 2.48 | 1.34 |
| | h (μm) | 40.06 | 42.31 | 35.49 | 33.13 | 27.61 |
| DTA Cath | $C_{\theta\theta}$ (MPa) | 1.02 | 0.73 | 0.76 | 0.64 | 0.58 |
| | $C_{ZZ}$ (MPa) | 1.18 | 2.32 | 1.72 | 2.23 | 1.27 |
| | h (μm) | 40.43 | 42.79 | 36.5 | 33.92 | 27.85 |

Lastly, another important aspect in a FSI simulation is the load exerted by perivascular tissue and other organs on the arterial wall. Among other effects, perivascular support helps to prevent non-physiological oscillations in the computed wall motion. A simple traction boundary condition was applied on the outer boundary of each vascular segment in the 3D model to represent the mechanical behavior of the perivascular tissue; details can be found in Moireau et al.[24]. This traction boundary condition consisted of a viscoelastic term with two parameters that can be adjusted to mimic the response of various physiological tissues: $k_s$ is a stiffness coefficient (assumed to be 10 Pa) and $c_s$ is a damping coefficient (assumed to be 10 Pa s m$^{-1}$). The complete weak form of the variational multi-scale FSI formulation of the blood flow problem solved with this approach is thus:

$$\int_{\Omega} \{\boldsymbol{w} \cdot (\rho\dot{\boldsymbol{v}} + \rho\boldsymbol{v}\cdot\nabla\boldsymbol{v} - \boldsymbol{f}) + \nabla\boldsymbol{w}\colon(-p\boldsymbol{I} + \boldsymbol{\tau}) - \nabla q\cdot\boldsymbol{v}\}d\boldsymbol{v} + \int_{\Gamma_{h1}} (q\boldsymbol{v}\cdot\boldsymbol{n} - \boldsymbol{w}\cdot\boldsymbol{t}^h)da$$
$$+ \int_{\Gamma_{h2}} (q\boldsymbol{v}\cdot\boldsymbol{n} - \boldsymbol{w}\cdot\boldsymbol{t}^h)\mathrm{da} + \int_{\Gamma_t} (q\boldsymbol{v}\cdot\boldsymbol{n})da + \int_{\Gamma_s} h\rho^s\boldsymbol{w}\cdot\dot{\boldsymbol{v}}\,dA$$
$$+ \int_{\Gamma_s} h\nabla\boldsymbol{w}\colon\mathcal{L}(\boldsymbol{P}\kappa_s)dA - \int_{\boldsymbol{\Gamma_s}} \boldsymbol{w}\cdot(k_s\boldsymbol{u} + c_s\boldsymbol{v})dA + stabilization\ terms = 0$$

$\forall x(t) \in \overline{\Omega}, \forall t \in [0,T]$.

Here, $\Omega$ is the 3D domain, $\boldsymbol{v}$ is the blood velocity, and $p$ the blood pressure; $q$ and $\boldsymbol{w}$ are test functions for mass and momentum balance; $\rho$ and $\rho^s$ are the mass densities for the blood and wall, respectively; $h$ is the wall thickness; $\Gamma_{h1}$ is the inlet boundary coupled to the heart model; $\Gamma_{h2}$ is the outlet boundary coupled to the Windkessel models; and $\Gamma_s$ and $\Gamma_t$ are the reference and current configurations of the arterial wall over the cardiac cycle, respectively Finally, $\mathcal{L}(\boldsymbol{P}\kappa_s)$ is the linearization of the nonlinear constitutive relation for the arterial wall based on the small-on-large theory[6].

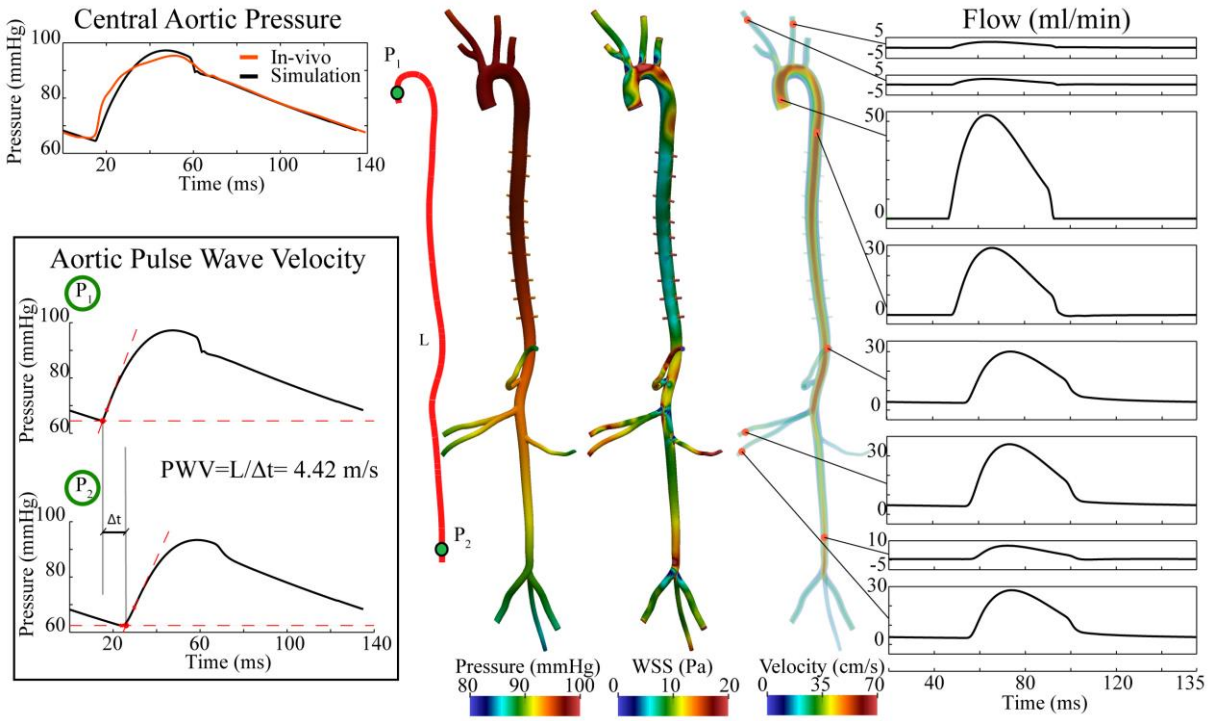


**Figure 5.2.** Computed hemodynamics for the baseline model. Left: Comparison between in vivo and computed central aortic pressure (top) and computed values of PWV based on pressure waves computed at two specific locations, $P_1$ and $P_2$ (bottom). Center: Computed maps of blood pressure, wall shear stress, and blood velocity at peak systole. Right: Illustrative computed flow waveforms at multiple sites along the mouse arterial tree.

**Table 5.6.** Comparison of regional distributions of blood flow (given as cardiac output percentage) between the baseline simulation and values available in the literature for comparable conditions.

| Location | Reference | Technique | # of mice | % CO (data) | % CO (baseline simulation) |
|---|---|---|---|---|---|
| Innominate artery | Feintuch et al.[16] | MRI | 5 | 16.9 | 17.4 |
| Left carotid | Feintuch et al.[16] | MRI | 5 | 10.4 | 10.0 |
| Infrarenal abdominal aorta | Greve et al.[21] | MRI | 5 | 17.5 | 16.6 |

## 5.3 Results

### 5.3.1 Baseline Hemodynamics

Our baseline model reproduced well diverse data from both the literature and our experiments. Figure 5.2 shows simulated central aortic pressures as well as pulse wave velocities, peak systolic pressures, wall shear stresses (WSS), a volume rendering of the magnitudes of velocity, and a series of flow waveforms at selected locations along the vasculature. The cardiac output produced by the heart model was tuned to 12.03 ml $min^{-1}$, consistent with values reported for the same strain of mice[25],[16]. The central aortic pressure was favorably tuned to match our *in vivo* invasive pressure measurements under anesthesia. Note that neither cardiac output nor ascending aortic pressure were imposed in the simulation; rather, they resulted from the choice of parameters in the heart and Windkessel models, which were adequately tuned to match the experimental data.

Values of PWV from the ascending aorta to the abdominal aorta just before the iliac bifurcation were calculated using an algorithm implemented in MATLAB[4] based on the transient time between two pressure waveforms recorded simultaneously at two different locations (Figure 5.2, left bottom panel). The simulated transient time $\Delta t$ was 10.8 ms, close to the experimentally measured time of 12.7 ms. Given that the distance between the two sites along the aortic centerline is 47.78 mm, a PWV of 4.42 m $s^{-1}$ was obtained in the computations, which is similar to values reported in the literature (3.79 m $s^{-1}$) for the same strain of mouse[26] (noting that each mouse has a slightly different geometry and material properties, and each experiment has a different depth of anesthesia).

The computed distribution of flow also matched data in the literature. In particular, we compared our results with those of Feintuch and colleagues (Table 5.6) who measured flow in the innominate artery and left common carotid using MRI[16]. Their measurements were under 1.6% isoflurane anesthesia, similar to that used in our *in vivo* studies. We also compared our computed flow waveforms to those reported by Greve and colleagues for the infra-renal abdominal aorta in anesthetized mice[21] (Table 5.6). Lastly, as revealed by the left panel of Figure 5.2, the qualitative shapes of the computed flows agreed well with those previously reported in experiments by Hartley[27]. Overall, because we reproduced cardiac output, ascending aortic pressure, aortic-iliac PWV, flow distributions, and qualitative shapes of the flow waveforms, we were confident that the model captured well the baseline hemodynamics of a healthy mouse under anesthesia.

### 5.3.2 Comparison of Hemodynamics in Baseline and Catheter Models

It is well known that anesthesia relaxes vascular tone and baroreflex sensitivity, thus resulting in hypotension[28]. Diminished blood pressure is due, in part, to a decrease in both peripheral vascular resistance and cardiac output due to the anesthesia. In particular, isoflurane disrupts normal cardiovascular function by affecting the vasculature, myocardium, and sympathetic and parasympathetic branches of the autonomous nervous system[29]. In general, it is difficult to assess the extent to which different drugs alter the ability of the cardiovascular system to react to changes in afterload following anesthesia, but it is well accepted that this ability is compromised[17,18]. Therefore, when modeling the hemodynamics in the catheter models, we assumed that characteristics of the arterial system (e.g., parameters defining the heart and Windkessel models) remained constant despite any changes in afterload introduced by the presence of the catheters. Figure 5.3 summarizes the computed hemodynamics for the baseline, ATA catheter, ATA+Femoral catheter, and DTA catheter models. The left side of the figure compares flow (dashed line) and pressure (solid line) at three different locations along the aorta: the ascending thoracic aorta, descending thoracic aorta, and abdominal aorta just proximal to the iliac bifurcation. In particular, we found:

**Ascending Thoracic Aortic (ATA) Location.** Peak and mean flows for the ATA catheter model (cf. Figure 5.1d) decreased by 7.4% and 7.1%, respectively, relative to the baseline model. The peak and mean flow decreased further for the ATA+Femoral catheter to 10.4% and 15.3% and for the DTA catheter model to 15.4% and 11.2%, respectively. In terms of pressure, the ATA catheter induced an increase in peak and mean pressure of 3.0% and 2.7% relative to the baseline model; the ATA+Femoral catheter induced an increase in peak and mean pressure of 4.7% and 4.9% relative to the baseline model; the DTA catheter induced a larger increase in peak and mean pressure of 5.2% and 2.3%.

**Descending Thoracic Aortic (DTA) Location.** The flows in the baseline and ATA catheter models were virtually the same. The peak and mean flows in the ATA+Femoral catheter model were smaller (4.6% and 7.3%) relative to those in the baseline model, and even smaller in the DTA catheter model (18.1% and 2.7%). These results were determined by a combination of reduced cardiac output due to higher afterload and diversion of flow to the upper branches due to the presence of the catheter in the descending aorta (Figure 5.4). In terms of pressure, the ATA catheter induced an increase in peak and mean pressure of 2.3% and 2.4% relative to the baseline model.

The ATA+Femoral catheter induced an increase in peak and mean pressure of 4.6% and 4.9% whereas in the DTA catheter model, the systolic and mean pressures increased by 3.1% and 1.4% relative to the baseline model, respectively.

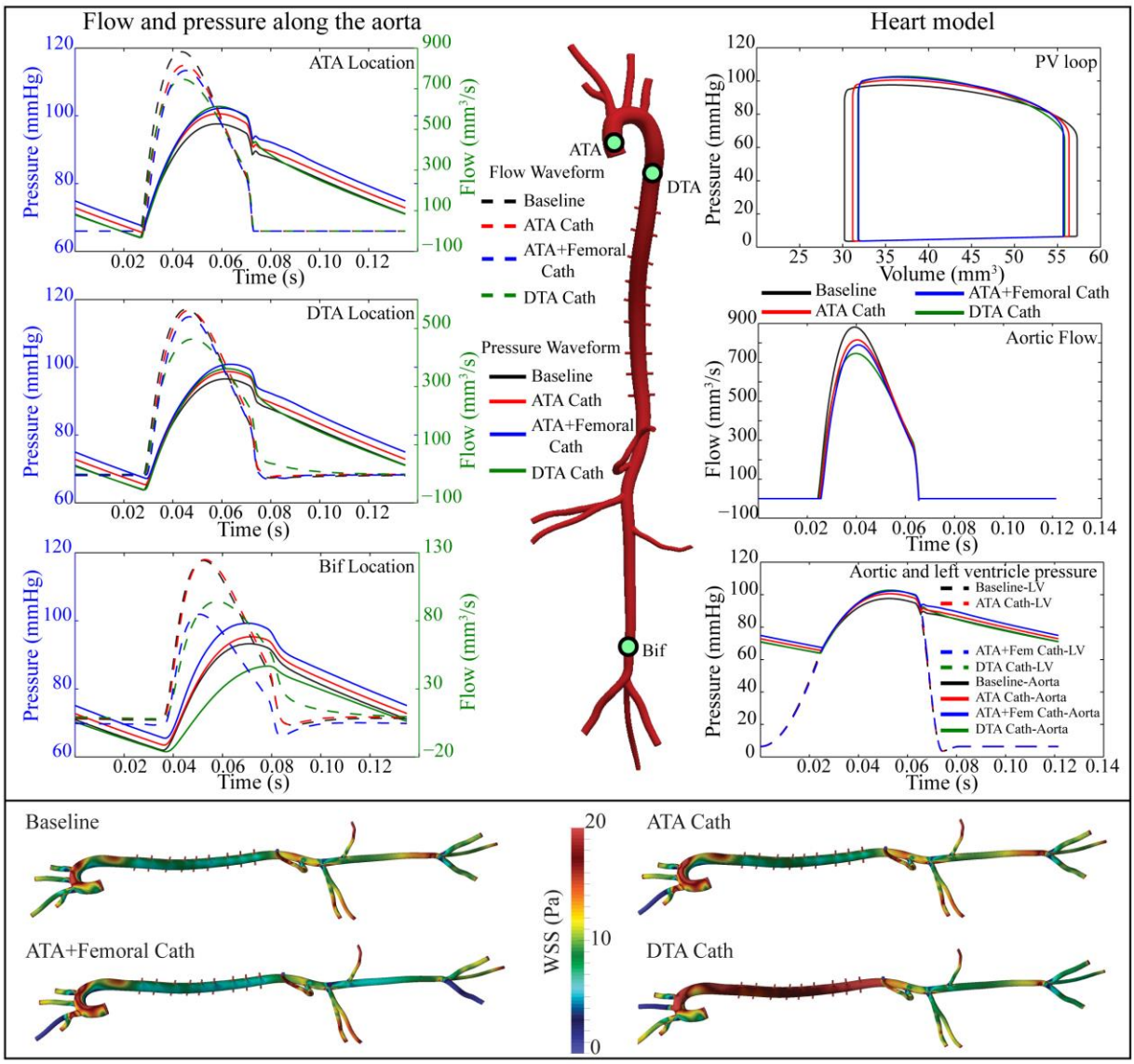


**Figure 5.3.** Comparison of hemodynamics at three sites (in the ATA, in the DTA, and near the aorto-iliac bifurcation – Bif) in the baseline, ATA catheter, ATA+Femoral catheter, and DTA catheter models.

**Aorto-Iliac Bifurcation (Bif) Location.** The flows in the baseline and ATA catheter were very similar. Peak and mean flow decreased, relative to the baseline model, for the ATA+Femoral catheter model by 31.8% and 38.0% and for the DTA catheter model by 24.3% and 3.0%, respectively. In terms of pressure, the ATA catheter induced an increase in peak and mean pressure of 2.1% and 2.3%, the ATA+Femoral catheter induced an increase in peak and mean pressure of

6.5% and 6.0%, and in the DTA catheter model, the systolic pressure and mean pressure decreased by 7.0% and 3.4% – all relative to the baseline model, respectively. All pressure traces at this location also revealed a clear phase lag relative to those at the ATA location, a clear sign of altered pulse wave propagation, which expectedly was more noticeable due to the longer distance between the ascending and most distal aortic locations.

| | Baseline | ATA Cath | ATA+Femoral Cath | DTA Cath |
|---|---|---|---|---|
| CO ($mm^3/s$) | 200.47 | 186.29 | 176.32 | 178.05 |
| % change | - | -7.1% | -12.1% | -11.2% |

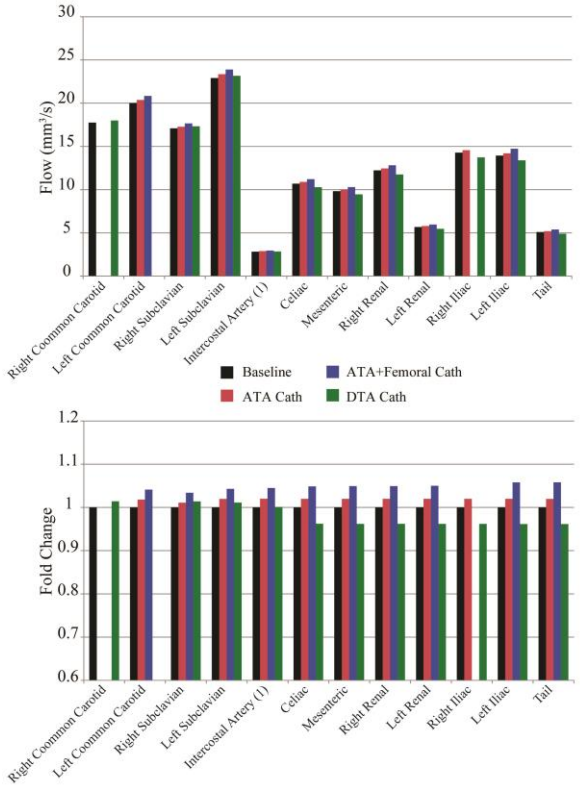


**Figure 5.4.** Comparison of flow splits for the baseline, ATA catheter, ATA+Femoral catheter, and DTA catheter models. The top plot provides total flows to different branches; the bottom plot shows differential splits as fold changes with respect to the baseline model for each catheter model.

The right side of Figure 5.3 also compares left ventricular function for the four models by examining the pressure-volume loop, aortic flow, and aortic and left ventricular pressures. Vessel occlusion and catheter insertion resulted in decreased stroke volume and increased left ventricular and ascending aortic pressure compared to the baseline model. These changes were smaller in the ATA catheter compared to the ATA+Femoral catheter and DTA catheter models. The bottom panel of Figure 5.3 shows a comparison between the contours of peak systolic WSS for the

different models. As expected, the DTA Cath has a high impact on aortic WSS due to the reduction of luminal area caused by the catheter. Conversely, both the ATA + Femoral Cath and the ATA Cath show similar WSS to the baseline model. Lastly, the occluded vessels at the various catheter insertion points have null WSS.

Figure 5.4 shows flow splits given as a fraction of total regional flow (top panel) and splits given as fold change with respect to the baseline (bottom panel) for all the models. As expected, the right and left common carotids and femoral arteries show no flow when they were the site of access for the different catheters. There was less flow in the lower vessels for the DTA catheter because of the larger resistance in the distal aorta. The ATA+Femoral case resulted in a larger proportion of flow going to all vessels that remained patent, as expected.

The computations revealed that the different catheters affect PWV in different ways (Table 5.7). A summary of the results is presented in Figure 5.5. Figure 5.5a shows results of global (aorto-iliac) PWV, whereas Figure 5.5b shows regional values of PWV for the different models. Briefly, the aortic-to-iliac PWV increased in the ATA+Femoral catheter model by 3.8% relative to the baseline case (4.59 m $s^{-1}$ vs. 4.42 m $s^{-1}$) due to an overall increase in pressure in the system. Conversely, the DTA catheter model showed a reduction in PWV of 7.7% relative to baseline (4.08 m $s^{-1}$ vs. 4.42 m $s^{-1}$). These results produced a total difference in the PWV estimate between the two cases of 11.5%, a discrepancy that may be considered significant. Finally, the ATA catheter model results in a modest increase in PWV of 2.9% relative to baseline (4.55 m $s^{-1}$ vs. 4.42 m $s^{-1}$). The bottom part of Panel a) compares PWV as measured by the "ATA+Femoral" and "DTA" configurations with corresponding values measured in the baseline model. These measurements show discrepancies larger than the above reported aorto-iliac PWV. The "ATA+Femoral" configuration over-estimated the baseline PWV by 7.29%, whereas the "DTA" configuration under-estimated it by 9.35%. It is important to recall that these two approaches fundamentally measure PWV at different locations. Panel b) of Figure 5.5 reports local PWV for the baseline and three catheter models. A theoretical justification for the changes in PWV due to the presence of a catheter can be found in the Bramwell and Hill equation, which is derived from the Moens-Korteweg formula through a few substitutions[30]. This relationship $PWV = \sqrt{(V\Delta P)/(\rho dV)}$ was applied to a control volume within the thoracic aorta (Figure 5.6) for all four simulations. Although local values of PWV were higher (5.10, 5.22, 5.42, 4.70 m $s^{-1}$ for baseline, ATA, ATA+Femoral and DTA cases, respectively) than those for aortic-to-iliac PWV extracted

from the simulations (4.42, 4.55, 4.59, 4.08 m $s^{-1}$), similar trends and values in PWV changes arose. It is important to note that these are PWV values within the aortic control volume rather than the aorto-iliac PWV extracted from the computations. In this analysis, diastolic volumes were used as a reference and differences in volume and pressure ($\Delta V$, $\Delta P$) were obtained between the systolic and diastolic configurations.

**Table 5.7.** Aortic pulse wave velocity (in m $s^{-1}$) and % changes relative to the baseline case for the three computational models.

| | **PWV** (m $s^{-1}$) (centerline length) | **PWV** (m $s^{-1}$) (projected length) | **% change** |
|---|---|---|---|
| **Baseline** | 4.42 | 3.52 | - |
| **ATA cath** | 4.55 | 3.62 | 2.86% |
| **ATA+Femoral** | 4.59 | 3.65 | 3.85% |
| **DTA cath** | 4.08 | 3.25 | -7.69% |

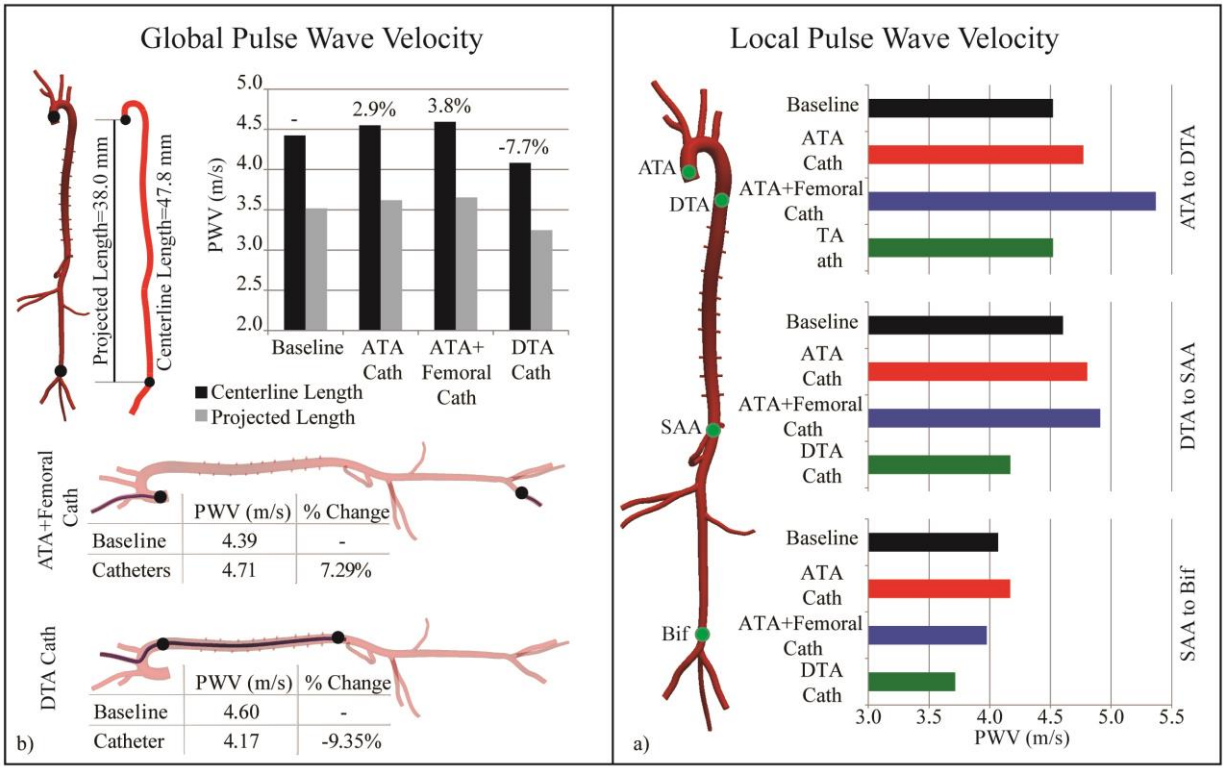


**Figure 5.5.** a) Comparison of aorto-iliac PWV in the baseline, ATA catheter, ATA+Femoral catheter, and DTA catheter models, where the percent change is given with respect to the baseline model (upper part); comparison of PWV measured by the catheters sensors in each feasible case, compared with the baseline model (bottom part); b) Comparison of computed local PWV in the baseline, ATA catheter, ATA+Femoral catheter, and DTA catheter models.

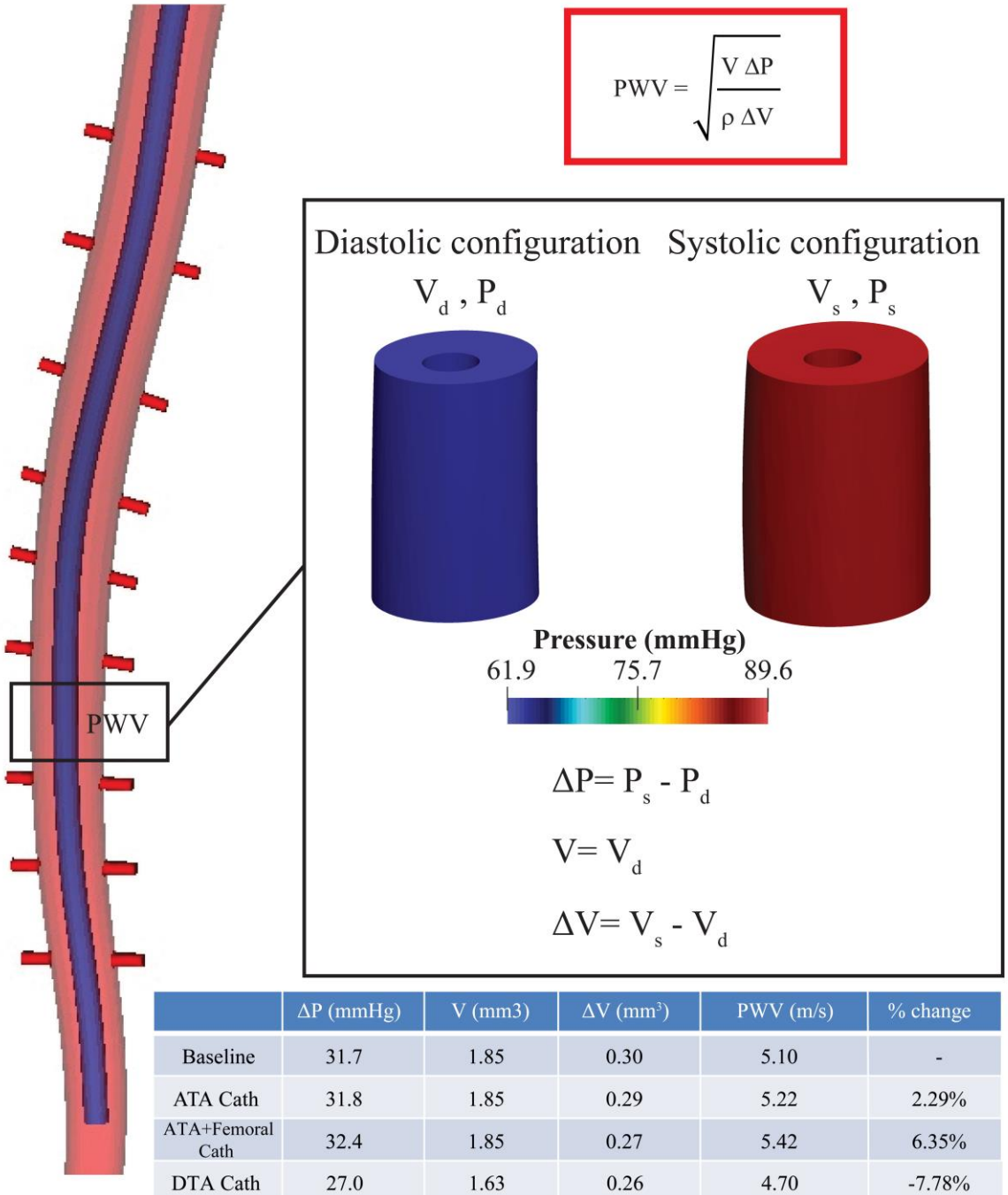


| | ΔP (mmHg) | V (mm3) | ΔV (mm³) | PWV (m/s) | % change |
|---|---|---|---|---|---|
| Baseline | 31.7 | 1.85 | 0.30 | 5.10 | - |
| ATA Cath | 31.8 | 1.85 | 0.29 | 5.22 | 2.29% |
| ATA+Femoral Cath | 32.4 | 1.85 | 0.27 | 5.42 | 6.35% |
| DTA Cath | 27.0 | 1.63 | 0.26 | 4.70 | -7.78% |

**Figure 5.6.** Control volume for the Bramwell and Hill analysis; volume and pressure are shown in systolic and diastolic configurations.

## 5.4 Discussion

Animal models offer many advantages in cardiovascular research, including the ability to match *in vivo* and *in vitro* data and to collect longitudinal information. In the case of mice, however, measurements can be complicated by the small size (inner diameter of central arteries ranging between 500 and 1500 μm) and fast heart rate (between 400 and 600 bpm). Central pulse

pressure (cPP) and pressure pulse wave velocity (PWV) have become important measurements in humans as well as in animal models. As the most sensitive marker of arterial stiffness, PWV has been measured in mice using a variety of experimental procedures, both invasive and non-invasive. Invasive procedures involve the insertion of a fluid-filled cannula or a catheter within the arterial lumen, hence allowing for measurements of blood pressure. The device diameter is often much smaller than the lumen diameter in humans, but such is not the case in mice because of their small vessels The inherent risk of such procedures is that the presence of the measuring tool can alter the global hemodynamics and thus affect the physical quantities of interest. Marque et al.[31] used chronically implanted polyethylene cannulas having an outer diameter of 1.83F to measure PWV between the descending thoracic aorta and the abdominal aorta in a mouse model of Marfan syndrome. Jung et al.[9] instead employed a smaller catheter (diameter of 1.2F) which was introduced through a large portion of the descending aorta and possibly into the abdominal aorta (cf. their Figure 5.5a and Figure 5.1e herein). Finally, Weisbrod et al.[10] used the same pressure catheter used in our measurements (diameter of ~1F) and recorded blood pressure waveforms simultaneously from two locations along the aorta (arch and infrarenal abdominal aorta).

Non-invasive procedures instead involve measurements of waveforms associated with the arterial pressure, such as the arterial distensibility and the blood velocity. Hartley et al.[22] showed that the upstroke of the blood velocity waveform measured via pulsed-wave Doppler in different sections of the aorta (arch and infrarenal abdominal aorta) coincides with the upstroke of the tonometric pressure waveform at the same sites, thus justifying measurements of PWV from the Doppler velocity signal. Currently, Doppler velocimetry represents the most reliable way to measure PWV non-invasively. Yet, the majority of studies in the literature employ commercial ultrasound systems such as the Visualsonic Vevo 770 or 2100 where measurement of the time intervals between the peak of the R-wave and the foot of the blood velocity signals must be performed manually within the commercial data analysis software. Based on our experience, automatic measurements performed on the recorded waveforms are much more reliable than manual measurements over few cardiac cycles. For this reason, we extracted raw blood velocity waveforms and measured pulse transit times over 25 to 30 cardiac cycles using a custom MATLAB script. Other non-invasive methods to assess PWV in mice include the measurement of local flow and cross-sectional area[32] or applanation tonometric signals[33]. The flow-area method represents only an indirect estimate of local PWV based on a set of assumptions rooted in linear elasticity,

while applanation tonometry is much more sensitive to noise and interfering respiratory movements than Doppler velocimetry. Finally, it should be noted that for each of the aforementioned methods, the major source of variability results from measuring the distance between the sites where the proximal and distal waveforms were recorded. Such distances should be evaluated along the centerline of the aortic region of interest, whereas most frequently is approximated by measuring the distance between the probe locations on the skin surface.

Instrumentation or equipment may disturb the characteristics of the system being assessed by perturbing different fields of interest. A tacit assumption is that such perturbations should be negligible in a well-designed experiment. One aim of this study was to assess, using a nonintrusive computational tool, the degree of changes in hemodynamics due to the presence of commercially available catheters used in murine experiments. To this end, four main scenarios were considered: a baseline model represented by a healthy mouse under anesthesia whereas the same overall geometric model and anesthetized conditions were used to model catheters placed within the ascending thoracic aorta and femoral artery or along the descending thoracic aorta. Our computational approach thus allowed us to assess roles of the catheter alone, independent of possible variations in experimental conditions as would be present in experimental assessments.

We were able to reproduce physiological pressure waveforms, flow distributions, and values of PWV using the following methods: a multi-domain method that couples a heart model with the ascending aorta and Windkessel models for all major vascular outlets in the 3D vascular model, a coupled-momentum method for FSI that included regional variations in anisotropy and wall stiffness, an external tissue boundary condition to represent perivascular support, and a method for a posteriori gradient-based mesh adaptation. This is the first time that this combination of methods has been achieved in the mouse vasculature, which was necessary to realistically capture all of the available experimental hemodynamic data. In contrast, most prior computational fluid dynamics models for mice employ the rigid wall assumption and/or simplified geometries (e.g. [3,16,34]), which disallow (or sometimes entirely preclude) accurate calculations of blood pressure and PWV despite possibly achieving good estimates of the velocity field.

Using a coupled heart model, rather than imposing flow or pressure as an inlet boundary condition, was of particular importance herein for it allowed us to investigate changes in cardiac output among all the different cases and, more importantly, to obtain more reliable results. The larger the volume occupied by the catheter within the vasculature, the greater the resistance that

the heart has to work against, and thus the lower the cardiac output. Assuming that the cardiovascular system is not able to adjust to a changing afterload under anesthesia, parameters tuned for the baseline model were fixed for each catheter simulation. That is, we assumed that following the initial vasodilatation or vasoconstriction induced by the anesthesia, the heart, arteries, arterioles and capillaries would lose most of their ability to adapt acutely. Such an assumption needs to be evaluated experimentally.

Placement of the DTA catheter caused, relative to the baseline model, a decrease in cardiac output, a decrease in flow to the distal branches, and a lower PWV. All of these outcomes appear to have been due primarily to the volume occupied by the catheter, which effectively represented a large resistance that reduced cardiac output and diverted more flow to the upper branches where the resistance was smaller. Larger catheters than used in our simulations can be found in literature (e.g. [35,36]), and therefore probably have even greater effects on the hemodynamics. Conversely, we found that the combination of catheters in the "ATA+Femoral" case resulted in similar drop in cardiac output, and an increase in PWV due to an overall increase in pressure in the system. Finally, it is important to note that the calculation of PWV is very sensitive to the distance between locations where the pressure is measured. Figure 5.5 compares values of PWV when computed with the actual length travelled by the pressure wave between measurement sites ("centerline length", 47.8 mm in the case considered here) and with the "projected length" between measurement sites (38.0 mm in this case). This "projected length" is what is utilized in most experiments, and it may significantly under-estimate the reported values of PWV: the difference was 21% for the example considered here, but this difference may be much larger for mice with more tortuous aortas.

**Limitations.** The baseline murine hemodynamics presented in this paper correspond to a single illustrative case, where different measurements were taken in different animals. We did not assess potential differences in errors across multiple mice, including those of different ages (and hence body mass), genotypes, or sex. Given the limited sizes of the commercially available catheters, it is likely that the degree of the errors will vary from mouse to mouse and similar simulations would be useful depending on the groups of mice to be studied. Indeed, there is variability even within the same age, sex, and genotype and variability in heart rate and blood pressure depending on the anesthetic used. Ultimately, a careful comparison across all possible variations would be useful, to include an uncertainty quantification given the spatial and temporal resolutions available for

measuring the requisite geometries, properties, and applied loads needed for formulate the initial boundary value problem. In our work cardiac output and central pressure were not measured in the same animal. However, the value of cardiac output is coherent with the combination of blood velocity and diameter of the vessel measured in the ascending thoracic aorta with Ultrasound. Lastly, in our FSI method, the edges of each outlet surface as well as the inlet surface are fixed in space; the latter does not allow the motion of the heart or its effects on the extension of the ascending aorta to be captured. Although future models should include this complexity, we do not expect that this limitation has an important impact on the computed PWV, which is mainly determined by the geometry of the aorta and the arterial stiffness.

### 5.4.1 Conclusion

The present results suggest that two catheter systems commonly used to assess PWV in mice perturb the hemodynamics in different ways: even though the reduction in cardiac output is similar, the dual catheter approach ("ATA+Femoral") increases PWV by increasing pressure in the system due to the higher peripheral vascular resistance offered by two completely occluded vessels. Conversely, the dual sensor, single catheter approach ("DTA") decreases the PWV by decreasing the pressure in the system due to higher viscous loses in the aorta. Furthermore, it is important to note that these two systems fundamentally measure PWV at two different locations, thus different values would be obtained even if the hemodynamic disturbances were negligible.

Whereas the present results reveal general considerations when using catheter-based methods to measure PWV, we note that the extents of these effects will likely be different in smaller versus larger mice, younger versus older mice, and wild-type versus mutant mice. A complete evaluation should address the specific mice to be used.

## Bibliography


1. Janssen BJA, De Celle T, Debets JJM, Brouns AE, Callahan MF, Smith TL. Effects of anesthetics on systemic hemodynamics in mice. *Am J Physiol Heart Circ Physiol*. 2004;287(4):H1618-24.

2. Ferruzzi J, Bersi MR, Uman S, Yanagisawa H, Humphrey JD. Decreased elastic energy storage, not increased material stiffness, characterizes central artery dysfunction in fibulin-5 deficiency independent of sex. *J Biomech Eng*. 2015;137(3):031007.

3. Trachet B, Renard M, De Santis G, et al. An integrated framework to quantitatively link mouse-specific hemodynamics to aneurysm formation in angiotensin II-infused ApoE -/- mice. *Ann Biomed Eng*. 2011;39(9):2430-2444.

4. Gaddum NR, Alastruey J, Beerbaum P, Chowienczyk P, Schaeffter T. A technical assessment of pulse wave velocity algorithms applied to non-invasive arterial waveforms. *Ann Biomed Eng*. 2013;41(12):2617-2629.

5. Ferruzzi J, Vorp DA, Humphrey JD. On constitutive descriptors of the biaxial mechanical behaviour of human abdominal aorta and aneurysms. *J R Soc Interface*. 2011;8(56):435-50.

6. Baek S, Gleason RL, Rajagopal KR, Humphrey JD. Theory of small on large: Potential utility in computations of fluid–solid interactions in arteries. *Comput Methods Appl Mech Eng*. 2007;196:3070-3078.

7. Figueroa CA, Baek S, Taylor CA, Humphrey JD. A computational framework for fluid–solid-growth modeling in cardiovascular simulations. *Comput Methods Appl Mech Eng*. 2009;198:3583-3602.

8. Guo X, Kono Y, Mattrey R, Kassab GS. Morphometry and strain distribution of the C57BL/6 mouse aorta. *Am J Physiol Heart Circ Physiol*. 2002;283:H1829-H1837.

9. Jung S, Jandu S, Steppan J. Increased tissue transglutaminase activity contributes to central vascular stiffness in eNOS knockout mice. *Am J Physiol Hear Circ Physiol*. 2013;305:H803-H810.

10. Weisbrod R, Shiang T, Sayah L Al, et al. Arterial stiffening precedes systolic hypertension in diet-induced obesity. *Hypertension*. 2013;62:1105-1110.

11. Sahni O, Müller J, Jansen KE, Shephard MS, Taylor CA. Efficient anisotropic adaptive discretization of the cardiovascular system. *Comput Methods Appl Mech Eng*. 2006;195:5634-5655.

12. Xiao N, Humphrey J, Figueroa C. Multi-scale computational model of three-dimensional hemodynamics within a deformable full-body arterial network. *J Comput Phys*. 2014;244:22-40.

13. Kim HJ, Vignon-Clementel IE, Figueroa CA, et al. On coupling a lumped parameter heart model and a three-dimensional finite element aorta model. *Ann Biomed Eng*. 2009;37(11):2153-2169.

14. Lau KD, Figueroa CA. Simulation of short-term pressure regulation during the tilt test in a coupled 3D–0D closed-loop model of the circulation. *Biomech Model Mechanobiol*. 2015;14(4):915-929. doi:10.1007/s10237-014-0645-x.

15. Shroff S, Janicki J, Weber K. Evidence and quantitation of left ventricular systolic resistance. *Am Jouornal Physiol Hear Circ Physiol*. 1985;249(18):H358-H370.

16. Feintuch A, Ruengsakulrach P, Lin A, et al. Hemodynamics in the mouse aortic arch as assessed by MRI, ultrasound, and numerical modeling. *Am J Physiol Heart Circ Physiol*. 2007;292(2):H884-H892.

17. Shimokawa A, Kunitake T, Takasaki M, Kannan H. Differential effects of anesthetics on sympathetic nerve activity and arterial baroreceptor reflex in chronically instrumented rats. *J Auton Nerv Syst*. 1998;72:46-54.

18. Usselman C, Mattar L, Twynstra J, Welch I, Shoemaker J. Rodent cardiovascular responses to baroreceptor unloading: Effect of plane of anaesthesia. *Appl Physiol Nutr Metab*. 2011;36:376-381.

19. Vignon-Clementel IE, Figueroa CA, Jansen KE, Taylor CA. Outflow boundary conditions for 3D simulations of non-periodic blood flow and pressure fields in deformable arteries. *Comput Methods Biomech Biomed Engin*. 2010;13:1-16.

20. Xiao N, Alastruey J, Figueroa CA. A systematic comparison between 1-D and 3-D hemodynamics in compliant arterial models. *Int J Numer Method Biomed Eng*. 2014;30(2):204-231. doi:10.1002/cnm.2598.

21. Greve JM, Les AS, Tang BT, et al. Allometric scaling of wall shear stress from mice to humans: quantification using cine phase-contrast MRI and computational fluid dynamics. *Am J Physiol Heart Circ Physiol*. 2006;291(4):H1700-H1708.

22. Hartley CJ, Taffet GE, Michael LH, Pham TT, Entman ML. Noninvasive determination of pulse-wave velocity in mice. *Am J Physiol Hear Circ Physiol*. 1997;273:H494-H500.

23. Figueroa CA, Vignon-Clementel IE, Jansen KE, Hughes TJR, Taylor CA. A coupled momentum method for modeling blood flow in three-dimensional deformable arteries. *Comput Methods Appl Mech Eng*. 2006;195:5685-5706.

24. Moireau P, Xiao N, Astorino M, et al. External tissue support and fluid-structure simulation in blood flows. *Biomech Model Mechanobiol*. 2012;11(1-2):1-18.

25. Lujan HL, DiCarlo SE. Cardiac output, at rest and during exercise, before and during myocardial ischemia, reperfusion, and infarction in conscious mice. *Am J Physiol Regul Integr Comp Physiol*. 2013;304:R286-R295.

26. Hartley C, Reddy A, Madala S, et al. Hemodynamic changes in apolipoprotein E-knockout mice. *Am J Physiol Heart Circ Physiol*. 2000;279(5):H2326-H2334.

27. Hartley CJ, Taffet GE, Reddy AK, Entman ML, Michael LH. Noninvasive cardiovascular phenotyping in mice. *ILAR J*. 2002;43(3):147-58.

28. Claeys MA, Gepts E, Camu F. Haemodynamic changes during anaesthesia induced and maintained with propofol. *Br J Anaesth*. 1988;60:3-9.

29. Schmeling W, Farber N. Anesthetic actions on cardiovascular control mechanisms in the central nervous system. *Adv Pharmacol*. 1994;31:617-642.

30. Bramwell JC, Hill A V. The velocity of the pulse wave in man. *Proc R Soc B Biol Sci*. 1922;93:298-306.

31. Marque V, Van Essen H, Struijker-Boudier HAJ, Atkinson J, Lartaud-Idjouadiene I. Determination of aortic elastic modulus by pulse wave velocity and wall tracking in a rat model of aortic stiffness. *J Vasc Res*. 2001;38(6):546-50.

32. Williams R, Needles A, Cherin E, et al. Noninvasive ultrasonic measurement of regional and local pulse-wave velocity in mice. *Ultrasound Med Biol*. 2007;33(9):1368-1375.

33. Leloup AJA, Fransen P, Van Hove CE, Demolder M, De Keulenaer GW, Schrijvers DM. Applanation tonometry in mice: a novel noninvasive technique to assess pulse wave velocity and arterial stiffness. *Hypertension*. 2014;64:195-200.

34. Huo Y, Guo X, Kassab GS. The flow field along the entire length of mouse aorta and primary branches. *Ann Biomed Eng*. 2008;36(5):685-699.

35. Okada H, Takemura G, Kosai K, et al. Postinfarction gene therapy against transforming growth factor-beta signal modulates infarct tissue dynamics and attenuates left ventricular remodeling and heart failure. *Circulation*. 2005;111:2430-2437.

36. Li Y, Takemura G, Okada H, et al. Treatment with granulocyte colony-stimulating factor ameliorates chronic heart failure. *Lab Invest*. 2006;86:32-44.

# Chapter 6. Future Computational Enhancements

***Contributions.*** *Dr. Nitesh Nama and Dr. Miquel Aguirre Font contributed to the implementation of the nonlinear membrane. Dr. Nan Xiao implemented Reduced Order Unscented Kalman Filter (ROUKF) in our computational framework. I performed the analysis using ROUKF in computational FSI models of murine hemodynamics.*

Our computational framework, like all others, remains to be improved in order to address the limitations of this thesis. Firstly, our Fluid-Structure Interaction (FSI) method employs a linear membrane model for the vessel wall. Under the assumption of small deformations, we are not able to capture the large motion of the ascending thoracic aorta (ATA) which moves under the weight of the heart during the cardiac cycle. Since the large axial extensibility of the ATA is not captured, changes in ATA volume during systole are underestimated. This therefore leads to an underestimation of the axial compliance of the ATA which in turn could lead to a larger central pulse pressure.

Secondly, our models rely on a large number of parameters, whose estimation is the most non-systematic and time-consuming task of the computational effort. Efficiently fitting 3D computational models to animal-specific measurements indeed requires running many iterations of the same simulation. To address this limitation, data assimilation methods can be employed to automatically estimate the parameters of the computational model.

In this chapter we illustrate our ongoing effort to overcome these limitations.

## 6.1. Nonlinear ALE-FSI Framework

An FSI method is fundamental to capture wave propagation and to investigate the effects of local changes in arterial wall properties on the global hemodynamics. To account for FSI, a number of methods such as Arbitrary Lagrangian-Eulerian (ALE) methods[1], immersed methods[2] etc. have been proposed in the literature. The computational framework employed in this dissertation utilizes a coupled momentum method[3], which couples the elastodynamics equations of the deformation of the vessel wall as boundary condition for the fluid domain. It is a robust

and efficient scheme whose computational cost is comparable to that of rigid wall formulations while accounting for wave propagation phenomena. This method considers a linearized kinematics approach for the coupled problem, which allows to use an Eulerian representation of the solid equations and keep the mesh fixed under the assumption of small deformations. A fixed mesh approach combined with a membrane representation of the vessel wall renders a low computational cost for this method. These assumptions are well suited for the problems considered in this dissertation, albeit without the consideration of the large axial extensibility experienced by the ATA during the cardiac cycle. Several studies tracked the aortic root motion and showed that it is displaced downward during systole by about 9 mm in humans with a clockwise twist of 6 degrees during systole, before returning to its previous position in diastole[4,5]. This motion is caused by the traction imposed by the heart at each heartbeat. For this reason volume changes of the ATA during the cardiac cycle are likely to be underestimated in our current formulation.

In order to account for large deformations, nonlinear models need to be considered for the vessel wall. To account for both the material as well as the geometrical nonlinearities, we considered an ALE method with a moving mesh approach. ALE methods combine the best features of Lagrangian and Eulerian approaches, allowing greater distortion than a purely Lagrangian approach with more clear delineation at the interfaces than a purely Eulerian method[6].

### 6.1.1 Implementation of Arbitrary Lagrangian Eulerian Method

Here we briefly explain the steps taken by our group to implement ALE methods in our computational framework. Our nonlinear ALE-FSI method considers a moving mesh approach wherein the stiffness of the membrane is affected by both the nonlinear constitutive model (e.g., Neo-Hookean, exponential models, etc.) as well as the geometrical changes. More specifically, to account for the nonlinear behavior of the arterial wall, we employ an ALE approach where the fluid is described in ALE configuration, while the arterial wall is modeled as a nonlinear membrane using a Lagrangian formulation. The large deformations of the vessel wall are handled through a moving mesh approach by modeling mesh motion as being driven by a linear elasticity equation with Dirichlet boundary conditions. Similar to coupled momentum method, we utilize a stabilized finite element formulation for Navier-Stokes equation. The resulting system of equations is solved in a semi-segregated manner, such that the fluid-solid equations are

solved monolithically as one system while the mesh equations are solved as a separate system. We employ a generalized-alpha method for numerical time integration.

To obtain the in-vivo state of pre-stress of the arterial wall, required for any subsequent FSI simulations, we utilize a forward incremental pre-stress approach for biological membranes based on the strategy presented by Gee et al.[7].

### 6.1.2 Representative Examples

In this section we present some preliminary results from our group's ongoing efforts to develop the nonlinear ALE-FSI framework described earlier. Firstly, we show results corresponding to our moving mesh ALE approach. Figure 6.1 exhibits the velocity distribution and mesh motion in a cylindrical vessel with prescribed inlet flow and zero pressure outlet boundary condition at two different time instants. It can be observed that the mesh motion follows the large deformations of the vessel wall to maintain a good aspect ratio throughout the simulations, thereby confirming the effectiveness of our moving mesh ALE approach.

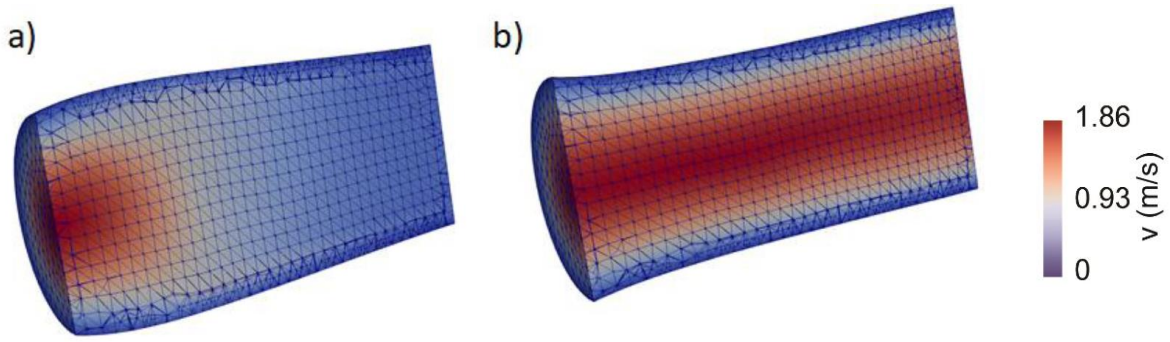


**Figure 6.1.** Blood velocity and mesh motion implemented in an ALE formulation of a cylindrical vessel at different time points.

Secondly, we demonstrate the effects of pre-stress on arterial wall mechanics by considering a pressure-inflation test on the geometry of a mouse aorta. Here, the arterial wall is modeled using a Neo-Hookean constitutive model (with c=8 kPa) with fixed-end boundary conditions. Two cases were considered: i) we employed our pre-stress algorithm to obtain the state of stress in the medically-imaged geometry at p = 80 mmHg; ii) we neglected the pre-stress and inflated the medically-imaged geometry using a standard forward analysis to obtain the state of stress at p = 80mmHg. Referring to Figure 6.2a and b, it can be observed that neglecting prestress results in significant over-estimation of von Mises stress and in an over-inflated geometry (Figure 6.2b) that deviates from the medically-imaged geometry by a non-zero displacement field. Further inflation of these configurations to p = 120 mmHg (Figure 6.2c and

d) again results in an overestimation of von Mises stress when prestress is neglected. Notably, neglecting the prestress results in unrealistically large deformations of the vessel geometry (Figure 6.2d).

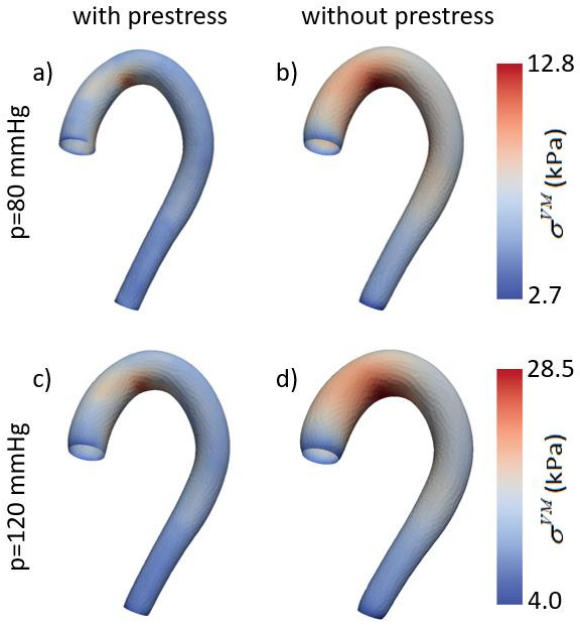


**Figure 6.2.** Pressure-inflation test on mice aorta with (a, c) and without prestress (b, d) at p=80 mmHg (a, b) and p=120 mmHg (c, d).

Next, we considered the effect of inclusion of prestress in an FSI simulation. To this end, we considered again a mouse aorta with a prescribed inlet flow (time period T=0.142 s), and three-element Windkessel outflow boundary conditions. Figure 6.3a and b show the spatial distribution of pressure at peak systole for cases with and without the inclusion of prestress, demonstrating significantly lower pressure for the case where prestress is ignored. Referring to Figure 6.3c, the pulse pressure is higher for the case where prestress is included. This can be attributed to the fact that the presence of prestress makes the vessel wall relatively stiffer, resulting in increased pulse pressure.

This formulation enhances the capabilities of our computational framework to allow investigations of cardiovascular flows in cases with large wall deformations, such as in the ascending thoracic aorta. Future work will focus on investigating cases with more complex subject-specific geometries as well as incorporating regionally-varying mechanical properties of the arterial wall.

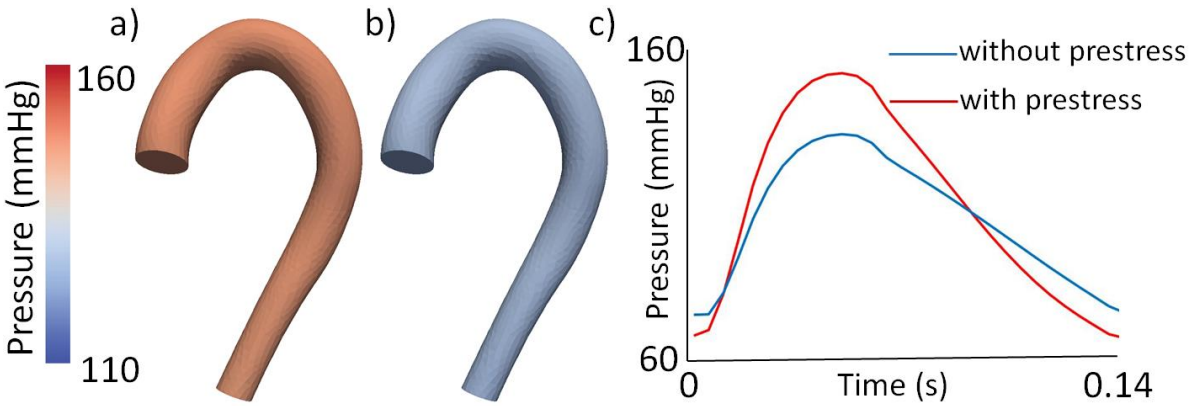


**Figure 6.3.** FSI simulation - Spatial distribution of pressure at peak systole for cases with (a) and without (b) prestress inclusion. c) Corresponding pressure waveform showing increased pulse pressure with inclusion of prestress.

## 6.2. Data Assimilation Methods

Patient- and animal-specific models require iterations over many simulations for parameter estimation, which can be a very time-consuming task. Data assimilation is the process of combining different sources of information to produce the best possible estimate of the true state of a physical system. The best estimate of the physical state of a system is evaluated by combining a mathematical model of the system with real-world measurements. Data assimilation techniques give a more accurate description of the true physical state than using a model or experimental measurements in isolation. They allow to identify the behavior of the "hidden" quantities and various parameter values of a physical system that often cannot be observed directly.

Herein, the mathematical model is our FSI computational framework which includes a formulation of 3D Navier-Stokes equations. The real-world measurements include ultrasound or magnetic resonance imaging measurements of blood velocity/flow and catheter based pressure measurements. The uncertain quantities that we wish to estimate include the parameters describing the boundary conditions at the outlets of the 3D model. The same methods can also be applied to estimate the stiffness of the vessel wall using data on vessel motion from time-resolved computed tomography or magnetic resonance imaging measurements.

There are two categories of data assimilation methods: variational approaches (optimization) and sequential approaches (filtering). Traditional optimization approaches to parameter estimation typically require substantial modification to the original simulation code, which can be quite challenging. Alternatively, sequential approaches offer easier integration with existing models, but the computational cost in terms of both the storage as well as the compute

time were prohibitive for large distributed mechanical models until recently. With the advent of ensemble and "unscented" filters and reduced-order variations, an effective and efficient estimation framework can be built around such modern filters. Our approach is built around the Reduced-Order Unscented Kalman Filter (ROUKF), first proposed by Moireau et al.[8]

### 6.2.1 Reduced-Order Unscented Kalman Filter (ROUFK)

In this work we employed ROUKF methods[8] which were previously implemented to work with our computational framework to perform parameter estimation. Further details of the implementation can be found in Xiao's thesis[9].

Briefly, the classical Kalman filter is a recursive least-squares estimator applied to linear dynamical models. Given an evolution equation $dX/dt = A(X)$, where $X$ is the state (e.g. velocity and pressure) and $A$ is a model operator (e.g., Navier-Stokes), the Kalman filter adds a correction $K(Z-H(X))$, where $Z-H(X)$ is an innovation (e.g., difference between a measurement $Z$ and observation of the state $H(X)$), and $K$ is a gain that reflects the level of confidence in a particular measurement. The evolution equation $dX/dt = A(X)+K(Z-H(X))$ can thus be seen as a balance between a model $dX/dt = A(X)$ and gain regulated data. The goal is to find the best guess ($\hat{X}$) of the true state so that the estimation error ($X - \hat{X}$) becomes smaller after accounting for each new measurement.

The Unscented Kalman filter allows to apply the Kalman filter to nonlinear systems using deterministically-generated set of states ($\hat{X}^{(i)}$) known as "sigma points", whose ensemble mean and covariance are used to approximate the true probability distribution of the estimation error.

ROUKF is designed for parameter estimation in large dynamical systems where the number of parameters to be estimated (on the order of a few dozen for our simulations) is smaller than the number of state variables (on the order of a million for our models) and where it is assumed that the uncertainty in the system can be attributed to the parameters.

Figure 6.4 shows the workflow of ROUFK in our computational framework, which can be summarized as follows:

i) We rewrite our finite element formulation of the blood flow problem in the general form of a discrete-time nonlinear dynamical system $X_n = A(X_{n-1})$ where $X$ is the unknown true state of the system and $A$ is a nonlinear forward operator. Given all measurements available before time $n$, $Z_1$ through $Z_{n-1}$, *a priori* estimate of the state $X_n$, denoted as $\hat{\chi}_n^-$, is the

estimate of the state before the measurement $Z_n$ is considered. *A posteriori* estimate, $\hat{\chi}_n^+$, is the estimate of the state after $Z_n$ is taken into account.

ii) The estimate of the true state ($\hat{X}_n$) can be split into its constituent parts: $\hat{X}_n = [\hat{\chi}_n, \hat{\theta}_n]^T$, where $\hat{\chi}_n$ represents the state vector for the internal state containing the finite element coefficients of velocity, acceleration, pressure and wall displacement fields and $\hat{\theta}_n$ is the state vector of the parameters to be estimated.

iii) Using the current *a priori* estimates $\hat{\chi}_n^+$, $\hat{\theta}_n^+$ and estimation error covariance factors matrices ($L_n^{\chi}$, $L_n^{\theta}$, $U_n$), a set of sigma points are first generated around the mean of the most recent estimate. The number of sigma points generated is *p+1*, where *p* is the number of parameters to be estimated.

iv) The sigma points are then propagated forward in time using the nonlinear forward operator, thus a total of *p+1* forward solves must be performed.

v) Upon completion of this step all the updated sigma points represent *a priori* estimate $\hat{\chi}_{n+1}^-$, $\hat{\theta}_{n+1}^-$.

vi) The observation operator (*H*) is applied to each sigma point to compute the innovation term: $\Gamma_{n+1}^{(i)} = Z_{n+1} - H(\hat{\chi}_{n+1}^{(i)-})$.

vii) Lastly, *a posteriori* estimate is computed using the Kalman filter equations.

viii) All the steps are repeated from step iii).

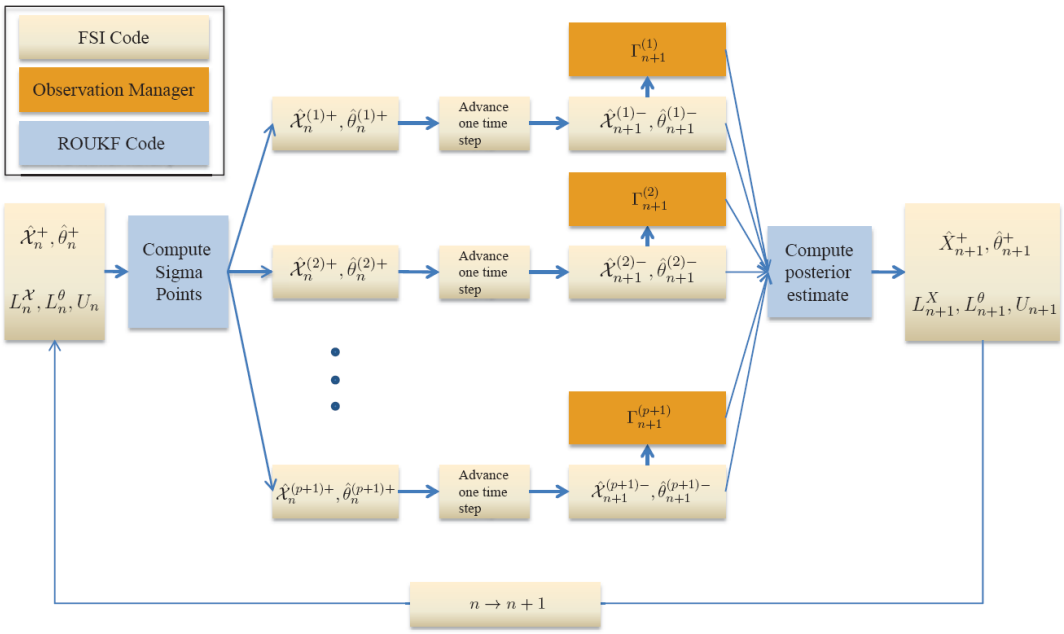


**Figure 6.4.** Schematic of the ROUFK workflow in our computational framework. Adapted from Xiao[9].

Different observation operators can be used to incorporate the clinical data into the estimation procedure: i) Nodal observation of pressure and velocity, ii) Cross-sectional observations of pressure and flow, and iii) Distance observations, which were implemented to take advantages of time-resolved medical images of vessel wall motion.

### 6.2.2 Representative Example

In this section, we present a preliminary numerical experiment demonstrating the estimation of Windkessel parameters in a mouse-specific model using ROUFK. Here, we considered a 20 week-old female wild type mouse and we attempted to estimate the Windkessel parameters of the two iliac arteries. The 3D model was reconstructed from micro-CT image data as explained in Chapter 3. The resulting finite element mesh contained ~1.8 million elements and ~340 thousands nodes. As before, spatially variable biaxial tissue properties were assigned to the arterial wall after in vitro characterization of the aorta at 4 different locations and at the carotid artery. The prescribed inlet flow was estimated from velocity and diameter ultrasound measurements at the ATA. Time resolved pressure acquired with a catheter at the ATA and noninvasive flow data measured with ultrasound at the infrarenal abdominal aorta (IAA) were used in this example to estimate the parameters. It is important to remark that the image data and the hemodynamics data (pressure and flow) were not acquired in the same animal. The flow and pressure waveforms were made periodic and repeated for as many cardiac cycles as necessary in the estimation. Figure 6.5 summarizes the estimation problem. We estimated the Windkessel parameters, $R_{prox}$, $R_{dist}$ and C, of right (1) and left (2) iliac arteries. The initial guess of the parameters are reported in Table 6.1 and they correspond to the parameter values tuned in Chapter 3. Values of the Windkessel parameters of all the other branches were fixed and they also corresponded to the values tuned in Chapter 3. The measurement error covariance was assumed to be a diagonal matrix with the diagonal entries taking the value $(10\ \text{mm Hg})^2$ for the pressure observations and $(5\ \text{mm}^3/\text{s})^2$ for the flow observations.

Figure 6.5b shows the evolution of the Windkessel parameters over six cardiac cycles. We observe that $R_{prox}$, after an initial increase followed by a decrease, stabilizes around a value of 20 $\text{Pa}/(\text{mm}^3\ \text{s}^{-1})$. $R_{dist}$ exhibits an overall increasing trend. The values of compliance C immediately deviate from the initial guess and stabilize.

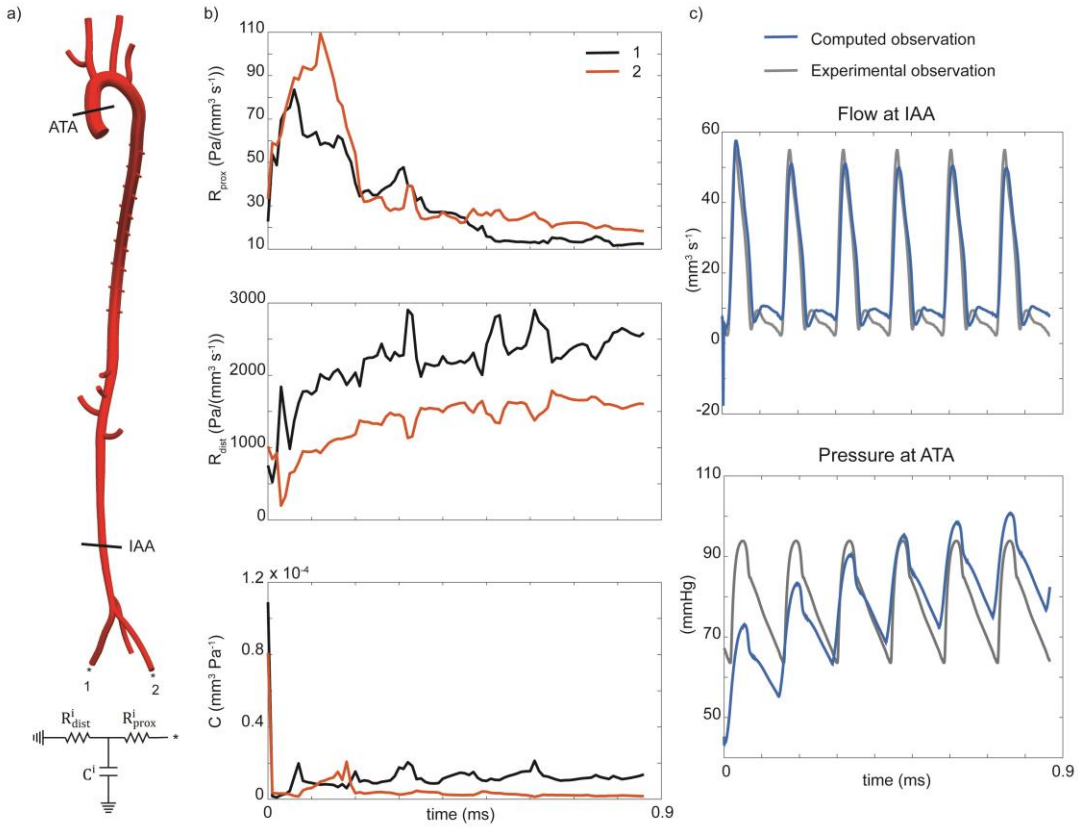


**Figure 6.5.** Representative example of parameters estimation using ROUFK in a mouse-specific anatomy. a) A 3D model of the aorta and its main branches for a 20 week-old female wild type mouse was reconstructed from micro-CT image data. Catheter-based pressure at the ATA and ultrasound flow at the IAA measurements were used to estimate the Windkessel parameters of right (1) and left (2) iliac arteries. b) Estimated values of $R_{prox}$, $R_{dist}$ and C for right (black) and left (red) iliac along 6 cardiac cycles. c) Comparison of computed (blue) and experimental (grey) observations at IAA and ATA.

Figure 6.5c shows the comparison between the measured data and the model observations, as computed from the mean estimate at each time step, at each of the observation sites, demonstrating a good match in the flow waveforms between model and data. The computed pressure increases during the six cardiac cycle due to increase in estimated $R_{dist}$.

This example is a preliminary result which aims to show that data assimilation techniques can be used for parameter estimation in computation hemodynamics. Flow data at more locations will be needed to be able to estimate a larger number of Windkessel parameters. Applying these techniques to all mouse models of vascular aging will allow us to estimate the boundary condition parameters in a systematic and automatic manner. This would therefore help to ultimately elucidate the changes that occur in the distal vasculature in hypertension and aging.

**Table 6.1.** Initial guess of the estimated Windkessel parameters.

| | $R_{prox}$ (Pa/(mm$^3$ s$^{-1}$)) | $R_{dist}$ (Pa/(mm$^3$ s$^{-1}$)) | C (mm$^3$ s$^{-1}$) |
|---|---|---|---|
| 1. Right iliac | 22.8 | 753.9 | 1.1 $10^{-4}$ |
| 2. Left iliac | 33.2 | 1016.9 | 8.1 $10^{-5}$ |

## Bibliography


1. Duarte F, Gomez R, Natesan S. Arbitrary Lagrangian-Eulerian method for Navier-Stokes equations with moving boundaries. *Comput Methods Appl Mech Eng*. 2004;193:4819-4836.

2. Mittal R, Iaccarino G. Immersed Boundary Methods. *Annu Rev Fluid Mech*. 2005;37:239-261. doi:10.1146/annurev.fluid.37.061903.175743.

3. Figueroa CA, Vignon-Clementel IE, Jansen KE, Hughes TJR, Taylor CA. A coupled momentum method for modeling blood flow in three-dimensional deformable arteries. *Comput Methods Appl Mech Eng*. 2006;195:5685-5706.

4. Stuber M, Scheidegger MB, Fischer SE, et al. Alterations in the local myocardial motion pattern in patients suffering from pressure overload due to aortic stenosis. *Circulation*. 1999;100:361-368.

5. Kozerke S, Scheidegger MB, Pedersen EM, Boesiger P. Heart motion adapted cine phase-contrast flow measurements through the aortic valve. *Magn Reson Med*. 1999;42(5):970-978. doi:10.1002/(SICI)1522-2594(199911)42:5<970::AID-MRM18>3.0.CO;2-I.

6. Donea J, Huerta A, Ponthot J, Rodr A. Chapter 14. Arbitrary Lagrangian-Eulerian Methods. In: *Encyclopedia of Computational Mechanics*.; 2004:413-437.

7. Gee M, Forster C, Wall W. A computational strategy for prestressing patient-specific biomechanical problems under finite deformation. *Int J Numer. Method. Biomed. Engng*. 2010;26:52-72. doi:10.1002/cnm.

8. Moireau P, Chapelle D. Reduced-order Unscented Kalman Filtering with application to parameter identification in large-dimensional systems. *ESAIM Control Optim Calc Var EDP Sci*. 2011;17(2):380-405. doi:10.1051/cocv/2011001.

9. Xiao N. Simulation of 3-D blood flow in the full systemic arterial tree and computational frameworks for efficient parameter estimation. PhD thesis, Stanford University, Stanford, CA, USA. 2014.

# Chapter 7. Discussion

## 7.1 General discussion

In this thesis, we used advanced computational models to investigate how local changes in wall mechanics impact global hemodynamics. We are motivated by the apparent insidious positive feedback loop that relates central artery stiffening and high blood pressure[1]. Central artery stiffening, indeed, plays critical roles in dictating both the local wall mechanics / mechanobiology and the global hemodynamics / pathophysiology[2]. *cf-PWV* is considered by many as the gold standard clinical measure of arterial stiffness[3,4], however it represents an average over a large portion of the arterial tree. Significant regional differences in aortic mechanics (geometry or properties) that could manifest with aging or disease and have detrimental effects on cardiac function can initially have limited impact on the numerical values of *cf-PWV*. The key question, therefore, is whether *cf-PWV* can detect early regional changes in aortic properties that could increase disease risk. Although this issue could be addressed via a lengthy clinical study, computational models enable time- and cost-efficient initial assessments.

We first presented FSI simulations for the human central vasculature using the best data available in the literature on age-dependent (30, 40, 60, and 75 years old) regional variations in aortic properties[5]. Results were generally consistent with clinical findings, including age-associated increases in pulse wave velocity and central pulse pressure, while rendering a higher resolution description of evolving local and global metrics of aortic stiffening. We then used these models to quantify spatial and temporal distributions of four different metrics of arterial stiffening (PP, Distensibility, *PWV* and elastic energy stored during the cardiac cycle) relative to the distribution of circumferential material stiffness. We found that, conversely to the other indices, *PWV* does not correlate well with the distribution of prescribed stiffness due to the dependency of *PWV* on other factors. *PWV* is influenced strongly by arterial tapering, branching, and wall properties heterogeneity. Importantly, we also quantified progressive age-related reductions in elastic energy stored during a cardiac cycle, which relates to local biomechanical functionality.

Limitations, however, included a lack of complete data on young healthy subjects as well as a lack of detailed anatomic changes with aging; to address these limitations, we ‘virtually aged’

a baseline aortic model by increasing luminal diameters and axial lengths numerically based on reported trends. Therefore, we next focused on mice models of vascular aging, which offer the advantages of allowing easier longitudinal studies and measurement of wall mechanics and hemodynamics than humans.

In order to create physiologically accurate FSI mouse models we first established a workflow to integrate *in vivo* and *in vitro* experimental data acquired on different subjects into a single computational model of murine vascular biomechanics. We then employed this workflow to develop FSI models for adult male and female wild type controls (C57BL/6 x 129/SvEv) under anesthetized conditions to which results from other models can be compared. In addition to wild type mice, we also developed FSI models of adult male and female fibulin 5-deficient mice and naturally-aged female mice. Fibulin 5-deficienct mice represent a model of vascular aging, due to loss of elastic fiber integrity[6]. In these models we observed that *cf-PWV* may not always capture regional differences in stiffness and we showed that higher spatial heterogeneity in wall structural stiffness results in lower values of measured *PWV*.

Many invasive methods of measuring cardiovascular parameters in mice alter the very quantity that is of interest. The potential impact of a pressure catheter on the hemodynamics of the mouse remains unclear from a theoretical perspective and cannot be evaluated experimentally without invoking many assumptions. Computational modeling offers an objective, nonintrusive approach for evaluating current methods of measurement. We investigated the effects of different commercially available catheter systems and observed that they alter the measured values of *PWV*. We found that a combination of two small profile catheters designed to measure pressure simultaneously in the ascending aorta and femoral artery increased *PWV* due to an overall increase in pressure within the arterial system. Conversely, a larger profile dual-sensor pressure catheter inserted through a carotid artery into the descending thoracic aorta decreased the *PWV* due to an overall decrease in pressure. In both cases, similar reductions in cardiac output were observed due to increased peripheral vascular resistance. As might be expected, therefore, invasive transducers can alter the very quantities that are designed to measure, yet advanced computational models offer a unique method to evaluate or augment such measurements.

Lastly, we employed a data assimilation technique based on a reduced-order unscented Kalman filter (ROUKF) to estimate boundary condition parameters. Parameter estimation is often the most time consuming and non-systematic task of the computational effort. We demonstrated

that previously developed methods[7] can be applied to mouse models of hemodynamics to estimate Windkessel model parameters from hemodynamic quantities measured experimentally.

### 7.2 Future work

In the future we want to expand our computational analysis to another mouse model of vascular aging. Hutchinson–Gilford (progeria) syndrome results in a severe form of premature aging in humans. Individuals affected by this syndrome tend to die between 8 and 21 years of age due to progressive arterial occlusions resulting in myocardial infarction or stroke. Transgenic mouse models of progeria have been developed and they exhibit, at 9–12 months of age, a thickened media in the thoracic aorta and carotid arteries due, in part, to diffuse accumulation of glycosaminoglycans associated with smooth muscle cell drop-out[8,9]. Increases in intramural collagen, thickening of the adventitia and calcification of the wall are also observed. Although more modest, the increases in glycosaminoglycan and collagen area fractions are also observed in both naturally aged mice[10], and fibulin-5 deficient models of premature aging[11]. Progeria mice represent the extreme case of a vascular aging phenotype. We want to investigate how changes in arterial wall mechanics in this mouse model affect the hemodynamics of the central vessels.

Notwithstanding the many similarities between human and murine cardiovascular systems that allow us to use mice as models for human cardiovascular disease, it is also important to remember the differences when considering application of the finds to humans. There are some fundamental differences between the murine and human cardiovascular systems from a physiologic and biomechanical perspective. For instance, mice have a much faster heart rate, much smaller dimensions, lower Reynolds numbers and, most critically for our purposes, a different distribution of aortic stiffness and pulse amplification along the aorta compared to humans. Humphrey et al.[12] reported the ratio of collagen to elastin in different species, showing how species with faster heart rates exhibit lower collagen to elastin ratios and higher *in vivo* axial stretches. Considering this, future work is needed to analyze differences between human and mice in regards to vascular aging. Specifically we want to investigate differences in biomechanics of the central vasculature and the impact of these differences on hemodynamics.

Lastly, in this thesis we performed preliminary work to demonstrate that data assimilation techniques can be employed in mouse models of hemodynamics to estimate values of boundary condition parameters. Applying these techniques to all mouse models of vascular aging will allow us to estimate the boundary condition parameters in a systematic and automatic manner. This can

help elucidate potential changes in the distal vasculature with hypertension and aging. Ultimately, we hope that these techniques and results can lead to advances in hypertension treatment and prevention.

## Bibliography


1. Humphrey JD, Harrison DG, Figueroa CA, Lacolley P, Laurent S. Central artery stiffness in hypertension and aging: a problem with cause and consequence. *Circ Res*. 2016;118(3):379-381. doi:10.1161/CIRCRESAHA.115.307722.

2. Laurent S, Boutouyrie P. The structural factor of hypertension: large and small artery alterations. *Circ Res*. 2015;116(6):1007-1021. doi:10.1161/CIRCRESAHA.116.303596.

3. Boutouyrie P, Vermeersch SJ. Determinants of pulse wave velocity in healthy people and in the presence of cardiovascular risk factors: Establishing normal and reference values. *Eur Heart J*. 2010;31:2338-2350. doi:10.1093/eurheartj/ehq165.

4. Barodka VM, Joshi BL, Berkowitz DE, Hogue CW, Nyhan D. Implications of vascular aging. *Anesth Analg*. 2011;112:1048-1060. doi:10.1213/ANE.0b013e3182147e3c.

5. Roccabianca S, Figueroa CA, Tellides G, Humphrey JD. Quantification of regional differences in aortic stiffness in the aging human. *J Mech Behav Biomed Mater*. 2014;29:618-634. doi:10.1016/j.jmbbm.2013.01.026.

6. Wan W, Gleason RL. Dysfunction in elastic fiber formation in fibulin-5 null mice abrogates the evolution in mechanical response of carotid arteries during maturation. *Am J Physiol Hear Circ Physiol*. 2013;304(5):H674-H686. doi:10.1152/ajpheart.00459.2012.

7. Moireau P, Bertoglio C, Xiao N, et al. Sequential identification of boundary support parameters in a fluid-structure vascular model using patient image data. *Biomech Model Mechanobiol*. 2013;12(3):475-496. doi:10.1007/s10237-012-0418-3.

8. Varga R, Eriksson M, Erdos MR, et al. Progressive vascular smooth muscle cell defects in a mouse model of Hutchinson-Gilford progeria syndrome. *Pnas*. 2006;103(9):3250-3255. doi:10.1073/pnas.0600012103.

9. Conneely KN, Ganesh SK, Collins FS, et al. A farnesyltransferase inhibitor prevents both the onset and late progression of cardiovascular disease in a progeria mouse model. *Proc Natl Acad Sci*. 2008;105(41):15902-15907. doi:10.1073/pnas.0807840105.

10. Ferruzzi J, Madziva D, Caulk AW, Tellides G, Humphrey JD. Compromised mechanical homeostasis in arterial aging and associated cardiovascular consequences. *Biomech Model Mechanobiol*. 2018;17(5):1281-1295. doi:10.1007/s10237-018-1026-7.

11. Ferruzzi J, Bersi MR, Uman S, Yanagisawa H, Humphrey JD. Decreased elastic energy storage, not increased material stiffness, characterizes central artery dysfunction in fibulin-5 deficiency independent of sex. *J Biomech Eng*. 2015;137(3):031007.

12. Humphrey JD, Eberth JF, Dye WW, Gleason RL. Fundamental role of axial stress in compensatory adaptations by arteries. *J Biomech*. 2009;42(1):1-8.